Reforming of methane over Ni-based catalyst : development of Ni-Zr materials

Ye Wang

Sorbonne Université

École doctorale SMAER (ED 391), Sciences Mécaniques Acoustique Électronique Robotique

Programme Doctoral Génie des Procédés, Institut Jean Le Rond d'Alembert

Sichuan University

School of Chemical Engineering

Reforming of methane over Ni-based catalyst: development of Ni-Zr materials

Reformage du méthane sur catalyseur à base de Ni: développement de matériaux Ni-Zr

镍基催化甲烷重整：Ni-Zr 材料的研究进展

By Miss YE WANG

Doctoral thesis in Chemical Engineering - Chemical Technology

Supervised by Prof. Patrick DA COSTA and Prof. Changwei HU

Presented in public on 14 September 2020

The scientific committee:

Mrs. FECHETE Ioana, Full Professor, Université de Technologie de Troyes, **Reviewer**

Mr. LIU Haichao, Full Professor, Peking University, **Reviewer**

Mr. GUIBERT Philippe, Full Professor, Sorbonne Université, Examinator

Mr. JIANG Bo, Professor, Sichuan University, Examinator

Mr. HU Changwei, Full Professor, Sichuan University, Supervisor

Mr. DA COSTA Patrick, Full Professor, Sorbonne Université, Supervisor

Dédicace

Acknowledgments

I sincerely thank China and the China Scholarship Council for my scholarship in the Sorbonne Universités, France.

First and foremost, I would like to thank my supervisors, Prof. Patrick DA COSTA and Prof. Changwei HU. They gave me the incentive and support to perform this research. Prof. Patrick DA COSTA and Prof. Changwei HU have profound knowledge, rigorous experimental attitude, and unique insights into the development of the research fields. This rigorous scientific attitude and spirit are very helpful for my future research work. Herein, I would like to express my sincere respect and sincere thanks to Prof. Patrick DA COSTA and Prof. Changwei HU.

I would like to thank my reviewers Prof. FECHETE Ioana and Prof. LIU Haichao. Meanwhile, I would like to thank my dissertation committee members, Prof. GUIBERT Philippe, Prof. JIANG Bo, thank all of you for willing to participate in my defense. Under your comments and suggestions, my doctoral dissertation has been greatly improved.

I am very grateful to the research group that gives me a lot of help both in research and life. Chao SUN, Hailong ZHANG, Mira IBRAHIM, Katarzyna Świrk, Bo WANG, Maria MIKHAIL, Yutao LI, Armando IZQUIERDO and my colleagues in China Qing ZHAO, Yannan WANG, Li LI, Chaojun CUI. I need to thank all of you for helping me so that I can complete my doctoral research.

I would like to thank all professors, researchers, administrators, engineers and technicians in Institut Jean le Rond d'Alembert. Prof. Stéphane ZALESKI, Prof.

Philippe GUIBERT, Prof. Guillaume LEGROS, Alexis MATYNIA, Evelyne MIGNON, Anne MARCHAL, Renaud JALAIN, Jean-François KRAWCZYNSKI, Jean-Marie CITERNE, Jérôme BONNETY, Hugo DUTILLEUL, Christian OLLIVON, Dominique BUSQUET, Jêrome PÉQUIN, and Frédéric SEGRETAIN. Thank all of you for providing support for my doctoral research.

In the end, I want to thank my friends for their constant companionship and encouragement. Thanks to my father: Chunjian WANG and mother: Youqun CHEN for giving me the best love. Thanks to my brother: Rensi WANG supports me in all aspects. Thanks to Fuhuan WANG for my companionship and help for the last five years, which make my life to be more full and warmer.

Résumé

Abstract

Abstract

Résumé

L'augmentation des émissions anthropiques de CO_2 encourage la recherche à developper de nouveaux procédés de recyclage du CO_2. Le reformage à sec du méthane (DRM: $CH_4(g) + CO_2(g) \leftrightharpoons 2CO(g) + 2H_2(g)$, $\Delta H^0_{298\,k} = +247\ KJ \cdot mol^{-1}$) représente un moyen intéressant de convertir deux gaz à effet de serre (CO_2 et CH_4) en produits à forte valeur ajoutée. Le Nickel, métal de transition, alternatif aux métaux nobles, est universellement considéré comme un métal actif la réaction de reformage à sec du méthane, en raison de sa forte activité et de son faible coût. Cependant, les catalyseurs à base de Ni peuvent se désactiver au cours de la réaction à cause du frittage de ou des phases actives et du dépôt de carbone, inhibant ainsi leurs applications industrielles. Il est donc nécessaire de développer un catalyseur à la fois rentable, capable de résister à des températures élevées et à la désactivation.

Ce travail de thèse se concentre sur de nouvelles stratégies visant à améliorer le frittage et le dépôt de carbone sur un catalyseur à base de nickel. Ces stratégies comprennent l'utilisation de différentes méthodes pour la préparation des catalyseurs et de différents promoteurs. La relation entre la performance et la structure est analysée par un test d'activité et de stabilité, et de multiples caractérisations, telles que la mesure de Surface Brunauer-Emmett-Teller (BET), la diffraction des rayons X (XRD), la réduction programmée en température d'H_2 (H_2-TPR), la désorption programmée de température du CO_2 (CO_2-TPD), la microscopie électronique à transmission (TEM), la spectroscopie Raman et la spectroscopie de photo-électrons X (XPS).

Tout d'abord, les catalyseurs Ni-Zr ont été préparés par la méthode d'hydrolyse de l'urée en une étape et ont été évalués pour la réaction de reformage à sec du méthane. Les catalyseurs Ni-Zr ont présenté une activité, une sélectivité et une stabilité supérieures à celles préparées par la méthode d'imprégnation traditionnelle à l'éthanol, ce qui pourrait

être attribué à la formation d'une solution solide NiO-ZrO_2, ainsi qu'à leur surface spécifique plus élevée et à des tailles plus petites de particules de nickel métallique.

Dans un deuxième temps, différents promoteurs tels que Y, Al, Mn et Mg ont été synthétisés par co-imprégnation lors de la synthèse des catalyseurs Ni-Zr par la même méthode (hydrolyse de l'urée). Les performances catalytiques des catalyseurs Ni-Zr promus ont été testés dans les même conditions opératoires en reformage du méthane. Le catalyseur modifié par l'Yttrium améliore la résistance au dépôt de carbone en augmentant les sites basiques de faible et moyenne intensité.
La présence d'Al permet quant'à elle d'améliorer les performances catalytiques grâce à un volume et un diamètre de pores plus importants due à l'introduction du promoteur.
L'addition de Mn entraîne une augmentation de l'activité avec le temps de travail en raison de la structure plus stable des espèces de ZrO_2 et de la redistribution des espèces de nickel pendant la réaction catalytique.
Seul le Mg a un effet inhibiteur sur les catalyseurs Ni-Zr.

Enfin, par rapport aux différents promoteurs et pour résumer, les choix de différents promoteurs se traduisent par une diversification de la surface spécifique, de la taille et de la basicité des cristallites de Ni^0, ce qui peut avoir un impact d'autant plus important sur les performances catalytiques des catalyseurs préparés.

Mots-clés : Reformage à sec du méthane, Gaz de synthèse, Catalyseurs au nickel, ZrO_2 synthétique, Solution solide

Abstract

The increase of anthropogenic CO_2 emissions is encouraging extensive research on CO_2 recycling processes. Dry reforming of methane (DRM: $CH_4(g) + CO_2(g) \leftrightharpoons 2CO(g) + 2H_2(g)$, $\Delta H^0_{298\,k} = +247\ KJ \cdot mol^{-1}$) represents an attractive way to the conversion of two greenhouse gases (CO_2 and CH_4) into valuable products. Transition metal Ni is universally considered as an alternative to noble metal for DRM, due to its high activity and low cost. However, Ni-based catalysts suffered deactivation resulted from sintering of the active phase and carbon deposition, thus its practical application is not actually possible. So, there is a need to develop a cost-effective catalyst, able to withstand high temperatures and able to resist deactivation.

Herein, this research concentrates on new strategies towards improving the sintering and carbon deposition over nickel-based catalysts. These strategies include the use of different methods to prepare catalysts and different promoters. Meanwhile, the relationship between performance and structure is analyzed by activity test and multiple characterizations, such as Brunauer-Emmett-Teller (BET), X-ray diffraction (XRD), H_2-temperature programmed reduction (H_2-TPR), CO_2-temperature programmed desorption (CO_2-TPD), Transmission electron microscopy (TEM), Raman spectroscopy and X-ray photoelectron spectroscopy (XPS).

First, the Ni-Zr catalysts were prepared by the one step urea hydrolysis method and were evaluated on the dry reforming of methane. Synthetic Ni-Zr catalysts generally presented higher activity, selectivity, and stability compared to the one prepared by the traditional ethanol impregnation method, which could be attributed to the formation of NiO-ZrO_2 solid solution, as well as its higher specific surface area and smaller particle size of metallic nickel.

Secondly, different promoters (such as Y, Al, Mn, and Mg) with Ni-Zr were co-synthesized by the same method (urea hydrolysis). The catalytic performance of synthetic Ni-Zr catalysts with promoters was tested in reforming for methane. Among them, the Y-modified catalysts improved the resistance to carbon deposition by increasing the weak and medium-strength basic sites. Also, the presence of Al could enhance the catalytic performance due to larger pore volume and diameter after aluminum introduction. The addition of Mn led to the increase of the catalytic activity with time on stream because of a more stable structure of ZrO_2 species and a redistribution of nickel species.

Thus, the choices of different promoters result in diversification in the specific surface area, Ni^0 crystallite size, and basicity, which may further affect the catalytic performance of prepared catalysts.

Keywords: Dry reforming of methane, Syngas, Nickel catalysts, Synthetic ZrO_2, Solid solution

Sommaire

Outline

Outline

Chapter I

Introduction

1. Introduction

1.1 Overview

Carbon dioxide reforming of methane also called dry reforming of methane (DRM) is of significant importance because of at least the following reasons. Firstly, since CO_2 and CH_4 were both greenhouse gases, the utilization of CO_2 and CH_4 could provide a way to reduce the greenhouse effect. Secondly, CO_2 and CH_4 were also produced in the pyrolysis of biomass, then the utilization of CO_2 and CH_4 could also make more valuable the pyrolysis gases, enhancing the whole process more practical. Thirdly, because the main components of the marsh gas from digestion were CO_2 and CH_4, the utilization of CO_2 and CH_4 could provide a way to make the biogas value-added. However, if pyrolysis gases and biogas were directly used as fuel, the purification of the gases to remove CO_2 was generally needed, since CO_2 could not contribute to combustion, providing heat. Gases with a high content of CH_4 could also be used in fuel cells for electricity generation, and synthesizing organic compounds such as $CHFCl_2$, CCl_4, CH_3OH, and HCOOH. On the other hand, in addition to the use of CO_2 in beverage additives, CO_2 could be used in supercritical extraction agents and synthesizing polyketide and polycarbonate. Whereas the DRM reaction utilizes directly both CO_2 and CH_4 simultaneously, which reduces the step of separation. Hence the DRM reaction is an effective way for the protection of the environment and the effective utilization of energy resources, thereby providing ways for sustainable development.

It is well known that the C-H bond in CH_4 is difficult to be activated, while CO_2 is the upmost oxidized state of carbon, which is also very stable. The co-activation of both C-H bond in CH_4 and C-O bond in CO_2 faced challenging difficulties. Besides, because of the thermodynamics limitation, DRM reaction was usually performed at high temperature (~800 °C). On that conditions, other reactions would influence the performance of the catalysts for DRM reaction (Equation 1), among which were

methane cracking (Equation 2), the reverse water-gas shift (RWGS) reaction (Equation 3), and the disproportionation of CO (Equation 4).

$$CH_4+CO_2 \rightarrow 2CO+2H_2 \quad \text{(Equation 1)}$$

$$CH_4 \rightarrow C+ 2H_2 \quad \text{(Equation 2)}$$

$$H_2+CO_2 \rightarrow H_2O+CO \quad \text{(Equation 3)}$$

$$2CO \rightarrow CO_2+C \quad \text{(Equation 4)}$$

Many researches already focused on Pt, Ir and Rh for DRM reaction, because noble metal exhibited high activity, stability and selectivity for DRM reaction even at so high temperature. However, noble metals are very expensive, so more and more researches investigate on Ni-based catalysts for dry reforming of methane. Because Ni-based catalysts with activity and selectivity comparable to those of noble metals, but with lower cost, have been extensively employed as promising catalysts for reforming of methane. While, high-temperature operation usually caused metal Ni sintering, which would lead to catalyst deactivation. Another challenge is that carbon could form on nickel metal, thereby leading to the deactivation of catalyst. So, research dose much investigation to solve those problems. Promoters, such as La, Ce, La, Zr and so on, can inhibit the sintering of nickel metal, restrain the formation of carbon and enhance the ability to remove coke. The supports possess basic sites, the periclase-like structure and mesoporous structure would enhance the activity for DRM reaction. Those special material supports would exert effect on nickel particle size and dispersion of nickel, thereby improve the property of the catalysts. Some special catalysts like core-shell catalysts could prevent the accumulation of carbon, thereby enhancing the stability of catalyst. Although many efforts, such as the addition of promoter, the special supports, mesoporous structure and Core-shell structure, have been made in solving the problems, there are many challenges to achieve industry for Ni-based catalysts. ZrO_2 had been widely used for reforming catalysts, because of the high oxygen mobilization, enhancement of metal dispersion, and the proper interaction between nickel and ZrO_2. Besides, ZrO_2 could increase the basic site, which could enhance the adsorption of CO_2, thereby enhance the ability for carbon deposition elimination, as a consequence, and

promote the performance of catalyst. While if it possesses too strong basic site, it could promote carbon deposition. So, we should adjust the interaction between nickel and zirconium by synthesis method and the promoter. My Ph.D. research concentrates on the Ni-based catalyst with new ZrO_2 support for dry reforming of methane. It also investigates the effect of synthesis method and mesoporous structure ZrO_2 adjusted by Al, Mg, Y and Mn on the performance of catalyst for dry reforming of methane.

The thesis is thus divided into 7 chapters. Chapters 1-3 include the general introduction, research background and experiments of catalytic activity and characterizations respectively. The fourth, fifth and sixth chapters introduce the main experimental results, including a series of Ni-Zr catalysts, synthetic Ni-Zr catalysts modified by Mg, Y, Al and Mn, and the relationship between structure and activity. The seventh chapter is a summary of the experimental results

The first chapter is a general introduction to this thesis. The general contents of various chapters and the research objectives are introduced.

The second chapter presents a literature review on the research background. At firstly, as carbon dioxide emissions increase, as well as the severe greenhouse effect, the utilization of carbon dioxide is becoming more and more important for our environment. The source of carbon dioxide is introduced. Secondly, the three aspects of the capture, fixation and utilization of carbon dioxide are described as the second part. Thirdly, synthetic fuels are introduced, which is developing potential in CO_2 resources utilization. The definition of synthetic fuels, synthetic routes and problems that need to be solved in the development of synthetic fuels are also discussed. The fourth part presents the introduction of the dry reforming of methane, including three aspects of experiment methods, mechanism and catalysts.

The third chapter mainly introduces the experimental part. In the first part an introduction of the catalytic test is presented, including the procedure of activity test

based on temperature effects, and the stability test, as well as the calculation methods of both CH_4, CO_2 conversion and H_2/CO ratio. The second part describes the different characterizations (BET, XRD, H_2-TPR, CO_2-TPD, TGA, TEM, XPS and Raman).

The four chapter focuses on the comparison of the catalytic performance between a series of Ni-Zr catalysts prepared by one-step urea hydrolysis method and Ni/ZrO_2 catalyst prepared by traditional ethanol impregnation method. The catalysts were tested in dry reforming of methane (DRM) at 750 °C with a mixed flow of CH_4:CO_2:Ar=10:10:80 and GHSV= 24,000 h^{-1}. The materials were characterized by means of N_2 adsorption-desorption, X-ray diffraction, temperature-programmed reduction by H_2, temperature-programmed desorption of CO_2, X-ray photoelectron spectroscopy, and thermogravimetry analysis coupled by mass spectrometry. In this work, the NiO–ZrO_2 solid solution could obtain by new method with strong interaction between nickel and zirconium, which leads to the high surface area, small nickel particle size and more content of weak and medium-strength basic sites. Besides, more adsorption oxygen species and just slight sintering occur on 10Ni-Zr and 15Ni-Zr catalysts during the reaction. Therefore, 10Ni-Zr and 15Ni-Zr exhibited higher activity and stability for dry reforming of methane.

In chapter fifth, the results of Ni-Zr catalysts modified by Y, Mg, Al and Mn are presented. All the catalysts are prepared by one-step urea hydrolysis method. In the first part, Y is introduced to Ni-Zr catalyst. And found that yttrium-doped NiO–ZrO_m catalyst was found to be novel for carbon resistance in the CO_2 reforming of methane. The second part is the Mg promoter. The NiO-ZrO_2 catalyst modified by Mg results in a decrease in the activity, selectivity, and stability of NiO-MgO-ZrO_2 catalyst for DRM. The promoter of Al is the third part. An enhancement in the sintering resistance and high resistance to loss of nickel during a long-term catalytic test was found on Al promoted catalyst. Mn is the last part. Mn could promote the stability of ZrO_2 support during the reaction process.

The chapter sixth compared the effect of the promoters on the catalytic performance of Ni-Zr catalysts for dry reforming of methane. The calcined, reduced or after reaction catalysts were characterized by H_2-TPR, CO_2-TPD, XRD, XPS, TGA, Raman and TEM. Meanwhile, the specific surface area, Ni^0 crystallite size, Ni reducibility, basicity, surface species and carbon deposition are studied to understand the relationship between structure and activity, selectivity and stability of Ni-Zr based catalysts.

Finally, I conclude this thesis by a summary of all experiments and the perspectives for further experiments on dry reforming of methane. The main results of the experimental chapters (chapter 4, chapter 5 and chapter 6) are summarized, which could contribute to the further study of Ni-Zr catalysts and synthetic ZrO_2 supported catalysts. Besides, based on doctoral research, some suggestions are provided for further research on dry reforming of methane.

1.2 Objectives of Ph.D. work

The aims of this Ph.D. thesis to:

- Investigate a series of Ni-Zr catalysts and Ni/ZrO_2 catalysts to obtain the optimal nickel content of Ni-Zr catalyst, at the same time, investigate the influence of different content nickel metal on performance of catalyst.

- Investigate Ni-Zr catalysts modified by Al, Mg, Y and Mn on performance of dry reforming of methane. as well as understand their physicochemical properties by a variety of characterization, such as H_2-TPR, CO_2-TPD, TG-MS, XPS, XRD, TEM, IR.

- Investigate the influence of the different promoters on the physicochemical properties of ZrO_2 materials to support Ni-based catalysts for dry reforming of methane.

Thus, this research topic could help to understand how to enhance the properties of ZrO_x materials, and then obtain the optimal catalyst for dry reforming of methane.

Chapter II

Literature review on the utilization of carbon dioxide

2. Literature review on the utilization of carbon dioxide

2.1 Source of carbon dioxide

With the development of the economic world, the demand for energy is increasing, such as, crude oil, natural gas and coal. However, those carbon resources would decrease with our utilization, simultaneously, release the CO_2. Thus, there is an urgent need to find a new renewable carbon resource. Except for the biomass and pyrolysis gases as the perfect gas for renewable resources, CO_2 could be also created renewable carbon resources [1]. Besides, the content of CO_2 in the air has increased rapidly since industrial time, because of the increasing of combustion of fossil fuels. Still in 2000, the amount of CO_2 in the atmosphere increased to 720 GT/year (1 GT = $1*10^9$ tons), and the detailed data showed in Figure 2-1. Interestingly, the carbon dioxide produced from the ocean can reach to 100 GT for one year. The amounts of biological respiration are the same as the photosynthesis land and water, which is approximately 60 GT. Except for the carbon dioxide produced by humans, plants and animals, about 500 GT comes from human activity, which mainly comes from fossil fuels. Large amounts of carbon dioxide are released into the atmosphere, leading to an increase in the content of CO_2 year-by-year.

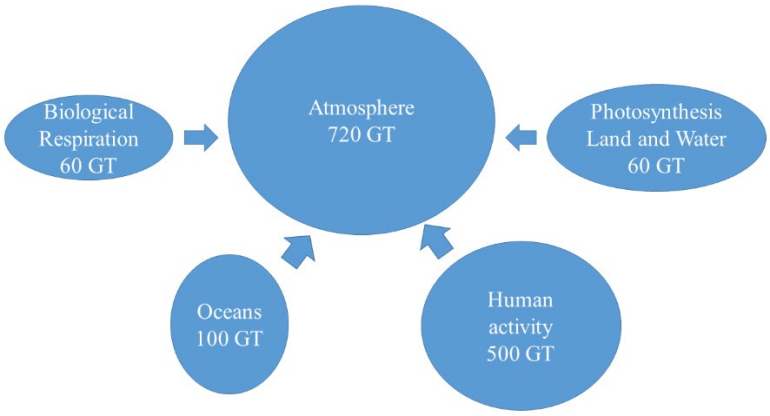

Figure 2-1 The detail of CO_2 emissions for one year

As the figure 2-2 shows, the World Meteorological Organization (WMO) announced that the concentration of heat-trapping greenhouse gases (CO_2) in the atmosphere have reached another new record high (407.8 parts per million in 2018 for CO_2). While in 2011, the atmospheric concentration of CO_2 and CH_4 was 393.1 and 1.8 ppm, respectively. Until April 2020, the CO_2 level has exceeded 416.21 ppm [2]. The global warming potential (GWP) of methane is about 28–36 times higher than that of CO_2, which also causes a serious Earth's radiative imbalance [3-5]. Thus, there are so many CO_2 resources we can use, especially the carbon dioxide produced by fossil fuels.

(A)

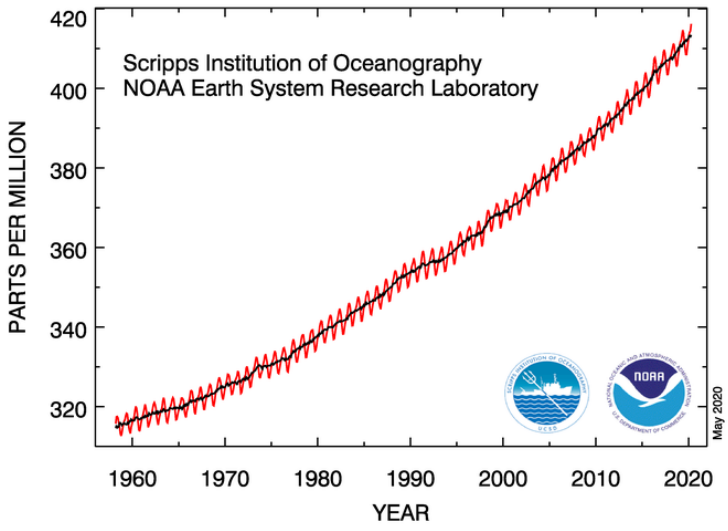

(B)

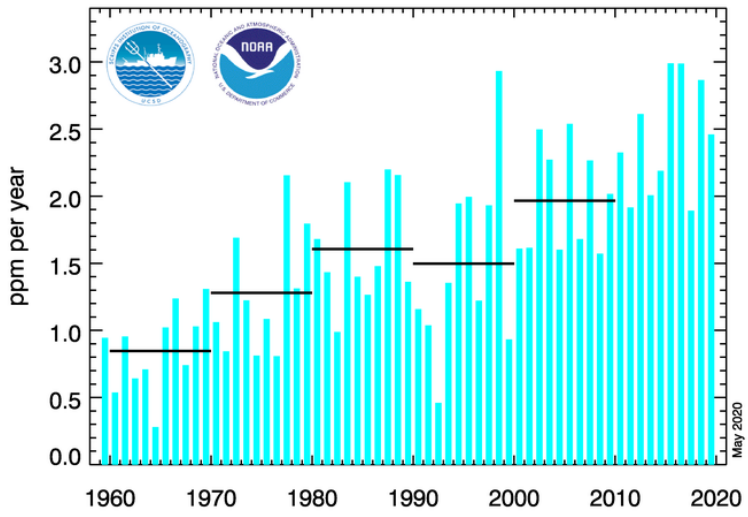

Figure 2-2 The annual mean carbon dioxide (A) and carbon dioxide growth rates (B) at Mauna Loa observatory [2].

Although that carbon dioxide comprises only about 0.034 % by volume in air, it can lead to the acidity (pH 5.7) of precipitations from the troposphere, as well as the natural acid rain, which could result in a series of social problems, such as corrosion of buildings. Besides, CO_2 is greenhouse gas, the same as methane, which is mainly responsible for global warming and environmental problems [6]. It is pointed out that the global greenhouse gas emission sources in 2004 of which approximately 77 % are represented by CO_2 emissions, as shown in Figure 2-3. [7]. 56.6 % comes from carbon dioxide derived from the consumption of fossil fuels.

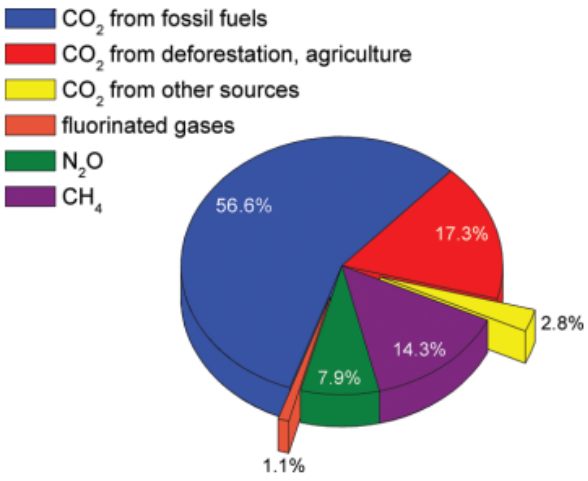

Figure 2-3 Global greenhouse gas emission sources in 2004 of which approximately 77% are represented by CO_2 emissions

In addition, the demand for energy increases year-by-year, as shown in Figure 2-4. Most of them are oil, coal and gas. The utilization of those energies (oil, coal and gas) could increase CO_2 emission. So, there is a desperation to decrease the emission of CO_2 and creating a renewable carbon resource. The reduction of fossil fuel consumption is the main way to decrease the emission of CO_2. However, we can't leave for the utilization of fossil fuel in the 21st. Therefore, in order to meet the amount of energy consumption, an alternative resource should be created. Thus, to reduce the amount of carbon dioxide in the atmosphere, the utilization of CO_2 plays a very important role in the environment and energy.

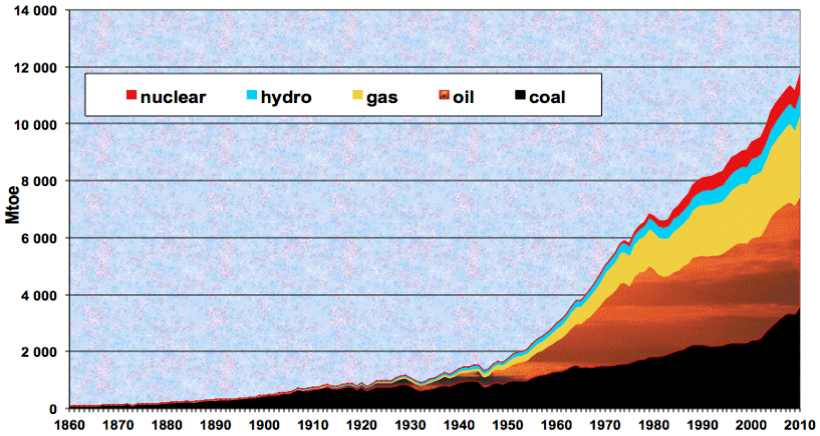

Figure 2-4 The annual demand for energy.

2.2 The utilization of carbon dioxide

2.2.1 Capture of carbon dioxide

It is widely accepted that the majority reduction of CO_2 in the atmosphere is now mainly due to the capture of carbon dioxide and storage (CCS). On one hand, the content of CO_2 in the atmosphere is very high. On the other hand, the huge emission of CO_2 from the fossil fuel would continue until 2030 and beyond. Therefore, the reduction of CO_2 in the atmosphere by the capture of carbon dioxide plays a very important role in the aspect of global warming [8].

There are two ways to capture CO_2. The most feasible solution is to compress the CO_2 in the flue gas of the power plant and inject it into a closed underground environment, which is convenient for the storage of CO_2 without causing leakage and has a small impact on the surrounding environment. This method is suitable for burying carbon dioxide in the exhausted oil and natural gas wells, coal, shale, and saline formations for a long time. The need for long burials and special terrain has hindered widespread development [9]. Another way is capturing the gaseous CO_2 by some adsorption material, such as the capture of CO_2 from power plant emissions. In general, carbon dioxide is absorbed by special materials, which are difficult to reuse and possess low adsorption capacity. Figure 2-5 presents the basic schemes showing the types of CO_2

capture by special materials.

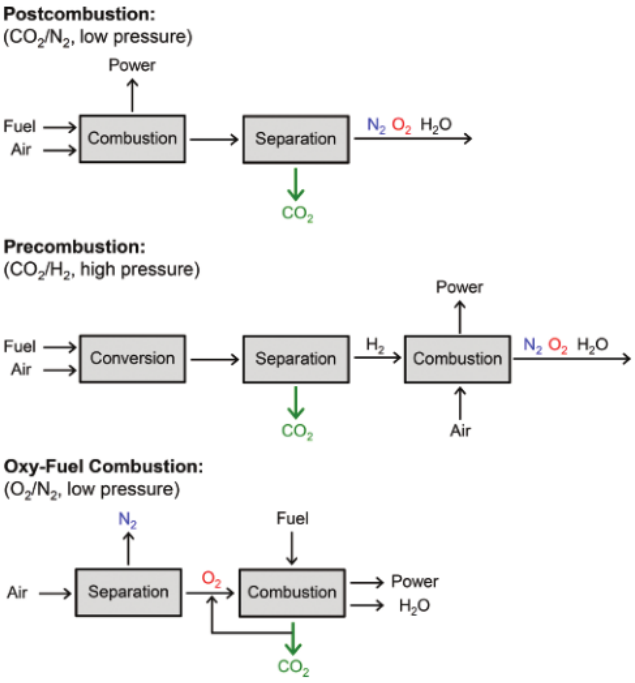

Figure 2-5 The basic schemes showing the types of CO_2 capture

It is generally known that the selectivity of CO_2 is the crucial performance parameter for the materials of CO_2 capture. High selectivity is fundamental, such that the CO_2 could be removed from the flue gas completely. However, the affinity between materials and CO_2 should be optimized. Because a too strong interaction would lead to higher energy for desorption of CO_2, while too weak interaction would result in too weak adsorption of CO_2. Furthermore, the high stability under the conditions of capture and regeneration also should be considered. Thus, some special materials, such as aqueous alkanolamine absorbents, solid porous adsorbent materials and metal-organic frameworks are widely concerned for CO_2 capture, due to the suitable interaction [10-13].

Many researchers have focused on the investigation of CO_2 capture in metal-organic frameworks (MOF) [12-14]. Because except for above affinity, metal-organic frameworks possess their potential applications in a variety of aspects, including gas

storage, drug delivery, heterogeneous catalysis, molecular separations, extraordinary surface areas, potential scalability to industrial scale, as well as finely tunable pore surface properties. Such as $Zn_4O(BDC)_3$ (MOF-5), as shown in Figure 2-6 [15, 16]. Thus, metal-organic frameworks show the good activity of the material for CO_2 capture. While metal-organic frameworks show low chemical and thermal stability, which is generally lower than that of zeolites and other porous inorganic solids. Because the coordination bonds of metal and ligand components are relatively weak [7].

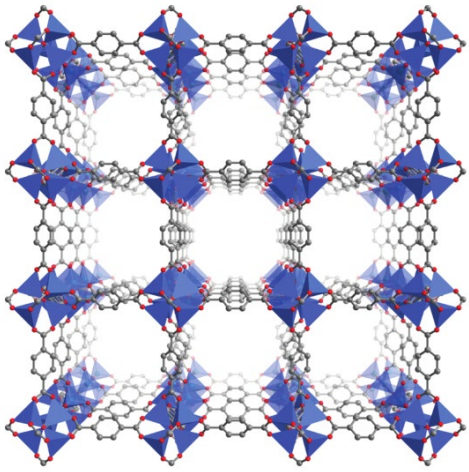

Figure 2-6 A portion of the crystal structure of $Zn_4O(BDC)_3$ (MOF-5). Blue tetrahedra represent ZnO_4 units, while gray and red spheres represent C and O atoms, respectively; H atoms are omitted for clarity.

McDonald [17] prepared metal-organic frameworks mmen-Mg2 (dobpdc) materials to capture CO_2. Dynamic gas adsorption/desorption cycling experiments indicated that the mmen-Mg2 (dobpdc) materials could be regenerated at the condition of repeated exposures to simulated air and flue gas mixtures. And the cycling capacities is 1.05 mmol/g (about 4.4 wt %) after 60 min of exposure to flowing carbon dioxide (390 ppm) in simulated air at 25 °C, and 2.52 mmol/g (about 9.9 wt %) after 15 min of exposure to flowing carbon dioxide (15%) in nitrogen at 40 °C. The purity of the carbon dioxide removed from dry air and flue gas in these processes reached to 96% and 98%, respectively. In brief, the good performance ≪ characteristics ≫ of mmen-Mg2 (dobpdc) materials manifested that compared with both amine-grafted aqueous and

silicas amine solutions, it would become to be an exceptional new adsorbent for carbon dioxide capture. Huang et al. [18] provided a new method by channel-wall functionalization for preparing a new adsorbent two-dimensional covalent organic frameworks (2D COFs) to capture CO_2, which exhibited the outstanding ability for CO_2 capture. They thought that the present channel-wall engineering method would be of vital importance to exploring high-performance 2D COFs in the field of gas storage and separation.

A lot of CO_2 is adsorbed and separated from the atmosphere, which is the first step, and the second one is the utilization of carbon dioxide, e.g. fixation or conversion.

2.2.2 Fixation of carbon dioxide

Carbon dioxide is a very widely available and cheaper carbon resource as important chemical intermediates, compounding to polymers, pharmaceuticals, and agrochemicals [19]. Besides, fixation CO_2 can be transformed to carbonate species, which are important for various applications, such as aprotic solvents, additives in fuel, monomers in polymeric structures, raw materials in various reactions, and electrolytes in secondary batteries [20]. Therefore, the fixation of carbon dioxide is the way as a carbon feedstock to build organic structures with high atom economy [21].

Actually, the main way of CO_2 fixation is fixed by photosynthesis in plants, microorganisms and algae. And the other way is the alternative autotrophic CO_2 fixation pathways [22, 23]. For the latter, there are many methods for fixation and utilization of carbon dioxide, such as, traditional catalytic, photocatalytic, electrochemical, photochemical, and photoelectrochemical. Most of them are catalytic systems, which have been investigated to catalyze the fixation of carbon dioxide in the past decades, for example, metal oxides, metal–salen complexes, N-heterocyclic olefins, N-heterocyclic carbenes, Schiff bases and Ionic liquids [24-28]. Among them, the Ionic

liquids (ILs) are a new outstanding research field. The utilization of ILs for the CO_2 fixation into value-added chemicals is considered a promising technology, due to the high thermal and chemical stability, high solubility, easy recyclability, non-flammability, low vapor pressure, functional variability, and biodegradability [29-31]. Dai et al. [32] found that amino-acid-based ILs act as bifunctional absorbing materials of CO_2 through the amine group and carboxylate group. It is pointed out that nontoxic, recyclable, and biodegradable ILs are more popular in the research of fixation CO_2. Saptal et. al [33] prepared a new multimolar Ionic Liquids (ILs) with a quaternary alkyl ammonium cation and an amine anio to fix the carbon dioxide. Those synthesized ILs not only exhibited highly catalytic performance, but also were the biodegradable sources with the Non-toxic and recyclable properties.

2.2.3 General application of carbon dioxide

CO_2 is also commonly used in the food, physics and agriculture industry. At first, CO_2 as food additives in beverages. CO_2 could be used for sparkling wine, soft drinks and beverages, and the amount depends on the requirements of normal production. For example, making soft drink, increased the amount of carbon dioxide by pressurizing, so that the carbonic acid of calcium carbonate reacts with water. Generally speaking, it is produced by fermentation of sugar, washed, purified, dried, cooled, and then compressed into a liquid. CO_2 is primarily used in carbonated drinks, such as carbonation agents, packaging gas, refrigerant, leavening agent, pH regulator and processing aid [34, 35].

Carbon dioxide, which would be a gas under standard conditions, forms a solid when cooled, called dry ice (Frozen solid CO_2), which is applied for refrigeration of foodstuffs, meat products and other frozen foods. Dry ice has also found application in many technical processes where low temperature is required.

CO_2 is the most used supercritical fluid. When the temperature and pressure are higher than the critical temperature (31°C) and pressure (73.8 atm) of CO_2, the properties of CO_2 will change. The density of CO_2 is close to liquid and its viscosity is close to gas. This CO_2 is called the supercritical state CO_2. There are several advantages to the use of supercritical fluid CO_2 as an extraction agent. Firstly, the solubility of many substances in carbon dioxide changes with pressure, so selective extraction can be carried out. Secondly, the CO_2 is very stable, thus the properties would not change during the process of extraction. Thirdly, CO_2 is less toxic and harmful to the environment. Therefore, CO_2 supercritical fluid has been used in the food industry, cosmetic industry, chemical industry and medical industry currently [36].

The use of CO_2 in agriculture is focused on application of carbon dioxide in photosynthesis systems by chlorophyll in plants. The biological technologies of CO_2 in man-made active photosynthesis systems to produce food biomass and biofuels have been obtained in the laboratory [37].

2.3 Synthetic fuels

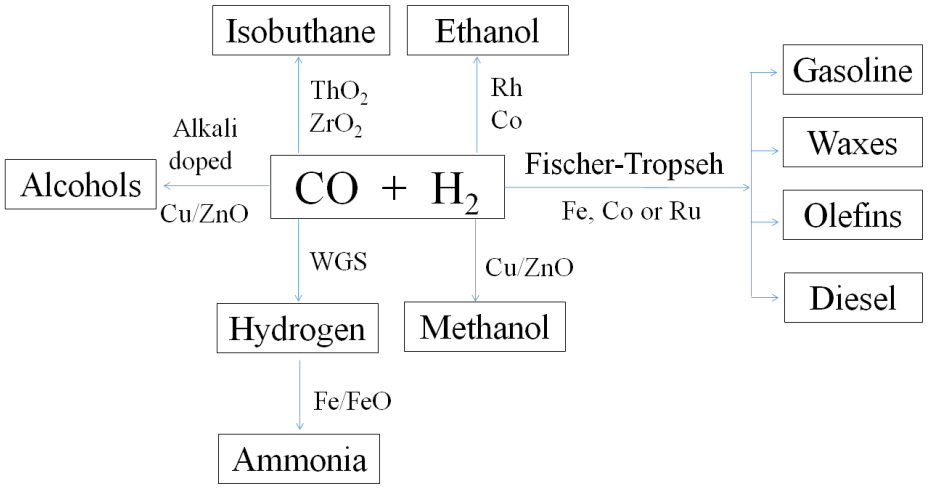

Figure 2-7 The ethanol, hydrogen, isobuthane, methanol and ammonia synthesized by syngas (adapted from Ref. [38])

Carbon-based fossil fuels, such as natural gas, oil, and coal supplied the main of the world's energy. However, the sources of fossil energy are nonrenewable, and they are used out finally. So, renewable energy sources have gained an increased attention. There is various way to synthesize fuels, most of them are synthesized by syngas. The syngas is a mixture of gas with CO and H_2. As shown in Figure 2-7, the syngas can synthesize ethanol, isobuthane, hydrogen, methanol, ammonia and so on. Co and Rh usually used to make ethanol. While Cu has been identified as the most active metal to synthesize methanol [38]. Another important utilization of syngas is the Fischer-Tropsch. This will be explained in detail in the next section.

2.3.1 Fischer–Tropsch (FT) synthesis

The Fischer-Tropsch (FT) synthesis is an extremely important route to utilization of the carbon monoxide hydrogenation to produce fuels, like higher hydrocarbons and oxygenates compounds. The Fischer Tropsch synthesis started in the 20th century and went through three periods [39]:

(i) 1910-1926: Development of the coal liquefaction by means of hydrogenation, and the Fischer-Tropsch (FT) synthesis from;

(ii) 1927-1945: Scientific works and industrialization of the coal-to-petroleum process and FT synthesis;

(iii) 1930-1990: Consolidation and expansion of the synthetic-fuel technology from Germany to other countries

Now, researches focus on the efficient large-scale production of synthetic fuels from FT synthesis. And those fuels are attractive, clean, carbon-neutral, and sustainable energy sources and also can replace non-renewable fuels in a wide range of applications. Cobalt-based catalysts were applied in most modern FT synthesis, especially for gas-to-liquids reaction (GTL) [40, 41]. Deelen et al. [41] found cobalt nanocrystals

supported on a carbon nanotube (CNT) exhibited high stability for FT synthesis even a reaction of 100 h. Because, the cobalt is relatively expensive, Fe is an alternative active metal [42]. However, some challenges still have to be faced. The Co-based catalyst suffered from the deactivation, due to the aggregation of active metal. The control of product selectivity depends on catalytic property and operational conditions, which is the main challenge of FT synthesis research [43].

2.3.2 other methods

In addition to Fischer–Tropsch (FT) synthesis, biomass offers the possibility to create a renewable synthetic fuel. Lignocellulosic biomass is the renewable resource, who has gained much attention. Because the production of biofuels has substantially less harmful effects on the environment when compared to the fossil non-renewable process. The following is the main routes of producing fuels from the Lignocellulosic biomass: (1) gasification to produce syngas, (2) liquefaction and pyrolysis to produce bio-oils, (3) hydrolysis to form aqueous phase sugars or lignin, which can be further processed via fermentation or reforming, and (4) transesterification of triglycerides to produce biodiesel [44, 45]. These four sustainable routes in the production of liquid biofuel by low-cost feedstock may reach the industrial level in the further.

Mixed alcohol synthesis (MAS) is another way to produce fuels [46]. MAS is a process that alcohol produces from coal or natural gas derived from syngas (Equation 4). The obtained mixed alcohols can be used as fuels, fuel additives for octane, and intermediates for value-added chemicals such as medicine, cosmetics and polyester [47]. This process realizes the efficient conversion of natural gas and clean utilization of coal resources. This process is a highly exothermal reaction (e.g. 2 CO(g) + 4 H_2 (g) → C_2H_5OH (g) + H_2O (g), $\Delta H_{298} = -253.6$ kJ/mol of ethanol, $\Delta G_{298} = -221.1$ kJ/mol of ethanol), which essentially needs the combination of CO insertion functions and carbon-chain growth over the catalysts. Thus, the key to the development of mixed alcohol synthesis is the selective control of alcohol. Usually, considering the

commercial production of mixed alcohols, it is most important to achieve higher C^{2+} alcohol selectivity and comparable alcohol yield. Those two side reactions composed of hydrocarbon formation (Equation 5) and water–gas-shift reaction equilibrium (Equation 6) should be avoided in this process [46].

$$2n\ H_2 + n\ CO \rightarrow C_nH_{2n+1}OH + (n-1)\ H_2O \qquad \text{(Equation 4)}$$

$$(2n+1)\ H_2 + nCO \rightarrow C_nH_{2n+2} + n\ H_2O \qquad \text{(Equation 5)}$$

$$H_2O + CO \rightarrow CO_2 + H_2 \qquad \text{(Equation 6)}$$

2.4 Dry reforming of methane

2.4.1 Experiment condition

Dry reforming of methane (DRM) is an effective way to use two greenhouse gas (methane and carbon dioxide) at the same time to produce syngas (hydrogen and carbon monoxide), which is not only waste utilization, but also beneficial to the environment. As the global warming problem is more serious, more and more researchers turned to investigate dry reforming of methane, due to the utilization of two greenhouse gas (methane and carbon dioxide). So, DRM reaction is very meaningful for environmental sustainability, especially for the shortage of energy. Besides, DRM reaction ($CH_4 + CO_2 \rightarrow 2CO + 2H_2$) produces the two gas with CO/H_2 ratio of 1, which could produce methanol by F-T synthesis because of the very suitable CO/H_2 ratio [5]. However, a large number of parallel side reactions, such as the CO disproportionation, CH_4 decomposition, reverse water gas shift and so on (Table 2-1), take place during the DRM reaction [48]. To avoid the side reactions, several methods are conducted on the dry reforming of methane, such as the traditional catalytic method, Plasma catalytic method, Photocatalytic method and Microwave-assisted catalytic method.

Table 2-1 Possible parallel reactions during dry reforming of methane

Reaction Number	Reaction	$\Delta H°_{298K}$ KJ/mol
	Dry reforming	
1	$CO_2 + CH_4 \rightarrow CO + H_2$	+247
	Reverse water gas shift	
2	$CO_2 + H_2 \rightarrow 2CO + H_2O$	+41
	Carbon forming reactions	
3	$CH_4 \rightarrow C + 2H_2$	+74.9
4	$2CO \rightarrow C + CO_2$	-172.4
5	$CO + H_2 \rightarrow C + H_2O$	-131.3
6	$CO_2 + 2H_2 \rightarrow C + 2H_2O$	-90
	Oxidative coupling of methane	
7	$CO_2 + 2CH_4 \rightarrow C_2H_6 + H_2O + CO$	+106
8	$2CO_2 + 2CH_4 \rightarrow C_2H_4 + 2H_2O + 2CO$	+284
	dehydrogenation	
9	$C_2H_6 \rightarrow C_2H_4 + H_2$	+136
	Hydrogenation of CO and CO_2	
10	$CO + 2H_2 \rightarrow CH_3OH$	-90.6
11	$CO + 3H_2 \rightarrow CH_3OH + H_2O$	-49.1
12	$CO_2 + H_2 \rightarrow HCOOH$	15
	Reforming	
13	$CH_3OCH_3 + CO_2 \rightarrow 3CO + 3H_2$	+258.4
14	$C_2H_6 + 2H_2O \rightarrow 2CO + 5H_2$	+350
15	$C_2H_6 + 2CO_2 \rightarrow 4CO + 3H_2$	+430
16	$C_2H_4 + 2CO_2 \rightarrow 4CO + 2H_2$	+290
17	$C_2H_4 + 2H_2O \rightarrow 2CO + 4H_2$	+210
	Dehydration	

18	$2CH_3OH \rightarrow CH_3OCH_3 + 2H_2O$	-37
	Hydration	
19	$CH_3OCH_3 + 3H_2O \rightarrow 2CO_2 + 6H_2$	+136
20	$CH_3OCH_3 + H_2O \rightarrow 2CO + 4H_2$	+204.8
	Methanation	
21	$CO_2 + 4H_2 \rightarrow CH_4 + 2H_2O$	-165
22	$CO_2 + 3H_2 \rightarrow CH_4 + H_2O$	-206.2

2.4.1.1 Traditional catalytic method

Most researchers investigated the traditional catalytic method for dry reforming of methane. The traditional catalytic method achieves the reaction temperature by heating, which is very convenient to operate. Because it needs a very high temperature, so that the energy consumption is too large, especially for industrial applications. Under traditional method, DRM reaction need high temperature (about 800 ºC), because DRM reaction ($CH_4 + CO_2 \rightarrow 2CO + 2H_2$, ΔH_{298K}= +247 kJ/mol) is a strong endothermic reaction [49]. Besides, the gas volume of the forwarding reaction increases. Therefore, increasing reaction temperature and decreasing pressure is beneficial to the reaction. Besides, traditional DRM also require efficient and selective catalysts to promote the forward reaction, however, the catalyst suffered from the deactivation by carbon deposition and/or sintering of active metal [50, 51].

2.4.1.2 Plasma catalytic method

In recent years, many researches pay attention to the plasma catalytic method for dry reforming of methane. X. Tu [52] investigated the influence of plasma-catalyst on activity for low temperature DRM reaction. They found that Ni/γ-Al_2O_3 catalyst showed high activity at 50 W conditions that correspond to 270 °C. Yabe [53] found

that 1 wt.%Ni/10 mol%La-ZrO_2 catalyst in 6.9 w electric field equivalently at 150 °C showed high DRM activity with about 77.2% CH_4 conversion and 87.6% CO_2 conversion. So, there are several advantages to the plasma catalytic method. At firstly, it can conduct at low-temperature (lower 300 ºC). Secondly, the synergistic effect of the low-temperature plasma and solid catalyst could strengthen both strong interaction of plasma-catalyst, thereby improving the activity of catalysts. Lastly, the catalyst could be restructured in the electric field, thereby enhancing the activity of the catalysts. However, there are also several disadvantages to plasma catalytic method. At firstly, after reaction at high degree plasma conditions, the structure of catalyst would change, thus it needs special catalysts. Secondly, the stability of catalyst is not very good, due to the structure of catalysts would change under plasma conditions. Lastly, it needs the special equipment [54-56].

2.4.1.3 Photocatalytic method

Only a few literatures investigate DRM through Photocatalytic method [57, 58]. Y. Kohno et al. [58] investigate that photocatalytic dry reforming of methane over ZrO_2 and MgO, and found that it could occur around room temperature. D. Shi et al. [59] reported that the photocatalytic CO_2 reforming of methane on Cu/CdS–TiO_2/SiO_2 catalyst at 393 K and they can obtain the main product of acetone. According to the literature, the use of photoenergy with photocatalyst would break the thermodynamic barrier of endothermic reaction, thus the reaction could occur at lower temperature. While unfortunately H_2 was scarcely obtained from methane, because other products such as H_2O, surface formate species and so on, were observed instead. So, the selectivity of catalyst is difficult to control.

2.4.1.4 Microwave-assisted catalytic method

Microwave-assisted catalytic method leads to a higher performance of the dry

reforming reaction. B. Fidalgo et al. [60] found that the conversion of CO_2 and methane under microwave heating is higher than those under electric furnace heating. Because the catalyst could be heated by the energy of microwave directly, while for traditional heating, the temperature of catalyst is higher than that of the surrounding atmosphere [61]. However, the CH_4 decomposition reaction and the CO_2 gasification reaction would be improved under the microwave conditions.

2.4.2 Mechanisms purposed for DRM

It is well known that the C-H bond in CH_4 is difficult to be activated, while CO_2 is the most stable state of carbon, which is also very stable. The co-activation of both C-H bond in CH_4 and C-O bond in CO_2 faced challenging difficulties [5]. Besides, because of the thermodynamics limitation, DRM reaction is usually performed at high temperature (~800 °C). Much progress and significant achievements have been reported to understand the mechanism of DRM reaction [49, 62-68].

Generally, CO_2 is adsorbed on surface of catalyst and forms bicarbonate, monodentate and/or bidentate carbonate species. The structure of those three types of carbonate species is shown as shown in Figure 2-8 [69]. Some studies showed that bidentate carbonates could promote coke elimination [69-71]. While Zhang et al. [72] thought that monodentate carbonates on Ni–ZrO_2 catalysts were the main active intermediates for CO_2 dissociation. Monodentate and bidentate carbonate species are derived from the CO_2 adsorption of medium-strength basic sites [69, 72, 73]. Therefore, medium-strength basic sites could promote the adsorption and/or activation of CO_2. Besides, different adsorption mechanism occurs in monodentate and bidentate carbonate species on different catalysts.

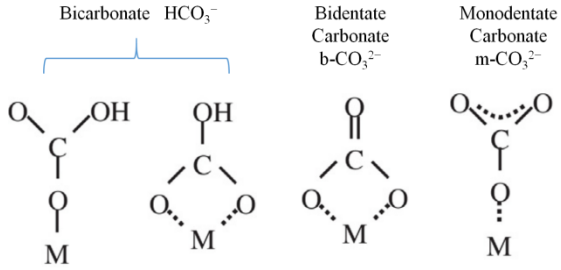

Figure 2-8 The adsorption carbonate species on metal sites (M).

Guo et al. [68] found that depending on the dissociation of CH_4, the formation of monodentate carbonate species might be as follows:

$CH_4 + * \rightarrow CH_x + (4 - x)/2H_2$

$H_2 + 2* \rightarrow 2H*$

$CO_2 * + H* \rightarrow CO + OH*$

$CO_2 * + OH* \rightarrow CO_3 * + H*$

where * denotes active sites on the Ni catalyst.

Bachiller-Baeza et al. [74] and Takano et al. [69] reported that the bidentate carbonate can be formed on the presence of oxygen vacancies in ZrO_2 as follows:

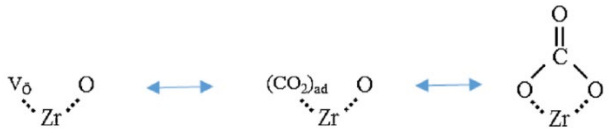

where v_δ denotes oxygen vacancies in ZrO_2.

It is pointed out that the mechanism of dry reforming of methane is similar to various catalysts. There are some differences between different catalysts. For example, Jiang et al. [66] reported the reaction mechanism over NiO-MgO. At first, CH_4 dissociates on the Ni^0 site to give out C and H species. CO_2 reacts with the surface C species to form CO. The adsorbed CO_2 also reacts with H and then decomposes to give CO. Therefore, the reaction mechanism was proposed as follows:

$CH_{4,g} \rightarrow CH_{x,s} + (4\text{-}x)H_s$ (1)

$CH_{x,s} \rightarrow C_s + xH_s$ (2)

$C_s + CO_{2,g} \rightarrow CO_g$ (3)

$CO_{2,g} \rightarrow CO_{2,s}$ (4)

$CO_{2,s} + Hs \rightarrow COOH_s$ (5a)

$COOH_s \rightarrow CO_g + OH_s$ (5b)

(s: adsorbed states, g: gas phase).

Wang et al. [62] reported that CH_4 could be dissociated and adsorbed as CH_3 and H species on Ni-Si/ZrO_2 catalyst, whereas CO_2 could be adsorbed and dissociated to form adsorbed CO and O species. Part of adsorbed H species could be combined by adsorbed CO_2 to form formate, while part of adsorbed O species could react with adsorbed CH_3 species, thereby promoted the dissociation of methane, which might be as follows:

I: $CH_4 \leftrightharpoons CH_{3(ads)}+H_{(ads)}$

$CO_{2(ads)} \leftrightharpoons CO_{(ads)}+O_{(ads)}$

$2H_{ads} \leftrightharpoons H_2$

$CO_{ads} \leftrightharpoons CO_g$

II: $CH_4 \leftrightharpoons CH_{3(ads)}+H_{(ads)}$

$CO_{2(ads)}+ H_{(ads)} \leftrightharpoons COOH_{ads} \leftrightharpoons CO_{ads}+OH_{ads}$ (like RWGS)

$2OH_{ads} \leftrightharpoons H_2+H_2O$

$CO_{ads} \leftrightharpoons CO_g$

2.4.3 DRM catalysts

Generally, many parallel reactions (Table 2-1) occur during the DRM process, which seriously influences the activity, selectivity and stability of the target products (H_2 and CO) [75]. Therefore, it is the key point of industrialization to explore an efficient and stable catalyst for DRM. Thus, studies on active metal [76-83], catalyst synthesis [2, 69, 84-87], as well as choice of precursors and supports [88-92], promotion effects [65, 93-97] and mechanism of carbon deposition [4, 35, 49, 50, 98, 99] are main strategies for improving DRM catalysts in recent years (Table 2-2).

Table 2-2 A brief description and comparative summary for catalysts of dry reforming of methane.

Method	Species/Approach	Reference
active metal	➢ Rh nanoparticles for CO_2 reforming of methane	[76]
	➢ Lattice Strained Ni-Co alloy as a high-performance	[77]
	➢ Elucidating the impact of Ni and Co loading on the selectivity of bimetallic NiCo catalysts	[78]
	➢ Pd-CeO_2 nanocatalyst for Low temperature dry reforming of methane	[100]
	➢ Pt, Ru doped TiO_2 for methane reforming	[80]
	➢ Rh and Co based catalysts for dry reforming of methane	[101]
catalyst synthesis	➢ Stable Ni–Mo nanocatalysts on single-crystalline MgO	[2]
	➢ Different calcination atmospheres (N_2, O_2 and H_2) for Ni/ZrO_2 catalyst	[102]
	➢ Sol–gel synthesis of Ni–Co/Al_2O_3–MgO–ZrO_2 nanocatalyst	[81]
	➢ Small-sized Ni@SiO_2 catalyst with shell-nuclear structure	[84]
	➢ Sequential impregnation vs. sol-gel synthesized Ni/Al_2O_3-CeO_2 nanocatalysts	[103]
	➢ A sintering and carbon-resistant Ni-SBA-15 catalyst prepared by solid-state grinding method	[104]
	➢ Facile one-pot synthesis of highly dispersed Ni nanoparticles embedded in HMS	[86]

	➢ Bimetallic mesoporous Ni-Co-CaO-ZrO_2 catalysts prepared by template-free method	[105]
supports	➢ The effect of support promotion (La, Al, Mn) over natural clay-based nickel catalysts	[88]
	➢ ZrO_2 with the reducing and oxidizing abilities, the unexceptionable thermal and chemical stability, and the high oxygen mobilization	[50, 62, 87, 102, 106-109]
	➢ SBA-15 support with mesoporous structure	[97, 104, 110-113]
	➢ Hydrotalcite-derived materials with special periclase-like structure	[89, 93, 94, 96, 114-116]
Promoters	➢ Yttrium promotes the dispersion of metal nickel, carbon-resistant, the formation of oxygen vacancy	[50, 69, 93, 96, 97, 110, 117]
	➢ Ce and/or Zr promoter could increase the basic sites and oxygen mobility of catalysts	[65, 89, 96, 97, 116, 118-121]
	➢ La promoter could enhance the reduction of the nickel and the increase the medium strength and weak basicity	[53, 88, 114, 119, 122]
	➢ $La_{0.8}Sr_{0.2}Ni_{0.8}M_{0.2}O_3$ perovskite modified by Bi, Co, Cr, Cu and Fe	[123]
carbon deposition limitation	➢ Highly Carbon-Resistant Y Doped NiO–ZrO_m Catalyst	[50]
	➢ Atomically dispersed nickel as coke-resistant active sites	[124]
	➢ Surface carbon as a reactive intermediate over Ni/MnO catalyst	[49]
	➢ Highly carbon-resistant Ni–Co/SiO_2 catalysts derived from phyllosilicates	[79]

➢ Carbon intermediates during CO_2 reforming of methane over $NiCaOZrO_2$ catalyst	[125]
➢ High coke-resistance $MgAl_2O_4$ islands decorated catalyst	[126]
➢ Coke tolerance of Ni/Al_2O_3 nanosheet catalyst	[98]

The noble metal-based catalysts exhibited high activity, stability and selectivity almost without carbon deposition, such as Rh, Ru, and Pt [80, 127-130]. However, nickel-based catalysts would be a more suitable choice for the DRM, because of the comparable activity, stability and selectivity to noble metal catalysts [102, 131, 132]. Considering the cost, Ni-based catalyst is the alternative active metal for dry reforming of methane. However, the fatal drawback of the Ni-based catalyst is the rapid deactivation deriving from carbon deposition and sintering of Ni species [107, 133]. Several methods have been studied in the resistance of coke and sintering [79, 84, 104, 126]. The carbon deposition on the active sites can via CH_4 decomposition (Equation 2), CO disproportionation (Equation 4) and the reverse carbon gasification reaction (Equation 7) [49, 107]. Thermodynamically, the equation (2) tends to be at high temperature and low pressure, while the other two equations (4) and (7) are favored at low temperature and high pressure. Herein, DRM reaction is processed under high temperature with an atmosphere, thus the coke usually comes from the equations (2).

$$CH_4 \rightarrow C + 2H_2,\ \Delta H°_{298K} = 75\ kJ{\cdot}mol^{-1} \qquad \text{(Equation 2)}$$

$$2CO \rightarrow C + CO_2,\ \Delta H°_{298K} = -172\ kJ{\cdot}mol^{-1} \qquad \text{(Equation 4)}$$

$$CO + H_2 \rightarrow C + H_2O,\ \Delta H°_{298K} = -131\ kJ{\cdot}mol^{-1} \qquad \text{(Equation 7)}$$

Generally, suitable supports and promoters improved the catalytic performance by adjusting the interaction between nickel and the support. Besides, the temperature of calcination, the order of materials loading on support, the reduction temperature, and the nickel particle size also altered the performance of the catalysts [89, 116, 120, 134].

It is suggested that by investigating the interaction with the supports, promoters with active metal, as well as their structural adjustment, the development of DRM catalysts to reach industrial level is feasible [5].

2.4.3.1 Effect of promoters

Promoters could enhance the activity of nickel-based catalysts via several mechanisms.

Firstly, promoters could increase the basic site, which could promote the adsorption and/or activation of CO_2. Debek et al. [135-137] found that Ce promoter would increase the moderate alkaline sites and new strong low-coordinated oxygen species, thereby enhancing the ability of CO_2 adsorption. The catalyst showed high activity at 550 °C, and the order of methane conversion was H-19Ni > H-18NiCe > 10Ni/Al_2O_3 > 10Ni/CZ ≈ H-8Ni，while the order of CO_2 conversion was H-18NiCe > H-19Ni > 10Ni/Al_2O_3 > H-8Ni > 10Ni/CZ. Debek et al. [135] also examined the influence of promoters Ce, Zr and CeZr for Ni-Mg-Al hydrotalcite-derived catalyst for DRM reaction at 550 °C. They evidenced that with the introduction of Zr promoter, CO_2 adsorbed preferentially in weak basic sites and formed active carbonate species that could react with methane. Comparing with other catalysts, the catalytic activity on the Zr-promoted catalyst decreased obviously with time-on stream and the ratio of H_2/CO was the lowest, due to the Zr contributing to both DRM reaction and reverse Boudouard reaction. Liu et al. [114] found that the promoter La would increase the medium strength and weak basicity, thereby enhance the activity of the catalyst. U.Oemar et al. [138] also found that La promoted the adsorption of CO_2 and removed coke, due to the basic property of La. It is well known that potassium was a good catalyst for carbon gasification, because the electronic effect of alkali atoms could lead to a weakening of the strength of C-O bond [139]. Barroso-Quiroga et al. [140] prepared Ni-based catalysts modified by alkaline (Li or K) for DRM reaction, and found that Ni/CeO_2 catalyst showed the highest initial conversion of both CH_4 (11.7%) and CO_2 (29.7%) comparing to other catalysts,

whereas the Ni/CeO_2 catalyst promoted by K or Li showed a better stability during the process of reaction, due to the methane cracking and the enhancement of carbon gasification. However, the activity of modified catalyst was lower than Ni/CeO_2 catalyst, because the alkaline metals blocked the Ni active sites [141]. Sc promoter could increase strong and moderate basic sites, thereby enhancing the ability of CO_2 adsorption and the stability of the catalysts [142].

Secondly, Promoters could enhance the dispersion of nickel particles. Liu et al. [88] found that the presence of La, Al and Mn on natural clay based nickel catalysts resulted in smaller Ni^0 crystallite size and further promoted Ni dispersion. After reduction, the Ni^0 crystallite size on Ni/Fe-clay catalyst is 13.4 nm, while it is 10.6, 9.8 and 9.2 nm on Ni/Fe-clay catalyst modified by Mn, La and Al, respectively. Świrk et al. [117] reported that yttrium promotes the formation of smaller Ni crystallite size, thereby enhancing the dispersion of nickel species. Nickel dispersion on reduced Y-promoted Ni-based double-layered hydroxides catalyst increased from 8.9 % to 19.8 %. A better dispersion of nickel would contribute to the catalytic performance of catalyst, due to the more accessible nickel metallic sites form on surface of catalyst [69, 117]. Thus, the Y-promoted catalyst exhibited higher catalytic performance for DRM. Sajjadi et al [81] prepared $Ni-Co/Al_2O_3-MgO-ZrO_2$ nanocatalysts were synthesized via sol-gel method with various amounts of Mg (5, 10 and 25 wt %). According to the results of TEM, the particle size distribution became narrower with the increase of Mg content. The average particle size for $Ni-Co/Al_2O_3-5MgO-ZrO_2$, $Ni-Co/Al_2O_3-10MgO-ZrO_2$ and $Ni-Co/Al_2O_3-15MgO-ZrO_2$ are 26.3, 21.2 and 17.1 nm, respectively.

Thirdly, promoters could increase the reduction of nickel oxide. Liu et al. [114] studied the effect of La promoter for 550 and 600 °C DRM reaction. They found that the addition of lanthanum would enhance the reduction of the nickel leading to Ni^0 species existing in the La-promoted catalyst. The H_2/CO increased with time-on-stream, because of the improvement of direct methane decomposition reaction, corresponded to the presence of Ni^0 species. The conversion of CH_4 and CO_2 on HN_2 catalyst

($Ni_{0.215}La_{0.012}Mg_{0.535}Al_{0.238}$) containing 2 wt.% La for DRM reaction at 550 °C was 33% and 36%, respectively, which was higher than non-promoted catalyst. Debek et al. [136] also studied the Ce-promoted Ni-containing hydrotalcite derived catalyst for DRM reaction and found that Ce promoter could increase the reduction of the nickel particle. The H_2-TPR results showed that the reduction peak of Ni-phase shifted to low temperature in the presence of promoter Ce, because the Ce^{3+}/Ce^{4+} redox pairs could transfer electron, which promoted the reduction of nickel oxides in the nearby site [143]. Albarazi et al. [144] studied the effect of $Ce_{0.75}Zr_{0.25}O_2$ mixed oxide on the performance for DRM reaction. The H_2-TPR results showed that $Ce_{0.75}Zr_{0.25}O_2$ mixed oxide could increase the content of nickel that could be reduced below 600 °C, thus enhance the reduction of the nickel particles.

Lastly, promoters could promote the formation of oxygen vacancies. The formation of oxygen vacancies (in samples containing ZrO_2 and Y_2O_3) seemed to promote removal of the coke deposited on the nickel surface during the reforming process [145, 146]. Asencios et al. [146] studied the $NiO/Y_2O_3/ZrO_2$ catalyst synthesized by the polymerization method in a single step. The formation of oxygen vacancies on Y-promoted catalyst, due to the generation of Y_2O_3–ZrO_2 solid solution, have a positive influence on the elimination of the coke deposited on the Ni^0 surface. Youn et al. [145] prepared mesoporous yttria-stabilized zirconia support by a sol–gel method and observed that oxygen vacancies was increased by the addition of yttria. The results of XRD showed that graphitic carbon was observed on non-promoted catalyst, while the peak of graphitic carbon became weak on Y-promoted catalyst. It implied that yttria also played an important role in enhancing the resistance against carbon deposition. The properties of ZrO_2 can be tailored by the introduction of a cation with valence lower than 4+, e.g. Y^{3+} [117]. Bellido et al. [147] found the surface oxygen vacancies are stabilized by the increasing Y_2O_3 load. Meanwhile the formation of ZrO_2-Y_2O_3 solid solution could increase the formation of oxygen vacancies in the synthesized support.

2.4.3.2 Effect of supports

Generally, the interaction between Ni and support plays a very important role in the catalytic performance of catalyst for DRM reaction. Bradford et al. [148] prepared Ni supported on TiO_2, SiO_2 and MgO catalysts for DRM reaction and Ni/TiO_2 catalyst exhibited the highest activity. Because the strong interaction of the metal and support increased the electron density in the metal crystallites, thereby promoting to activate C-H bond of methane. Kumar et al. [149] found that the activity on 5% Ni/$Ce_{0.6}Zr_{0.2}O_2$ catalyst was higher than Ni/CeO_2 or Ni/ZrO_2. The conversion of CH_4 was above 68% at 700 °C even reaction for 70 h. The author suggested that the nickel particles on $Ce_xZr_{1-x}O_2$ support were smaller than those on CeO_2 or ZrO_2 supports. It was attributed to the enhanced nickel dispersion and the interaction of the nickel and support. Lemonidou et al. [150] reported that the 5 wt.% Ni/CaO-Al_2O_3 catalyst exhibited high stability, and the conversion of CH_4 did not decrease even reaction for 50 h. The strong interaction between the CaO-Al_2O_3 support and metal could increase the stability of the catalyst. While the strong interaction between nickel and CeO_2 support did not enhance the activity of Ni/CeO_2 catalyst for DRM. Because, Ni/CeO_2 catalyst promoted the reverse water-gas shift reaction during the process of DRM reaction, resulting in the decrease of hydrogen selectivity [149]. However, on Ni/SiO_2 and Ni/C catalysts, filamentous carbon is formed under reaction conditions leading to the deactivation of the catalysts [148], because of the weaker interaction of the nickel and support SiO_2 [65, 120, 148]. The above reports indicated that the nature and strength of the interaction of nickel with the supports would alter the performance of the catalysts.

Besides, the supports with special structure could promote the catalytic performance of catalysts for DRM reaction. For example, mesoporous material could limit the sintering of nickel species during the reaction, thus improve the performance of the catalysts [151-154]. Sokolov et al. [154] discussed the influence of the morphology of the La_2O_3-ZrO_2 support on catalytic stability. Three types of La_2O_3-ZrO_2 supports nonstructured (LaZr-ns), mesostructured (LaZr-meso) and macropore skeleton (LaZr-macro) were

prepared to supported nickel. Ni/LaZr-meso catalyst showed the highest stability in 180 h with almost no inactivation, due to the pore confinement effect and high dispersion of NiO_x species Ni/LaZr-meso catalyst. Hydrotalcite derivative with the periclase-like structure has been widely studied in DRM reaction [114, 135, 136, 155]. Debek et al. [155] showed that the Ni-containing hydrotalcite-derived materials (HT-NiAl) showed high catalytic performance for DRM. The average conversions of CH_4 and CO_2 were 48% and 54% at 550 °C, respectively. Hydrotalcite derivative materials were beneficial to the activity for DRM reaction, which was attributed to the mixed oxide with the periclase-like structure. Besides, the interaction between nickel species and hydrotalcite derivative supports could restrain the sintering of nickel. Simultaneously, prevent the formation of inactive phases, such as $NiAl_2O_4$ or NiO-MgO solid solution [156]. $Ce_xZr_{1-x}O_2$ support has defect structure due to the formation of the CeO_2-ZrO_2 solid solution and the high oxygen mobility, which led to celerity oxidoreduction ability by releasing and getting oxygen rapidly [149, 157-159]. 5% $Ni/Ce_{0.6}Zr_{0.2}O_2$ catalyst showed remarkable stability for DRM reaction, due to the cubic $Ce_xZr_{1-x}O_2$ support offered mobile oxygen species to nickel particles, reported by Kumar [149]. TPO experiment implied that $Ni/Ce_xZr_{1-x}O_2$ catalyst inhibited carbon deposition. $Ce_xZr_{1-x}O_2$ solid solution could enhance reducibility, confirmed by H_2-TPR. Those special material supports would exert effect on nickel particle size and dispersion of nickel, thereby improve the property of the catalysts for DRM reaction.

2.4.3.3 The carbon deposition limitation

Carbon deposition is one of the main issues for the deactivation of Ni-based catalysts for DRM reaction. Thus, many researchers investigated how to decrease the coke or restrain the formation of coke. Generally, there are several methods to decrease the carbon deposition [53, 85, 114, 137, 154, 160, 161].

Firstly, the enhancement of the ability for carbon deposition elimination could decrease

the formed coke during the DRM reaction. Liu [114] reported that La promoters could increase the formation of medium strength and strong basic sites, thereby enhancing the ability of CO_2 adsorption and further remove carbon deposition. Besides, the presence of La may favor the formation of lanthanum oxycarbonates, able to gasify the amorphous carbon deposits. Thus, the content of coke on La-promoted catalyst was 12.6 mg, which was lower than non-promoted catalyst (16 mg). Ce and Zr promoters could enhance the ability of CO_2 adsorption on count for the increase of basic sites, reported by Debek [137, 160]. Those properties contributed to removing carbon deposition, as well as the stability of Ni-based catalysts. In addition, the ratio of Ce/Zr could also affect the carbon deposition. The H-$ZrCe_{1.2}$catalyst (Ce/Zr loading of 1.2) exhibited the least carbon deposition and highest stability comparing to those on H-$ZrCe_{0.6}$ (Ce/Zr loading of 0.6) and H-$ZrCe_{0.6}$ (Ce/Zr loading of 0.3) catalysts. The results of CO_2-TPD showed a higher concentration of strong basic sites on H-$ZrCe_{0.3}$ and H-$ZrCe_{0.6}$ catalysts, leading to too strong CO_2 adsorption on H-$ZrCe_{0.6}$ and H-$ZrCe_{0.3}$ catalysts, and then promoting carbon deposition. The surface oxygen species on catalysts could react with the coke, thereby decreasing the carbon deposition [162]. Stthiumporn et al. [163] found modified $La_{0.8}Sr_{0.2}Ni_{0.8}M_{0.2}O_3$ perovskite by Fe could contribute to the formation of abundant lattice oxygen species, which reacted with CO_2 forming $La_2O_2CO_3$, thereby removed the surface carbon.

Secondly, the enhancement of the ability of carbon deposition resistance could decrease the formed coke during the DRM reaction. Li [161] prepared a series of $BaTiO_3$-Al_2O_3 catalysts with different content of $BaTiO_3$. The Ni/32.4%$BaTiO_3$-Al_2O_3 catalyst exhibited the best carbon deposition resistance property on DRM reaction with 4% coke after reaction for 10 h at 690 ^oC. $BaTiO_3$ could adjust the electronic donor intensity of Ni/$BaTiO_3$-Al_2O_3 catalysts, thereby modifying the interaction between nickel and supports and further enhancing the dispersion of Ni species. And as a consequence, Ni/$BaTiO_3$-Al_2O_3 catalysts showed higher carbon deposition resistance and stability on DRM reaction. Xu et al. [85] investigated the effect of core-shell structure on the performance of catalysts for DRM. NiO-MgO@SiO_2 catalyst exhibited higher carbon

deposition resistance, compared with the traditional NiO-MgO/SiO_2 catalyst. After reaction at 670 ºC, the carbon deposition was 5 % and 23 % on NiO-MgO@SiO_2 and NiO-MgO/SiO_2 catalyst, respectively.

Thirdly, optimum process parameters could decrease the carbon deposition. Maneerung et al. [164] discovered that the introduction of hydrogen into feed gas enhanced the stability of catalysts, where hydrogen could react with the excess carbon, thereby reduced the rate of catalytic deactivation. Yabe [53] found that Ni/La-ZrO_2 catalyst showed lower carbon deposition in the electric field than traditional conditions for DRM reactions. The content of coke was 0.15% and above 3.81% in the electric field and no electric conditions, respectively. The catalyst could be restructured in the electric field, thereby decreasing the carbon deposition of catalysts.

2.4.3.4 ZrO_2 materials

ZrO_2 had been widely used for reforming catalysts, because of the high oxygen mobilization, enhancement of metal dispersion, and the proper interaction between nickel and ZrO_2 [62, 165-167]. Jing et al. [166] prepared Ni/SiO_2 catalyst modified by ZrO_2 and the DRM reaction conducted at 1023 K with the feed gas ratio of CH_4:CO_2:O_2=1:0.4:0.3, GHSV=9000 h^{-1}. Ni/5%ZrO_2-SiO_2 catalyst exhibited higher activity and stability than Ni/SiO_2 catalyst, due to higher Ni dispersion, which might be responsible for its high activity and good resistance to Ni sintering. Gonzalez et al. [108] discussed the nickel metallic particle size on Ni/ZrO_2 catalyst modified by H_2 or CO treatment. The reaction conducted at 750 ºC with a mix flow (CH_4:CO_2:He=10:10:80, GHSV=$1.5\cdot10^5$ L/kg·h). They found that after CO reduction， Ni/ZrO_2 catalyst exhibited more stable than that after H_2 reduction. After reduction at CO, the $Ni(CO)_4$ compound formed on catalyst, while this compound would decompose nearby the surface, due to the interaction between nickel and ZrO_2, which increase the disposition of nickel, thereby enhancement the stable of catalyst. Lercher et al. [167] found the rate

of carbon filament formation is proportional to the particle size of Ni. Below a critical Ni particle, size (d<2 nm), the formation of carbon slowed down dramatically. Well dispersed Ni supported on ZrO_2 is thus a viable alternative to the noble metal-based catalysts.

ZrO_2 could inhibit carbon deposition and enhance carbon removal [167-169]. Pompeo et al. [168] found ZrO_2 presence that plays a fundamental role in minimizing the carbon formation process, promoting the dissociation chemisorption of CO_2 that enables the gasification of carbon intermediate precursors responsible for the deactivation mechanism in DRM. Katsutoshi et al. [169] compared between Pt/ZrO_2 and Pt/Al_2O_3 catalysts for the carbon deposition over DRM reaction. They found that more carbon deposited on Ni/Al_2O_3 catalyst, which would cover on Ni, thereby leading to the deactivation of Ni/Al_2O_3 catalyst. While coke is hardly formed on Pt/ZrO_2 catalyst, because it lacks a significant concentration of strong Lewis acid sites. This result is corresponded with Lercher et al. [167] and found that the rate of carbon formation on the support is proportional to the concentration of Lewis acid sites. Besides, the CO_2-TPD results showed that CO_2 easier reactive with coke on Pt/ZrO_2 than that on Pt/Al_2O_3 catalyst. Wei et al. [165] studied the influence of the preparation method on performance of Ni/ZrO_2 catalyst at 1037 K for DRM reaction. Ni/ZrO_2-A is prepared by impregnation with 18 nm particle of ZrO_2, Ni/ZrO_2-B is prepared by impregnation with 6 nm particle of ZrO_2, and Ni/ZrO_2-C is prepared by co-precipitation with 7 nm particle of ZrO_2, Ni/ZrO_2-B catalyst showed highly active and stable even reaction for 600 h, while other two catalysts showed the same initial activity as Ni/ZrO_2-B but deactivate rapidly. The extremely stable activity of Sample B catalyst may be induced by a higher concentration of oxygen defects or higher concentrations of basic sites for CO_2 activation at the support surface derived from the ultra-fine ZrO_2-B. Lou et al. [87] designed a Ni/ZrO_2 with 1.1 nm nickel particle diameter, which exhibited outstanding stability in DRM reaction with very little carbon deposition after reaction. Because small nickel particles could result in more interface of Ni-O-Zr, which could promote the removal of carbon.

In this work, I focused on the Ni-based with new ZrO_2 catalysts prepared by a one-step synthesis method. I also Investigated the effect of synthesis method and the promoter of Al, Mg, Y and Mn on the performance of catalyst for dry reforming of methane. In order to understand the relationship between structure and activity of ZrO_2-based catalyst.

Chapter III

Experiment

3. Experiment

3.1 Activity test of dry reforming of methane

3.1.1 Activity test

The dry reforming activity test was carried out with a rising temperature from 550 °C to 800 °C (interval of each 50 °C in 30 min) in a fixed-bed flow microreactor (inner diameter 10 mm). A thermocouple (Type K) was placed near to the catalytic bed to monitor the reaction temperature for each test. The total reactant gas flow rate was 100 mL/min with a molar composition of $CH_4/CO_2/Ar$ = 1/1/8. The total gas hourly space velocity (GHSV) values were 24,000 h^{-1} or 48,000 h^{-1}. For time on stream tests, the same reactant gas was introduced through the catalytic bed held at target temperature for time on stream. Prior to DRM reaction, the catalysts were reduced at 700 or 750 °C for 1 h in the stream of 5 vol% H_2/Ar. Those steps were shown in Figure 3-1. The outgases were detected by a gas micro chromatography (Agilent Varian GC490, Agilent, Les Ulis, France), equipped with a TCD detector to analyze the composition of products.

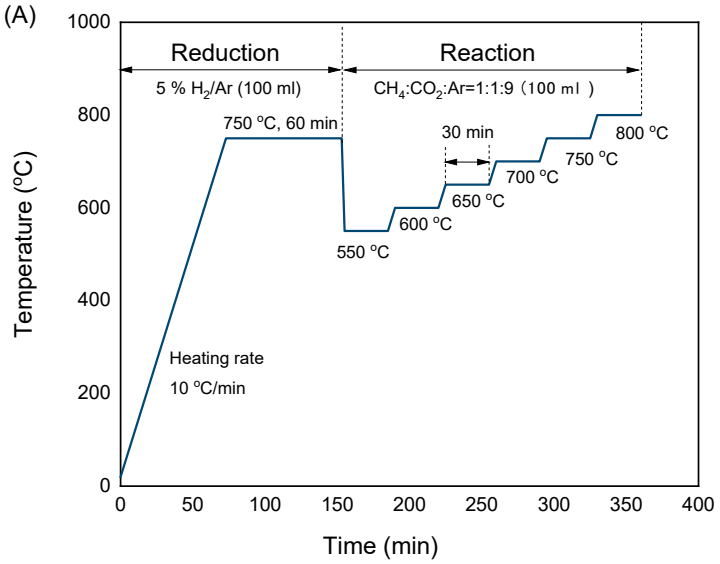

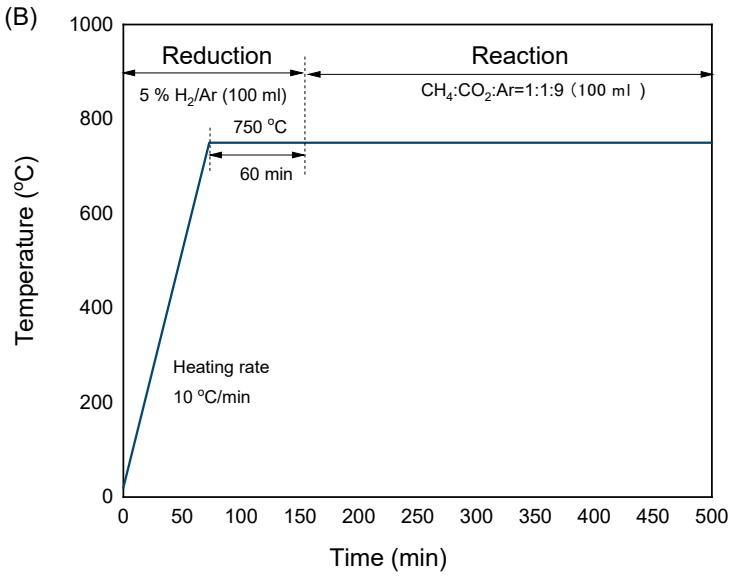

Figure 3-1 Programs used during dry reforming of methane: (A) Multi-Steady experiment at different temperatures and (B) Isothermal experiments.

3.1.2 computational formula

The conversion of CH_4 (X_{CH_4}) and CO_2 (X_{CO_2}), and H_2/CO molar ratio were calculated according to the following equations:

$$X_{CH_4} = \frac{n_{CH_4,in} - n_{CH_4,out}}{n_{CH_4,in}} \times 100\% \qquad \text{(Equations 8)}$$

$$X_{CO_2} = \frac{n_{CO_2,in} - n_{CO_2,out}}{n_{CO_2,in}} \times 100\% \qquad \text{(Equations 9)}$$

$$H_2/CO = n_{H_2,out}/n_{CO,out} \qquad \text{(Equations 10)}$$

The total gas hourly space velocity (GHSV) values were calculated according to the following equations (Equations 11):

$$GHSV = \frac{\text{Volumetric flow rate of the gaseous feed}}{\text{Volume of catalyst}} \qquad \text{(Equations 11)}$$

(A)

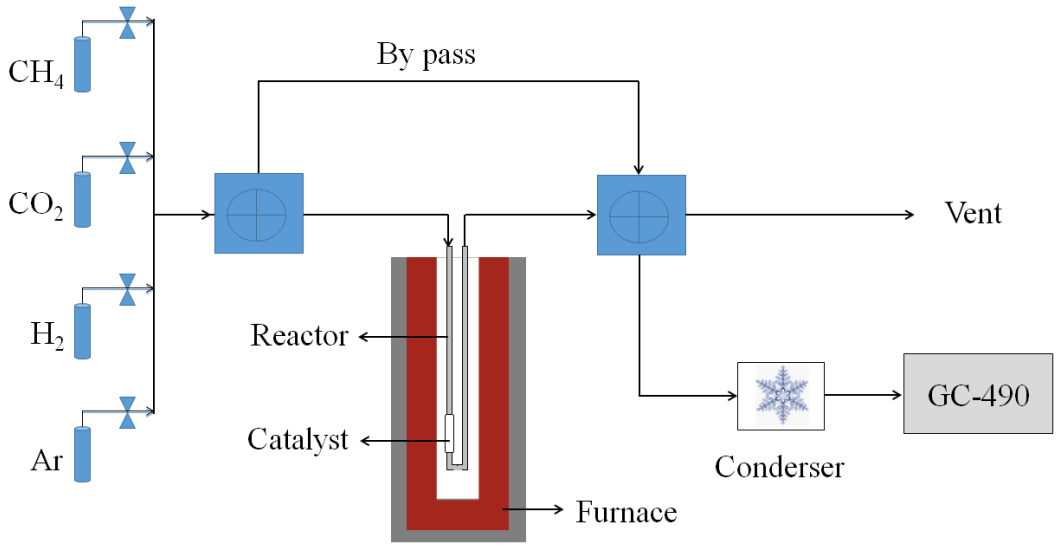

(B)

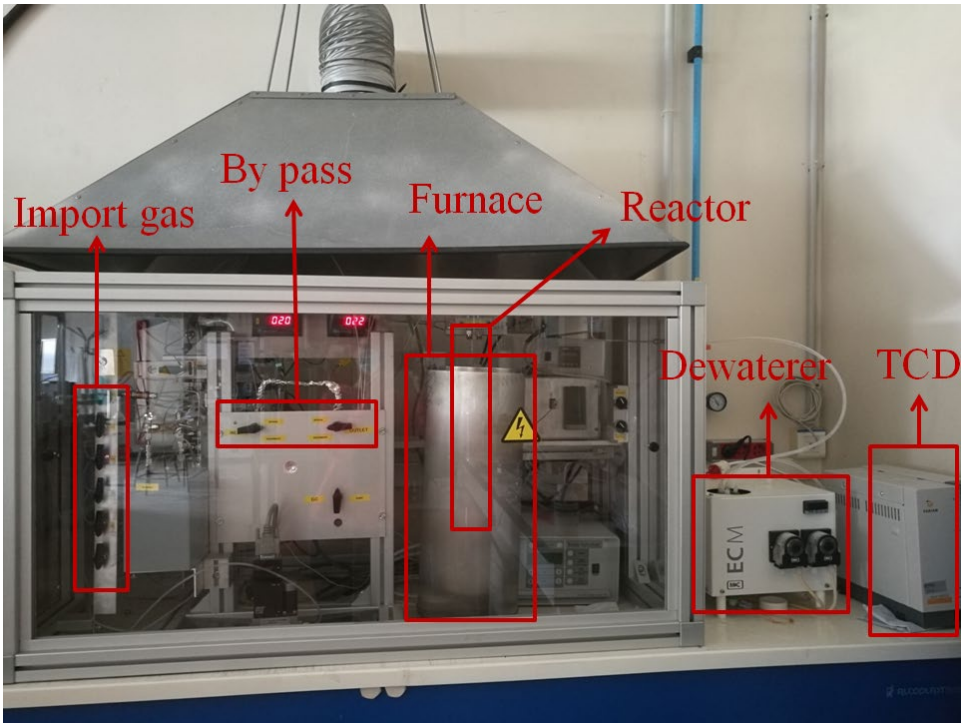

Figure 3-2 (A) Scheme and (B) physical profile of dry reforming of methane set-up.

3.2 Characterization of the catalyst

3.2.1 Temperature-Programmed Reduction (TPR)

Temperature-programmed reduction by H_2 (H_2-TPR) is a widely used technique for the characterization of metal oxides, mixed metal oxides, and metal oxides dispersed on a support. The TPR method yields quantitative information on the reducibility of the oxide's surface, as well as the heterogeneity of the reducible surface. Generally, the reducing gas is a mixture flow with 3-17 % hydrogen diluted in argon or nitrogen [170]. The test for the reducibility of catalysts was measured on a BELCAT-M (BEL Japan, BEL Europe GmbH, Krefeld, Germany) instrument. The mass of catalyst was about 60 mg. Figure 3-3 shows the programs and Scheme for H_2-TPR. Before the test, the catalyst was pretreated at 150 °C for 30 min under helium flow. Then the sample was reduced under 5 % (vol.) H_2/Ar mixture flow with a heating rate of 10 °C/min from 100 °C to 900 °C. The data was collected by TCD and recorded from 100 °C to 900 °C.

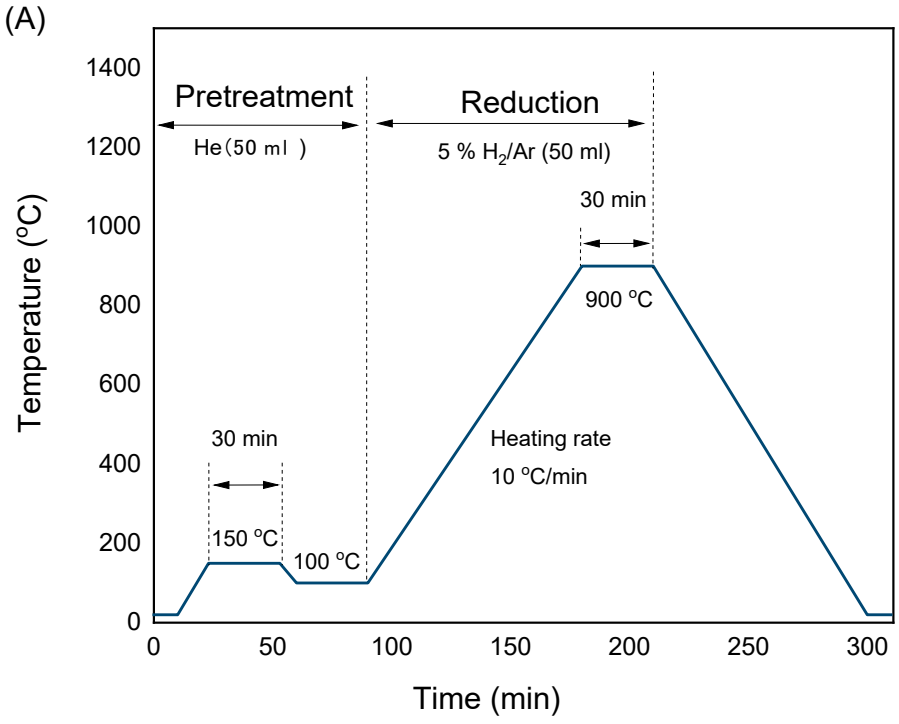

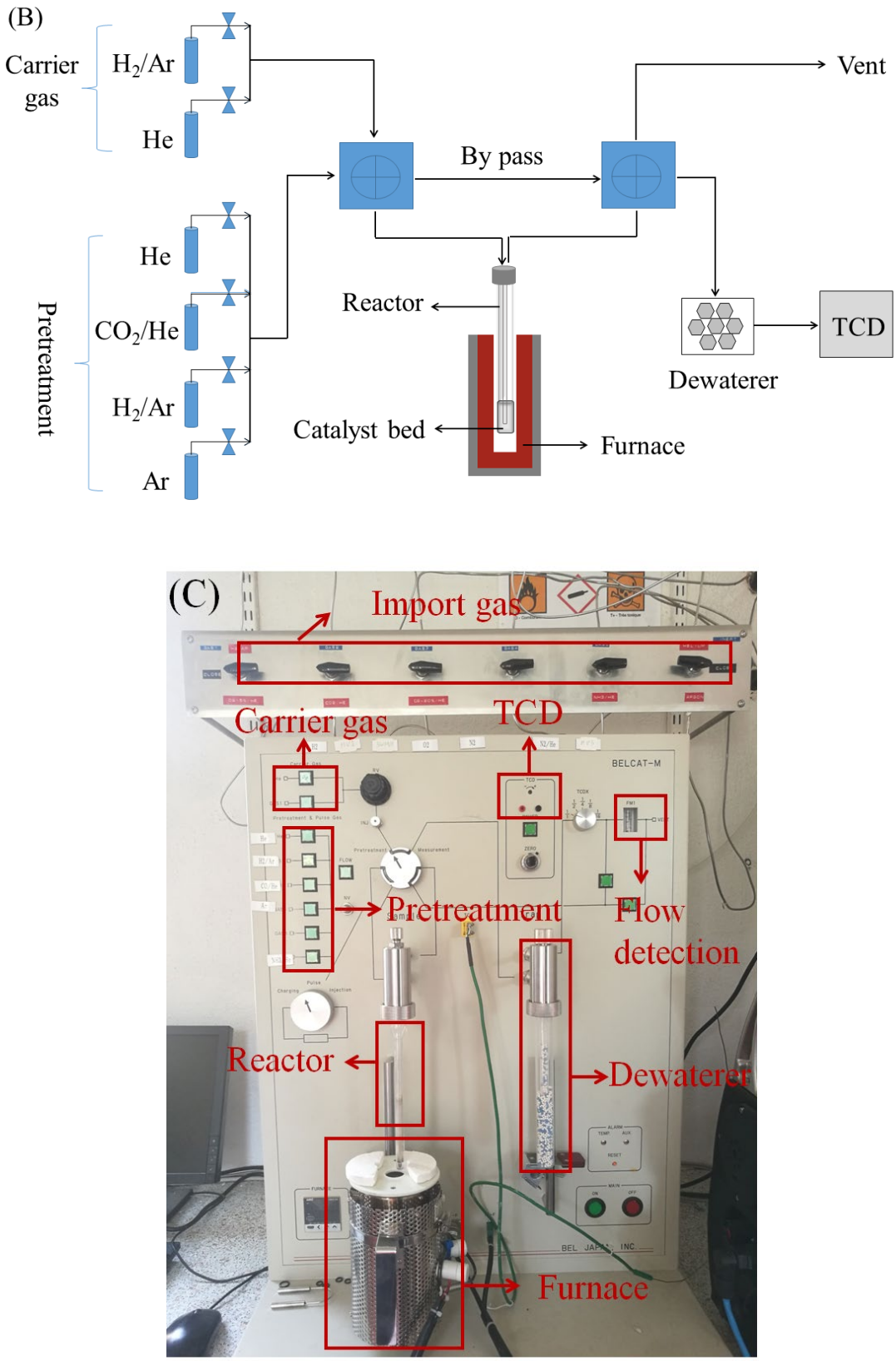

Figure 3-3 Programs (A), scheme (B) and set-up (C) used the temperature-programmed reduction of H_2 (H_2-TPR).

3.2.2 Temperature-Programmed Desorption (TPD)

Temperature programmed desorption of CO_2 (TPD) technique allows to study the interaction of CO_2 gas reaction with solid surfaces, due to its natural tendency to get adsorbed (strong-pair acceptor) on the most basic sites (electron-pair donor) on the surface, thereby, is a powerful tool for both the evaluation of active sites on catalyst surfaces and the understanding of the mechanisms of catalytic reactions including adsorption, surface reaction and desorption [171, 172].

The measurement of CO_2-TPD was carried out on the same equipment, and the scheme of set-up for CO_2-TPD was shown in Figure 3-3 (B). The catalysts were reduced at 700 °C under a 5% H_2/Ar flow for 60 min. CO_2 was adsorbed at 80 °C for 60 min under a mixture flow of 10% CO_2/He. Afterward, cleaned the weakly adsorbed CO_2 by helium flow for 30 min. Last, the catalysts were heated to 900 °C (10 °C/min) under a He flow. The process of CO_2-TPD is presented in Figure 3-4. The data collected from 80 to 900 °C.

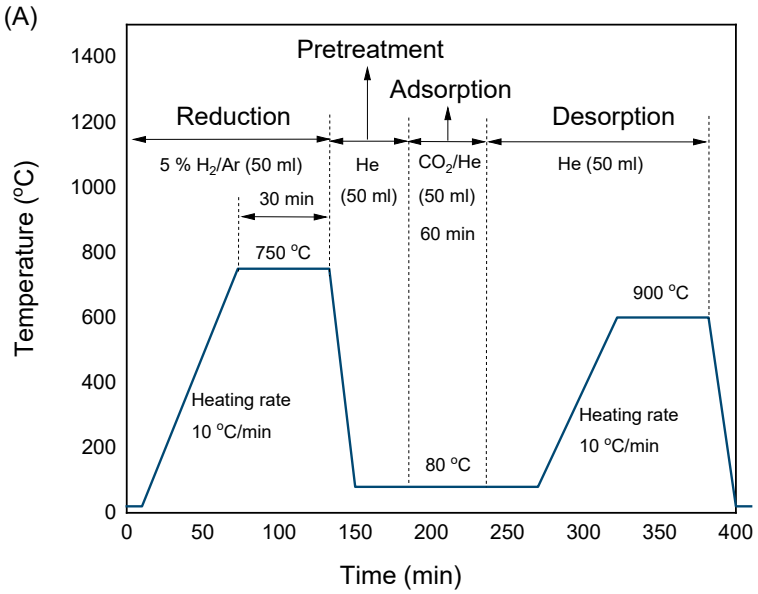

Figure 3-4 The programs for temperature-programmed desorption of CO_2 (CO_2-TPD)

3.2.3 X-Ray Diffraction (XRD)

The X-Ray Diffraction technique is very important and most frequently characterization applied in the structure of catalysts. It is an indispensable method of material investigation, characterization and quality control. Figure 3-5 illustrates schematically how diffraction of X-rays by crystal planes allows one to derive lattice spacings by using the Bragg relation. X-ray diffraction occurs in the elastic scattering of X-ray photons by atoms in a periodic lattice. The scattered monochromatic X-rays that are in phase give constructive interference [173].

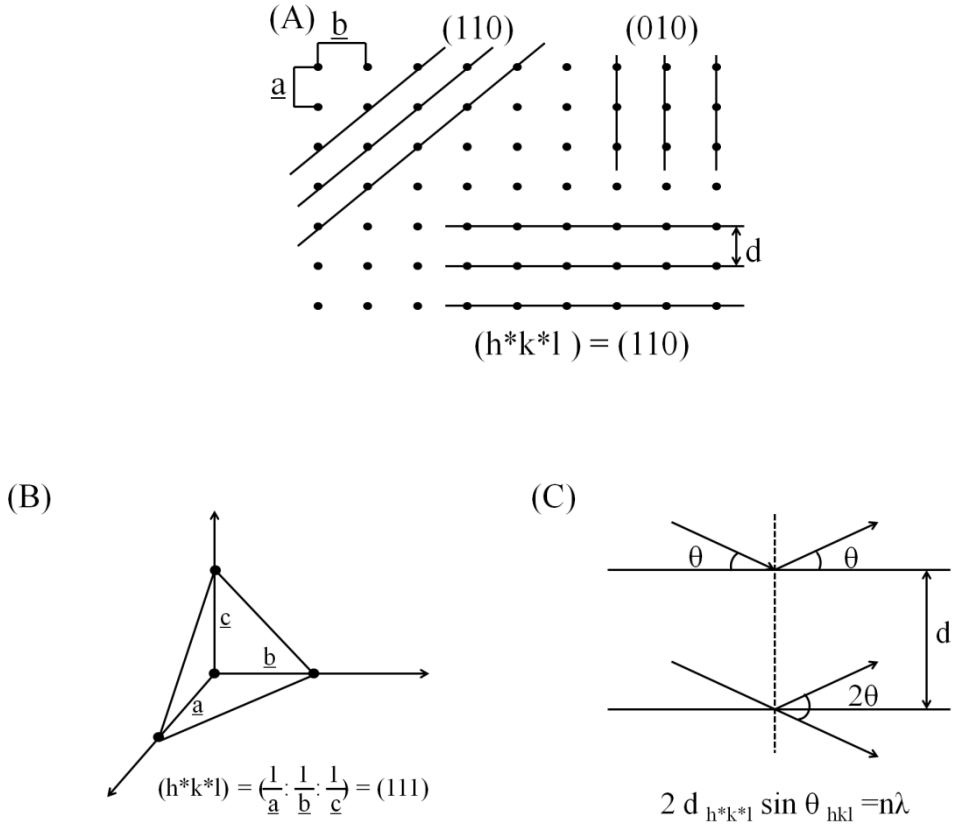

Where d_{h*k*l} is the lattice spacing of (h*k*l) crystal planes, n is the diffraction series, λ is the incident wavelength.

Figure 3-5 X-rays scattered by atoms in an ordered lattice interfere constructively in directions

Herein, focuses the crystal planes 2-Theta and the lattice spacing (d) of ZrO_2, as is repented in Figure 3-6 and Table 3-1. Besides, the crystallite sizes of Ni^0 play a key role in the activity of Ni-based catalysts for dry reforming of methane. Thus, the crystal particle size on catalysts before and after reaction was calculated using the Scherrer Equation (Equation 12) to understand the relationship between activity and crystallite sizes of Ni^0 [174]. Where τ is the mean size; K is a dimensionless shape factor, with a value close to unity about 0.9, λ is the X-ray wavelength, β is the line broadening at half the maximum intensity (FWHM), θ is the Bragg diffraction angle.

$$\tau = \frac{K\,\lambda}{\beta\,cos\theta} \qquad \text{(Equation 12)}$$

The XRD patterns were recorded by a DX-1000 CSC diffractometer with a Cu Kα radiation source (λ=0.15406 nm). The anode current and voltage were 25 mA and 40 kV, respectively. All the XRD diffractograms were registered at 25°C. The diffraction patterns were recorded in a range of $10° < 2\theta < 80°$, with a scan step size of 0.03° and a scan speed of 0.3 s $step^{-1}$.

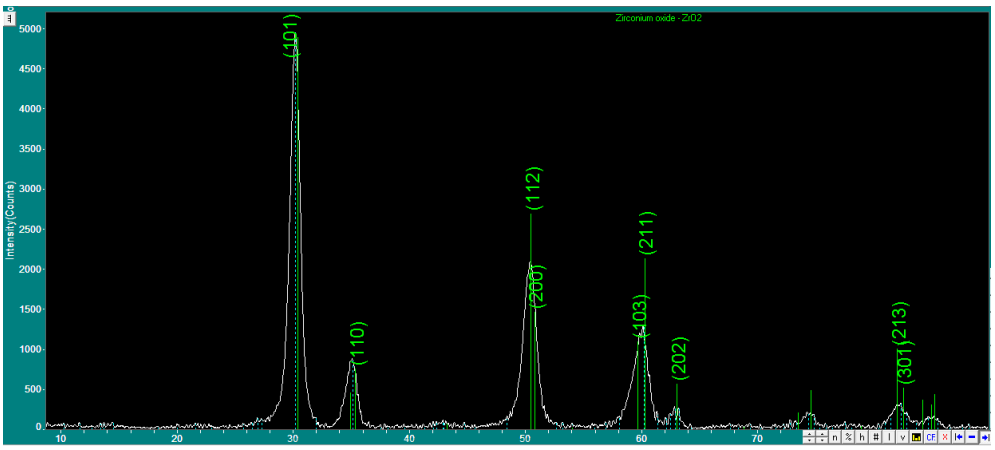

Figure 3.6 Crystallographic parameters for ZrO_2, according to the standard ICSD # 88-1007

Table 3-1 The Peak list for Pattern ZrO_2, according to the ICSD standard # 88-1007

	2-Theta	d(Å)	I(v)	(h k l)	Theta	1/(2d)	2pi/d
1	30.271	2.9501	100.0	(1 0 1)	15.136	0.1695	2.1298
2	34.798	2.5760	9.2	(0 0 2)	17.399	0.1941	2.4391
3	35.243	2.5445	15.3	(1 1 0)	17.622	0.1965	2.4694
4	43.153	2.0946	1.3	(1 0 2)	21.577	0.2387	2.9997
5	50.366	1.8103	54.9	(1 1 2)	25.183	0.2762	3.4709
6	50.697	1.7992	29.8	(2 0 0)	25.349	0.2779	3.4922
7	53.934	1.6986	0.2	(2 0 1)	26.967	0.2944	3.6990
8	59.603	1.5499	22.3	(1 0 3)	29.801	0.3226	4.0540
9	60.194	1.5361	43.4	(2 1 1)	30.097	0.3255	4.0905
10	62.961	1.4750	11.4	(2 0 2)	31.481	0.3390	4.2597
11	68.719	1.3648	0.4	(2 1 2)	34.359	0.3663	4.6037
12	73.460	1.2880	4.1	(0 0 4)	36.730	0.3882	4.8783
13	74.523	1.2722	9.7	(2 2 0)	37.262	0.3930	4.9387
14	78.869	1.2127	0.5	(1 0 4)	39.435	0.4123	5.1813
15	81.987	1.1743	20.3	(2 1 3)	40.993	0.4258	5.3508
16	82.502	1.1682	10.4	(3 0 1)	41.251	0.4280	5.3784
17	84.180	1.1492	7.4	(1 1 4)	42.090	0.4351	5.4676
18	84.951	1.1407	6.2	(2 2 2)	42.476	0.4383	5.5082
19	85.208	1.1379	8.8	(3 1 0)	42.604	0.4394	5.5217

3.2.4 Brunauer-Emmett-Teller (BET)

The surface area, mean pore size, and pore volume were obtained by the N_2 adsorption-desorption method using a Belsorp Mini II apparatus (BEL Japan) instrument. Before measurement, the sample was degassed under vacuum condition at 200 °C for 2 h. Then the test was carried out under liquid nitrogen temperature (-196 °C). The surface area of the sample was calculated according to the Brunauer-Emmett-Teller (BET) equation (Equation 13) [175]. p and p0 are the equilibrium and the saturation pressure of adsorbates at the temperature of adsorption. *v* is the adsorbed gas quantity. v_m is the monolayer adsorbed gas quantity. And *c* is the BET constant. The pore volume and pore diameter were calculated by the Barrett-Joyner-Halenda (BJH) equation (Equation 14) [176]. $V_{ads}(x_k)$ is the total adsorption amount at $x_k = P_k/P_0$. r_i is the radius of capillary condensation. r_k is the Kelvin radius of capillary condensation. ΔV_i is the total adsorption amount at r_i $(r_i \leq r_k)$. ΔS_j is the total adsorption amount at r_j $(r_j \geq r_k)$. t_j is the thickness of the liquid film on the wall of the tube.

$$\frac{1}{v\{\left(\frac{P0}{P}\right)-1\}} = \frac{c-1}{v_m c}\left(\frac{P0}{p}\right) + \frac{1}{v_m c} \qquad \text{(Equation 13)}$$

$$V_{ads}(x_k) = \sum_{i=1}^{k} \Delta V_i(r_i \leq r_k\,(x_k)) + \sum_{j=k+1}^{n} \Delta S_j t_j\left(r_j \geq r_k\,(x_k)\right) \qquad \text{(Equation 14)}$$

The majority of physisorption isotherms might be divided into six types [177], as is shown in Figure 3-7. The most main features of the Type IV isotherm are the hysteresis loop and the plateau at high p/po. Isotherms of this type are associated with the mesoporous adsorbents such as support in this work. Hysteresis appearing in the multilayer range of physisorption isotherms is given by the capillary condensation in mesopore structures.

(A)

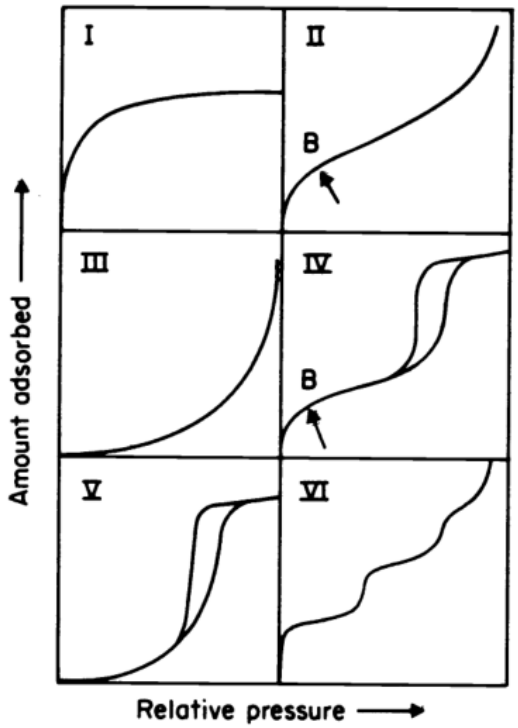

(B)

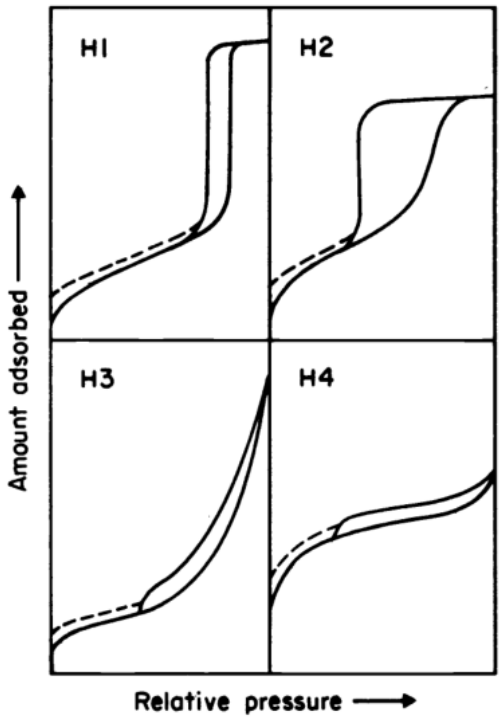

Figure 3-7 The types of physisorption isotherms (A) and (B) hysteresis loops

3.2.5 Thermal Gravimetric Analysis (TGA)

Thermogravimetric analysis (TGA) is a technique for measuring the relationship between the quality of a sample and temperature (or time). The thermogravimetric curve (TGA curve) is carried out by the heat balance with time on stream, as shown in Figure 3-8 (A). Differential scanning calorimetry analysis (DSC) is a technique in which the difference in energy inputs into a substance and a reference material is measured as a function of temperature. There are two modes, power compensation DSC and heat flux DSC depending on the method of measurement used. Figure 3-8 (B) shows the scheme of power compensation DSC instrument [178].

Herein, used to characterize the carbon deposition of used catalysts. The sample (10 mg) was treated under air atmosphere with a flow rate of 30 mL/min^{-1} at room temperature until the scales balanced. Then, the temperature increased from room temperature to 800 °C with a heating rate of 5 °C/min^{-1}. The data was recorded (the weight of the sample) from room temperature to 800 °C.

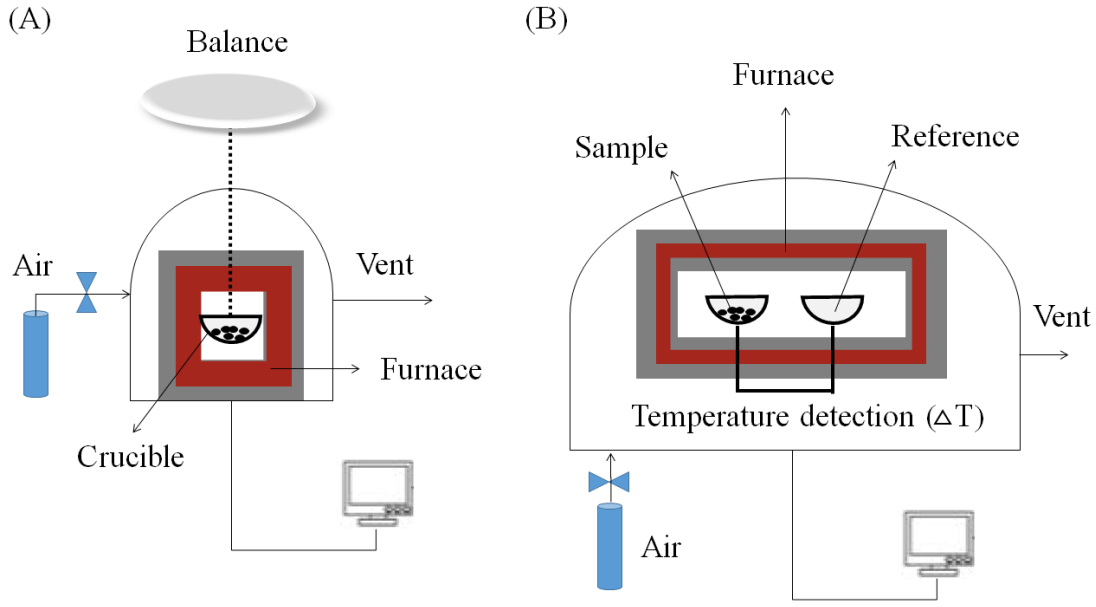

Figure 3-8 The scheme of set-up for TGA (A) and TGA-DSC (B).

3.2.6 Transmission Electron Microscope (TEM)

Transmission electron microscopy (TEM) is a characterization method that could provide the information in nanoscale. The size distribution, and catalyst morphology also could be determined by the TEM characterization [62]. Electron diffraction is the main contrast mechanism of sample imaging in TEM, which usually uses to study large particle crystals with defects [179]. According to the schematic diagram of diffraction (Figure 3-9), the lattice spacing d can be calculated by the equation (Equation 15). L is the length of the camera. *r* is the distance from the diffraction point to the transmission point. λ is the electron wavelength. Besides, single, polycrystalline, and amorphous shapes can be distinguished by diffraction patterns, as shown in Figure 3-8 (B) [180]. In this work, the morphology of catalysts was obtained by on an FEI Tecnai G2 20 Twin instrument with an acceleration voltage of 200 kV.

$$\frac{r}{L} = 2\theta = \frac{\lambda}{d} \quad \text{(Eq. 15)}$$

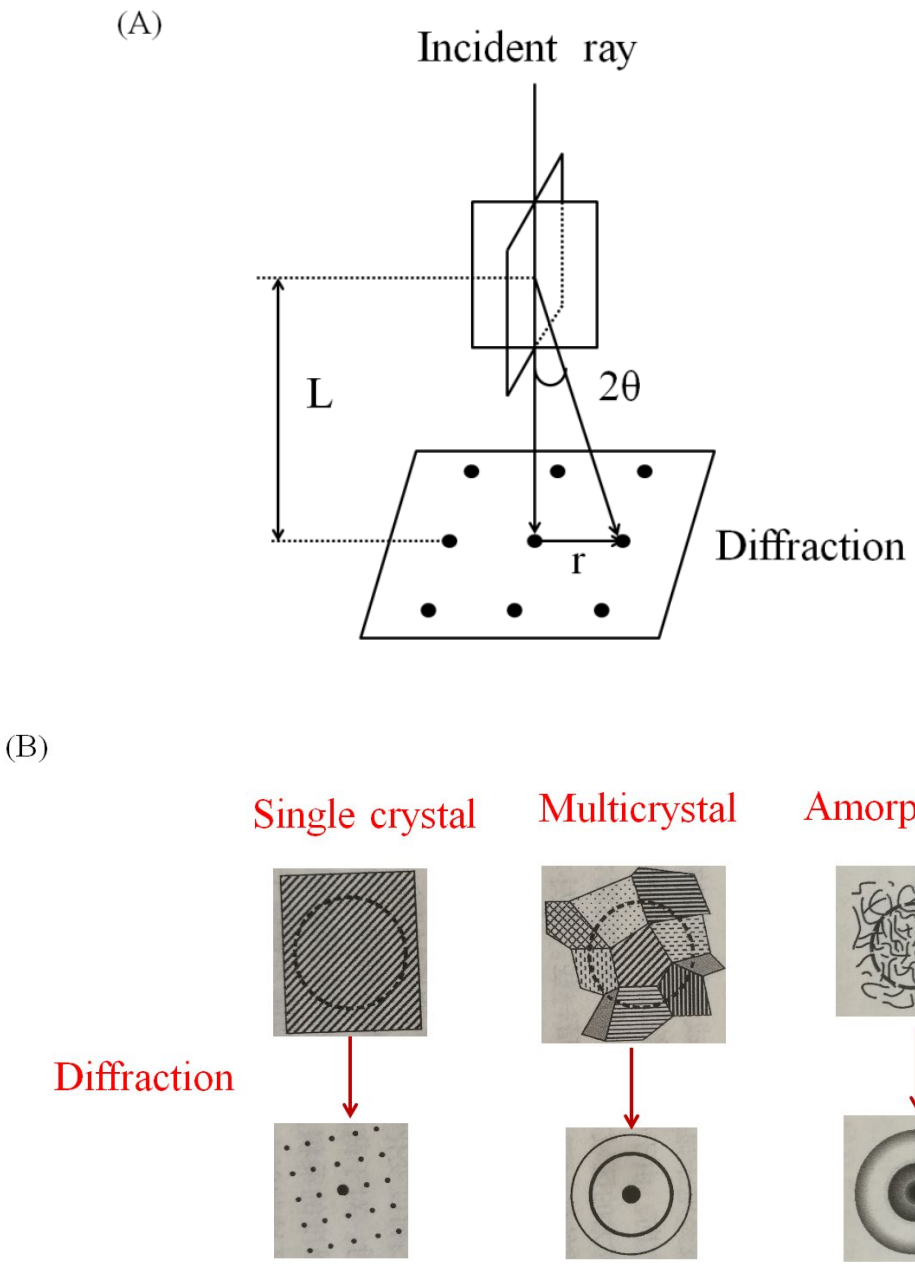

Figure 3-9 Schematic diagram of diffraction (A) and diffraction of various crystals.

3.2.7 Raman Spectroscopy (Raman)

Raman spectroscopy has been used in the field of catalysis since the 1970s. Brown, Makovsky and Rhee reported the MoO_3/λ-Al_2O_3, CoO-MoO_3/λ-Al_2O_3 catalysts were characterized by Raman [181]. Later, Raman was widely used to characterize catalysts, such as transition metal oxide, molecular sieve and carbon [182, 183]. Herein, Raman characterization was carried out for the in-depth study of carbon species deposited on the used catalysts. For example, on used Ni-Si/ZrO_2 and Ni-Zr/SiO_2 catalyst (Figure 3-10), two distinct peaks at about 1328 cm^{-1} (D band) and 1585 cm^{-1} (G band) were observed [62]. D band corresponded to the disorder-induced band, ascribed to the structural imperfections on defective carbon materials. G band corresponded to graphitic carbon, ascribed to the in-plane C-C stretching vibrations of sp^2 atoms in coke [184-186]. Raman spectroscopy experiments were conducted on an objective (X50LWD) with a Laser of 532.17 nm, a Grating of 600 gr/mm, a Filter of D1and a Hole of 200 μm. The data was collected from the wavenumber values of 40−4000 cm^{-1}.

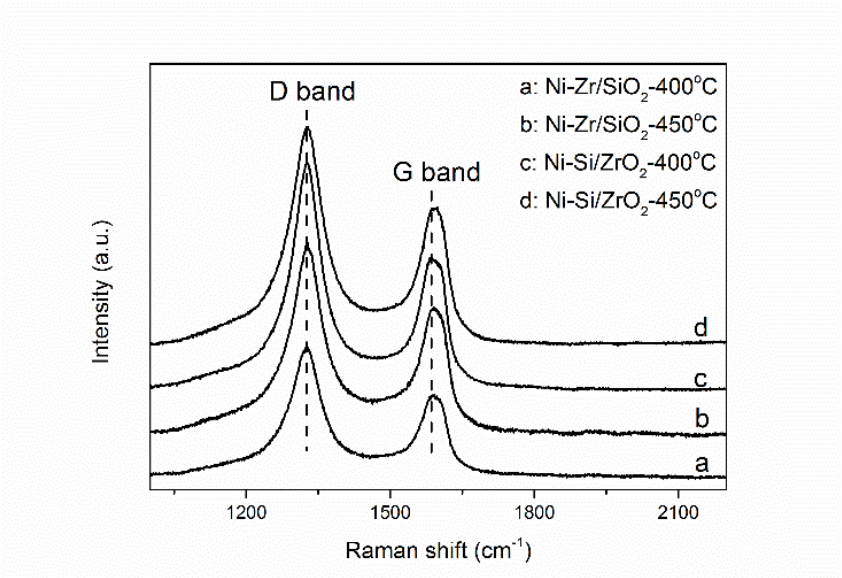

Figure 3-10 Raman result of carbon deposited on Ni-Zr/SiO_2 catalyst after reforming at 400 °C (a) and 450 °C (b) and Ni-Si/ZrO_2 catalyst after reforming at 400 °C (c) and 450 °C (d).

3.2.8 X-ray photoelectron Spectroscopy (XPS)

X-ray photoelectron spectroscopy (XPS) is very widely applied in the field of surface analysis. XPS is based on the photoelectric effect of electrons (photoelectrons) generated when high-energy photons (usually in the keV range) collide with a material. The photoelectron kinetic energy, E_k, which is the measured quantity in the experiment, is given by Einstein's law (Equation 16) [187].

$$E_k = h\nu - E_b \quad \text{(Equation 16)}$$

where $h\nu$ is the energy of the incident radiation and E_b the binding energy of the electron at a particular level. According to the E_b, we will know the element, like E_b (C 1s) = 284.5 eV, E_b (O 1s) = 531 eV, and E_b (Al 2p) = 73 eV [188]. Except for the qualitative information, we can know the quantitative information about the element. Quantitative information arises from the element specificity of the binding energies and the relation between the intensity of the photoelectron peaks and the element concentration [187]. The database of XPS is listed following:

https://xpssimplified.com/periodictable.php

https://srdata.nist.gov/xps/selEnergyType.aspx

In this work, the XPS spectra were recorded on an AXIS Ultra DLD (KRATOS) spectrometer instrument with monochromated Al radiation. All of the data (the electron binding energy) were referenced to the C1s peak at 284.5 eV [189]. For quantitative analysis of the surface, composition was determined by the peak areas and the element-specific Scofield factors.

Chapter IV

One-step synthesis of highly active and stable Ni-ZrO_x for dry reforming of methane

4. One-step synthesis of highly active and stable Ni-ZrO_x for dry reforming of methane

4.1 Introduction

Methane and carbon dioxide could be obtained from natural gas, shale gas, marsh gas, and biomass pyrolysis. CO_2 reforming of methane (DRM) could not only utilize the CO_2 and CH_4, which are the main greenhouse gases but also produce synthesis gas (a mixture of CO and H_2). The latter can be used in the synthesis of high-value chemicals [190, 191]. Furthermore, the syngas with a H_2/CO ratio close to unity is attractive for the synthesis of hydrocarbon fuels, e.g. in Fischer-Tropsch synthesis over iron-based catalysts [77, 95, 192]. However, side reactions could occur during the DRM reaction, such as the reverse water-gas shift (RWGS) reaction, methane cracking, and CO disproportionation, resulting in the deactivation of catalyst and/or the lower H_2/CO molar ratio. Thus, many researches have paid much attention to enhance both high catalytic activity and stability of used catalysts. Although numerous efforts have been given to these issues, several problems like low stability, coke deposition, and metal sintering are still main obstacles towards the large-scale application of DRM catalysts [85, 99, 193].

ZrO_2 support has been widely used in the preparation of catalysts, such as Pt/ZrO_2 [63, 127, 194], Ru/ZrO_2 [195, 196], Co/ZrO_2 [197, 198] and Ni/ZrO_2 [35, 53, 62, 87, 102], for DRM reaction. Among them, Ni-based catalysts are known to be one of the most promising materials for CO_2 reforming of methane, due to their good catalytic performance, low cost, and high availability as compared to noble-metal based catalysts. Therefore, Ni modified ZrO_2 catalyst is a viable alternative for DRM, as it is possible to obtain: (i) high dispersion of the active sites, (ii) medium-strength metal interaction between Ni and ZrO_2 matrix which suppress the sintering of metallic nickel, (iii) high concentration of medium-strength basic sites. Apart from that, Ni/ZrO_2 catalyst also

exhibits a high concentration of surface oxygen species, which are favorable for CO_2 adsorption and decomposition [53, 62, 87, 102, 108, 165, 199]. Jing et al. [199] found that Ni/SiO_2 catalysts modified with ZrO_2 had better Ni dispersion, improving DRM activity and resistance of nickel sintering. Gonzalez-Delacruz et al. [108] also observed that Ni/ZrO_2 catalyst had better dispersion of nickel metallic phase upon modification with CO, due to the formation of $Ni(CO)_4$ complexes, which deposited on the zirconia surface by colliding. This process contributed to the re-dispersion of nickel without nickel loss, due to the interaction between Ni and Zr, thereby made the catalyst exhibit excellent stability. According to Pompeo et al. [200], ZrO_2 played an important role in promoting adsorption of CO_2, thereby enhancing the C removal. Besides, the surface oxygen species on Ni/ZrO_2 influenced the acidity and basicity, affecting the adsorption and activation of CO_2. Despite these advantages, many studies have been focused on the enhancement of long-term stability by applying different types of Ni/ZrO_2 syntheses [87, 102, 154, 165]. Wei et al. [165] prepared Ni/ZrO_2 by impregnation method with different $Zr(OH)_4$ particles size, and co-precipitation of ultra-fine nickel-zirconium hydroxide method. It revealed that the smaller ZrO_2 particles size contributed to the formation of more basic sites and oxygen vacancies for CO_2 activation. Zhang et al. [102] synthesized Ni/ZrO_2 catalysts by a deposition-precipitation method with different calcination atmosphere (H_2 , N_2 and O_2) and reported that the stability of Ni/ZrO_2 catalyst under the calcination ambience of H_2 was improved by the higher content of adsorbed oxygen species, which were beneficial in carbon removal. Moreover, Lou et al. [87] prepared Ni/ZrO_2 catalyst by the impregnation method and found smaller nickel particle sizes which led to the increased interface between metal and support, promoting the carbon accessibility towards oxygen and hindering the carbon accumulation. Sokolov et al. [154] reported that a one-step synthesis of mesoporous La_2O_3–ZrO_2 supported Ni catalysts resulted in good stability, due to the high dispersion of nickel particles and the confinement effect of pore structure.

Considering the advantages of material prepared by the one-step method and increasing the interface between Ni and Zr, in this work, we prepared $Ni\text{-}ZrO_x$ catalysts with

different Ni loadings as described in the synthesis of Ni-Zr and Ni/ZrO_2 catalysts part, and investigated their catalytic behavior in dry reforming of methane. The applied characterization techniques allowed us to further investigate the Ni-Zr interactions in dry reforming of methane, showing a new understanding of this catalytic system.

4.2 Synthesis of a series of Ni-Zr catalysts and Ni/ZrO_2 catalyst.

4.2.1 Synthesis of Ni-Zr catalysts

The Ni-Zr materials were prepared by the urea hydrolysis method reported everywhere [201, 202]. In a typical process, 5 g $ZrO(NO_3)_2 \cdot 2H_2O$ (Aldrich), 7 g urea (Sigma-Aldrich) and x g $Ni(NO_3)_2 \cdot 8H_2O$ (x=0.57, 1.14, and 1.71) were dissolved in 375 mL of deionized water, then, 7 g of Pluronic P123 (Aldrich) amphiphilic block copolymer was added into the solution above. After stirring at 95 °C for 48 h, the mother solution was aged at 100 °C for 24 h. Afterward, the material was isolated by filtration, washed thoroughly with deionized water, and placed at an ambient atmosphere. Finally, the solid material was calcined in flowing air at 800 °C for 5 h with a heating rate of 1 °C/min. The obtained materials were denoted as 5Ni-Zr, 10Ni-Zr, and 15Ni-Zr catalyst, regarding Ni% loading, respectively.

4.2.2 Synthesis of 10Ni/ZrO_2 catalyst

The ZrO_2 support was prepared by the same method used above. The synthesized support was employed to prepare 10Ni/ZrO_2 catalyst by the impregnation method reported everywhere [62]. Particularly, 0.991 g of $Ni(NO_3)_2$ was dissolved in ethanol (Sigma, 99%), then, 2 g of synthesized support was added into this solution and mixed well, afterward, impregnation was carried out in the ambient atmosphere for 24 hours. After that, the material was placed in a dryer at 80 °C to evaporate ethanol, and the second step of drying was carried out at 110 °C for 4 hours immediately. Finally, the material was calcined at 800 °C for 5 h with a heating rate of 1 °C/min. The sample was denoted as 10Ni/ZrO_2.

4.3 The formation of NiO–ZrO_2 solid solution

4.3.1 The formation of NiO–ZrO_2 solid solution confirmed by H_2-TPR

The results of H_2-TPR profiles were presented in Figure 4-1. A broad reduction peak was found in the temperature range from 350 to 600 °C on the 10Ni/ZrO_2 catalyst. The main peak at low temperature (at about 404 °C) is ascribed to bulk nickel oxide on the surface of catalyst because it shows very weak interaction between nickel and zirconium [203, 204]. The other peak at ca. 500 °C is assigned to the reduction of NiO species in the pores of ZrO_2, which needs a higher temperature to be reduced, due to the pore confinement effect and strong interaction between nickel and zirconia [205, 206]. In comparison to the 10Ni/ZrO_2 catalyst, the reduction peaks on the 10Ni-Zr catalyst shifted to higher temperature, indicating that the interaction between nickel and zirconia on the 10Ni-Zr catalyst was higher than that on 10Ni/ZrO_2 catalyst. Also, two broad peaks (423 and 660 °C) can be observed. The peak at 423 °C can be assigned to the NiO on the surface of catalyst, and the maximum reduction peak at about 660 °C can be ascribed to NiO species that is inset in the skeleton of ZrO_2, which is the NiO-ZrO_2 solid solution according to the literature [207, 208]. Besides, the reduction peak on Ni-Zr catalysts shifts to higher temperature with the increase of nickel content. The reduction peak on 15Ni-Zr catalyst shifts to 450 and 690 °C, respectively. The later ascribed to the increase of NiO–ZrO_2 solid solution, resulting in a stronger interaction between zirconia and nickel oxide. The NiO in the NiO-ZrO_2 solid solution becomes more difficult to be reduced when NiO content is increased. There are two reasons for this. Firstly, the content of NiO-ZrO solid solution increases with the increase of nickel content. Considering the second reduction peak starts at the same temperature for 5Ni-Zr, 10Ni-Zr, and 15Ni-Zr catalysts. Therefore, the reduction peak shifts to high temperature with the increase of NiO-ZrO_2 solid solution. Secondly, the higher the nickel content, the more stable the formed NiO-ZrO_2 solid solution. Because of the temperature of crystallization increases with the increase of NiO content (from 405 °C for 0 mol% NiO to 600 °C for 30 mol% NiO) [209]. Chen et al. [210] also found that

the extra nickel NiO species located intergranular and acted as pinning particles. Those the intergranular NiO particles surrounded by ZrO_2 possess strong interaction between Ni and ZrO_2. Both the intergranular and intragranular NiO particles could enhance again the interaction, led to the more stable the NiO-ZrO_2 solid solution. This stable nickel oxide could enhance the stability of the catalyst because the strong interaction would limit the nickel sintering during the DRM reaction [82, 86].

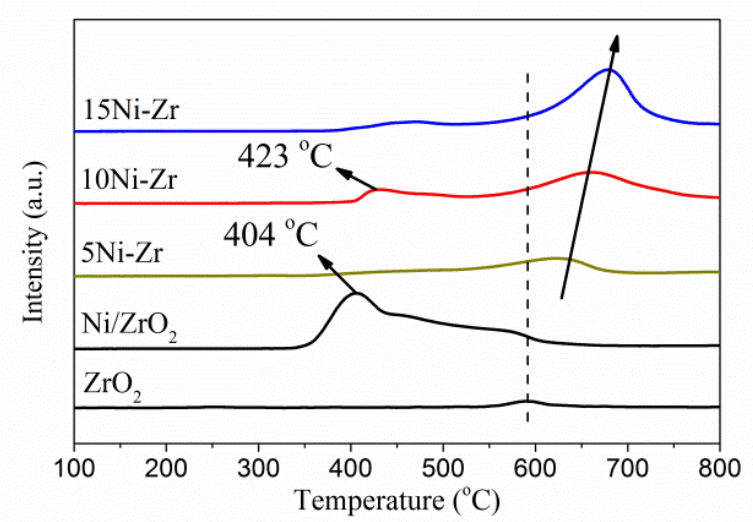

Figure 4-1 The H_2-TPR profiles of a series of Ni-Zr and 10Ni/ZrO_2 catalysts, and ZrO_2.

4.3.2 The formation of NiO–ZrO_2 solid solution confirmed by XRD

Figure 4-2 showed the results of XRD experiment, and the Bragg angles and d-spacing of ZrO_2 listed in Table 4-1. The peaks of tetragonal and monoclinic zirconia are identified on 10Ni/ZrO_2, while only tetragonal ZrO_2 forms on series of Ni-Zr catalysts [207, 211], which indicates that the addition of nickel into ZrO_2 can modify the structure of ZrO_2. It is worth noting that the addition of nickel to zirconia causes a shift of ZrO_2 peaks (2θ=30.14 ° for 10Ni/ZrO_2) to higher Bragg angles (2θ=30.19, 30.38 and 30.43 ° for 5NI-Zr, 10Ni-Zr and 15NI-Zr, respectively), meanwhile, NiO crystal peaks on 10Ni/ZrO_2 is very evident, but it becomes weak and wide on the series of Ni-Zr catalysts, which indicates that NiO could be dispersed well or part of nickel enters the lattice of ZrO_2 to form the solid solutions (NiO–ZrO_2) [105, 132, 212]. This result

corresponds with the results of H_2-TPR. Besides, the d-spacing of ZrO_2 (2θ=30.14) on the 10Ni/ZrO_2 catalyst is about 2.9627 Å, while it is about 2.9576, 2.9402 and 2.9352 Å on the 5Ni-Zr, 10Ni-Zr and 15Ni-Zr catalysts, respectively. The radius of Zr^{4+} ion is larger than that of Ni^{2+} ion [146]. Therefore, the Ni^{2+} ion probably inserts into the crystal lattice of ZrO_2 and replaces some Zr^{4+} ions at the lattice site to form NiO–ZrO_2 solid solution, resulting in the reduction of the lattice parameter.

Table 4-1 The XRD and H_2-TPD results of 10Ni/ZrO_2, 5Ni-Zr, 10Ni-Zr and 15Ni-Zr catalysts.

Catalyst	Bragg angles /°	d-spacing /Å
10Ni/ZrO_2	30.14	2.9627
5Ni-Zr	30.19	2.9576
10Ni-Zr	30.38	2.9402
15Ni-Zr	30.43	2.9352

Štefanić et al [209]. reported that the maximum solubility of Ni^{2+} ions in the ZrO_2 lattice in metastable crystallization products prepared by the incorporation method was 5 mol%. The lattice parameters of ZrO_2 decreased with the increase in the content of Ni^{2+} when the content of Ni^{2+} was less than 5 mol%. While the further increase in the content of Ni^{2+} could not affect the lattice parameters, but increased stabilization of the t-ZrO_2-type phase, due to the strong interaction between NiO and ZrO_2. Actually, according to Table 4-1, the d-spacing of ZrO_2 was decreased with the increase of nickel content, indicating that the solubility of Ni into ZrO_2 was not saturated in this system. There were some nickel species on the surface instead of in the ZrO_2 lattice. Because part of NiO was dissolved under 800 °C calcination. Interestingly, more amount of Ni^{2+} ion embeds into the skeleton of ZrO_2 with the increase of nickel content. Those NiO–ZrO_2 solid solutions in the 10Ni-Zr and 15Ni-Zr catalysts contribute to a higher nickel oxide dispersion and a stronger interaction between NiO and ZrO_2 [212].

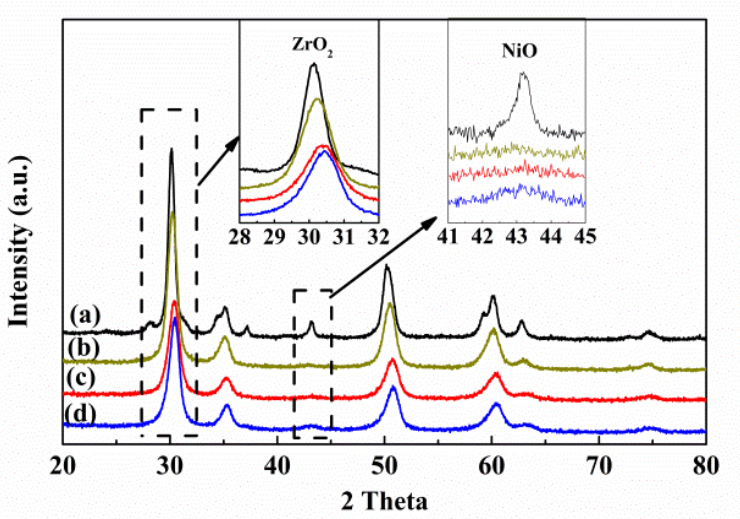

Figure 4-2 The XRD profiles of catalysts: (a) 10Ni/ZrO_2, (b) 5Ni-Zr, (c) 10 Ni-Zr and (d) 15 Ni-Zr.

4.4 Physicochemical properties

4.4.1 The BET results

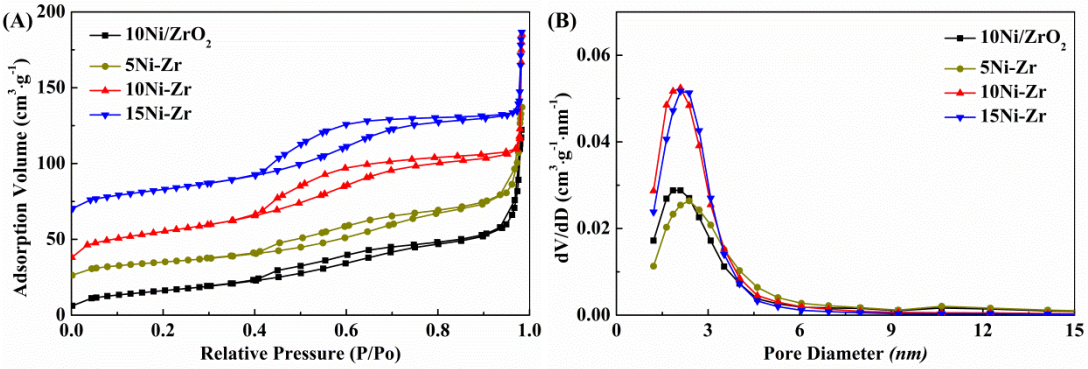

Figure 4-3 (A) N_2 adsorption-desorption isotherms and (B) the pore size distribution of 10Ni/ZrO_2, 5Ni-Zr, 10Ni-Zr, and 15Ni-Zr catalysts.

The physical property of catalysts was evaluated by nitrogen adsorption-desorption isotherms, the specific surface area via the BET method, and the pore volume and pore diameter by means of the BJH method. The results were shown in Table 4-2 and Figure 4-3. All the shapes of the isotherms were assigned to the type IV isotherm with the H3 type of adsorption hysteresis [177]. Compared with the 10Ni/ZrO_2, the adsorption hysteresis on the 10Ni-Zr catalyst could be observed more evident, which corresponded with the results of pore size distribution. The pore diameter on 10Ni/ZrO_2 and 10Ni-Zr catalysts almost distributed at about 2 nm. While, according to the pore size distribution, the later exhibited larger pore volume. Except for the pore volume and pore diameter, the particle size also affects the surface area, because the large particle size of Ni species can lead to a lower surface area [213]. The NiO particle size on 10Ni/ZrO_2 catalyst was about 15 nm, while NiO crystal peaks could not be observed mostly on the 10Ni-Zr catalyst, therefore, 10Ni/ZrO_2 catalyst exhibits lower surface area of 72 m^2/g, whereas surface area increases obviously to 113 m^2/g for the 10Ni-Zr catalyst.

Table 4-2 The BET results of 10Ni/ZrO_2, 5Ni-Zr, 10Ni-Zr and 15Ni-Zr catalysts.

Catalyst	Pore diameter nm	Surface area m^2/g	Pore volume cm^3/g
10Ni/ZrO_2	2	72	0.19
5Ni-Zr	2	66	0.17
10Ni-Zr	2	113	0.20
15Ni-Zr	2	103	0.18

4.4.2 The particle size of nickel species

Table 4-3 The XRD and H_2-TPD results of 10Ni/ZrO_2, 5Ni-Zr, 10Ni-Zr and 15Ni-Zr catalysts.

Catalyst	Reduced		Post-Reaction		Reduced	Post-Reaction		D_{Ni}
	B-a/^{o}	d-s/Å	B-a/^{o}	d-s/Å	Ni^0/nm	Ni^0/nm	NiO/nm	(%)
10Ni/ZrO_2	30.28[a]	2.9521	30.26	2.9534	20[b]	31	15	1.3[c]
5Ni-Zr	30.24	2.9556	30.27	2.9522	31	26	16	3.2
10Ni-Zr	30.32	2.9480	30.48	2.9332	11	15	-	4.3
15Ni-Zr	30.38	2.9421	30.44	2.9363	11	13	-	2.6

a: The results of Bragg angles (B-a) and d-spacing (d-s) of ZrO_2 on catalysts, determined by XRD.

b: The Ni^0 and NiO crystallite sizes on catalysts, determined by XRD.

c: The Ni dispersion (D_{Ni}) of catalysts, determined by H_2-TPD.

XRD profiles of the catalysts before and after reaction are reported in Figure 4-4 (A) and (B). After reduction, from Scherrer Equation, the nickel particle size formed (11 nm) on the 10Ni-Zr catalyst is smaller than that on 10Ni/ZrO_2 (20 nm), which shows the 10Ni-Zr catalyst prepared by one-step synthesis method could enhance the dispersion of nickel species. 5Ni-Zr catalyst exhibits the lowest surface area and the smallest pore volume and diameter, which might go against the distribution of nickel metal species after reduction, thereby resulting in the sintering of nickel on 5Ni-Zr catalyst. The small size of particles contributes to the increase of the activity for the

DRM reaction because it is well known that the nickel particle size can affect the activity of the catalyst [214]. Meanwhile, according to the results of H_2-TPD, the Ni dispersion of 10Ni/ZrO_2, 5Ni-Zr, 10Ni-Zr and 15Ni-Zr catalyst is 1.3 %, 3.2 %, 4.3 % and 2.6 %, respectively. Obviously, 10Ni-Zr catalyst exhibits the highest dispersion, while the 10Ni/ZrO_2 shows the lowest dispersion. A better dispersion of nickel would contribute to the catalytic performance of catalyst, due to the more accessible nickel metallic sites form on surface of catalyst [69, 117]. The higher dispersion of nickel species might promote the performance of catalysts for dry reforming of methane.

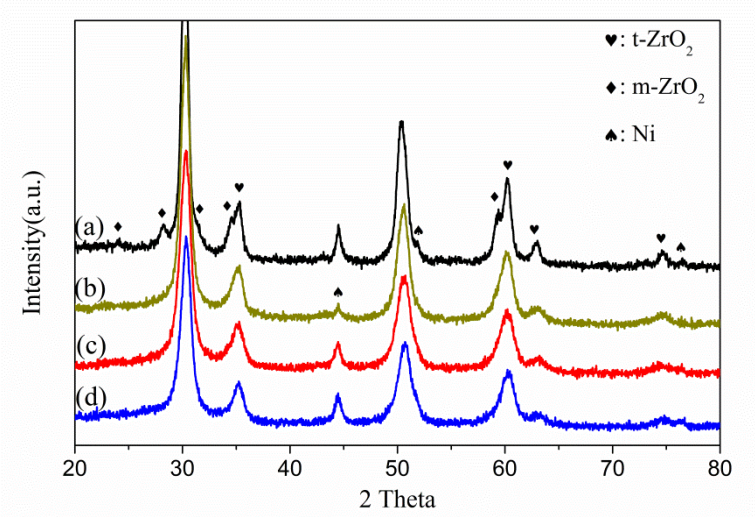

Figure 4-4 XRD profiles of (a) 10Ni/ZrO_2, (b) 5Ni-Zr, (c) 10Ni-Zr and (d) 15Ni-Zr catalysts after reduction at 750 °C.

Besides, The Bragg angles and d-spacing of ZrO_2 on all catalysts after reduction and reaction were listed in Table 4-3. Compared with calcined catalyst, the peak of ZrO_2 on 10Ni/ZrO_2 catalyst after reduction shifted to higher Bragg angles (30.28 °), as well as the decreased d-spacing (2.9521). After reaction, it mostly kept at 30.26 ° and 2.9534 for Bragg angles and d-spacing of ZrO_2 on 10Ni/ZrO_2 catalyst, respectively. While the Bragg angles and d-spacing of ZrO_2 on 5Ni-Zr catalyst after reduction and reaction were similar to those on 10Ni/ZrO_2 catalyst, indicating that 5Ni-Zr shifted to traditional catalyst after reduction, like 10Ni/ZrO_2 catalyst. Therefore, the nickel particle on 5Ni-Zr catalyst was easy to sinter after reduction, as well as to be oxidized after reaction.

Whereas the Bragg angles of ZrO_2 on 10Ni-Zr catalyst decreased, and the d-spacing increased after reduction. While after reaction, the Bragg angles increased from 30.32 to 30.48 °, meanwhile the d-spacing decreased from 2.9480 to 2.9332, which manifested that part of nickel can be released from the skeleton of ZrO_2 under the reduction condition, and can enter into the structure of ZrO_2 under the reaction conditions. Similar phenomenon could be observed on 15Ni-Zr catalyst. Those phenomena indicated that NiO-ZrO_2 solution could be kept on both 10Ni-Zr and 15Ni-Zr catalyst during the reaction, thereby restraining the sintering and oxidation of nickel metal. Moreover, the Bragg angles of ZrO_2 on 10Ni-Zr catalyst were lower than that on 15Ni-Zr catalyst after reduction, while it was higher than that on 15Ni-Zr catalyst after reaction. It means more nickel could insert into the structure of ZrO_2 on 10Ni-Zr catalyst during the reaction.

4.4.3 The basicity of the catalysts

The CO_2 temperature-programed desorption profiles, which are commonly used to describe the basicity of catalysts, are shown in Figure 4-5. First, we can observe that the number of basic sites on one step Ni-Zr catalysts slightly increases, as a list in Table 4-4. The total basicity of 10Ni/ZrO_2 and 10Ni-Zr catalysts is about 65 and 73 μmol CO_2 per gram of catalyst respectively. Besides, it can be also noted that desorption peaks on the 10Ni-Zr catalyst slightly shift to lower temperature, compared with the 10Ni/ZrO_2 catalyst, which indicates that the introduction of nickel into ZrO_2 structure can decrease the strength of basicity. In order to further investigate the CO_2 desorption on catalysts, the curve is fitted to three peaks according to the literature [215-217], and the results are also shown in Table 4-4. The peak at low temperature area is the weak basic site, which is mainly consisted of weak Brønsted basic sites such as surface OH groups, the peak at intermediate temperature area (medium-strength basic sites) consists of Lewis base sites such as unsaturated (cus) O^{2-} and Zr^{4+}–O^{2-} centers, and the peak at high temperature area (strong basic sites) corresponds the CO_2 adsorption of the cus Zr^{4+}

centers with strong Lewis acidity [72, 114]. Takano et al. found that the CO_2 desorption occurred below 250 °C during H_2/CO_2 TPR experiment. Thus they presumed that the CO_2 adsorbed on the weak basic sites was less reactive with H_2, due to the weak adsorption of CO_2 [218]. Therefore, the weak basic sites might restrain the reverse water-gas shift reaction (RWGS).

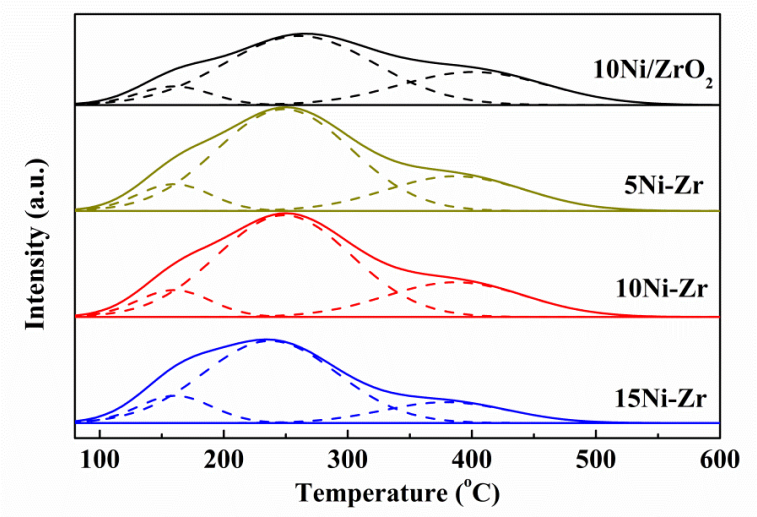

Figure 4-5 The CO_2-TPD profiles of 10Ni/ZrO_2, 5Ni-Zr, 10Ni-Zr, and 15Ni-Zr catalysts.

Besides, CO_2 adsorbed on the medium-strength basic sites (cus-O^{2-} and Zr^{4+}–O^{2-} centers) to form monodentate and bidentate carbonates, respectively [72, 73, 218]. Some studies showed that bidentate carbonates could promote coke elimination [70, 71, 218]. On the other hand, Zhang et al.[72] thought that monodentate carbonates on Ni–ZrO_2 catalyst were the main active intermediates for CO_2 dissociation, while polydentate carbonate species could lead to a reduction of the activity for CO_2 dissociation. These polydentate carbonate species were derived from the CO_2 adsorption of strong basic site. Therefore, weak and medium-strength basic sites could promote the performance of catalyst for DRM reaction. The weak and medium-strength basic sites on 10Ni-Zr were higher than those on 10Ni/ZrO_2 catalyst. And the content of weak basic sites increases with the increase of Ni content for series of Ni-Zr catalysts.

Table 4-4 The Peak position and deconvolution of the CO_2-TPD profiles obtained for the 10Ni/ZrO_2, 5Ni-Zr, 10Ni-Zr, and 15Ni-Zr catalysts.

	CO_2 desorbed (%)						Total basicity (μmol CO_2/g)
	Weak		medium-strength		Strong		
Catalyst	Position	Content	Position	Content	Position	Content	
10Ni/ZrO_2	180	14.7	273	56.8	409	28.5	65
5Ni-Zr	180	16.7	260	60.5	392	22.8	77
10Ni-Zr	180	20.8	260	59.4	385	19.8	73
15Ni-Zr	180	27.8	260	53.6	399	18.6	67

4.4.4 Structure and morphology of the catalysts

Figure 4-6 presented the TEM results. Similar morphology formed on all the catalysts, and it looked like an elliptic grain. It can be observed that the 10Ni/ZrO_2 and 5Ni-Zr catalysts have quite large sizes, especially on 5Ni-Zr catalyst with the randomly-distributed particles, between 10 and 40 nm. While the particle size decreased on 10Ni-Zr and 15Ni-Zr catalysts, and the range significantly changed to 8-12 nm. It implied a significant enlargement in their sizes on 10Ni/ZrO_2 and 5Ni-Zr catalysts compared to 10Ni-Zr and 15Ni-Zr catalysts, in agreement with the XRD results.

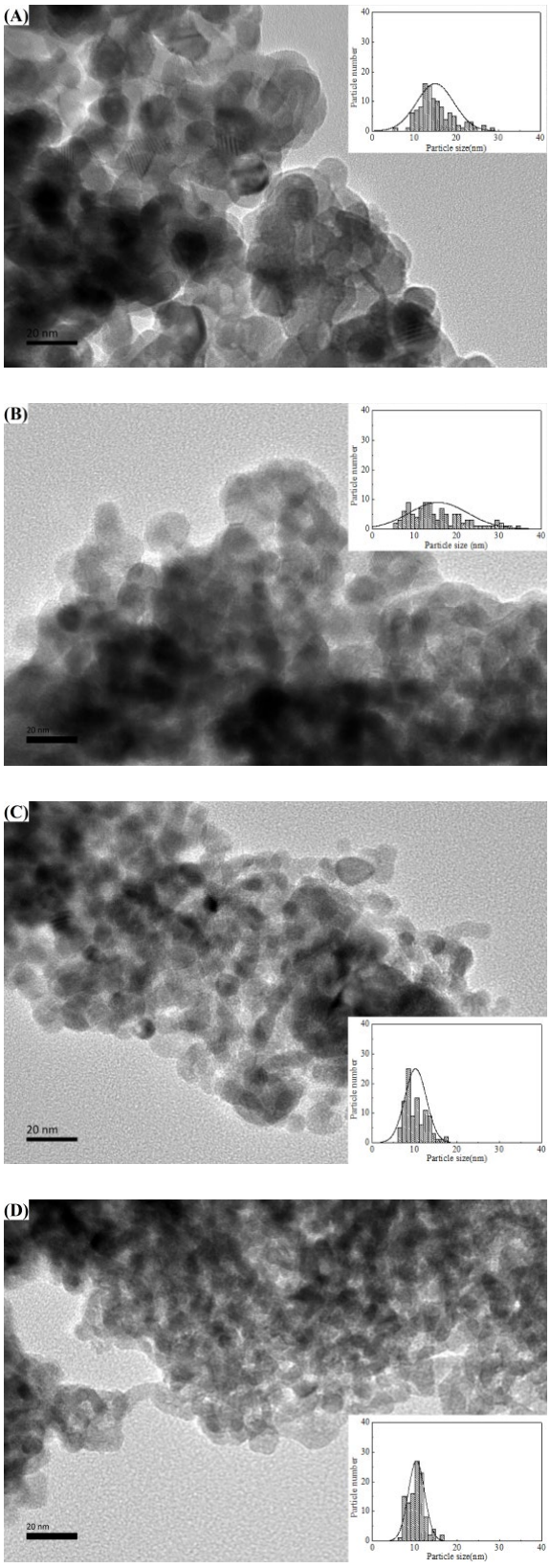

Figure 4-6 The TEM profiles of (A) 10Ni/ZrO_2, (B) 5Ni-Zr, (C) 10Ni-Zr, and (D) 15Ni-Zr catalysts after reduction.

4.5 Catalytic performance in DRM

4.5.1 Zirconia support nickel catalysts for dry reforming of methane

Table 4-5 the performance of the 10Ni/ZrO_2 catalysts at various temperatures for DRM reaction.

Catalysts	Ni[a] %	T[b] °C	Reactant GSHV Gas flow	Conversion (%) CH_4	Conversion (%) CO_2	Ratio H_2/CO	Lost in activity %.h^{-1}	Ref.
			36 $L \cdot h^{-1} \cdot g^{-1}$					
Ni/ZrO_2	8.1	850	CH_4:CO_2:N_2=1:1:1	~95	~97	-	S [c]	[219]
			-					
Ni/ ZrO_2	5	800	CH_4:CO_2=1:1	~11	~10	-	-	[220]
			24 $L \cdot h^{-1} \cdot g^{-1}$					
Ni/ZrO_2	12	757	CH_4:CO_2 =1:1	~87	-	1.2	S	[221]
			24 $L \cdot h^{-1} \cdot g^{-1}$					
Ni/ZrO_2	10	750	CH_4:CO_2 =1:1	83.8	84.2	1.18	S	[165]
			64.3 $L \cdot h^{-1} \cdot g^{-1}$					
NiO–ZrO_2	10	750	CH_4:CO_2 =1.5:1	~35	~57	0.84	~1.8	[222]
			150 $L \cdot h^{-1} \cdot g^{-1}$					
Ni/ZrO_2	26	750	CH_4:CO_2:He=1:1:8	~55	-	-	1.7	[108]
			120 $L \cdot h^{-1} \cdot g^{-1}$					
Ni/ZrO_2	8	750	CH_4:CO_2:He=3:2:5	~50	~79	0.93	~1-2	[223]
			12,000 h^{-1}					
Ni-ZrO_2	20	700	CH_4:CO_2:N_2=1:1:3	~86	73	-	~0.29	[224]
			24 $L \cdot h^{-1} \cdot g^{-1}$					
Ni/ZrO_2	3	700	CH_4:CO_2 =1:1	~70	~80	~0.99	4	[102]
Ni/ZrO_2	2	700	37.4 $L \cdot h^{-1} \cdot g^{-1}$	65.9	67.9	-	-	[225]

			CH_4:CO_2:He=33:33:34 37.6 $L \cdot h^{-1} \cdot g^{-1}$					
Ni/ZrO_2	5	700	CH_4:CO_2 =1:1 150 $L \cdot h^{-1} \cdot g^{-1}$	~95	-	-	4	[149]
Ni/ZrO_2	5	700	CH_4:CO_2 =1:1 240 $L \cdot h^{-1} \cdot g^{-1}$	59.3	63.7	0.92	0.1	[213]
Ni/ZrO_2	10	600	CH_4:CO_2:He=1:1:2 40.7 $L \cdot h^{-1} \cdot g^{-1}$	34	33	-	0.08	[226]
Ni/ZrO_2	10	550	CH_4:CO_2=1:1 15.6 $L \cdot h^{-1} \cdot g^{-1}$	10.4	30.6	-	1.10	[140]
10Ni/ZrO_2	10	750	CH_4:CO_2:Ar=1:1:8 15.6 $L \cdot h^{-1} \cdot g^{-1}$	74.5	79.4	0.86	5.32	This work
10Ni-Zr	10	750	CH_4:CO_2:Ar=1:1:8 15.6 $L \cdot h^{-1} \cdot g^{-1}$	96	96.7	0.95	S	This work
10Ni-Zr	10	700	CH_4:CO_2:Ar=1:1:8	92.9	93.1	0.97	S	This work

a: The content of nickel

b: The reaction temperature

c: Calculation by methane

d: After reaction for 5 h

e: After reaction for 8 h

~: About, read by the figure

S: Stable

D: Deactivation

-: No data

Table 4-5 summarizes the studies of different 10Ni/ZrO_2 catalysts in dry reforming of methane. As presented in Table 4-5, 10Ni/ZrO_2 catalyst from the work of Wei [165], at

750 °C exhibited the highest CH_4 and CO_2 conversion, and the best H_2/CO ratio about 83.8 %, 84.2 % and 1.2, respectively. And at 700 °C, the highest CH_4 and CO_2 conversion, and the best H_2/CO ratio on one of 10Ni/ZrO_2 catalysts from the work of Gonzalez-Delacruz [102] were 70 %, 80 % and 0.99, respectively. In our work, we also prepared 10Ni/ZrO_2 catalyst, which showed about 74.5 % for CH_4 and 79.4 % for CO_2 conversion at 750 °C. The most important is that the 10Ni-Zr catalyst prepared via one-step synthesis method shows the best performance for the DRM reaction. At 750 °C, the CH_4 and CO_2 conversion on 10Ni-Zr catalyst are 96 % and 96.7 %, respectively. The ratio of H_2/CO is very close to 1, about 0.95. Besides, the CH_4 and CO_2 conversion on 10Ni-Zr catalyst could respectively reach to 92.9 % and 93.1 % even at 700 °C. The H_2/CO ratio is higher than that at 750 °C, which was closer to 1, about 0.97.

4.5.2 The performance of 10Ni/ZrO_2, 5Ni-Zr, 10Ni-Zr, and 15Ni-Zr catalysts.

The performance in CO_2 reforming of methane (activity and stability) of 10Ni/ZrO_2 and the series of Ni-Zr catalysts was conducted in isothermal conditions at 750, as shown in Figure 4-7. A loss of 26.3 % in CH_4 conversion is observed on the 10Ni/ZrO_2 catalyst for 5 h time on stream. The CH_4 and CO_2 conversions of the 10Ni/ZrO_2 catalyst decrease in the first hour (Figure 4-7 A and B). The H_2/CO ratio decreases within 3 hours, finally stabilize at about 0.8 (see in Figure 4-7 C). A similar phenomenon can be observed on the 5Ni-Zr catalyst that CH_4 and CO_2 conversions decrease from respective 50.7 and 60.0 % to 24.5 and 29.0 % within the 5 h period. In brief, 5Ni-Zr catalyst exhibits the lowest activity and the lowest H_2/CO ratio. The CO_2 conversion is slightly higher than CH_4 conversion on both 10Ni/ZrO_2 and 5Ni-Zr catalysts, while the lower H_2/CO, especially for the 5Ni-Zr catalyst, even lower than 0.5, indicates that it promotes the reverse water-gas shift reaction (RWGS) on both 10Ni/ZrO_2 and 5Ni-Zr catalysts. 10Ni-Zr and 15Ni-Zr catalysts exhibit high stability without deactivation upon 5 h time-

on-stream under the same situation. Simultaneously, the H_2/CO ratio on the 10Ni-Zr catalyst oscillates between 0.9 and 0.96.

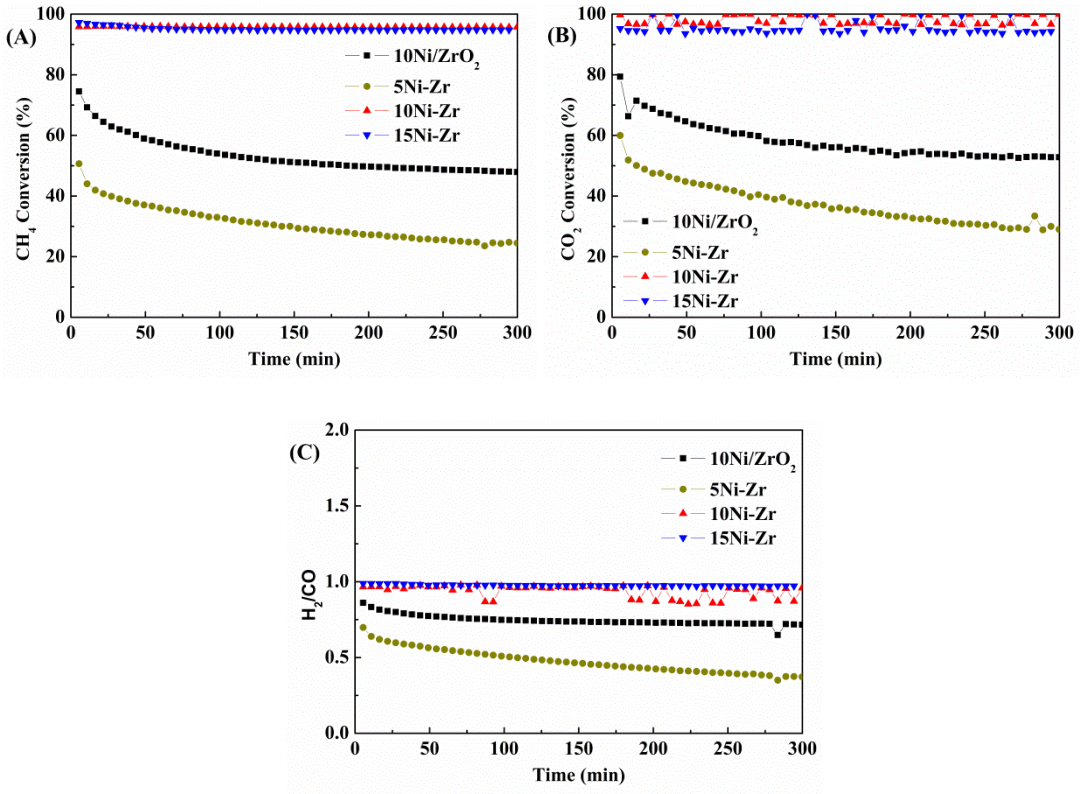

Figure 4-7 The (A) CH_4 conversion, (B) CO_2 conversion and (C) H_2/CO ratio of 10Ni/ZrO_2, 5Ni-Zr, 10Ni-Zr and 15Ni-Zr catalyst at 750 °C.

There are several reasons for the oscillations of the CO_2 conversion and H_2/CO molar ratio for 10Ni-Zr catalyst. Firstly, it might be a systematic error. Secondly, the activation of CO_2 maybe become weaker or stronger during the reaction. Lastly, the ability of CO_2 adsorption might vary under reaction conditions. The latter two reasons might be attributed to the re-dispersion of Ni species. Because the re-dispersion of Ni could occur under an alternating condition between oxidation and reduction atmosphere. Under DRM condition, CO_2 is a source of oxygen, while the CO and H_2 are the reductants. Therefore, the nickel metal may be oxidized when CO_2 adsorption and/or activation on the surface of catalyst. While the NiO species might be reduced by the production of H_2 and CO, and thereby the re-dispersion of nickel particles [89, 93, 117,

227]. Besides, according to the XRD results, the nickel 10Ni-Zr and 15Ni-Zr catalysts could be released from the NiO-ZrO_2 solid solution under reduction condition and enter into the NiO-ZrO_2 solid solution under the reaction condition. Meanwhile, the shift on 10Ni-Zr catalyst was more than that on 15Ni-Zr catalyst. Those shifts might affect the adsorption and activation of CO_2. Therefore, 10Ni-Zr catalyst exhibited the oscillations of the CO_2 conversion, as well as the H_2/CO molar ratio, because the CO_2 conversion could influence the H_2/CO molar ratio. For the 15Ni-Zr catalyst, the shift was too weak to arise the activation and/or adsorption of CO_2.

4.5.3 The performance of 10Ni-Zr catalyst at different temperatures

As shown in Figure 4-8 A, except for the same high stability at 700 °C DRM reaction, the 10Ni-Zr catalyst exhibits slightly higher selectivity than that at 750 °C, resulting in the slightly higher H_2/CO ratio, stabilizing at 0.97 (see in Figure 4-8 B), which is almost unity. Besides, the conversion of CO_2 is more stable at 700 °C than that at 750 °C, resulting in a more stable H_2/CO ratio, which implies that the conversion of CO_2 can affect the H_2/CO ratio. This phenomenon suggests that lower temperature can adjust the H_2/CO ratio.

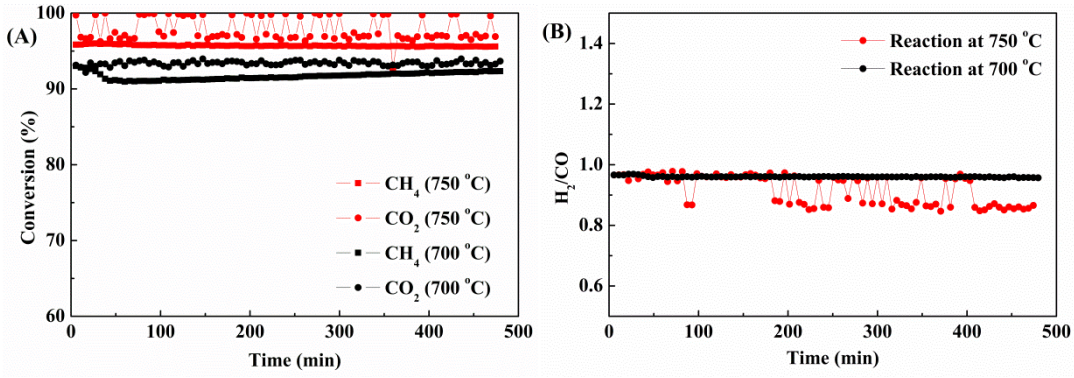

Figure 4-8 The (A) CH_4 and CO_2 conversion and (B) the ratio of H_2/CO of 10Ni-Zr catalyst at 700 and 750 °C time-on-stream.

4.6 Structure of used catalysts

4.6.1 Carbon formation during the DRM

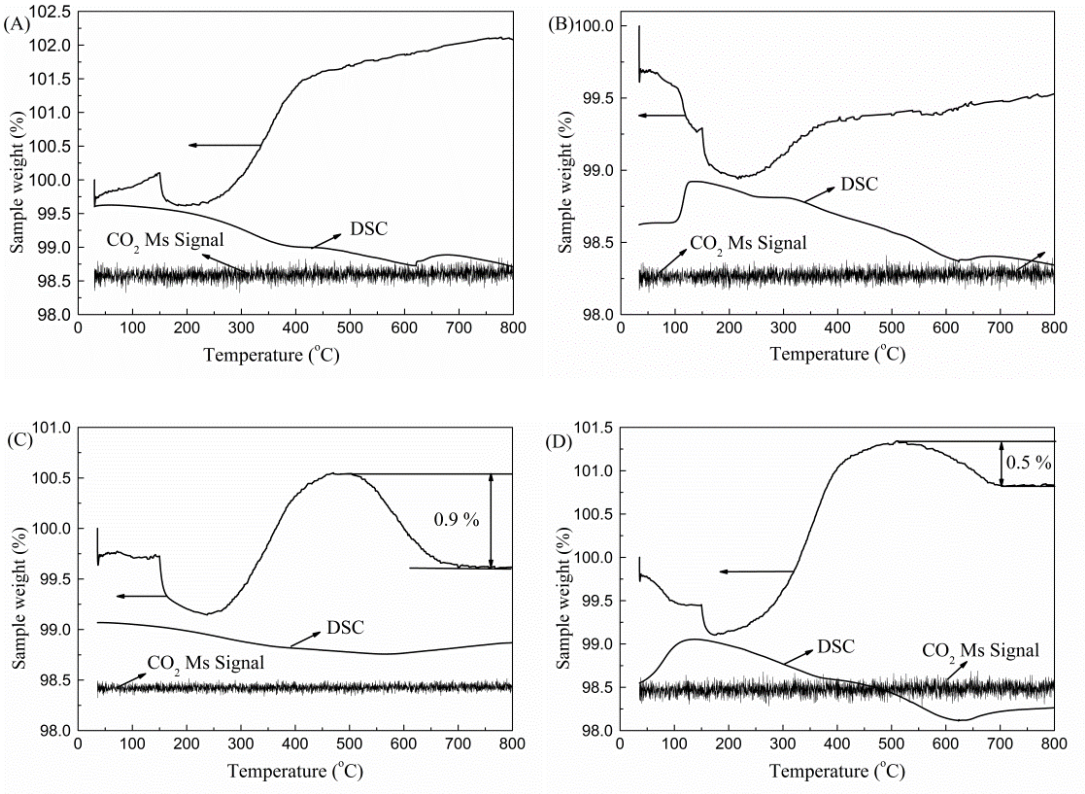

Figure 4-9 TG-DSC-MS profiles of (A) 10Ni/ZrO_2, (B) 5Ni-Zr, (C) 10Ni-Zr and (D) 15Ni-Zr catalysts after reaction at 750 °C.

In order to understand the deactivation of the 10Ni/ZrO_2 catalyst, a series of experiments have been carried out. The carbon deposition was detected by TG-MS experiment, as shown in Figure 4-9. No carbon deposition could be detected in 10Ni/ZrO_2 and 5Ni-Zr catalyst, while only low amounts of carbon of about 0.9 % and 0.5 % on 10Ni-Zr and 15Ni-Zr catalysts are measured, respectively. Besides, the little increase peak in the sample weight curve can be observed on all the catalysts, as well as the endothermic peak on DSC curve, due to the oxidation of the nickel metal. It implies that there is nickel metal on all of the catalysts after reaction. Thus, the coke formation is not the main reason for the deactivation of 10Ni/ZrO_2 and 5Ni-Zr catalysts.

In addition, according to the sample weight curve, the decrease of weight on 10Ni-Zr and 15Ni-Zr catalysts starts at about 500 °C. A similar observation was reported that the coke might be the graphitic carbon, which was difficult to be removed [62].

4.6.2 Evolution of Ni particle size

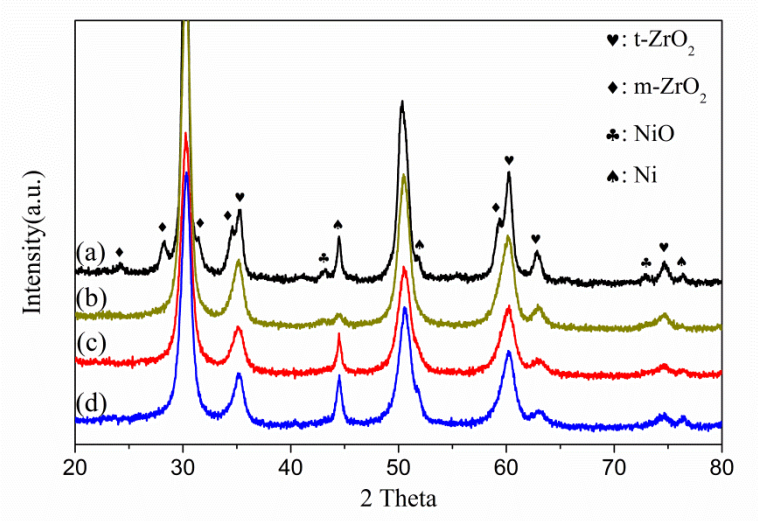

Figure 4-10 XRD profiles of (a) 10Ni/ZrO_2, (b) 5Ni-Zr, (c) 10Ni-Zr and (d) 15Ni-Zr catalysts after reaction at 750 °C in an isothermal run for 5 h.

In order to investigate the sintering of nickel metal on catalyst, the XRD experiment was conducted for testing catalysts after reaction, as shown in Figure 4-10 (B) and Table 4-6. Compared with before reaction, serious sintering of nickel metal can be observed on the 10Ni/ZrO_2 catalyst, and the nickel metal particle size increases from 20 nm to 31 nm, causing to the deactivation of 10Ni/ZrO_2 catalyst. It is worth noting that NiO peak arises on 10Ni/ZrO_2 catalyst with the particle size of 15 nm. This NiO particle can lead to a decrease in the activity in DRM, resulting in the lower stability [214]. For the 5Ni-Zr catalyst, the nickel metal particle size decreased from 31 to 26 nm under reaction condition, because part of nickel metal was re-oxidized to NiO during the reaction. Thus, the NiO crystal size of 16 nm on the 5Ni-Zr catalyst causes the decreased catalytic performance of the catalyst. While slightly sintering can be observed on 10Ni-Zr and 15Ni-Zr catalysts since the nickel metal size increases from 11 nm to 15 and 13 nm for

10Ni-Zr and 15Ni-Zr catalysts, respectively. Moreover, no NiO peak was detected on both 10Ni-Zr and 15Ni-Zr catalysts. Because of the formation of the NiO–ZrO_2 solid solution, the structure of nickel particle is more stable, and the sintering of nickel is then minimized, further leads to stability of catalyst for dry reforming of methane. Thus, the increase in the NiO-ZrO_2 solid solution is more likely linked to an enhancement of the ability to avoid sintering.

Table 4-6 The XRD results of 10Ni/ZrO_2, 5Ni-Zr, 10Ni-Zr and 15Ni-Zr catalysts.

Catalyst	Reduced	Post-Reaction	
	Ni^0/nm	Ni^0/nm	NiO/nm
10Ni/ZrO_2	20	31	15
5Ni-Zr	31	26	16
10Ni-Zr	11	15	-
15Ni-Zr	11	13	-

4.6.3 Surface analyses

Table 4-7 The surface content of Zr 3d and Ni 2p over 10Ni/ZrO_2, 5Ni-Zr, 10Ni-Zr, and 15Ni-Zr catalysts after reaction at 750 °C for 5 hours.

	The surface elemental content		Ni 2p (%)[a]	
	Ni 2p (%)	Zr 3d (%)	Ni^0	Ni^{2+}
10Ni/ZrO_2	13.2	50.4	9.6	90.4
5Ni-Zr	3.6	55.9	17.5	82.5
10Ni-Zr	4.8	50.9	24.3	75.7
15Ni-Zr	6.4	53.7	34.8	65.2

a: The content of Ni^0 and Ni^{2+} species in nickel species, calculated by Figure 4-11 (A).

XPS experiments are conducted in order to obtain the information of Nickel and Carbon oxidation states and chemical environment on the surface of catalyst. As shown in Figure 4-11 (A), it is worth noting that after reaction, Ni^0 species can be observed on all the catalysts. The surface content of Ni^0 on $10Ni/ZrO_2$ and 5Ni-Zr catalysts are 9.6 % and 17 % (Table 4-7), respectively, while 10Ni-Zr and 15Ni-Zr catalysts possess higher surface content of Ni metal, about 24.8 %, and 34.1 %, respectively. NiO crystal phase can be observed evidently on $10Ni/ZrO_2$ and 5Ni-Zr catalysts, while no NiO peak are detected on 10Ni-Zr and 15Ni-Zr catalysts according to the XRD results. According the the XPS results, there are two reasons for the NiO species on the surface of 10Ni-Zr and 15Ni-Zr catalysts after reaction. At first, part of Ni^0 species might be oxidized when it exposes in air. Second, the oxide materials such as CO_2 and H_2O might be adsorbed on Ni^0 site [120]. However, 10Ni-Zr and 15Ni-Zr catalysts show higher content of Ni^0 species on the surface. Because surface content of Ni^0 is related to the activity of catalyst for DRM reaction [228], thus 10Ni-Zr and 15Ni-Zr catalysts exhibit higher activity for DRM reaction. Besides, the two resolvable peaks at a binding energy of about 854.1 and 856.3 eV on $10Ni/ZrO_2$ catalyst are assigned to NiO with weak and strong interaction with ZrO_2, respectively. Whereas, those two resolvable peaks shift to higher values of about 855.5 eV and 857.8 eV on the 10Ni-Zr catalyst, indicating that the interaction between Ni and Zr is very strong, due to the NiO–ZrO solid solution, corresponding with the XRD and H_2-TPR results. The content of Zr $3d_{5/2}$ on $10Ni/ZrO_2$, 5Ni-Zr, 10Ni-Zr, and 15Ni-Zr catalysts is similar to Figure 4-11 (B).

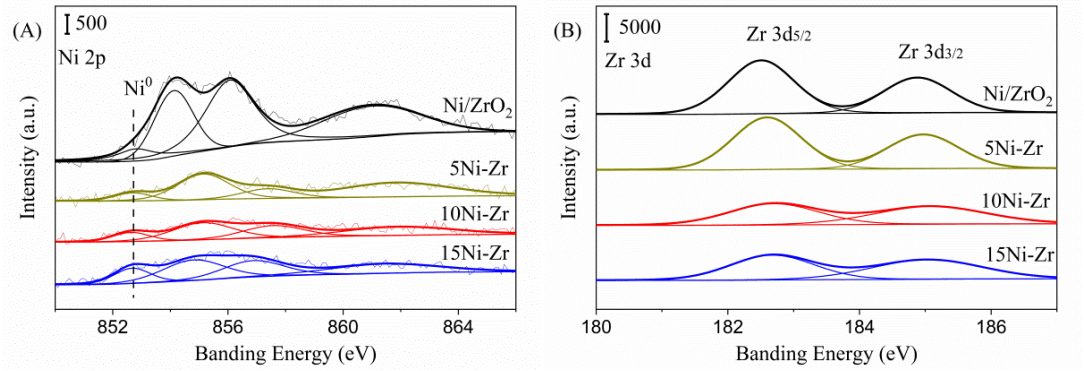

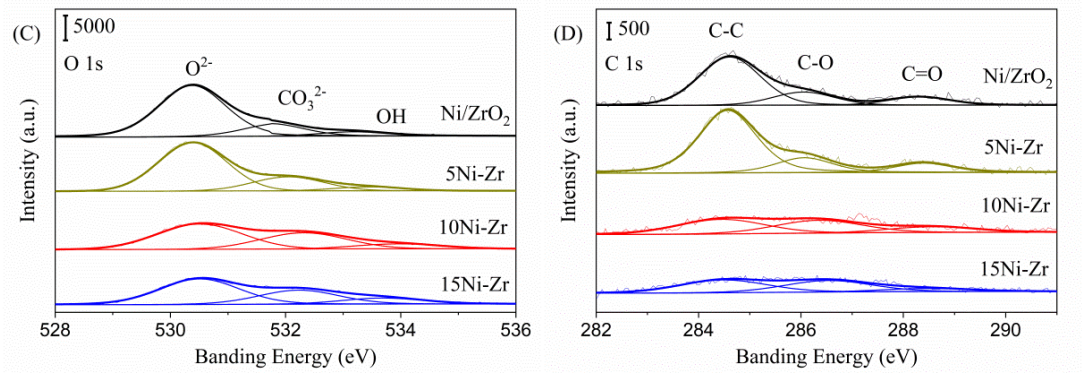

Figure 4-11 XPS profiles of 10Ni/ZrO$_2$, 5Ni-Zr, 10Ni-Zr, and 15Ni-Zr catalysts after reaction at 750 °C.

The O 1s profile is shown in Figure 4-11 (C). There are three kinds of oxide species that exist on all the catalysts: lattice oxygen, carbonate species, and hydroxyl species. Carbonate species mainly come from the adsorption of CO_2, while the hydroxyl species come from the adsorption of water or hydrogen atom [123]. Interestingly, 10Ni-Zr and 15Ni-Zr catalysts possess similar content of surface oxide species (carbonate species and hydroxyl species) of about 45 % and 44 % (Table 4-8), which are higher than those on 5Ni-Zr (28 %) and 10Ni/ZrO$_2$ (25 %) catalysts. Because adsorption oxide species can promote the adsorption and activation of CO_2, as well as dissociation of CH_4, further promote the removal of carbon deposition and enhance the activity [229]. After DRM reaction, more carbonate species and hydroxyl species form on 10Ni-Zr and 15N-Zr catalysts, contributing to higher activity and stability. While more lattice oxide species exist on 5Ni-Zr and 10Ni/ZrO$_2$ catalysts, manifesting less adsorption oxide species can be observed on the catalysts, resulting in lower activity and stability. A similar phenomenon can be observed, as shown in Figure 4-11 (D), that is, similar content of C–O and C=O species on 10Ni-Zr (56 %) and 15Ni-Zr (51 %) catalysts, which is higher than those on 5Ni-Zr (28 %) and 10Ni/ZrO$_2$ (30 %) catalysts.

Table 4-8 The surface content of C 1s and O 1s over 10Ni/ZrO$_2$, 5Ni-Zr, 10Ni-Zr, and 15Ni-Zr catalysts after reaction at 750 °C for 5 hours.

	C 1s (%) [a]				O 1s (%) [b]			
	C-C	C-O	C=O	C-O + C=O	O^{2-}	CO_3^{2-}	OH^-	CO_3^{2-} + OH^-
10Ni/ZrO_2	69.5	18.9	11.6	30.5	75.2	18.5	6.3	24.8
5Ni-Zr	71.9	17.2	10.9	28.1	72.3	21.9	5.8	27.7
10Ni-Zr	44.1	38.8	17.1	55.9	54.5	34.9	10.6	45.5
15Ni-Zr	48.9	41.2	9.9	51.1	56.0	30.8	13.2	44

a: The content of C-C, C-O and C=O species in C species, calculated by Figure 4-11 (C).

b: The content of O^{2-}, CO_3^{2-} and OH^- species in O species, calculated by Figure 4-11 (D)

4.7 Discussion

The 10Ni-Zr catalyst prepared from direct synthesis exhibits better catalytic performance for dry reforming of methane, compared with traditional impregnation 10Ni/ZrO_2 catalyst. The conversion of CO_2 and CH_4 can reach c.a. 96 % on 10Ni-Zr catalyst even after 5 hours reaction. while on 10Ni/ZrO_2 catalyst, a deactivation is observed with time on stream. The activity and the stability of the 10Ni-Zr catalyst can be explained by the presence of NiO–ZrO_2 solid solution, which increases the surface area, and also by small nickel particle size (Ni°) (11 nm). The NiO–ZrO_2 solid solution with those special properties can contribute to the activity for dry reforming of methane [102, 214, 230]. The strong interaction in NiO–ZrO_2 solid solution on the 10Ni-Zr catalyst can limit the sintering of nickel particles under the reaction conditions, contributing to the stability of the 10Ni-Zr catalyst. Besides, adsorption oxide species can promote the adsorption and activation of CO_2, as well as dissociation of CH_4, and further promote the removal of carbon deposition and then the enhancement of the activity in DRM as described in the literature [229]. Besides, more content of weak basic sites and medium-strength basic sites exists on the 10Ni-Zr catalyst, thus exhibits the highest H_2/CO ratio, about 0.95, which is very close to 1. Because CO_2 preferential adsorbed on weak basic sites and at the same time formed active carbonate species that less react with H_2 and more react with methane [5, 89, 116, 218]. Whereas, 10Ni/ZrO_2 catalyst, prepared by impregnation, presents bigger nickel particle (20 nm), higher content of strong basic sites and lower surface area, leading then to lower activity and selectivity for DRM reaction. Besides, severe sintering takes place on 10Ni/ZrO_2 catalyst, due to the weak interaction between NiO and ZrO_2 support. More lattice oxygen species form on 10Ni/ZrO_2 catalyst after reaction, leading to less adsorption oxygen species. Therefore, the 10Ni/ZrO_2 catalyst shows the bad performance of the catalyst for the dry reforming of methane. Besides, the big nickel particle size of 31 nm forms on the 5Ni-Zr catalyst, as well as the lower surface area, leading lower activity and lower selectivity for DRM reaction. Whereas, the same nickel particle size of 11 nm forms on 10Ni-Zr and 15Ni-Zr catalysts, as well as similar surface area and content

of adsorption oxygen species after reaction. Therefore 10Ni-Zr and 15Ni-Zr catalysts exhibit similar activity for DRM reaction. Considering the cost, the 10Ni-Zr catalyst is the optimal for DRM reaction.

4.8 Summary

10Ni-Zr catalyst exhibits the higher performance of catalyst for CO_2 reforming of methane, compared with 5Ni-Zr and 10Ni/ZrO_2 catalysts. Because 10Ni-Zr catalyst possesses more NiO–ZrO_2 solid solution with strong interaction between nickel and zirconium, which leads to the high surface area, small nickel particle size and more content of weak and medium-strength basic sites. Besides, more adsorption oxygen species and just slight sintering occur on 10Ni-Zr and catalyst during the reaction. Therefore, the conversion of CO_2 and methane at 750 °C on 10Ni-Zr catalyst is over 96 % even reaction for 5 hours. The H_2/CO ratio on 10Ni-Zr catalyst is very close to 1. While big nickel particle size and low surface area lead to lower activity and selectivity on 5Ni-Zr and 10Ni/ZrO_2 catalysts for DRM reaction. The weak interaction between nickel and ZrO_2 on the 10Ni/ZrO_2 catalyst can cause severe sintering, thereby leading to deactivation.

Chapter V

Modified mesoporous Ni-Zr catalysts by the promotion of Al, Mn, Y and Mg: on the change of surface properties of the catalysts

5. Modified mesoporous Ni-Zr catalysts by the promotion of Al, Mn, Y and Mg: on the change of surface properties of the catalysts

5.1 Promotion of Ni-Zr catalyst by Y addition

5.1.1 Introduction

In general, noble metal catalysts (Pt, Ir, Rh) exhibit good performance for dry reforming of methane [100, 231, 232]. Considering the high cost of noble metals for the industrial scale, many efforts have focused on the Ni-based catalysts, because nickel metal has a high potential for industrial application in DRM [5, 101, 233, 234]. However, it was well known that Ni-based catalysts suffered deactivation caused by carbon deposition and/or sintering. Therefore, the development of nickel-based catalysts, with the significantly promoted Ni-sintering resistance and coke-tolerance, has been extensively investigated in recent years [51, 98, 235]. According to the literature [236-238], larger Ni particles on the surface of the catalyst led to catalytic selectivity towards methane cracking (Equation (2)), thereby causing carbon deposition. Another approach of the coke deposition was the disproportionation of CO (Equation (4)).

$$CH_4 \rightarrow 2H_2 + C \qquad \text{(Equation 2)}$$

$$2CO \rightarrow CO_2 + C \qquad \text{(Equation 4)}$$

It is found that the adjustment of the catalyst by promoters is an efficient approach to restrain the formation of carbon [97, 110, 239]. Thus, the modification of the raw catalyst with rare earth elements has been reported to enhance both the activity of the catalyst and inhibition of carbon formation, such as La and Y. The later has attracted huge interest in reforming catalyst [53, 110, 147, 237]. Taherian et al. [97] found that comparing with mesoporous Ni/SBA-15, Ni/SBA-15 modified by Y_2O_3 can promote the control of the nickel particle size and thus enhance the dispersion of nickel.

Moreover, Ni-Y/KIT-6 catalyst exhibited better dispersion of nano-size Ni particle inside the pores of the support as compared to Ni/KIT-6 material, leading to lower carbon deposition in the initial stability test at 700 °C [238]. Li et al. [239] investigated the effect of different types of impregnation for yttrium introduced on performance of $Ni/Y/Al_2O_3$ catalyst, and observed that compared with Y-free catalyst, the activity and stability of Y-modified catalyst increased, because of smaller nickel metallic particle size, more basic sites, the less amount of carbon deposit, and the small degree of graphitization. Furthermore, Li et al. [112] also observed highly carbon-resistance for Ni-SBA-15 catalyst modified by yttrium promoter, because of high dispersion of the nano-particles of yttrium and nickel. Moreover, more oxygen vacancies were created by introducing of yttrium.

Except for the active metal and promoter, the support also plays an important role in the catalytic test for DRM. The ZrO_2 is considered to be a promising support for dry reforming of methane, because of the special property, e.g. the reducing and oxidizing abilities, the unexceptionable thermal and chemical stability, and the high oxygen mobilization [62, 87, 102, 110]. These properties of ZrO_2 can be improved by adding a cation with valence lower than 4+, e.g. Y^{3+} [110, 147], which results in the formation of solid solution, together with oxygen vacancies. Furthermore those oxygen vacancies play a key role in gasifying carbon deposits during the activation of CO_2 and O_2 [147]. Bellido et al. [147] prepared a series of Y_2O_3-ZrO_2 catalysts with different yttrium content (4 to 12 mol%). 5Ni8YZ (mole fraction of Y=8 mol%) catalyst showed the best activity and stability for DRM. Because Y^{3+} increased the formation of oxygen vacancies in YZ support. Those modification properties of ZrO_2 could improve the performance of catalyst. Asencios et al. [146] investigated the effect of solid solution on performance of NiO-Y_2O_3-ZrO_2 catalyst and found that the formation of NiO-Y_2O_3 and Y_2O_3-ZrO_2 solid solution could enhance the activity of catalyst for oxidative reforming of model biogas. Moreover, the formation of oxygen vacancies could promote the removal of carbon deposition. Świrk et al. [94, 96] also found that the formation of Y_2O_3-ZrO_2 solid solution could improve the stability of catalyst modified by yttrium.

In order to understand the ability of carbon-resistant on the Y-modified ZrO_2 catalyst, the NiO-ZrO_m and NiO-ZrO_m-YO_n catalysts were prepared by one step urea hydrolysis method, and the performance of which was discussed here in detail. This latter catalyst, which was not the most active catalyst in DRM exhibited, however, a high resistance against carbon deposition. We investigate the ability of carbon resistance on NiO-ZrO_m-YO_n catalyst, further to understand the relationship between structure and carbon-resistance on Y-modified catalyst.

5.1.2 Preparation of the NiO-ZrO_m-YO_n catalyst

5.03 g zirconium(IV) oxynitrate hydrate (Aldrich), 1.14 g nickel(II) nitrate hexahydrate (Emsure) 7.06 g urea (Sigma-Aldrich), 0.86 g yttrium(III) nitrate hexahydrate (Aldrich) (corresponding to a loading of 10 wt.%) and 7.96 g of Pluronic P123 (Aldrich) amphiphilic block copolymer were dissolved in 375 mL of distilled water. The mixed liquor was heated from room temperature to 95 °C with constant stirring for 48 h. After that, the mixture was aged at 100 °C for 24 h. Then the slurry was filtered, washed with a little of distilled water and dried at room temperature. The catalysts were calcined in air at 800 °C for 5 h with an increasing rate of 1 °C/min. The obtained materials were denoted as NiO-ZrO_m-YO_n ($Y_{wt\%}$=10 %). In order to understand the function of yttrium, NiO-ZrO_m without yttrium was prepared by the above method and denoted as NiO-ZrO_m.

5.1.3 The physicochemical properties of NiO-ZrO_m-YO_n catalyst

5.1.3.1 The BET results of Y-doped and Y-free NiO-ZrO_m catalysts

The physical properties of Y-doped and Y-free NiO-ZrO_m material were investigated by the N_2 adsorption-desorption method (Table 5-1). Both of the samples display the same narrow pore size of about 2 nm. The NiO-ZrO_m catalyst shows a surface area of 113 m^2/g and a pore volume of 2 nm; while, the NiO-ZrO_m-YO_n catalyst exhibits the lower specific surface area (79 m^2/g) and the smaller pore volume (0.1

cm^3/g), which may decrease the activity of the catalyst, because the high surface area can enhance the activity of catalyst [213].

Table 5-1 The results of the BET experiment for $NiO\text{-}ZrO_m$ and $NiO\text{-}ZrO_m\text{-}YO_n$ calcined catalysts.

Catalyst	Pore diameter nm	Specific surface area m^2/g	Pore volume cm^3/g
$NiO\text{-}ZrO_m\text{-}YO_n$	2	79	0.1
$NiO\text{-}ZrO_m$	2	113	0.2

5.1.3.2 The reducibility of Y-doped and Y-free $NiO\text{-}ZrO_m$ catalysts

Table 5-2 The H_2 consumption of calcined catalysts determined by H_2-TPR. The content of Zr^{4+} and Zr^{3+} on both catalysts after reduction determined by XPS. And the content of Ni on both catalysts determined by ICP.

Catalyst	H_2 consumption, mmol H_2/g				Zr 3d (%)		Ni
	Total	Theory[a]	α	β	Zr^{4+}	Zr^{3+}	(wt %)
$NiO\text{-}ZrO_m\text{-}YO_n$	0.37	0.39	0.10	0.27	16	84	10
$NiO\text{-}ZrO_m$	0.62	0.47	0.13	0.49	10	90	12

a : Calculated by ICP and the consumption of reduction of pure NiO

The H_2-TPR profile of Y-doped and Y-free $NiO\text{-}ZrO_m$ catalysts is presented in Fig. 5-1 (A). Two reduction peaks at about 450 and 650 °C, denominated α and β, respectively, are observed on both catalysts. The first peak (α) corresponds to the reduction of the NiO species of weak and strong interaction with Y and/or Zr [62, 147]. This first peak shifts to low temperature on $NiO\text{-}ZrO_m\text{-}YO_n$ catalyst, as compared to $NiO\text{-}ZrO_m$ catalyst. This shift may be attributed to the increase of oxygen vacancies by the addition of the yttrium promoter, because oxygen vacancies can promote the reduction of NiO by weakening the Ni-O bond [240, 241]. β peak on $NiO\text{-}ZrO_m$ catalyst is related to the reduction of the solid solution of $NiO\text{-}ZrO_2$ and/or ZrO_2, while on $NiO\text{-}ZrO_m\text{-}YO_n$ catalyst, β peak may be assigned to the reduction of solid solution ($NiO\text{-}ZrO_2$ and/or $NiO\text{-}Y_2O_3$), ZrO_2 and/or surface-capping oxygen ions of the $Y_2O_3\text{-}ZrO_2$ solid solution [146, 242]. On the contrary, the β peak shifts to a higher temperature for $NiO\text{-}ZrO_m\text{-}YO_n$ catalyst. A similar phenomenon about the shift was found by Asencios et al. [146] on $NiO–Y_2O_3–ZrO_2$ catalysts. The yttrium addition could promote the reduction of surface-capping oxygen ions of $NiO\text{-}ZrO_m\text{-}YO_n$ catalyst, leading to the formation of new surface oxygen vacancies at about 700 °C [146]. Therefore, the β

peak shifts to about 700 °C. Except for the shift of peak, the total amount of H_2 consumption on NiO-ZrO_m catalyst (0.62 mmol H_2/g) is higher than that on NiO-ZrO_m-YO_n catalyst (0.37 mmol H_2/g), presented in Table 5-2. The latter result is consistent with the theoretical value of 0.39 mmol H_2/g, while the H_2 consumption on NiO-ZrO_m catalyst is higher than the theoretical value of 0.47 mmol H_2/g. This phenomenon proves that the ZrO_2 is also reduced by hydrogen. Besides, for α peak, the amount of H_2 consumption on NiO-ZrO_m-YO_n catalyst decreases by adding the yttrium, which indicates that part of this free NiO would be inserted into the structure of ZrO_2 and/or Y_2O_3 to form NiO-ZrO_2 and/or NiO-Y_2O_3 solid solution. Thus, yttrium can promote nickel embedding into the structure of ZrO_2 and/or Y_2O_3. For β peak, the amount of H_2 consumption on NiO-ZrO_m catalyst is higher than that obtained on NiO-ZrO_m-YO_n catalyst.

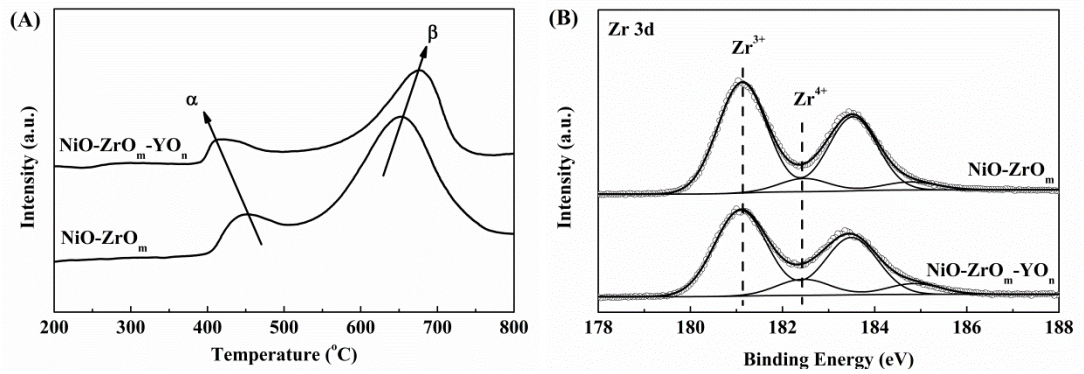

Figure 5-1 (A) the H_2-TPR profiles of NiO-ZrO_m-YO_n and NiO-ZrO_m calcined catalysts, and (B) the Zr 3d profiles from XPS measurements of NiO-ZrO_m-YO_n and NiO-ZrO_m catalysts after reduction.

In order to understand the reduction of ZrO_2, the Zr 3d peak is resolved into two peaks, which is shown in Fig. 5-1 (B). The peaks at about 181.4 and 182.3 eV are ascribed to Zr^{3+} and Zr^{4+}, respectively [243, 244]. It is very obvious to be observed that most Zr^{3+} formed on both catalysts, indicating that the most Zr^{4+} is reduced to Zr^{3+} after reduction. From Table 1, the content of Zr^{3+} on NiO-ZrO_m catalyst (90 %) is higher than that on NiO-ZrO_m-YO_n catalyst (84 %), which manifests that more Zr^{4+} is reduced to Zr^{3+} on NiO-ZrO_m catalyst, which is conformed to H_2-TPR results (Figure 5-1 (A) and Table 5-2), that is, NiO-ZrO_m catalyst consumes more H_2 during the reduction. These phenomena indicate that the formation of ZrO_2 defected by Ni^{2+} on NiO-ZrO_m

catalyst is very easy to be reduced from Zr^{4+} to Zr^{3+} in the presence of hydrogen. While the ZrO_2 defected by Y^{3+} is very stable, which is very hard to be reduced. Therefore, the introduction of the Y^{3+} into ZrO_2 lattice can also stabilize the crystal structure, and create new oxygen vacancies.

5.1.3.3 Basicity of Y-doped and Y-free NiO-ZrO_m catalysts

Table 5-3 Basicity measured by the content of CO_2 desorption on CO_2-temperature program

Catalyst	CO_2 peak identification						
	Peak 1 (weak)		Peak 2 (medium-strength)		Peak 3 (strong)		Total basicity (μmol CO_2/g)
	Position (°C)	Content (%)	Position (°C)	Content (%)	Position (°C)	Content (%)	
NiO-ZrO_m	185	15.5	252	64.4	380	20.1	73
NiO-ZrO_m-YO_n	150	36.9	240	55.4	380	13.0	100

CO_2 temperature programmed desorption (CO_2 TPD) experiment was conducted to determine the basicity of the Y-doped and Y-free NiO-ZrO_m catalysts (Figure 5-2). The peaks on NiO-ZrO_m-YO_n catalyst shift to low temperature, as compared to NiO-ZrO_m catalyst. The total number of basic sites increases from 73 to 100 μmol CO_2/g on NiO-ZrO_m catalyst before and after introducing of yttrium (see in Table 5-3), which indicates that the yttrium can enhance the total number of basic sites. As already described elsewhere [89, 117, 245], there are three types of basic sites (weak, medium-strength and strong). The content of weak peak on NiO-ZrO_m-YO_n catalyst (36.9 %) is higher than that on NiO-ZrO_m catalyst (15.5 %). While the content of strong peak decreases to 13.0 % on NiO-ZrO_m-YO_n catalyst. Besides, the position of weak and medium-strength peaks on NiO-ZrO_m-YO_n catalyst are at about 150 and 240 °C, which is lower than those on NiO-ZrO_m catalyst (185 and 252 °C), respectively. This phenomenon manifests that yttrium can promote the formation of weak basic sites on NiO-ZrO_m-YO_n catalyst. Thus, one can note that the addition of yttrium modifies both the distribution and the number of basic sites. A similar phenomenon can be observed in our group previous works [115, 117]. According to the literature [5, 89, 245], the weak and medium-strength basic sites can promote the formation of activation

carbonate species, thereby enhancing the ability to remove the carbon deposition. While, too strong basic sites lead to too strong CO_2 adsorption, thereby promoting more carbon deposition. Therefore, the weak and medium basic sites present on NiO-ZrO_m-YO_n catalyst can enhance the ability to eliminate coke.

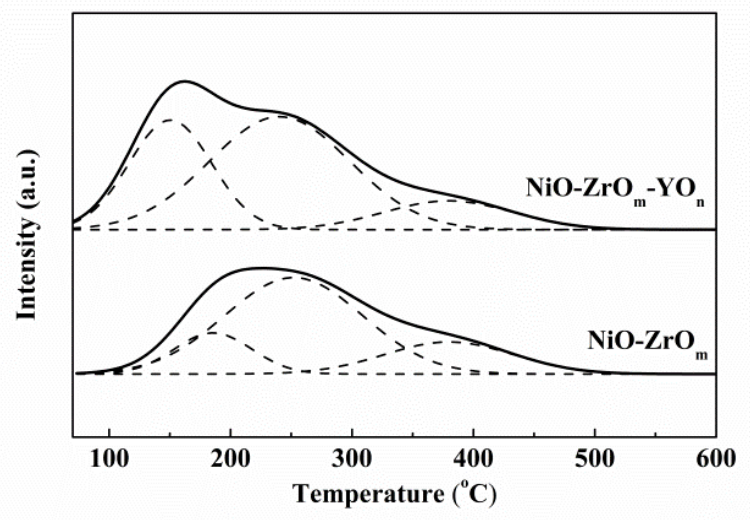

Figure 5-2 The CO_2-TPD profiles of NiO-ZrO_m-YO_n and NiO-ZrO_m catalysts.

5.1.3.4 Nickel particle size and crystallized phases of Y-doped and Y-free NiO-ZrO_m catalysts

Table 5-4 Crystallite sizes of ZrO_2 and Ni^0 on NiO-ZrO_m-YO_n and NiO-ZrO_m catalysts after reduction at 700 °C for 1 hour and after reaction at 700 °C for 8 hours, determined by XRD.

Catalysts	ZrO_2 (nm)		Ni^0 (nm)	
	Reduction	reaction	Reduction	reaction
NiO-ZrO_m	7	7	12	24
NiO-ZrO_m-YO_n	7	7	16	10

Fig. 5-3 shows XRD patterns of NiO-ZrOm-YOn and NiO-ZrOm catalysts after reduction and after catalytic reaction. Tetragonal and/or cubic phase ZrO_2 appear in both catalysts. The crystallite sizes of ZrO_2 on both catalysts exhibit the same value of 7 nm from Scherrer Equation and do not change even after reaction for 8 hours (Table 5-4). The peak at about 44.5^o can be attributed to the metallic nickel [246]. The Ni^0 size

on NiO-ZrO_m catalyst is about 12 nm after reduction, and it increases to 24 nm after reaction. While for NiO-ZrO_m-YO_n catalyst, it decreases from 16 nm to 10 nm after reaction for 8 hours, which indicates the re-dispersion of Ni^0. Similar phenomenon had been reported by other researches [89, 93, 117]. Nakayam et al. [227] found the re-dispersion of Ni under an alternating condition between H_2 reduction and oxidation atmosphere. Under dry reforming of methane condition, CO_2 is a source of oxygen. When CO_2 adsorption and activation on the surface of catalyst, the nickel metal may be oxidized. The production of H_2 and CO as reduction atmosphere, may contribute to the reduction of the NiO, and thereby the re-dispersion of nickel particles. On one hand, the Ni^0 size is related to the sintering of nickel. Severe sintering takes place on NiO-ZrO_m catalyst, due to the lower interaction between Ni and Zr, which is confirmed by the results of H_2-TPR. Furthermore, the addition of yttrium can limit the sintering of nickel during the reaction. On the other hand, It is well known that the large nickel particle size maybe favor for selective reactions that lead to carbon deposition [237, 238]. As a consequence, NiO-ZrO_m-YO_n can limit the carbon deposition. Besides, NiO-ZrO_m-YO_n exhibits more basic sites, which could enhance the ability of adsorption of CO_2, thereby promoting the removal of carbon deposition. both sintering and carbon deposition could contribute to the deactivation of catalyst, thereby reducing the stability of the catalyst.

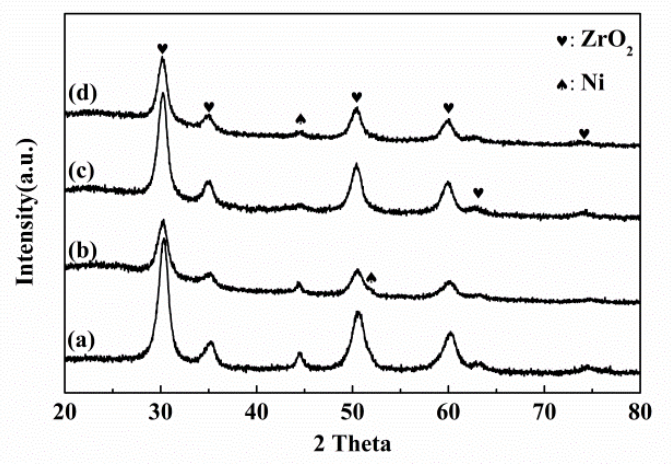

Figure 5-3 The XRD profiles of (a) NiO-ZrO_m and (c) NiO-ZrO_m-YO_n catalysts after reduction at 700 °C for 1 hour and after reaction at 700 °C for 8 hours, and (b) NiO-ZrO_m and (d) NiO-ZrO_m-YO_n catalysts after reaction at 700 °C for 8 hours.

5.1.4 The performance of Y-doped and Y-free NiO-ZrO_m catalysts

The catalytic performance of the catalysts was investigated at 700 °C for 8 hours (Figure 5-4). The conversion of methane on both catalysts decreases within 1 hour, and finally stabilizes at 67 % and 85 % for NiO-ZrO_m-YO_n and NiO-ZrO_m catalyst, respectively. Except for the higher methane conversion on NiO-ZrO_m catalyst, the CO_2 conversion and the ratio of H_2/CO are higher than those on NiO-ZrO_m-YO_n catalyst. The CO_2 conversion on the NiO-ZrO_m catalyst is about 89 % with the H_2/CO ratio of 0.95, which is very close to one. When adding yttrium into NiO-ZrO_m catalyst, the CO_2 conversion decreases within 60 min and stabilizes at 70 % for 8 hours on stream. At the same time, the H_2/CO ratio decreases to about 0.85. Because NiO-ZrO_m-YO_n catalyst exhibits the lower specific surface area, the smaller pore volume, and the bigger metallic nickel particle size. Those properties could lead to the lower performance of NiO-ZrO_m-YO_n catalyst. However, the catalyst activity remained stable during time on stream.

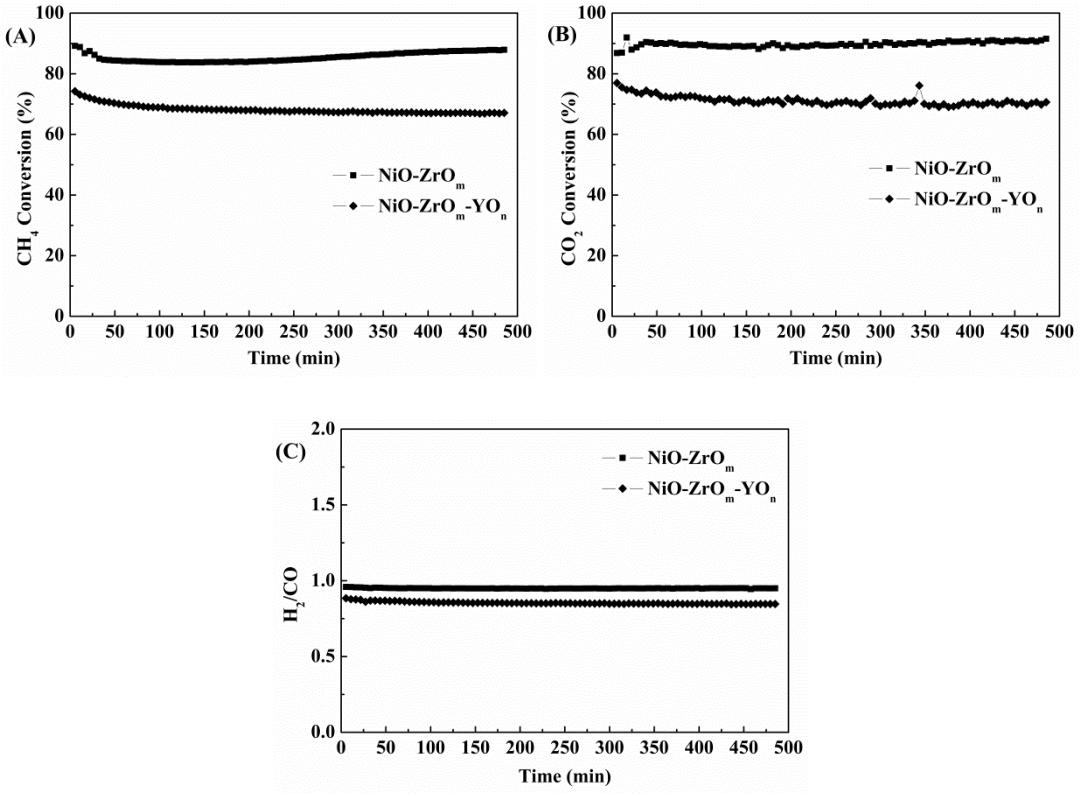

Figure 5-4 The conversion of CH_4 (A) and CO_2 (B), and the H_2/CO ratio (C) of NiO-ZrO_m-YO_n and NiO-ZrO_m catalysts at 700 ^oC with the mixed flow of CH_4:CO_2:Ar=10:10:80, GSHV=48,000 h^{-1}.

5.1.5 On the carbon deposition on used Y-doped and Y-free NiO-ZrO_m catalysts

5.1.5.1 Carbon formation evidenced by TGA and XPS Spectroscopy

Table 5-5 The particle size and carbon deposition on NiO-ZrO_m-YO_n and NiO-ZrO_m catalysts

Catalyst	Particle Size (nm)	Coke Content (%)	C-C content (%)	I_G/I_D
NiO-ZrO_m	15-20[a]	3.7[b]	42[c]	1.7[d]
NiO-ZrO_m-YO_n	10-15	1.0	38	-

a: The particle size of nickel after reaction for 8 hours determined by TEM.
b: The coke content after reaction for 8 hours was determined by TGA.
c: The C-C content after reaction for 8 hours determined by XPS.
d: The I_G/I_D after reaction for 8 hours determined by Raman spectroscopy.

The content of coke on both catalysts are determined by TGA experiment, and the results are shown in Table 5-5. The content of the coke on NiO-ZrO_m catalyst is about 3.7 %, which is higher than that on NiO-ZrO_m-YO_n catalyst (1.0 %), indicating that yttrium can decrease the carbon deposition on NiO-ZrO_m-YO_n catalyst. Fig. 5-5 represents the results of C 1s profiles. The intensity of C 1s on NiO-ZrO_m-YO_n catalyst is lower than that on NiO-ZrO_m catalyst, showing that the content of surface carbon deposition on NiO-ZrO_m-YO_n catalyst is lower, about 63 %. While the coke on the surface of NiO-ZrO_m catalyst is about 69 %.

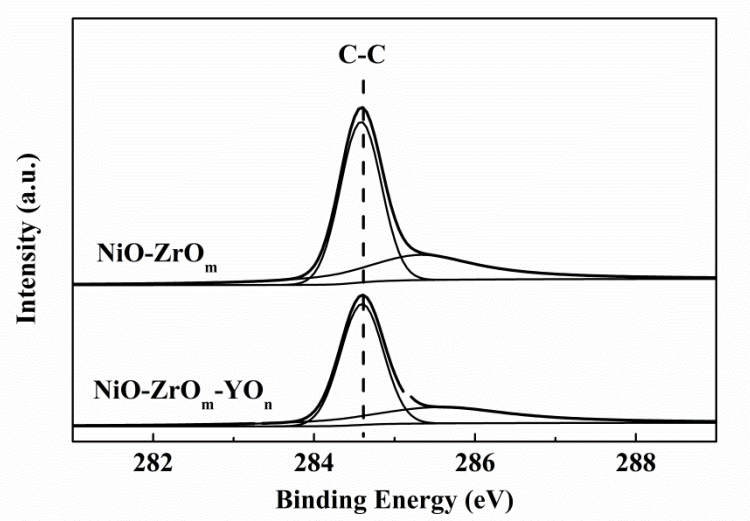

Figure 5-5 The C 1s profiles of used NiO-ZrO_m and NiO-ZrO_m-YO_n catalysts.

5.1.5.2 Carbon formation evidenced by Raman Spectroscopy

Fig. 5-6 shows the results of Raman experiment. Two peaks can be found on NiO-ZrO_m catalyst and no peak can be observed on NiO-ZrO_m-YO_n catalyst, which manifests that no or less coke form on NiO-ZrO_m-YO_n catalyst. The peak at about 1328 cm^{-1} is attributed to the structural imperfections on not-organized carbon materials, namely disorder-induced band (D band), and another peak at about 1585 cm^{-1} is corresponded to the in-plane C-C stretching vibrations of sp^2 atoms in coke, namely graphitic carbon (G band) [98, 247, 248]. The intensity of peak is named I, while the ratio of I_G/I_D is about 1.7 (Table 5-5), indicating that more graphitic carbon forms on NiO-ZrO_m catalyst, which is conformed to the results of XPS, more C-C species on NiO-ZrO_m catalyst. All those phenomena show that the carbon deposition on NiO-ZrO_m catalyst is higher than that on NiO-ZrO_m-YO_n catalyst.

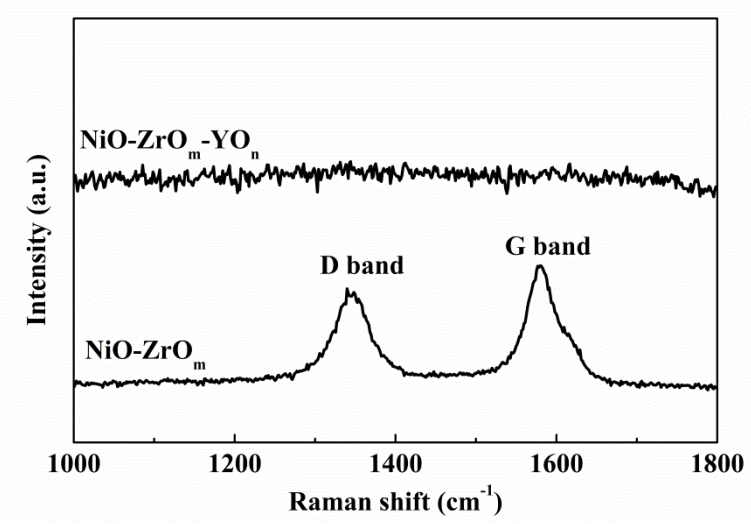

Figure 5-6 The Raman profiles of used NiO-ZrO_m and NiO-ZrO_m-YO_n catalysts.

5.1.5.3 On the study of the morphology of carbon studied by TEM

The morphology structure of carbon on the catalysts after reaction is determined by the transmission electron microscopy experiment (Fig. 5-7). After reaction, the nickel particle size decreases on NiO-ZrO_m by adding the yttrium promoter (Fig. 5-7 (A) and (C)). The nickel particle size formed on NiO-ZrO_m-YO_n is about 10-15 nm (Fig.

5-7 (D)), while about 15-20 nm formed on NiO-ZrO_m (Fig. 5-7 (B)), which is corresponding to the results of XRD. It can be noted that large Ni particle (over 20 nm) can be observed on NiO-ZrO_m catalyst. According to the results of H_2-TPR, the interaction between Ni and ZrO_m on NiO-ZrO_m catalyst is lower than that on NiO-ZrO_m-YO_n catalyst, leading to nickel sintering. Therefore, bigger particles of Ni^0 are present on NiO-ZrO_m catalyst. These large nickel particles maybe favor selective reactions that tend to form carbon deposition [237, 238], thereby resulting in formation of carbon deposition. Thus, a lot of carbon deposition can be observed on NiO-ZrO_m catalyst in the form of carbon nano tube (Fig 5-7 (A)), and no carbon deposition is observed on NiO-ZrO_m-YO_n catalyst (Fig 5-7 (C)), which indicates that no or little carbon formes on NiO-ZrO_m-YO_n catalyst. These carbon nanotubes are graphitic carbon, which is in agreement with the results of Raman experiment. This phenomenon shows that yttrium can suppress the sintering of nickel particles, and also inhibits the formation of carbon during the DRM reaction.

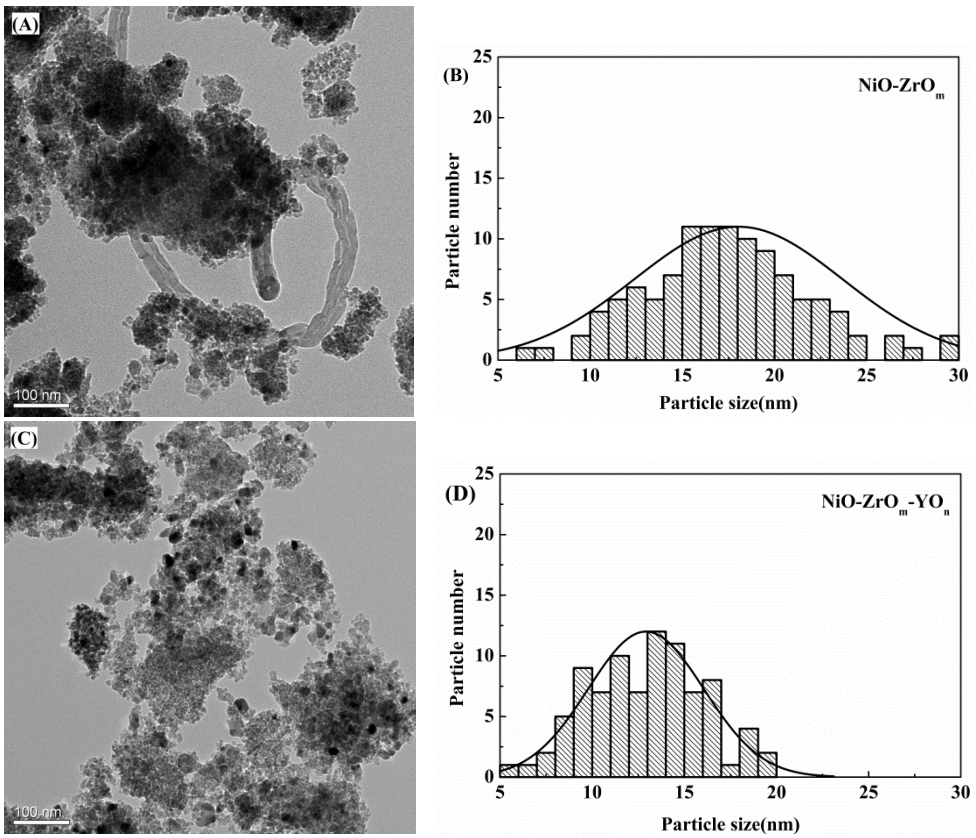

Figure 5-7 TEM images of used catalysts (A) NiO-ZrO_m and (C) NiO-ZrO_m-YO_n and particle sizes of catalysts (B) NiO-ZrO_m and (D) NiO-ZrO_m-YO_n.

5.1.6 Summary

NiO-ZrO_m and NiO-ZrO_m-YO_n catalysts were prepared by urea hydrolysis method and were characterized by BET, TPR-H_2, CO_2-TPD, XRD, TEM, and XPS. After adding yttrium, the strong interaction between Ni and ZrO_m formed on NiO-ZrO_m-YO_n catalyst, resulting in the small size of nickel particle distributed on catalyst after reaction. While for NiO-ZrO_m catalyst, large particles formed on catalyst after reaction, contributing to the deposition of carbon. Besides, more amount of weak and medium-strong basic sites formed on NiO-ZrO_m-YO_n catalyst, which could enhance the ability of removal of carbon. Except for the advantages, the NiO-ZrO_m-YO_n catalyst showed lower specific surface area and the smaller pore volume. Thus, from the results of the activity test at 700 °C for 8 hours, NiO-ZrO_m catalyst exhibited higher methane and CO_2 conversion, while NiO-ZrO_m-YO_n catalyst exhibited highly carbon-resistant for dry reforming of methane at 700 °C. Therefore, yttrium can modify the interaction between Ni and ZrO_m, in enhancing the dispersion of nickel particles during the reaction, and promote the formation of more weak and medium-strength basic sites.

5.2 Syngas production by dry methane reforming over Mg doped NiO-ZrO_2 catalysts

5.2.1 Introduction

The literature data showed that nickel-based catalysts presented high activity in dry reforming of methane reaction [213, 226, 249]. However, Ni-based catalysts easily deactivated, mainly due to the sintering of nickel and/or carbon deposition [5, 62]. The former could be modified by adjusting the interaction between nickel and support [250]. Wang et al. [250] investigated the effect of calcination temperatures and Ni loadings on the stability of Ni/MgO catalyst for DRM dry reforming of methane. They found that the formation of NiO-MgO solid solution could enhance the interaction between Ni and MgO, thereby the promotion of stability of Ni/MgO catalyst. Because the interaction between Ni and MgO on NiO-MgO solid solution was so strong that could resist the sintering of nickel [249]. In addition, it was demonstrated that the nickel particle size was not only related to the sintering of nickel but also affected the formation of carbon deposition. In our previous results, larger particles of nickel on the support surface may be responsible for the carbon deposition, due to the catalytic selectivity towards carbon forming reactions [115, 238]. Except for the nickel particle size, the basicity of catalyst also has an influence on carbon deposition. Koo et al. [251] studied the effect of MgO content on performance of MgO-promoted Ni/Al_2O_3 catalyst for CO_2 reforming of methane and carbon deposition after reaction. The authors found that MgO could enhance the basic strength over the surface of catalyst, thereby increase the adsorption of CO_2, which could contribute to suppressing carbon deposition. As the consequence, the catalyst containing 20 % MgO exhibited the highest activity and stability for steam and carbon dioxide reforming of methane. It was shown, in the last years, that the addition of alkali oxide into support could modify the support, eg. CaO, MgO. The later

has attracted extensive research as a promoter for dry reforming of methane [5, 62, 122, 226, 249].

In order to understand the effect of MgO on performance of NiO-ZrO_2 catalyst for dry reforming of methane, NiO-ZrO_2 and NiO-MgO-ZrO_2 catalysts were prepared and characterized by the means of H_2-TPR, TG, CO_2-TPD, and TEM. The results are explained here in detail.

5.2.2 Preparation of the NiO-MgO-ZrO_2 catalyst

The two catalysts were prepared by a one-step synthesis method [154]. The loadings of nickel and magnesium were both fixed at 10 wt%. A certain mass of zirconium (IV) oxynitrate hydrate (Aldrich), magnesium acetate tetrahydrate (Alfa Aesar), nickel(II) nitrate hexahydrate, Pluronic P123 (Aldrich), urea (Sigma-Aldrich) was dissolved in distilled water. The obtained solution was heated to 95 °C with stirring constantly for 48 h, after that, transferred into the oven (100 °C) for 24 hours, then filtrated, washed and dried at room temperature. At last, the precursor was calcined at 800 °C for 5 hours under airflow with an increasing rate of 1 °C/min. The obtained sample was denoted NiO-MgO-ZrO_2. The free Mg catalyst prepared by the same method without Mg, was named NiO-ZrO_2.

5.2.3 Characterization of NiO-MgO-ZrO_2 and NiO-ZrO_2

5.2.3.1 The reducibility of NiO-MgO-ZrO_2 and NiO-ZrO_2 catalysts

The reducibility of NiO-MgO-ZrO_2 and NiO-ZrO_2 catalysts was studied by H_2-TPR, and the results are shown in Figure 5-8. Two distinct peaks could be observed on both catalysts, the one at the low-temperature area and the other one at high-temperature area. According to the literature [122, 226, 252], the peak at low temperature corresponded to the weak interaction between Ni and Zr, and the peak at high

temperature was attributed to the NiO-ZrO_2 solid solution. These two peaks shifted to higher temperature area on NiO-MgO-ZrO_2 catalyst, compared to NiO-ZrO_2 catalyst, which proved that the interaction between Ni and Zr could be enhanced by introducing the Mg. This stronger interaction might be attributed to the NiO-MgO solid solution, which could restrain the sintering of nickel [226, 249].

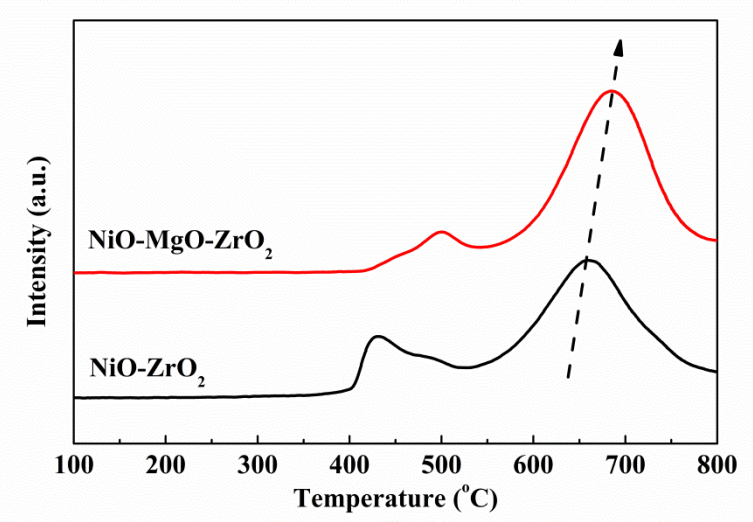

Figure 5-8 The H_2-TPR profiles of NiO-MgO-ZrO_2 and NiO-ZrO_2 catalysts

5.2.3.2 The basicity of NiO-MgO-ZrO_2 and NiO-ZrO_2 catalysts

Table 5-6 The content of CO_2 desorption on the CO_2-TPD experiment over NiO-MgO-ZrO_2 and NiO-ZrO_2 catalysts.

	CO_2 desorbed (%)						Total basicity (μmol CO_2/g)
	Peak 1 weak		Peak 2 medium-strength		Peak 3 strong		
Catalyst	Position	Content	Position	Content	Position	Content	
NiO-ZrO_2	185	15.5	252	64.4	380	20.1	73
NiO-MgO-ZrO_2	165	37.5	256	53.9	370	16.1	69

Figure 5-9 showed the CO_2-TPD patterns of NiO-MgO-ZrO_2 and NiO-ZrO_2 catalysts. Three kinds of basic sites were identified on both catalysts: weak, medium-strength and strong basic sites [114]. The desorption peaks on NiO-MgO-ZrO_2 catalyst shifted to low temperature. Moreover, the total basicity of NiO-MgO-ZrO_2 catalyst decreased

from 73µmol CO_2/g to 69 µmol CO_2/g by introducing of Mg (Table 5-6). However, the weak basic sites increased to 37.5 % on NiO-MgO-ZrO_2 catalyst. This phenomenon showed that Mg could promote the creation of weaker basic sites, thereby weaken the strength of basicity. This too weak basic sites might weaken the adsorption of CO_2, which might result in the carbon deposition for dry reforming of methane [5].

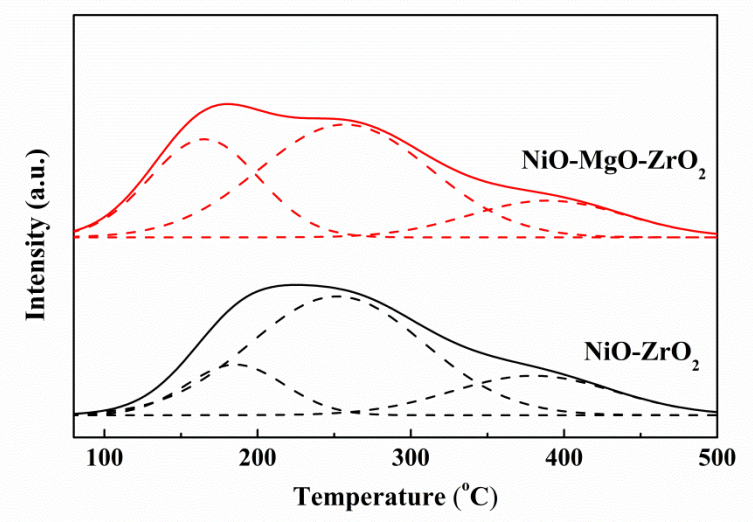

Figure 5-9 The CO_2-TPD profiles of NiO-MgO-ZrO_2 and NiO-ZrO_2 catalysts

5.2.3.3 The Physical Properties of NiO-MgO-ZrO_2 and NiO-ZrO_2 catalysts

Table 5-7 The specific surface area determined by BET method; the pore volume and the pore diameter determined by BJH method on both catalysts.

Catalyst	pore diameter nm	specific surface area m^2/g	pore volume cm^3/g
NiO-ZrO_2	1.9	113	0.20
NiO-MgO-ZrO_2	1.6	90	0.10

Table 5-7 exhibited the results of BET experiment. NiO-ZrO_2 showed higher value of surface area, pore-volume, and pore diameter than those on NiO-MgO-ZrO_2 catalyst, which indicated that the introduction of Mg did not modify the main structure of NiO-ZrO_2 catalyst, on the contrary, those low physical properties on NiO-MgO-ZrO_2 catalyst might result in the low performance for dry reforming of methane [213].

5.2.3.4 The crystalline Size and content of Ni^0 over NiO-MgO-ZrO_2 and NiO-ZrO_2 catalysts

Table 5-8 Crystallite sizes of Ni^0 and content of Ni^0 over NiO-MgO-ZrO_2 and NiO-ZrO_2 catalysts

	Ni^0 Crystalline Size (nm)[a]		Ni^0 content (%)[b]		Coke
Catalyst	Reduction	Reaction	Reduction	Reaction	%
NiO-ZrO_2	12	24	34	28	3.7
NiO-MgO-ZrO_2	20	17	22	22	16.3

a: Crystallite sizes of Ni^0 determined by XRD
b: The content of Ni^0 determined by XPS

Table 5-8 shows the crystallite size and content of Ni^0 species. It is worth noting that the crystallite size of Ni^0 species increases from 12 nm to 20 nm by introducing of Mg into the NiO-ZrO_2 catalyst after reduction. There is a different observation on both catalysts after reaction, it decreases to 17 nm over NiO-MgO-ZrO_2 catalyst, while it increases to 24 nm on NiO-ZrO_2 catalyst. The content of Ni^0 species on NiO-ZrO_2 catalyst is higher than those on NiO-MgO-ZrO_2 catalyst all the time. However, the variation in content of Ni^0 species is different. It decreases from 34 % to 28 % on NiO-ZrO_2 catalyst after reaction, while it keeps at 22 % on NiO-MgO-ZrO_2 catalyst all the time. Generally, the content and crystallite size of Ni^0 species could influence the catalytic performance of catalyst for DRM reaction [62]. Thus those different changes might affect the activity and/or stability for DRM reaction.

5.2.4 The performance of NiO-MgO-ZrO_2 and NiO-ZrO_2 catalysts

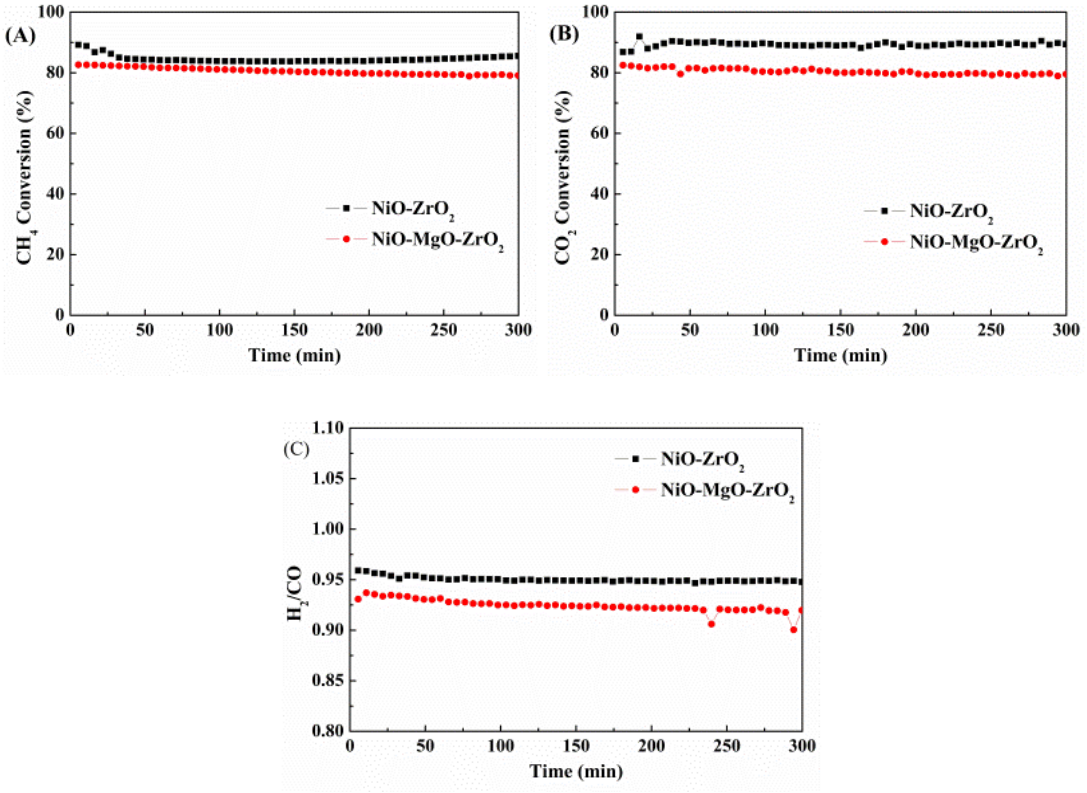

Figure 5-8 The conversion of (A) CH_4 and (B) CO_2, and (C) the H_2/CO ratio on NiO-MgO-ZrO_2 and NiO-ZrO_2 catalysts at 700 °C with the mixed flow of CH_4:CO_2:Ar=10:10:80, GSHV=48000 h^{-1}

Figure 5-8 reported the results of the activity test. NiO-ZrO_2 catalyst exhibited better performance for dry reforming of methane. The methane and CO_2 conversion on NiO-ZrO_2 catalyst were slightly higher than those on NiO-MgO-ZrO_2 catalyst. Because NiO-ZrO_2 catalyst showed better physical properties, eg. higher surface area, bigger pore volume, and larger pore diameter. Besides, smaller Ni^0 crystallite size (12 nm) and lower Ni^{2+} content (66 %) could be observed on NiO-ZrO_2 catalyst after reduction (Table 5-8), which contributed to the activity of catalyst for dry reforming of methane [62]. It was worth noting that the conversion of methane on NiO-ZrO_2 catalyst decreased a little bit within 50 min, and increased to 87 %. While CO_2 conversion increased a little bit within 50 min and stabilized at 90 %. Those results indicated that the stability of NiO-MgO-ZrO_2 catalyst was slightly higher than NiO-ZrO_2 catalyst,

because the formation of NiO-MgO solid solution could enhance the interaction between Ni and support, which could restrain the sintering of nickel. Therefore, severe sintering happened on NiO-ZrO_2 catalyst. The crystallite size of Ni^0 on NiO-ZrO_2 catalyst increased from 12 nm to 24 nm after reaction (Table 5-8), while it decreased from 20 nm to 17 nm on NiO-MgO-ZrO_2 catalyst.

5.2.5 The carbon deposition on NiO-MgO-ZrO_2 and NiO-ZrO_2 catalysts

The content of carbon formed during DRM test was determined by TG experiment. The content of coke on NiO-MgO-ZrO_2 catalyst was about 16.3 % (Table 5-8), which was clearly higher than that obtained on NiO-ZrO_2 catalyst (3.7 %). Figure 5-9 presented the TEM images and the particle size of spent catalysts. A lot of carbon nanotube could be observed easily on NiO-MgO-ZrO_2 catalyst, while a little carbon nanotube could be observed on NiO-ZrO_2 catalyst, which corresponded to the results of TG. Those phenomena indicated that Mg could promote the formation of carbon, due to the formation of a large amount of very weak basic sites on NiO-MgO-ZrO_2 catalyst. Those weak basic sites exhibited very weak adsorption of CO_2, resulting in lower CO_2 conversion. The particle size of nickel after reaction on NiO-MgO-ZrO_2 catalyst was about 15-17 nm (Fig. 5-9 (B)), while it was 15-20 nm on NiO-ZrO_2 catalyst (Fig. 5-9 (D)), which conformed to the results of XRD. Those phenomena manifested that Mg could restrain the sintering of nickel by formation of NiO-MgO solid solution during the reaction process.

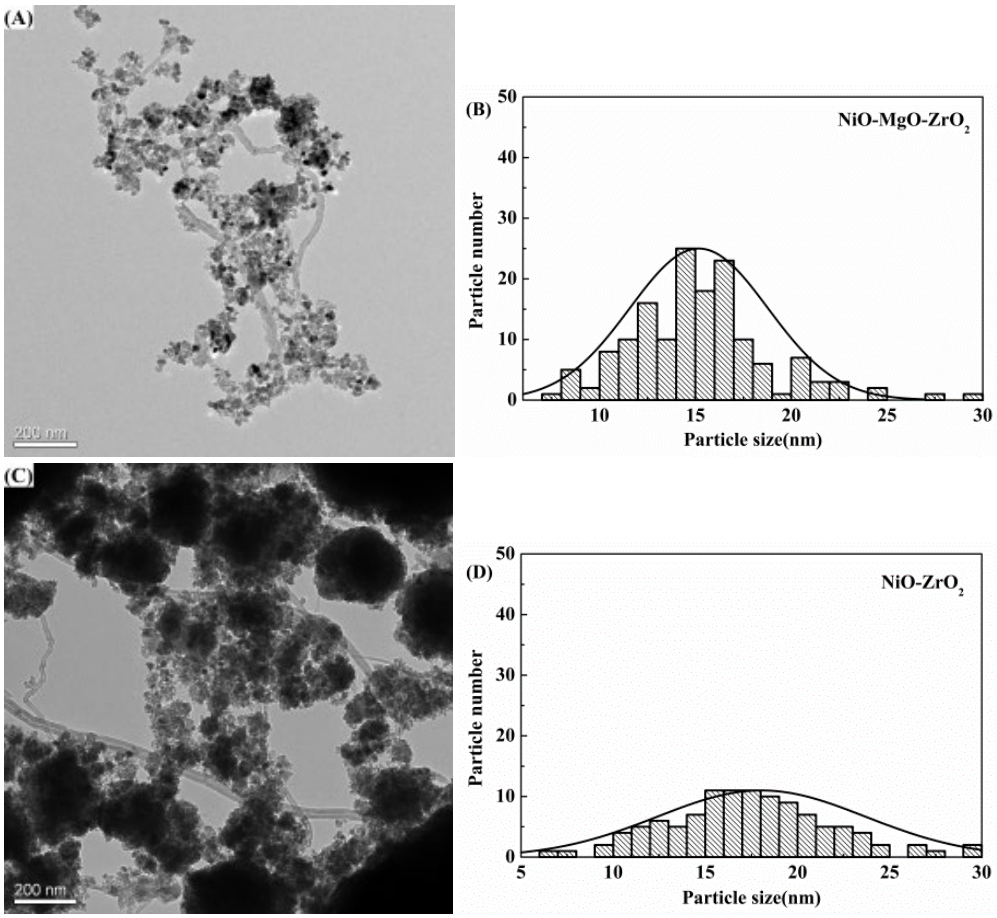

Figure 5-9 TEM images of used catalysts (A) NiO-MgO-ZrO_2 and (C) NiO-ZrO_2 catalysts and particle sizes of catalysts (B) NiO-MgO-ZrO_2 and (D) NiO-ZrO_2 catalysts.

5.2.6 Summary

The dry reforming of methane has been carried out at 700 ºC with a very high GHSV of 48000 h^{-1} over NiO-MgO-ZrO_2 and NiO-ZrO_2 catalysts prepared by one-step synthesis. The NiO-MgO-ZrO_2 catalyst showed slightly lower activity and selectivity of catalyst, due to the lower surface area, smaller pore volume, smaller pore diameter, and bigger particle size of nickel after reduction. Besides, a lot of carbon deposited on NiO-MgO-ZrO_2 catalyst after reaction owing to the formation of a large amount of very weak basic sites. On the other hand, NiO-MgO-ZrO_2 catalyst exhibited a higher sintering resistance, due to the strong interaction between Ni and Zr on such catalyst. The NiO-ZrO_2 catalyst exhibited slightly higher activity and selectivity for DRM reaction, however, a severe sintering happened on NiO-ZrO_2 catalyst due to the weaker interaction between Ni and Zr.

5.3 Syngas production via CO_2 reforming of methane over Aluminium promoted $NiO–ZrO_2–Al_2O_3$ catalyst: On the role of aluminum species

5.3.1 Introduction

Since nickel shows as excellent catalytic activity as noble ones (Pt, Ru, and Rh), Ni-based catalysts have been widely reported on the DRM reaction [80, 129, 168, 232]. Pompeo et al. [168] compared the catalytic performance of Ni and Pt supported on α-Al_2O_3, ZrO_2 and α-Al_2O_3–ZrO_2 catalysts for dry reforming of methane. They found nickel was slightly more active than platinum. Moreover, the nickel-based catalysts served as the optimal alternatives considering economic viability [113]. However, the deactivation of Ni-based catalysts due to sintering and/or carbon deposit needs to be addressed in order to achieve facile scaling-up in industrial process. Thus tremendous efforts have been focused on the development of promoters or novel support materials to address these two problems, further contributing to the design of catalysts with higher stability [84, 99].

It has been found that aluminum (Al) as a promoter and/or support could enhance the catalytic performance mainly because Al could improve the reducibility and dispersity of nickel. Liu et al. [88] investigated the effect of La, Al and Mn promoter on Fe modified natural clay supported Ni catalysts for dry reforming of methane, and confirmed that Al promoted catalyst exhibited the highest catalytic performance in dry reforming of methane. Talkhoncheh et al. [253] studied the effect of Ni-based nanocatalysts supported on clinoptilolite, ceria, and alumina on the catalytic performance for DRM reactions. Ni/Al_2O_3 nanocatalysts exhibited the best performance, due to even dispersion of nickel, homogenous distributions and high specific surface area. On the other hand, although various supports have been employed as the support, such as CeO_2, ZrO_2 , SiO_2, La_2O_3 and Al_2O_3 [87, 165, 254]. ZrO_2 exhibits favorable properties such as thermal stability, oxygen storage capacity, enhancement of

the metallic dispersion, and the ability of CO_2 adsorption. Therefore, many researchers have focused on the utilization of ZrO_2 support for DRM [81, 140, 149]. Pompeo et al. [168] found that ZrO_2 as a basic support could promote the adsorption of CO_2, thereby inhibiting the carbon deposition. Mesoporous La_2O_3-ZrO_2 could promote the stability of the catalyst due to the high dispersion of nickel species and the pore confinement effect [154]. Ni supported on SBA-15 and mesoporous ZrO_2 also exhibit a better catalytic performance owing to the special pore confinement. Liu et al. [255] found mesoporous ZrO_2 with a specific surface area of 198 m^2 g^{-1} could be obtained even calcination at 700 ºC via a sol-gel approach treated by NaOH or KOH solution. Miao et al. [256] found M-ZrAl-10 with the Al content of 10 % exhibited better physical properties even treated at a high temperature of 800 ºC with a high specific surface area of 56 m^2/g, a large pore volume of 0.13 cm^3/g and narrow pore size distribution of 8.2 nm. On one hand, the properties of ZrO_2 support could be modified by the introduction of alumina species. On the other hand, ZrO_2 could enhance the performance of the catalyst with Al_2O_3 support for dry reforming of methane. Therdthianwong et al. [257, 258] demonstrated that Ni/Al_2O_3 catalyst modified by ZrO_2 exhibited higher stability for dry reforming of methane. Because ZrO_2 could promote the elimination of carbon deposition by the dissociation of CO_2 to form oxygen intermediates. Souza et al. [83] also found Pt/ZrO_2/Al_2O_3 showed higher stability than Pt/Al_2O_3 for dry reforming of methane due to the Pt–Zr^{n+} interfacial sites, which could suppress the carbon deposition. The performance of the catalyst could be affected by the spinel $NiAl_2O_4$ formed on the catalyst of Ni supported on Al_2O_3 during the reduction. While zirconia could avoid the formation of spinel $NiAl_2O_4$, which could enhance the performance of the catalyst. Li et al. [259] showed that the catalyst of nickel supported on Al_2O_3–ZrO_2 catalyst prepared via a direct sol-gel process exhibited excellent activity and stability for dry reforming of methane compared with Ni/Al_2O_3 catalyst. Because of the small metallic Ni particles with the properties of highly and uniformly dispersed on Al_2O_3–ZrO_2 support. Besides, the interaction between nickel and Al_2O_3–ZrO_2 support could avoid the formation of spinel $NiAl_2O_4$.

In the present work, the enhancement of catalytic performance by a combination of

zirconia and alumina is reported. Thus, a series of $10NiO–xAl_2O_3–(90-x)ZrO_2$ (x=0, 10, 20, 45, 90) catalysts were prepared by a one-step synthesis method and characterized by BET, XRD, XPS, H_2-TPR, ICP, Raman and physical chemisorption then tested in dry reforming of methane as a function of temperature and in steady-state in isothermal conditions at 700 °C. A correlation between the structure and the reactivity of promoted and non-promoted catalyst was proposed here in order to highlight the positive effects of aluminum promotion.

5.3.2 Synthesis of a series of $10NiO–xAl_2O_3–(90-x)ZrO_2$ Catalysts

At the First, the dissolution of P123, $Ni(NO_3)_2·6H_2O$, $ZrO(NO_3)_2·xH_2O$, CH_4N_2O, and $C_9H_{21}AlO_3$ in distilled water. The molar ratio of Ni, Al, and Zr was 10, x, 90-x (x=0, 10, 20, 45, 90), as listed in table 5-9, respectively. Second, the obtained suspension was heated to 95 °C under vigorous stirring for two days. Nest, the suspension was subsequently placed at 100 °C for one day. After filter, washing, and dry at 25 °C, the obtained precursor was calcined at 800 °C for 300 min. Lats, white powder were denoted as $NiO–ZrO_2$, $NiO–10Al_2O_3–ZrO_2$, $NiO–20Al_2O_3–ZrO_2$, and $NiO–45Al_2O_3–ZrO_2$, $NiO–Al_2O_3$, respectively.

Table 5-9 The dosage of Al, Ni and Zr for prepare a series of $10NiO–xAl_2O_3–(90-x)ZrO_2$

Catalyst	Al %	Zr %	Ni %
$NiO–ZrO_2$	-	90	10
$NiO–10Al_2O_3–ZrO_2$	10	80	10
$NiO–20Al_2O_3–ZrO_2$	20	70	10
$NiO–45Al_2O_3–ZrO_2$	45	45	10
$NiO–Al_2O_3$	90	0	10

5.3.3 Catalytic performance in dry reforming of methane

5.3.3.1 The series of 10NiO–xAl$_2$O$_3$–(90-x)ZrO$_2$ catalysts for DRM reaction

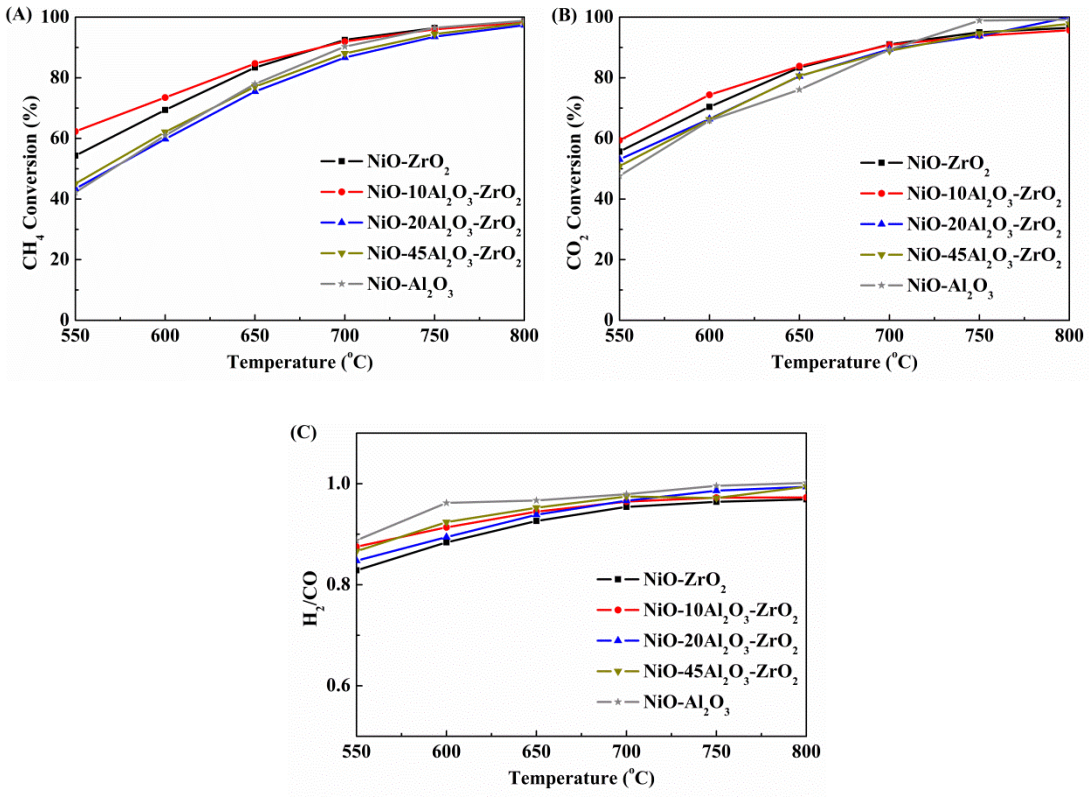

Figure 5-10 (A) CH_4 conversion as function of temperature, (B) CO_2 conversion as function of temperature, and (C) H_2/CO ratio as function of temperature for all the catalysts, CH_4:CO_2:Ar=10:10:80, GSHV=48000 h^{-1}.

The catalytic results of the DRM in terms of CO_2 and CH_4 conversion and the ratio of H_2/CO with the range of 550-800 ºC were presented in Figure 5-10. Within the series of 10NiO–xAl$_2$O$_3$–(90-x)ZrO$_2$ catalysts, NiO–10Al$_2$O$_3$–ZrO$_2$ exhibited the highest CH_4 conversion in the whole temperature range during the DRM experiment. This advantage became more prevalent with the decrease of the temperature, especially at 550 ºC. From the Figure 5-10 (A), the conversion of methane at 550 ºC obtained for NiO–ZrO$_2$, NiO–10Al$_2$O$_3$–ZrO$_2$, NiO–20Al$_2$O$_3$–ZrO$_2$, NiO–45Al$_2$O$_3$–ZrO$_2$, NiO–Al$_2$O$_3$ catalysts were 54 %, 62 %, 43 %, 45 % and 42 %, respectively. A similar trend was observed in CO_2 conversion with the following results obtained at 550 ºC: 56 %, 59 %, 53 %, 50 % and 48 % respectively for NiO–ZrO$_2$, NiO–10Al$_2$O$_3$–ZrO$_2$, NiO–

$20Al_2O_3–ZrO_2$, $NiO–45Al_2O_3–ZrO_2$, $NiO–Al_2O_3$ catalysts (Figure 5-10 (B)). From Figure 5-10 (C), the H_2/CO ratio increased by adding aluminum, indicating that the aluminum could enhance the selectivity to H_2 of the catalyst. Similar results on the effect of Al, have also been reported by Liu et al. [88] and Chai et al. [260].

5.3.3.2 The stability test of $NiO–10Al_2O_3–ZrO_2$ and $NiO–ZrO_2$ catalyst

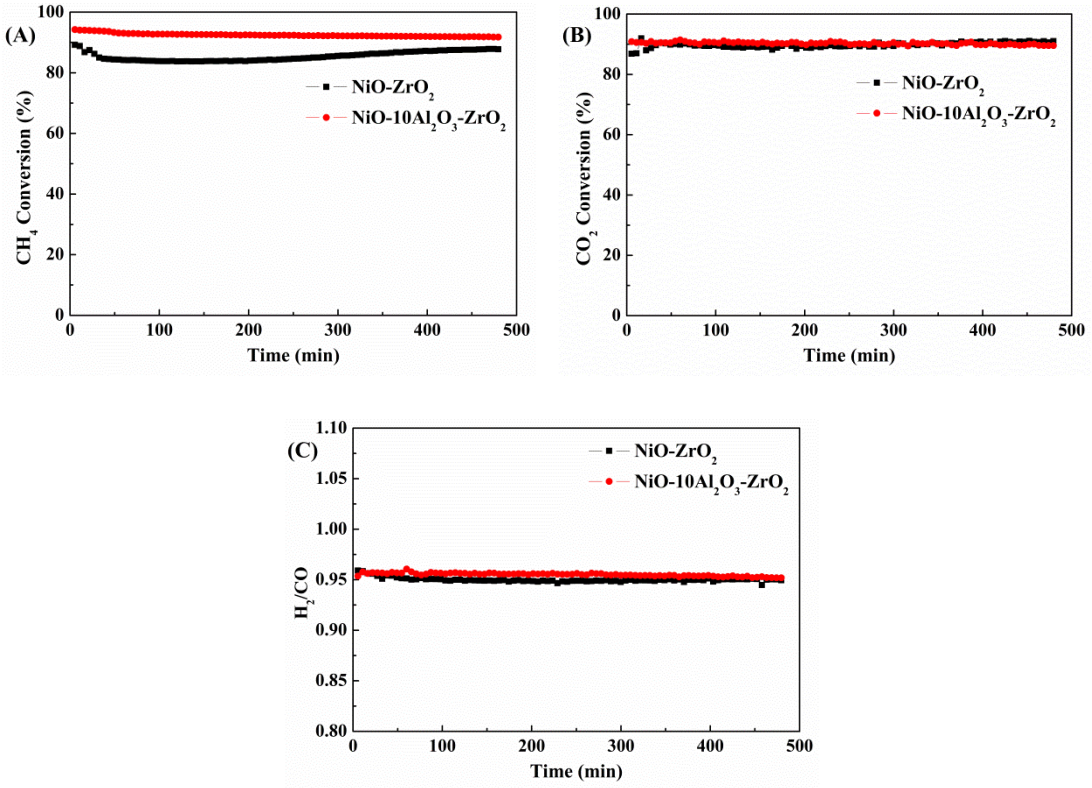

Figure 5-11 (A) CH_4 conversion , (B) CO_2 conversion and (C) H_2/CO ratio in isothermal conditions (700°C) on $NiO–10Al_2O_3–ZrO_2$ in the presence of CH_4:CO_2:Ar=10:10:80, GSHV=48,000 h^{-1}

Stability runs were performed on $NiO–10Al_2O_3–ZrO_2$ catalysts at 700 °C and the results were presented in Figure 5-11. $NiO–10Al_2O_3–ZrO_2$ catalyst showed high stability for dry reforming of methane with 8 h time-on-stream. The initial CO_2 and CH_4 conversion on $NiO–10Al_2O_3–ZrO_2$ were about 91 % and 92 %, respectively, which were slightly higher than those on $NiO–ZrO_2$ catalyst. Besides, $NiO–10Al_2O_3–ZrO_2$ catalyst exhibited a slightly higher H_2/CO ratio of about 0.96 even up to reaction for 8 hours.

Those phenomena indicated that NiO–10Al_2O_3–ZrO_2 catalyst was notably active towards methane dry reforming even upon 8 h time-on-stream. In addition, the CO_2 conversion was higher than CH_4 conversion on NiO–ZrO_2 catalyst, with a lower H_2/CO ratio, indicating that side reaction reverse water-gas shift (RWGS) occurred on NiO–ZrO_2 catalyst. While for NiO–10Al_2O_3–ZrO_2 catalyst, the CO_2 conversion was lower than CH_4 conversion, which indicated that the NiO–10Al_2O_3–ZrO_2 catalyst could inhibit the reverse water-gas shift (RWGS) reaction, thereby enhancing the selectivity of the catalyst.

5.3.4 Carbon formation on NiO–ZrO_2 and NiO–10Al_2O_3–ZrO_2 catalysts

5.3.4.1 The content and the type of carbon deposition

The carbon deposition of both catalysts was followed by TGA experiments and were shown in Figure 5-12. The carbon formation on NiO–10Al_2O_3–ZrO_2 catalyst (5.3 %) (Figure 5-12 (B)) was slightly higher than that on NiO–ZrO_2 catalyst (3.7 %) (Figure 5-12 (A)), which can be ascribed to the slight reduction of CO_2 conversion observed for NiO–10Al_2O_3–ZrO_2 catalyst during 8 hours time-on-stream. From the DSC curve, one peak corresponding to the maximum of carbon consumption at c.a. 560 °C for NiO–10Al_2O_3–ZrO_2 catalyst was observed. Whereas a shift to higher temperature (630°C) was observed for NiO–ZrO_2 catalyst. It is worth noting that the initial carbon removal temperatures (the initial decrease of sample weight) on NiO–ZrO_2 and NiO–10Al_2O_3–ZrO_2 catalysts are 550 and 420 ^oC, respectively. Thus, the formed carbon was easier to be removed on NiO–10Al_2O_3–ZrO_2 catalyst, which contributes to the stability of the catalyst. According to the different initial carbon removal temperature, two types of carbon were named as C1 and C2 for 550 and 420 ^oC, respectively.

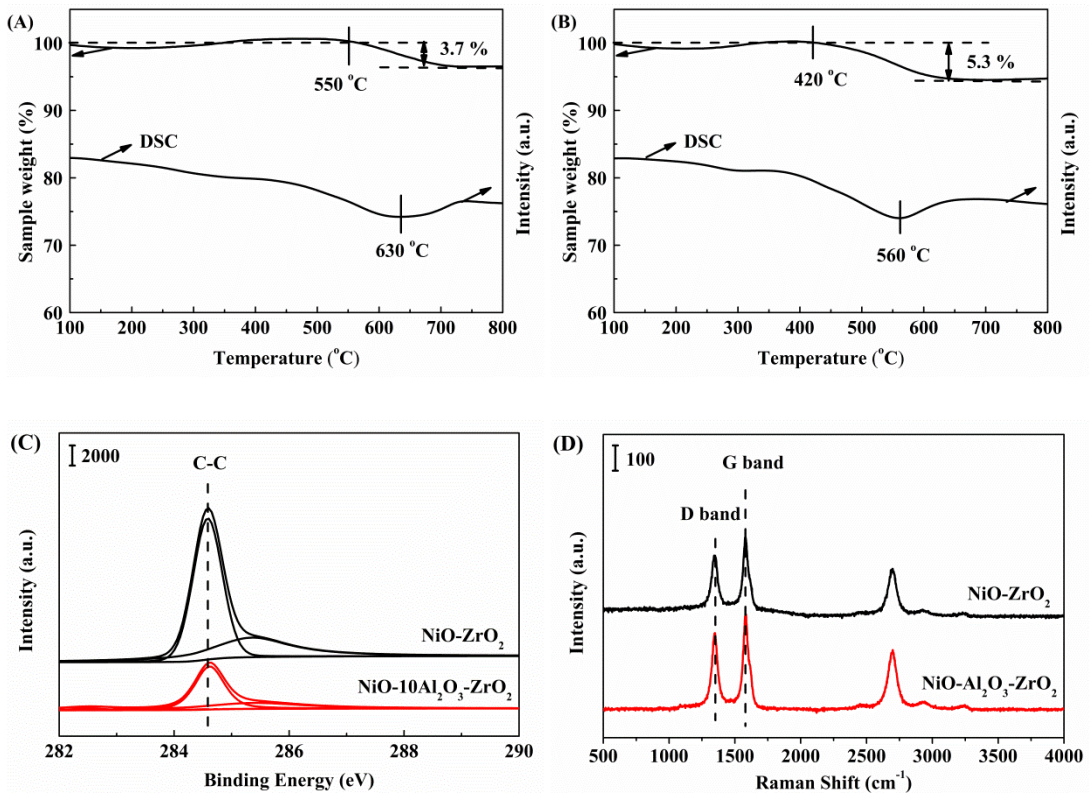

Figure 5-12 TGA profiles of (A) NiO–ZrO_2 and (B) NiO–$10Al_2O_3$–ZrO_2 catalysts after reaction at 700 °C for 8 hours. (C) The C 1s profiles from XPS spectroscopy and (D) Raman profiles of NiO–ZrO_2 and NiO–$10Al_2O_3$–ZrO_2 catalysts after reaction at 700 °C for 8 hours

In order to distinguish the type of formed carbon, XPS and Raman spectroscopy were conducted (Figure 5-12 (C) and (D)). From the C 1s extracted from XPS data, the peak at about 284.6 eV is attributed to the C–C species. Another peak at 285.5 eV was assigned to the C–O and C=O species [120, 261]. The C–C, C–O and C=O species are observed on both NiO–ZrO_2 and NiO–$10Al_2O_3$–ZrO_2 catalysts. From the Raman experiments, three distinct peaks (1345, 1580 and 2694 cm^{-1}) could be observed for both NiO–ZrO_2 and NiO–$10Al_2O_3$–ZrO_2 catalysts. The peaks at about 1345 and 1580 cm^{-1} were assigned to D (disorder) and G (graphite) bands of carbon materials, respectively. The peak at about 2694 cm^{-1} was ascribed to the overtone of the D band ($2\times1345\ cm^{-1}=2690\ cm^{-1}$) [247, 262]. The intensity of D and G band is named as I_D and I_G, respectively. The ratio of I_D/I_G on NiO–ZrO_2 and NiO–$10Al_2O_3$–ZrO_2 catalysts are 0.6 and 0.8, respectively. Namely, the type of carbon deposition was mainly in the form of graphite on both catalysts and more graphite formed on NiO–ZrO_2 catalyst.

Combined with XPS results, the graphic consisted of C–C species, while disorder carbon materials were composed of C–O and C=O species.

5.3.4.2 The morphology of carbon deposition

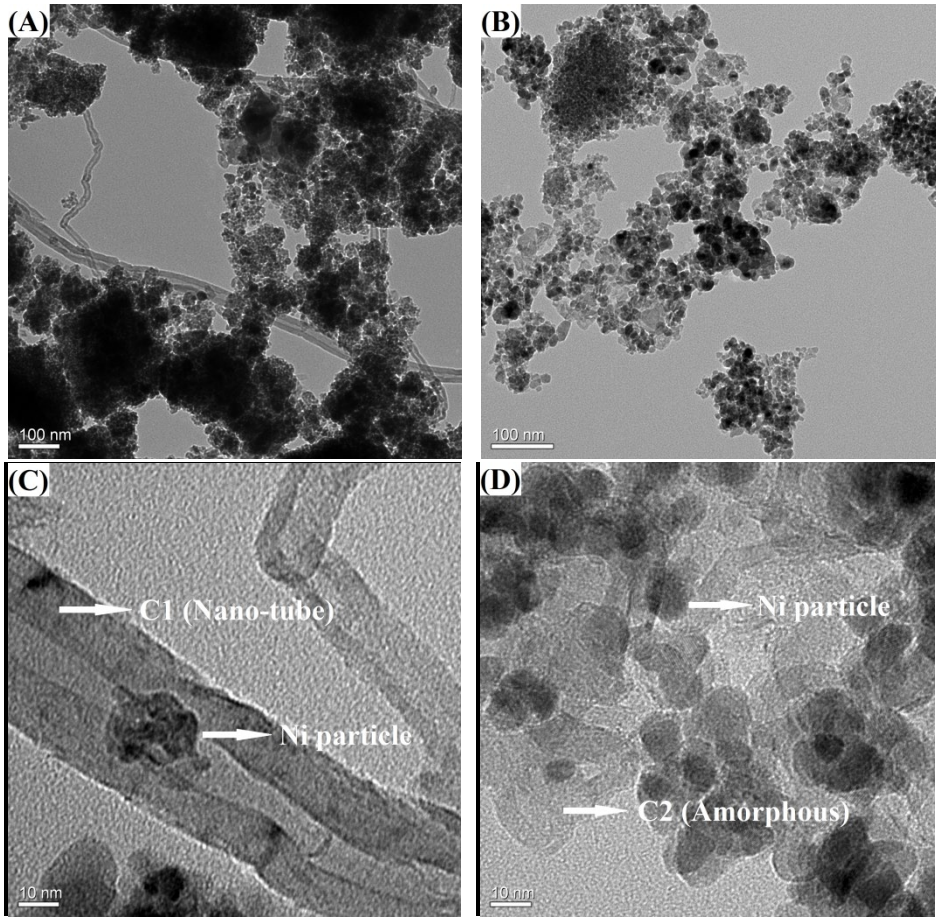

Figure 5-13 The morphology of ((A) and (C)) $NiO–ZrO_2$, and ((B) and (D)) $NiO–10Al_2O_3–ZrO_2$ catalysts after reaction, determined by TEM.

The morphology structure of carbon deposition on $NiO–ZrO_2$ and $NiO–10Al_2O_3–ZrO_2$ catalysts was determined by using transmission electron microscopy. The results are reported in Figure 5-13. A large amount of carbon in the form of nano-tubes was deposited on $NiO–ZrO_2$ catalyst (Figure 5-13 (A)), while only some carbon spots could be observed on $NiO–10Al_2O_3–ZrO_2$ catalyst (Figure 5-13 (B)). However, according to the results of TGA, slightly more carbon was formed on $NiO–10Al_2O_3–ZrO_2$. Those phenomena indicated that amorphous carbon deposition may be favorable on NiO–

$10Al_2O_3$–ZrO_2 catalyst. In phase with the results of TGA, XPS and Raman, the nano-tube carbon formed on NiO–ZrO_2 catalyst and observed by TEM is denoted C1, namely C–C species and graphite. This latter type of carbon is generally very difficult to be removed, as shown in Figure 5-13 (C). On the other hand, the amorphous carbon formed on NiO–$10Al_2O_3$–ZrO_2 catalyst and observed by TEM is denoted C2, namely C–O and C=O species and disorder carbon, which corresponds to active carbon and is easier to be removed (Figure 5-13 (D)). Similar results have been observed on Ni-Si/ZrO_2 catalyst [62].

Those phenomena indicate that the disordered carbon with the form of C–O and C=O species is easy to be removed on the Al modified NiO–ZrO_2 catalyst. Those different types of carbon might play a role in the DRM reaction mechanisms. From the results of the stability test, the reverse water-gas shift (RWGS) reaction occurred on NiO–ZrO_2 catalyst. A part of CO_2 reacted with hydrogen rather than carbon, thus this carbon may be transformed into an inactive carbon gradually. And due to the accumulation, further forming a type of coke very difficult to be removed, namely graphite nano-tubes of carbon [62]. On the other hand, the RWGS reaction was inhibited on NiO–$10Al_2O_3$–ZrO_2 catalyst. Therefore, amorphous carbon that could be easily eliminated was formed on NiO–$10Al_2O_3$–ZrO_2 catalyst. This is in agreement with the fact that the CO_2 conversion was lower than CH_4 conversion on NiO–$10Al_2O_3$–ZrO_2 catalyst, which indicated that the rate of carbon deposition was higher than that of carbon elimination, thus leading to more amorphous carbon on NiO–$10Al_2O_3$–ZrO_2 catalyst.

5.3.5 Physicochemical features of NiO–ZrO_2 and NiO–10Al_2O_3–ZrO_2 catalysts

5.3.5.1 The BET results

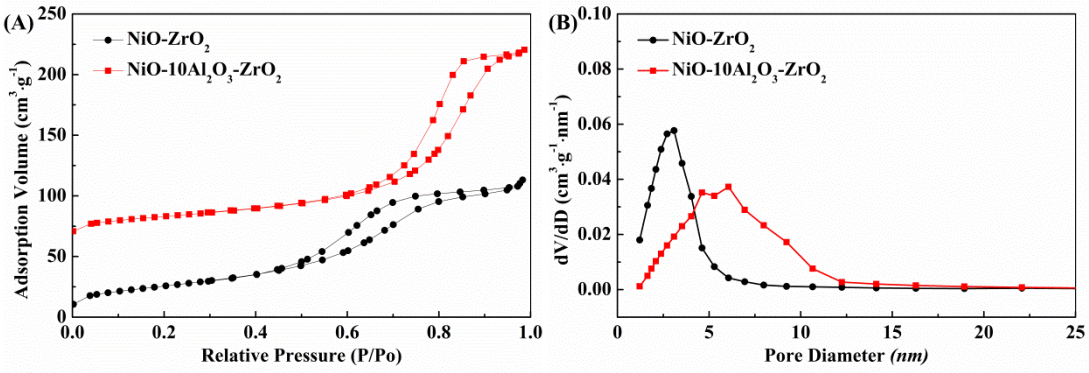

Figure 5-14 Isotherm (A) and pore size distribution (B) of NiO–ZrO_2 and NiO–Al_2O_3–ZrO_2 catalysts.

Figure 5-14 presented the adsorption/desorption isotherms. The adsorption isotherms for NiO–10Al_2O_3–ZrO_2 and NiO–ZrO_2 catalysts were type IV, with an H2 hysteresis loop according to the literature [263], typical of mesoporous materials. The pore size distribution (Figure 5-14 (B)) indicated the most probable pore size of 3 and 6 nm for NiO–ZrO_2 and NiO–10Al_2O_3–ZrO_2 catalysts, respectively. The pore volume (V_P) and the specific surface area (S_{BET}) were listed in Table 5-10. Large pore volume (0.25 cm^3/g) and pore diameter (6 nm) were observed on NiO–10Al_2O_3–ZrO_2 catalyst. Thus, the physical properties (pore volume and pore diameter) could be promoted by the introduction of aluminum. This large pore volume and pore diameter may increase the proportion of metal nickel dispersed in the porous structure of the catalysts.

Table 5-10 The results of the BET experiment for NiO–ZrO_2 and NiO–Al_2O_3–ZrO_2 catalysts, the pore diameter (D_P) and the pore volume (V_P) determined by BJH method, and the specific surface area (S_{BET}) was determined by the BET method.

Catalyst	D_P, nm	S_{BET}, m^2/g	V_P, cm^3/g
NiO–ZrO_2	3	113	0.18
NiO–10Al_2O_3–ZrO_2	6	86	0.25

5.3.5.2 The reducibility of $NiO–ZrO_2$ and $NiO–10Al_2O_3–ZrO_2$ catalysts

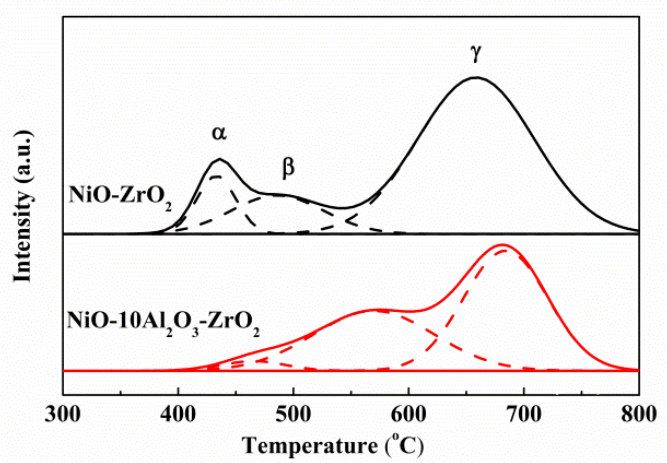

Figure 5-15 The H_2-TPR profiles of $NiO–ZrO_2$ and $NiO–10Al_2O_3–ZrO_2$ catalysts.

The reducibility of $NiO–ZrO_2$ and $NiO–10Al_2O_3–ZrO_2$ catalysts were determined by H_2-TPR experiments, as shown in Figure 5-15. The reduction temperatures on the $NiO–10Al_2O_3–ZrO_2$ catalyst shifted towards higher values as compared to the $NiO–ZrO_2$ catalyst, which was an indication for a stronger interaction between Ni and support on the promoted catalyst. This stronger metal-support interaction could inhibit the sintering of Ni particles, hence enhancing the stability of the catalyst [264]. The total H_2 consumption on $NiO–10Al_2O_3–ZrO_2$ catalyst was about 479 µmol H_2/g (Table 5-11), which was higher than the theoretical value (434 µmol H_2/g), indicating that this 9 % ((479-433)/479*100 %=9 %) of H_2 consumption was assigned to the reduction of Zr^{4+} to Zr^{3+}, as proved by Zr 3d profiles. While more amount of Zr^{4+} was reduced to Zr^{3+} on $NiO–ZrO_2$ catalyst (about 25 %), manifesting that the structure of ZrO_2 might be more stable by adding the Al into $NiO–ZrO_2$ catalyst. However, three peaks could be distinguished (denominated α, β and γ) on both catalysts. The first peak (α) at 400-500 °C was related to the reduction of NiO species with weak interaction between zirconia, which might be easy to sinter. The second peak (β) at 500-600 °C corresponded to the reduction of NiO species inside mesoporous with strong interaction between zirconium, which could maintain the original state even after reduction and reaction, due to the pore confinement effect. The third peak (γ) at 600-800 °C was assigned to the NiO

species in the skeleton of ZrO_2 and ZrO_2 species [50, 265]. The proportion of three peaks on NiO–10Al_2O_3–ZrO_2 and NiO–ZrO_2 catalysts was shown in Table 5-11. The content of the β peak was about 40 % on NiO–10Al_2O_3–ZrO_2 catalyst, which was higher than the one on NiO–ZrO_2 catalyst (15 %). Because NiO–10Al_2O_3–ZrO_2 catalyst exhibited large pore volume and pore diameter. Considering the content of α peak, about 44 % (40+4=44 %) H_2 consumption came from the reduction of NiO species out of the skeleton. The ratio of the NiO species out/in of skeleton was about 24:51 and 44:47 on NiO–ZrO_2 and NiO–10Al_2O_3–ZrO_2 catalysts, respectively. Besides, part of nickel species could be released and distributed on the surface of ZrO_2 or enter into the porosity. Then, this shift could lead to an increase of the proportion of NiO species on the surface, which could promote the activity of the catalyst, due to the probability of the contact of the reactant with the active metal.

Table 5-11 The consumption of H_2 and the proportion of three peaks on the H_2-TPR experiment.

	Total μmol H_2/g		H_2 consumption (%)				
			α	β	γ		The ratio
Catalyst	Actual	Theoretical	NiO	NiO	NiO	ZrO_2	of out:in
NiO–ZrO_2	626	468 [a]	9	15	51 [b]	25	24:51[c]
NiO–10Al_2O_3–ZrO_2	479	434	4	40	47	9	44:47

a: The H_2 consumption of the theory calculated by ICP and the consumption of reduction of pure NiO.
b: The proportion of NiO in the skeleton of ZrO_2.
c: The ratio of the NiO species out:in of skeleton.

5.3.5.3 The crystallite sizes of Ni^0 and ZrO_2 on $NiO–ZrO_2$ and $NiO–10Al_2O_3–ZrO_2$ catalysts

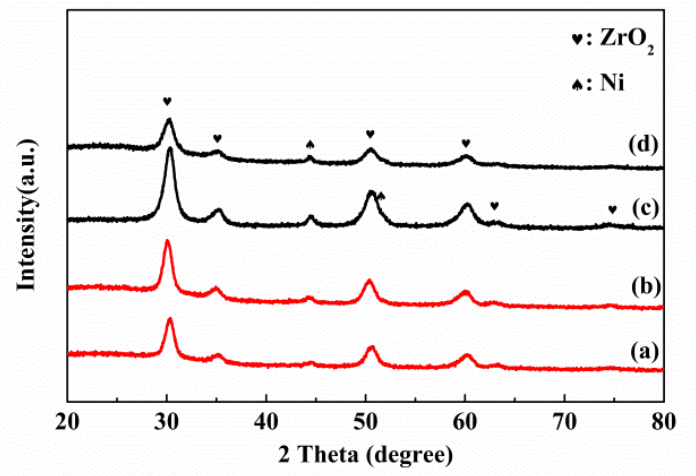

Figure 5-16 XRD profiles of (a) $NiO–ZrO_2$ and (c) $NiO–10Al_2O_3–ZrO_2$ catalysts after reduction at 700 °C for 1 hour, and (b) $NiO–ZrO_2$ and (d) $NiO–10Al_2O_3–ZrO_2$ catalysts after reaction at 700 °C for 8 hours.

The crystallite sizes on $NiO–ZrO_2$ and $NiO–10Al_2O_3–ZrO_2$ catalysts were determined by XRD, as shown in Figure 5-16. NiO peak could not be observed on both catalysts after reduction, indicating that all the Ni species were reduced. Ni metal peaks were obvious on both catalysts before and after reaction, and the crystallite size of Ni metal was shown in Table 5-12. Before reaction, those two catalysts exhibited the same Ni^0 crystallite size (12 nm). According to the H_2-TPR results, $NiO–ZrO_2$ catalyst exhibited higher content of α peak (the NiO is well known to be easily sintered) and lower content of β peak (the NiO was hard to sinter), which led to very severe sintering. Therefore, the Ni metal particle size increased to 24 nm on $NiO–ZrO_2$ catalyst after reaction, which corresponded to the nickel particle size determined by the TEM experiment, concentrated at 15-20 nm. On the contrary, it decreased to 11 nm on $NiO–10Al_2O_3–ZrO_2$ catalyst after reaction, and according to the TEM results, the nickel particle size mainly distributed at 10-15 nm. Because lower content of α peak and higher content of β peak formed on $NiO–10Al_2O_3–ZrO_2$ catalyst, the Ni species might be better to stay pristine in the porosity, as compared with $NiO–ZrO_2$ catalyst. There were several reasons to explain the decrease of Ni metal particle size. Firstly, the Ni metal can be

redispersed during reaction. Secondly, part of metallic Ni (Ni^0) could be oxidized to NiO or $NiCO_x$ by CO, and CO_2 could be adsorbed on Ni^0. Thirdly, part of Ni^0 could be covered by carbon present on the catalysts [93, 96, 117, 227].

Obviously, the structure of the nickel particle on NiO–$10Al_2O_3$–ZrO_2 catalyst was more stable, contributing to the stability of the catalyst. Therefore, NiO–$10Al_2O_3$–ZrO_2 catalyst exhibited higher stability for the dry reforming of methane. Besides, the large nickel metal particle size could affect the selectivity of catalyst towards carbon deposition [237, 238]. Hence, the carbon deposited on NiO–ZrO_2 catalyst was difficult to be removed because of its graphite form.

Table 5-12 The ZrO_2 and Ni^0 crystallite size on both catalysts before and after DRM reaction, determined by XRD. The particle size of Ni after DRM reaction, determined by TEM.

	ZrO_2 crystallite sizes (nm)		Ni^0 crystallite sizes (nm)		particle size of
Catalyst	initial	8 h	initial	8 h	Ni[a] (nm)
NiO–ZrO_2	7	7	12	24	15-20
NiO–$10Al_2O_3$–ZrO_2	7	7	12	11	10-15

a: measured on catalyst after DRM reaction for 8 h.

5.3.5.4 The surface content of Zr and Ni on NiO–$10Al_2O_3$–ZrO_2 and NiO–ZrO_2 catalysts

From XPS, the Zr 3d profiles of NiO–$10Al_2O_3$–ZrO_2 and NiO–ZrO_2 catalysts before and after reduction were studied and the results were presented in Figure 5-17 (A). The peak at 182.3 and 181.4 eV were assigned to Zr^{4+} and Zr^{3+}, respectively [50, 243]. The proportion of Zr^{4+} and Zr^{3+} was listed in Table 5-13. The proportion of Zr^{4+} on NiO–ZrO_2 and NiO–$10Al_2O_3$–ZrO_2 catalysts were respective 11 and 14 %, which indicated that part of Zr^{4+} could be reduced to Zr^{3+} after reduction on both catalysts and more Zr^{4+} could be reduced on NiO–ZrO_2 catalyst, corresponding with the results of H_2-TPR. After reaction, part of Zr^{3+} species was reduced to lower valence, eg Zr^{2+} and Zr^{1+} [266, 267]. Then, NiO–ZrO_2 catalyst exhibited higher content of lower valence zirconium,

especially containing Zr^{1+} species of 35 %, while no Zr^{1+} species could be observed on $NiO–10Al_2O_3–ZrO_2$ catalyst, manifesting that the structure of ZrO_2 might be more stable by the modification of Al.

Table 5-13 The content of Zr and Ni species on both catalysts before and after reaction at 700 °C for 8 hours, determined by XPS.

	Zr proportion (%)						Ni content (wt %)			
	initial		8 h				initial		8 h	
Catalyst	Zr^{4+}	Zr^{3+}	Zr^{4+}	Zr^{3+}	Zr^{2+}	Zr^{1+}	Ni	Ni^0	Ni [a]	Ni^0 [b]
$NiO–ZrO_2$	11	89	17	25	23	35	5.6	1.9	-21 %	-42 %
$NiO–10Al_2O_3–ZrO_2$	14	86	22	34	44	-	5.8	1.0	-3 %	+10 %

a: The loss of surface nickel species after DRM reaction for 8 h.
b: The loss of surface nickel metal species after DRM reaction for 8 h.

We also followed the Ni species at the surface by XPS. Figure 5-17 (B) presented the Ni 2p profiles of $NiO–10Al_2O_3–ZrO_2$ and $NiO–ZrO_2$ catalysts before and after reaction. The peak at about 852.8 eV was attributed to Ni^0 species, while another peak was assigned to NiO species [62]. After reaction (DRM, 700 °C, 8 h), the NiO peak shifted slightly to lower binding energy on $NiO–10Al_2O_3–ZrO_2$. It suggested that the electrons could transfer to Ni species during the reaction, which might contribute to the catalytic performance of the catalyst. While the NiO peak shifted slightly to higher binding energy on $NiO–ZrO_2$ catalyst, which indicated that the ability of nickel species to donate electrons on $NiO–10Al_2O_3–ZrO_2$ catalyst was stronger than the one on $NiO–ZrO_2$ catalyst. Except for the electron transfer, the nickel content also varied visibly. Before reaction, the content of surface nickel species on $NiO–ZrO_2$ catalyst was about 5.6 wt%, while after reaction for 8 h, it decreased by 24 %. A larger amount of reduction could be observed in the content of surface Ni^0 species. It decreased by 42 % after reaction. Thus, the activity on $NiO–ZrO_2$ catalyst also decreased. However, nickel species were relatively stable on $NiO–10Al_2O_3–ZrO_2$ catalyst after reaction, the surface nickel content was 5.8 wt% at the beginning, while it just decreased by 3 % after reaction for 8 h. Meanwhile, the initial content of surface Ni^0 species was about 1.0 wt%, and increased by 10 % on $NiO–10Al_2O_3–ZrO_2$ catalyst after reaction for 8 h. The

content of nickel species at the surface of NiO–10Al_2O_3–ZrO_2 catalyst was more stable than that on NiO–ZrO_2 catalyst, which might contribute to the stability of the catalyst. Therefore, NiO–10Al_2O_3–ZrO_2 catalyst exhibited higher stability for the dry reforming of methane. After reduction, a large amount of NiO species could be detected, which may be explained by the following three reasons. First of all, Ni^0 species on the surface of the catalyst could adsorb the oxygen in the air; secondly, the Ni^0 species may be re-oxidized when the reduced catalyst exposed to air; and the last, it could be due to the strong interaction between metal and support [120, 268].

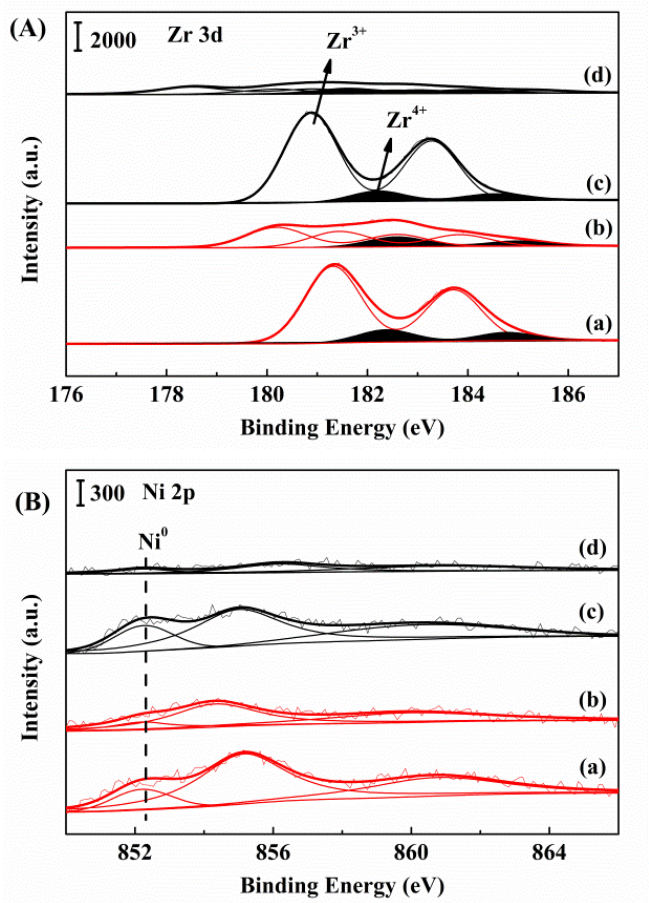

Figure 5-17 (A) Zr 3d and Ni 2p profiles of (a) NiO–10Al_2O_3–ZrO_2 and (c) NiO–ZrO_2 catalysts after reduction at 700 °C for 1 hour and (b) NiO–10Al_2O_3–ZrO_2 and (d) NiO–ZrO_2 catalysts after reaction at 700 °C for 8 hours.

5.3.6 Discussion

The aluminum could be embedded into the skeleton of zirconia during the synthesis of $NiO–10Al_2O_3–ZrO_2$ catalyst, which could then modify the structure of zirconia, resulting in the increase of the pore volume (0.25 cm^3/g) and pore diameter (6 nm). The larger pore volume can accommodate higher content of nickel species and the larger pore diameter can restrict grain growth, due to the confinement effect, thereby enhancing the dispersion and interaction. This pore confinement effect and the strong interaction enhanced by the introduction of aluminum could restrain the sintering and the loss of nickel during the DRM reaction. Meanwhile, the introduction of Al could enhance the stability of the zirconia species, which might promote the stability of the content and the grain size of Ni^0. Therefore, the content and particle size of nickel metal can maintain the original state during the DRM reaction, thereby promoting the stability of the catalyst.

5.3.7 summary

In this study, we clearly showed that Al, as promoter could enhance the activity, the selectivity and the stability of NiO–ZrO_2 catalyst for dry reforming of methane. The activity tests were conducted from 550 °C to 800 °C, and the NiO–10Al_2O_3–ZrO_2 catalyst exhibited the highest catalytic performance for dry reforming of methane at lower temperature.

Furthermore, the stability tests, carried out at 700 °C for 8 hours, showed that the NiO–10Al_2O_3–ZrO_2 catalyst presented higher activity, selectivity and stability than those on NiO–ZrO_2 catalyst. This high activity was directly linked to the higher content at surface of nickel particles and the smaller particle size, which was attributed to the larger pore volume and pore diameter on NiO–10Al_2O_3–ZrO_2 catalyst.

Therefore, NiO–10Al_2O_3–ZrO_2 catalyst exhibited higher stability for DRM reaction. In fact, after 8h runs, on NiO–10Al_2O_3–ZrO_2 catalyst, formed easier to be eliminated coke as a form of amorphous and disordered carbon (C–O and C=O species). Also, on NiO–ZrO_2 catalyst, a severe metal sintering occurred and more nano-tube carbon (graphite) that was very difficult to be removed formed.

5.4 Dry reforming of methane over Ni–ZrO_x catalysts doped by Manganese: On the effect of the stability of Zirconia structure

5.4.1 Introduction

As already presented in the previous chapter. ZrO_2 has received much attention as promoter and/or support in dry reforming of methane, due to its high carbon resistance [116, 130, 169, 269]. Katsutoshi et al. [169] compared Pt/ZrO_2 and Pt/Al_2O_3 catalysts for the carbon deposition over DRM reaction. They found that more carbon deposited on Pt/Al_2O_3 catalyst, which would cover on Pt, thereby leading to the deactivation of Ni/Al_2O_3 catalyst. While coke is hardly formed on Pt/ZrO_2 catalyst. Besides, the structural properties, like thermal and mechanical stability, particle size, and crystal phase are very important for reforming reactions [106, 119, 269-271]. Xu et al [271] reported that the Ni/ZrO_2 catalyst with the smaller size of ZrO_2 exhibited higher stability for dry reforming of methane than the one with a bigger particle size of ZrO_2 (>25 nm). The Ni/am-ZrO_2 catalyst (amorphous) exhibited the highest activity and stability for DRM reaction than Ni/t-ZrO_2 (tetragonal) and Ni/m-ZrO_2 (Monoclinic) catalysts, reported by Zhang et al.[106].

It is well known that manganese (Mn) based catalysts possess a high oxygen storage capacity and limit agglomeration at high reduction temperatures [269, 272]. Wang et al. [273] reported that the improved catalytic performance of Co-Ce-Zr-O_x catalyst modified by Mn was mainly attributed to the increase of oxygen mobility and the surface oxygen species. Because of larger amount of mobile oxygen, the coke on the surface could be easily oxidized to CO_x on Mn-promoted Co-Ce-Zr-O_x catalyst. Yao et al. [121] and Seok et al. [274] showed that the Mn promoter could enhance the dispersion of Ni and less carbon deposition through resisting the aggregation of nickel metal. Özkara-Aydınoğlu et al. [119] noticed that the addition of Mn could reduce carbon deposition with a decrease in catalytic activity. Similar phenomenon has been

reported by Luna et al. [275] and Liu et al. [88].

On the contrary to that is presented in the literature. In this study, we showed an increase with time on stream. In order to understand the positive effect of Mn on the activity for DRM, we developed here Ni–ZrO_x and Ni–Mn–ZrO_x catalysts prepared by a one-step synthesis method. The relationships between the catalytic performance and surface properties of Ni–ZrO_x and Ni–Mn–ZrO_x catalyst were discussed as function of time on stream

5.4.2 Preparation of the Ni-Zr catalyst modified by Mn

Ni–ZrO_x and Ni–Mn–ZrO_x materials were prepared by the urea hydrolysis method (one-step synthesis) according to [50]. For Ni-ZrO_x material, 7.06 g urea (Sigma-Aldrich), 1.14 g nickel (II) nitrate hexahydrate (Emsure), 7.96 g of Pluronic P123 (Sigma-Aldrich) amphiphilic block copolymer and 5.03 g zirconium(IV) oxynitrate hydrate (Sigma-Aldrich) were dissolved in distilled water. The synthesis mixture for Ni-Mn-ZrO_x material contained the same amounts of reactants plus 0.93 g Manganese (II) nitrate tetrahydrate (Sigma-Aldrich) (corresponding to a loading of 10 wt %). In both cases, a light blue precipitate was formed at 95 °C with constant stirring for 48 h. Then, the obtained precipitate was aged at 100 °C for 24 h. After that, the slurry was isolated by filtration, washed by a small amount of distilled water and then placed at room temperature. Finally, these two precipitates were calcined in flowing air at 800 °C for 5 h (heating rate 1 °C/min). The obtained materials were denoted as Ni–ZrO_x and Ni–Mn–ZrO_x catalysts.

5.4.3 Characterization of Ni-Zr catalyst modified by Mn

5.4.3.1 The reducibility of catalysts

Figure 5-18 presented the H_2-TPR results of calcined samples. According to our previous works [50], the peak at about 400 °C on Ni-ZrO_x catalyst was attributed to the reduction of NiO species with weak interaction between Ni and Zr. The main reduction peak (600 °C) was attributed to the reduction of NiO species with strong interaction between Ni and Zr, and the ZrO_2 species. The last peak at 850 °C was also assigned to the reduction of ZrO_2 species. The introduction of Mn promoter could affect the reduction properties of Ni–Mn–ZrO_x catalyst. Whereas, A new weak peak appeared between 200-400 °C, which was assigned to the reduction of MnO_2 to Mn_2O_3 [88, 276]. A wide peak between 400-700 °C came from the reduction of NiO species, Mn_2O_3 and ZrO_2 [50, 88, 276]. Thus, the reduction peaks shifted to lower temperature on Mn-promoted catalyst. Similar observation was reported [121, 133, 273]. These shifts implied that the interaction between Ni and support on Ni–Mn–ZrO_x catalyst was relatively weaker than that on Ni–ZrO_x catalyst, which might result in the sintering of nickel under reduction condition.

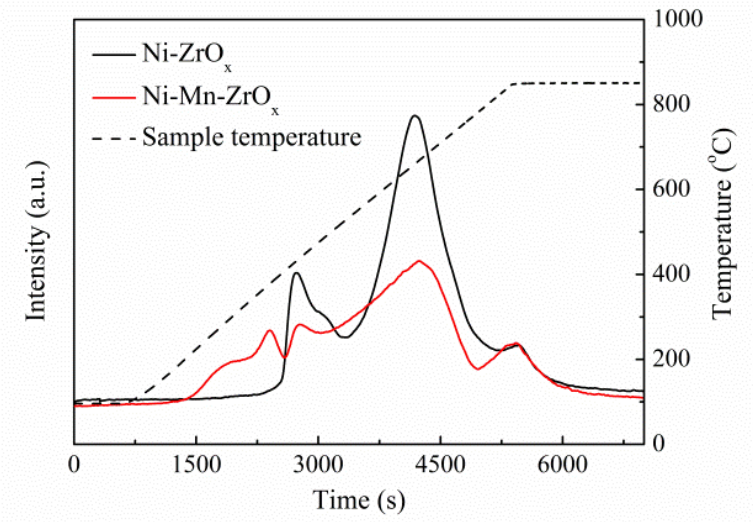

Figure 5-18 The H_2-TPR profiles of Ni–ZrO_x and Ni–Mn–ZrO_x catalysts

5.4.3.2 The basic of catalysts

Table 5-14 The deconvolution of the CO_2-TPD profiles obtained for the Ni–ZrO_x and Ni–Mn–ZrO_x catalysts

	CO_2 desorbed (μmol CO_2 /g)			Total basicity
	Weak	medium-strength	Strong	(μmol CO_2/g)
Ni–ZrO_x	21	59	20	73
Ni–Mn–ZrO_x	34	48	10	92

Figure 5-19 shows the CO_2-TPD curves of the reduced catalysts. In agreement with the literature [277], the three desorption peaks on Ni–ZrO_x catalyst centered at 159, 249 and 395 °C were attributed respectively for weak, medium and strong basic sites, which corresponded to surface OH^- groups, zirconium-oxygen ion pairs, and isolated O^{2-} anions, respectively [278, 279]. Whereas, the desorption peaks on Ni–Mn–ZrO_x catalyst shifted to low temperature. The three peaks shifted to 140, 232, and 375 °C for weak, medium, and strong basic sites, respectively. According to Table 5-14, Mn promoted the formation of weak basic sites and decreased the strong basic sites. Besides, the total basic sites increased from 73 to 92 μmol CO_2/g by the introduction of Mn.

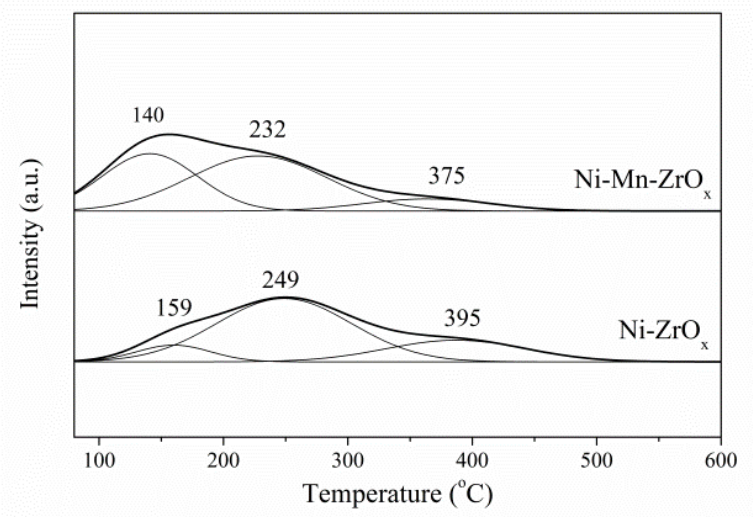

Figure 5-19 The CO_2-TPD profiles of Ni–ZrO_x and Ni–Mn–ZrO_x catalysts.

5.4.4 The effect of Ni-Zr catalyst modified by Mn on performance for reforming of methane

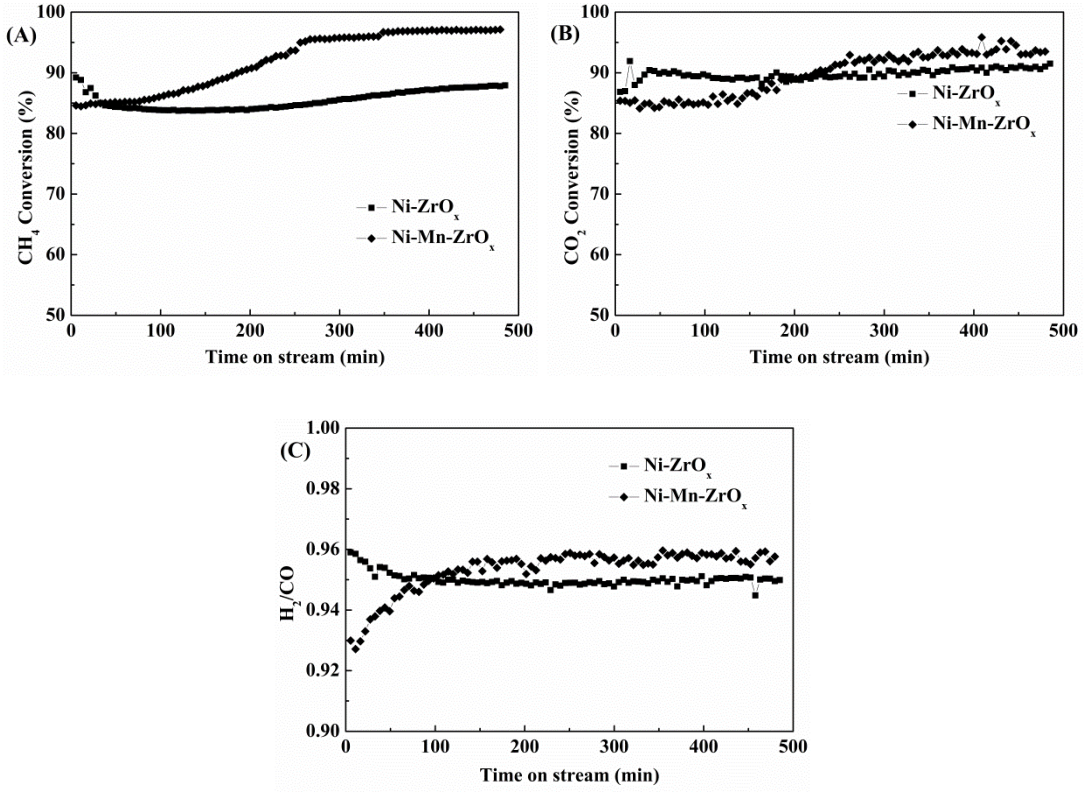

Figure 5-20 The CH_4 and CO_2 conversion, and the H_2/CO ratio with time on stream over Mn-promoted and non-promoted catalysts.

The results of activity test were presented in Figure 5-20 and Table 5-15. It was shown that the initial conversions of CO_2 and CH_4 on Ni–ZrO_x catalyst were about 89.2 and 86.8 %, respectively, and were higher than those obtained on Ni–Mn–ZrO_x catalyst (85.4 % and 84.6 % for CO_2 and CH_4, respectively). It was worth noting that CH_4 conversion on Ni–ZrO_x catalyst decreased to 83.8 % after reaction for 100 min. Finally, it stabilized at about 87.8 % after 300 min. The H_2/CO ratio showed a similar trend. It decreased from 0.96 to 0.95 within 100 min and then stabilized at 0.95. The stability of CO_2 conversion was relatively higher. On the whole, it slowly increased to 91.0 %. While for Ni–Mn–ZrO_x catalyst, the CH_4 conversion slowly increased to 97.1 % with time on stream and almost stabilized after reaction 300 min. Similar phenomena could be observed on CO_2 conversion and H_2/CO ratio. After 480 min, the CO_2 conversion

and H_2/CO ratio on Ni–Mn–ZrO_x catalyst increased to 93.5 % and 0.96, respectively. In order to understand this activation during the time on stream, catalysts after reduction, and after reaction for 100 min, 300 min and 480 min time on stream were characterized. The results are presented in the section below.

Table 5-15 Stability results showing initial activity and after 100 min, 300 min and 480 min tests.

	CH_4 Conversion (%)				CO_2 Conversion (%)				H_2/CO ratio			
	initial	100	300	480	initial	100	300	480	initial	100	300	480
Ni–ZrO_x	89	84	86	88	87	90	89	91	0.96	0.95	0.95	0.95
Ni–Mn–ZrO_x	85	86	96	97	85	85	92	94	0.93	0.95	0.96	0.96

5.4.5 The relationship between the stability of ZrO_2 and activity of catalyst

5.4.5.1 Ni crystallite size and dispersion

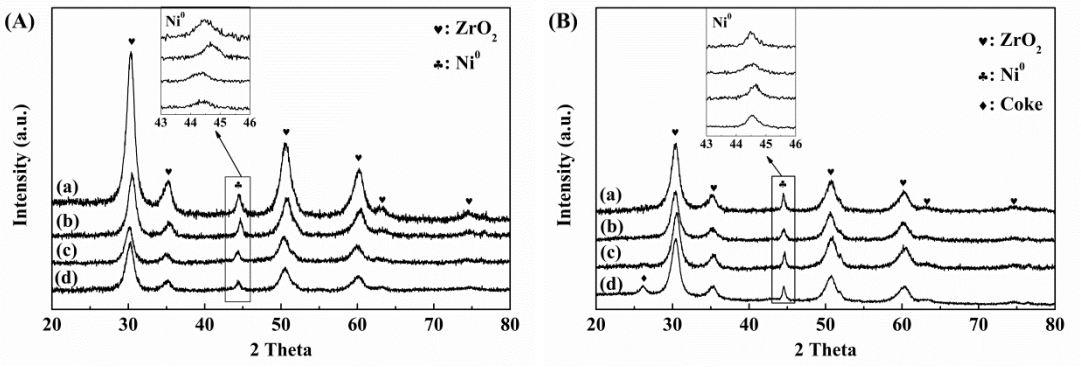

Figure 5-21 The XRD profiles of (A) Ni–ZrO_x and (B) Ni–Mn–ZrO_x catalyst. (a) reduced and after reaction for 100 min (b), 300 min (c) and 480 min (d).

Figure 5-21 presented the XRD results after different time on stream. The reflection peaks at 30.5, 35.3, 51.0, 60.5 and 74.9 º can be attributed to the tetragonal phase of ZrO_2. Another peak about at 44.5 º corresponded to the most intense peak of the Ni^0 phase [246]. The tetragonal phase ZrO_2 was evidenced in all the catalysts. No

monoclinic ZrO_2 and NiO phases were detected in these catalysts. Significantly, the Ni^0 reflection plane (2θ=44.5 º) on Ni–ZrO_x catalyst shifted to bigger Bragg angles after reaction for 100 min, while it shifted to smaller Bragg angles after reaction for 300 min. The maximum shift distance for Ni^0 was about 0.22 º during the reaction. For Ni–Mn–ZrO_x catalyst, the swing became gentler. The shift is slightly lower (0.07 º). Except for the Bragg angles, the d-spacing of Ni^0 plane on Ni–ZrO_x catalyst shrunk from 2.04 Å to 2.03 Å, while d-spacing of ZrO_2 (2θ=30.4 º) reflection plane increased from 2.94 Å to 2.95 Å. In our previous work [277], it is about 2.96 Å on Ni/ZrO_2 catalyst that prepared by traditional impregnation method without NiO-ZrO_2 solid solution. Because the radius of Ni^{2+} ion (0.78 Å) is smaller than that of Zr^{4+} ion (0.84 Å), thus the lattice parameter of ZrO_2 would shrink after the substitute of same of zirconium sites by nickel. On the contrary, the expansion of ZrO_2 manifested that some nickel was set free from the skeleton of ZrO_2 phase [146]. Thus, For Ni–Mn–ZrO_x catalyst, the d-spacing of Ni^0 plane kept to 2.03 Å. Those phenomena indicated that the structure of nickel species was more stable on the Mn-promoted catalyst [121, 274, 280]. Yao et al. [121] reported the addition of Mn could enhance the interaction between Ni and support by the formation of $NiMn_2O_4$. Besides, some manganese oxide species MnO_x can cover on nickel particles, thereby inhibiting the sintering of nickel species, reported by Seok et al. [280]. Both of those two effects could limit the aggregation and migration of metal Ni. The crystallite sizes of both catalysts calculated from the Scherrer equation was presented in Table 5-16. the Ni metal particle size on Ni–ZrO_x catalyst increased from 12 to 22 nm after reaction for 100 min, manifesting severe sintering on Ni–ZrO_x catalyst in the first 100 minutes of the reaction, and then leading to the decrease of activity in DRM within reaction for 100 min. After 480 min reaction, the particle size of Ni^0 slowly increased to 24 nm, which corresponded with the results of activity test-stabilized from 100 minutes. On the contrary, for Ni–Mn–ZrO_x catalyst, the particle size of Ni^0 decreased from 29 to 25 nm after reaction for 300 min and to 24 nm after 480 min, corresponding to an increase in the DRM activity up to 97 % after reaction 300 min. The redispersion of Ni^0 species might occur in the condition of continuous alternating reduction and oxidation [50, 93, 117]. This redispersion indicated that the particle size

of Ni^0 was related to the activity in DRM. Li et al. [281] found Mn could improve the dispersion of nickel and enhance the interaction between nickel and support during the dry reforming of methane, and further improve the catalytic performance of Mn-modified catalyst. It was worth pointing out that the graphite peak could be observed after reaction for 300 min with the graphite crystal size of 20 nm. While after reaction for 480 min, it decreased to 14 nm. Mn could avoid carbon deposition or lead to its suppression as reported by Yao et al. [121] and Seok et al. [274], due to the formation of smaller Ni particle size on Mn-modified catalyst. Small Ni particles showed better resistance against coke formation [282]. The particle size greater than 20 nm on Ni–Mn–ZrO_x catalyst led to catalytic selectivity towards methane cracking (Equation (1)), and caused carbon deposition [50, 236, 238].

Table 5-16 The ZrO_2 and Ni^0 crystal size of Ni–ZrO_x and Ni–Mn–ZrO_x catalysts.

	Ni^0 (nm)				C (nm)		
	initial	100 min	300 min	480 min	100 min	300 min	480 min
Ni–ZrO_x	12	22	18	24	-	-	
Ni–Mn–ZrO_x	29	18	25	24	-	20	14

5.4.5.2 X-rays photoelectron spectroscopy (XPS) analysis

XPS experiment is conducted for both catalysts at different reaction times in order to analyze the Ni and Zr at the surface of the catalysts. Figure 5-22 (A) and (B) presented the results of Ni $2p_{3/2}$ profiles for non-promoted and promoted catalysts. According to the literature [283, 284], the obtained curve of Ni 2p spectra was deconvoluted in three peaks. The peaks centered at about 852.3 eV, 855 eV, and 861 eV are assigned to Ni^0 species, $Ni^{2+,}$ and satellite, respectively [62, 63]. And the percentage of Ni^0 species from XPS analysis was listed in Table 5-17. The percentage of surface Ni^0 species on Ni–ZrO_x and Ni–Mn–ZrO_x catalysts at the initiation of the reaction was about 24.4 and 20.0 % respectively. This is in agreement with the fact that Ni–ZrO_x catalyst exhibited higher initial activity than the one on Ni–Mn–ZrO_x catalyst. It was worth noting that

the percentage of NiO species was higher that of Ni^0 species at the initiation of both catalysts. The higher content of NiO species might be oxidized by air/CO_2 or CO_2/CO adsorb on Ni^0, which is explained elsewhere [50, 120]. The percentage of surface Ni^0 species on two catalysts saw an opposite trend with time on stream. It decreased to 17.4 % after reaction for 100 min and to 13.3 % after reaction for 480 min on Ni–ZrO_x catalyst. On the contrary, for Ni–Mn–ZrO_x catalyst, it increased to 40.0 % after 100 min reaction, to 23.2 after 300 min reaction and finally kept at about 22.6 % after reaction for 480 min. Those observations were consistent with the XRD and activity test results.

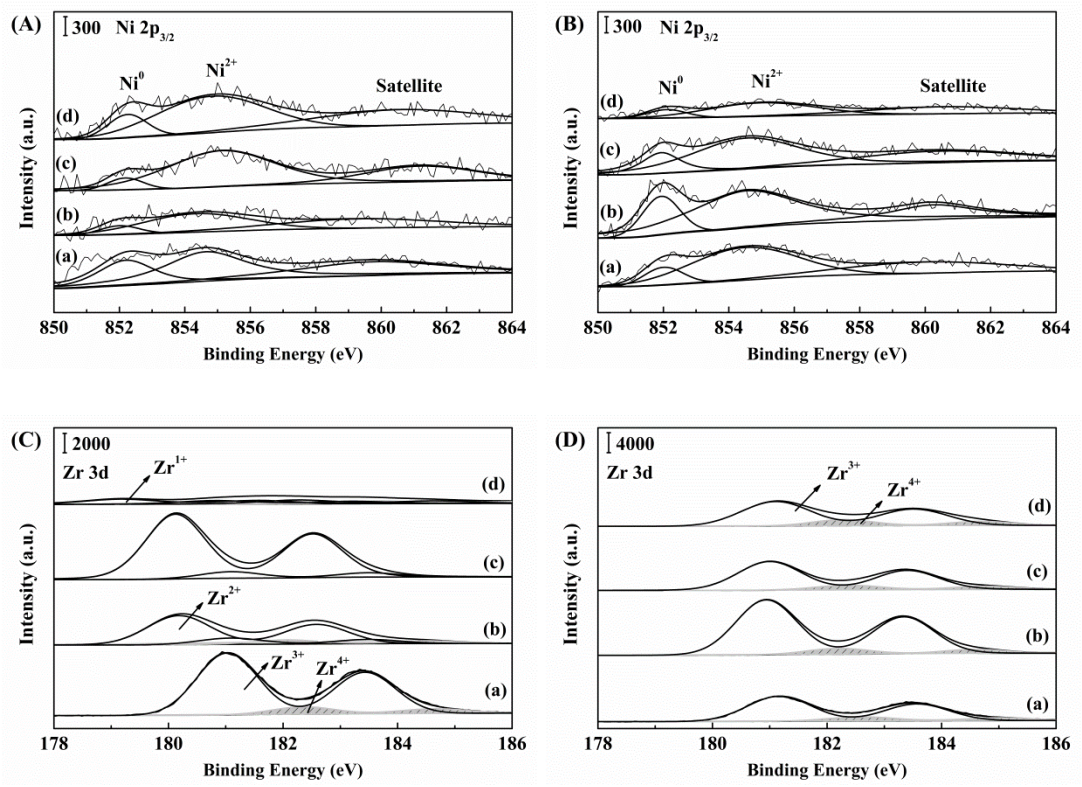

Figure 5-22 The Ni $2p_{3/2}$ and Zr 3d profiles of Ni–ZrO_x ((A) and (C)) and Ni–Mn–ZrO_x ((B) and (D)) catalysts. (a) reduced and after reaction for 100 min (b), 300 min (c) and 480 min (d).

Figure 5-22 (C) and (D) presented the Zr 3d results. The Zr 3d binding energies on Ni–ZrO_x catalyst shifted to lower values with the time on stream. While it kept on almost the original states over Ni–Mn–ZrO_x catalyst. This shift manifested that the Zr species could be reduced during the reaction. According to the literature, the Zr3d peak is

resolved into several peaks [267, 285]. The peaks at about 182.3 eV, 181.4 eV, 180.5 eV and 179.3 eV were attributed to the Zr^{4+}, Zr^{3+}, Zr^{2+} and Zr^{1+}, respectively [50, 266, 286]. At the beginning of the reaction, the percentage of Zr^{4+} and Zr^{3+} on Ni–ZrO_x catalyst was about 12 and 88 %, respectively. About 73 % of surface Zr species were reduced to Zr^{2+} on Ni–Zr catalyst after reaction for 100 min. It was pointed out that the Zr^{1+} species could be observed after reaction for 480 min. This indicated that the Zr species on Ni–ZrO_x catalyst were reduced during the reaction. Generally, the Zr cations in ZrO_2 are very difficult to be reduced [266, 287]. Herein, the Zr^{4+} species were gradually reduced to Zr^{1+}, indicating that this material has high solubility of oxygen, like TiO_2 [288]. However, unlike the redox cycle between Ti^{2+} and Ti^{3+}, the Zr^{4+} species were being reduced all the time, which might affect the stability of ZrO_2 structure. While for Ni–Mn–ZrO_x catalyst, the initial percentage of Zr^{4+} and Zr^{3+} was about 15.7 % and 84.3 %, respectively. The surface Zr species were not reduced after reaction. The percentage of Zr^{4+} and Zr^{3+} species after 300 min reaction was about 20 % and 80 %, respectively. And after 480 min reaction, it was found about 22 % and 78 % for Zr^{4+} and Zr^{3+} species. In conclusion, Ni–Mn–ZrO_x catalyst exhibited a more stable structure for ZrO_2 species.

Table 5-17 The percentage of zirconium and nickel in different valence states on Ni–ZrO_x and Ni–Mn–ZrO_x with time on stream, determined by XPS.

catalysts	Time (min)	Zr species (%)				Ni species (%)	
		Zr^{4+}	Zr^{3+}	Zr^{2+}	Zr^{1+}	Ni^0	NiO
Ni–ZrO_x	initial	12	88	-	-	24.4	75.6
	100	10.5	15.9	73.6	-	17.4	82.6
	300	-	9.1	90.9	-	12.9	87.1
	480	17.1	25.4	23.4	34.1	13.3	86.7
Ni–Mn–ZrO_x	initial	15.7	84.3	-	-	20	80
	100	15.3	84.7	-	-	40	60
	300	20	80	-	-	23.2	76.8
	480	22.1	77.9	-	-	22.6	77.4

5.4.6 carbon deposition

The carbon deposition of both catalysts after for 480 min was analyzed by TGA, Raman and TEM. The results were presented in Figure 5-23. The carbon deposition on Ni–Mn–ZrO_x catalyst (5.3 %) was higher than that on Ni–ZrO_x catalyst (3.7 %). Generally, the presence of Zr could promote the adsorption and/or activation of CO_2, thereby decreasing the carbon deposition in DRM process [96, 116]. Meanwhile, the addition of Mn could result in less carbon deposition since the small nickel particles [121, 274]. However, the existence of both Mn and Zr results in higher carbon deposition, which might be attributed to the large nickel particles. Because [50, 238]. From the TGA results, the carbon on both catalysts might be the same type, because it could be removed at the same temperature. In order to understand the nature of carbon deposition, Raman experiments were carried out, as shown in Figure 5-23 (B). Two peaks could be observed on both catalyst after reaction. D band and G band were ascribed to the disorder and graphite of carbon materials, respectively [62, 247, 262]. The I_D and I_G represented the intensity of D band and G band, respectively. The ratio of I_G/I_D was related to the crystalline degree of the carbon materials. According to our previous work, it was about 1.7 on Ni–ZrO_x catalyst [50]. While it was 2.0 on Ni–Mn–ZrO_x catalyst, indicating that the coke exhibited a higher crystalline degree. The morphology of coke was characterized by TEM experiment, as presented in Figure 5-23 (C) and (D). It observed that the carbon nanotubes formed on both catalysts after reaction for 480 min. And more carbon nanotubes existed on Ni–Mn–ZrO_x catalysts, which was agreement with the results of TAG and Raman. Besides, similar distribution of nickel particles could be observed on both catalysts, almost at 15-20 nm, which corresponded to the XRD results.

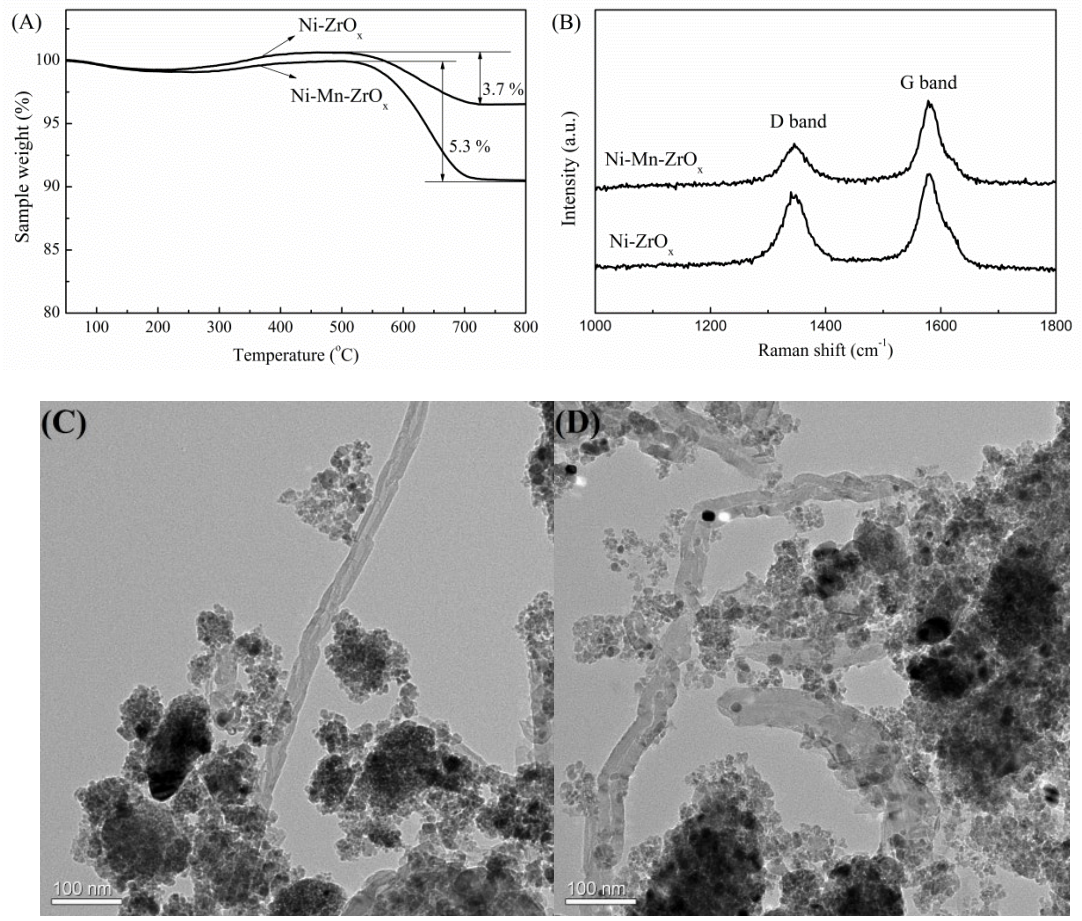

Figure 5-23 the TGA (A) and Raman (B) profiles of Ni–ZrO_x and Ni–Mn–ZrO_x catalysts. And the TEM profiles of Ni–ZrO_x (C) and Ni–Mn–ZrO_x (D) catalysts.

5.4.7 Discussion

Methane could be dissociated on the nickel metal site, while CO_2 could be adsorbed and activated on nickel metal sites and/or support [289]. Thus, the physicochemical properties of nickel metal and support are directly linked to the performance of catalyst. After reduction, the nickel particle on Ni–Mn–ZrO_x catalyst (29 nm) was bigger than that on Ni–ZrO_x catalyst (12 nm), which was attributed to weaker interaction between Ni and support. Thus, Ni–Mn–ZrO_x catalyst exhibited lower activity for DRM reaction. Özkara-Aydınoğlu et al. [119], Luna et al. [275] and Liu et al. [88] also found the Mn promoter could result in a lower activity for DRM. With increasing reaction time, the nickel particle size decreased and the content of surface nickel increased on Ni–Mn–ZrO_x catalyst, while the former increased and the later decreased on Ni–ZrO_x catalyst. Simultaneously, the activity increased on Ni–Mn–ZrO_x catalyst, while decreased on Ni–ZrO_x catalyst. It implied that small particle and higher surface nickel content could enhance the activity for DRM. In this work, this promotion during the reaction might be ascribed to more stable Zr species on Ni–Mn–ZrO_x catalyst. According to the XPS, the Zr species on Ni–ZrO_x catalyst was reduced at the whole process and part of Zr species even reduced to Zr^{1+} after reaction for 480 min. This un-stable structure of ZrO_2 might be led to the loss and sintering of nickel species on Ni–ZrO_x catalyst. Whereas on Ni–Mn–ZrO_x catalyst, the Zr species were almost no change. The ZrO_2 modified by Mn could keep the structure during the reaction. Besides, the Mn promoter could increase dispersion during the reaction. Yao et al. [121] and Seok et al. [274] thought that Mn could enhance the dispersion of nickel. Generally, Mn promoter could reduce the carbon deposition [88, 119, 121]. Whereas, it increased the carbon after adding Mn since the large particle size of nickel. Besides, the activity increased on Ni–Mn–ZrO_x catalyst, resulting in more carbon deposition. The CO_2 conversion was lower than CH_4 conversion. Thus, the rate of carbon elimination was less than the rate of carbon accumulation, thereby led to more coke on Ni–Mn–ZrO_x catalyst and further formed the carbon nanotubes. This might be attributed to the weaker adsorption of CO_2.

5.4.8 Summary

The DRM activity test was carried out at 700 °C for 8 hours, with a GSHV of 48,000 h^{-1}. In this work, we clearly showed on Ni/ZrO_2 catalysts that the presence of Mn enhanced the percentage of surface metallic nickel and led to a redistribution of the Ni^0 species during the reaction, leading to a decrease in nickel particle size, which might be assigned to the more stable structure of ZrO_2 species. Furthermore, the catalytic activity increased with time on stream. Whereas for Ni-Zr catalyst, because Zr species were reduced to Zr^{2+} with time on stream, the content of surface Ni° decreased and the Ni° particle size increased, exhibiting a decrease of DRM activity in the first 100 min reaction. Thus, the structure of ZrO_2 might play a key role in active sites for dry reforming of methane, enhancing the performance of ZrO_2 catalyst.

Chapter VI

Discussion on the promotion of Nickel Zirconia based catalysts

6. Discussion on the promotion of Nickel Zirconia based catalysts

6.1 Introduction

Generally, promoters could enhance the activity of nickel-based catalyst via following mechanisms: i) promoters could increase the basic site, which could promote the adsorption and/or activation of CO_2; ii) promoter could enhance the dispersion of nickel particles; iii) promoters could increase the reduction of nickel oxide; iiii) promoters could promote the formation of oxygen vacancies [65, 96, 135, 137, 146, 230]. Jang et al. [122] prepared Ni-$Ce_{0.8}Zr_{0.2}O_2$ catalysts modified by Metal oxide (MgO, CaO, and La_2O_3). The MgO promoted catalyst exhibited the highest activity and stability for DRM reaction, because of strong basicity of MgO, small Ni metal crystallite size, and an intimate interaction between Ni and MgO. Pompeo [290] investigated the influence of supports α-Al_2O_3, ZrO_2 and α-Al_2O_3-ZrO_2 on performance of catalysts. Found that Ni/α-Al_2O_3-ZrO_2 showed higher stable for 700 ^oC DRM reaction, due to the lower coke formation on Ni/α-Al_2O_3-ZrO_2 catalyst. Because the ZrO_2 could decrease the carbon deposition and increase the CO_2 adsorption. Świrk et al. [117] reported Ni-based double-layered hydroxides modified by Yttrium. 1.5 wt% Y-promoted catalyst exhibited the highest activity, selectivity and stability for 700 ^oC DRM reaction. The conversion of CH_4 and CO_2, and the ratio of H_2/CO were 78.6 %, 74.4 % and 0.925, respectively. After reaction for 10 h, they were 77.8 %, 73.3 % and 0.92 for the conversion of CH_4 and CO_2, and the ratio of H_2/CO , respectively. While for other two catalyst, the initial conversions of CH_4 on 0.6 wt% Y-promoted and non-promoted catalysts were 78.1 % and 75.7 %, respectively. After reaction for 10 h, the conversion of CH_4 was 74.3 % and 72.1 % on 0.6 wt% Y-promoted and non-promoted catalysts, respetively. Because higher specific surface area, smaller Ni crystallite size, and higher distribution of weak and medium basic sites formed on 1.5 wt% Y-promoted catalyst, as compared to Y-free catalyst. Kumar et al. [149] found that the 5% Ni/$Ce_{0.6}Zr_{0.2}O_2$

(CTAB) catalyst showed higher activity at 650 °C and 700 °C than Ni/CeO_2 or Ni/ZrO_2. The conversion of CH_4 after 70 h was above 68% at 700 °C. Kumar et al. suggested that the nickel particle was smaller on $Ce_xZr_{1-x}O_2$ support than that on CeO_2 or ZrO_2 support, due to the interaction of the nickel and support, and the enhanced nickel dispersion. $Ce_xZr_{1-x}O_2$ support also possessed defect structure due to the formation of the solid solution and the high oxygen mobility, which led to celerity oxidoreduction ability by releasing and getting oxygen rapidly. Wang et al. [273] investigated Mn doping nanocrystalline Co–Ce–Zr–O_x catalysts for DRM reaction. The conversions of CO_2 and CH_4 were74 % and 70 %, respectively. While the conversions of CO_2 and CH_4 were both lower 40 % on non-promoted nanocrystalline Co–Ce–Zr–O_x catalyst. The promoted activity was attributed to the increasing availability of surface oxygen species and the better oxygen mobility on Mn-modified catalyst, as well as the better dispersed nano-sized Co_3O_4. Bellido et al. [147] prepared nickel supported on ZrO_2 stabilized with various content of Y_2O_3. The $Ni/8Y_2O_3–ZrO_2$ (with a Y_2O_3 load of 8 mol%) catalyst showed the best catalytic performance for DRM reaction. The initial conversions of methane on $Ni/12Y_2O_3–ZrO_2$ $Ni/8Y_2O_3–ZrO_2$ $Ni/4Y_2O_3–ZrO_2$ and Ni/ZrO_2 at 800 °C were about 72 %, 82 %, 45 % and 13 %, respectively. The author found the interaction between the surface oxygen vacancies and nickel species on the $Y_2O_3–ZrO_2$ support enhanced by the increasing Y_2O_3 load, which could improve the CH_4 and CO_2 conversion in the dry reforming reaction. Besides, the surface oxygen vacancies could promote the elimination of coke, because the surface oxygen vacancies could induce oxygen radicals from the CO_2 to react with carbon deposition.

Herein, we prepared Ni-Zr materials by promoted metal (Y, Mg, Al and Mn) to apply to the dry reforming of methane. To understand the relationship between the modified structure and the promoter metal, H_2-TPR, CO_2-TPD, TEM, XPS, Raman and TGA was conducted. Meanwhile, we compared the catalytic performance of catalysts modified by the several metal.

6.2 The preparation of a series of promoted Ni-Zr catalysts

A certain amount of pluronic P123 amphiphilic block copolymer, nickel (II) nitrate hexahydrate, zirconium (IV) oxynitrate hydrate, urea, and aluminum isopropoxide (or Manganese (II) nitrate tetrahydrate or yttrium (III) nitrate hexahydrate or magnesium acetate tetrahydrate) were dissolved in distilled water. The molar ratio of Ni, Al, Y, Zr, Mg and Mn was listed in Table 6-1. The obtained suspension was heated from room temperature to 95 °C under vigorous stirring for 48 h. And then this suspension was subsequently aged at 100 °C for 24 h. Next, this suspension was filtered and washed with a little distilled water, and dried at room temperature. Finally, the obtained precursor was calcined at 800 °C for 5 h with an increasing rate of 1 °C/min under airflow. The obtained catalysts were denoted as Ni–Zr, Ni–Zr–Al, Ni–Zr–Mn, Ni–Zr–Y and Ni–Zr–Mg respectively.

Table 6-1 The dosage of Ni, Al, Y, Zr, Mg and Mn on a series of promoted Ni-Zr materials

Catalyst	Ni %	Zr %	Al %	Mn %	Y %	Mg %
Ni–Zr	10	80	-	-	-	-
Ni–Zr–Al	10	80	10	-	-	-
Ni–Zr–Mn	10	80	-	10	-	-
Ni–Zr–Y	10	80	-	-	10	-
Ni–Zr–Mg	10	80	-	-	-	10

6.3 The physicochemical features on a series of promoted Ni-Zr catalysts

6.3.1 The reducibility of a series of promoted Ni-Zr catalysts

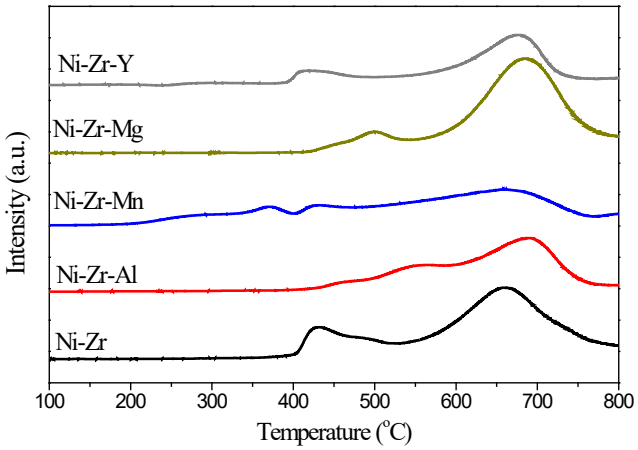

Figure 6-1 the H_2-TPR profiles of Ni-Zr catalysts with different metal promoters.

The reducibility of catalysts was carried out by the H_2-TPR experiment, as shown in Figure 6-1. Two peaks at about 430 and 670 °C were observed clearly on Ni-Zr catalyst. Both peaks shifted to higher temperature area on Ni-Zr-Mg and Ni-Zr-Al catalysts. It implied that the Mg and Al promoter could enhance the interaction between nickel and support. The stronger interaction might inhibit the sintering of catalysts. Jang [122] found that the formation of MgO-NiO solid solution could enhance the interaction between Ni and Mg, thereby inhibition of catalyst sintering under the condition of the DRM reaction, and further promote the stability of Mg-modified catalyst. It was worth noting that a broad peak formed on Ni-Zr-Mn catalyst, which might result from the multistep reduction of Mn oxides ($MnO_2 \rightarrow Mn_2O_3 \rightarrow Mn_3O_4 \rightarrow Mn^{2+}$) [88]. On the whole, the reduction peak on Ni-Zr-Mn catalyst shifted to low temperature area, as compared with the Ni-Zr catalyst. This phenomenon manifested that the Mn promoter weakened the interaction between the nickel and the support, which might result in the sintering of nickel on Ni-Zr-Mn catalyst. While almost no changes observed on Y-promoted catalyst.

6.3.2 Texture properties of a series of promoted Ni-Zr catalysts

Table 6-2 The results of BET experiment for Ni-Zr catalysts with different metal promoters.

Catalyst	D_p nm	V_p cm^3/g	S_{BET} m^2/g
Ni-Zr	1.9 [a]	0.20 [b]	113 [c]
Ni-Zr-Al	6.1	0.25	82
Ni-Zr-Mn	1.6	0.12	103
Ni-Zr-Mg	1.6	0.10	90
Ni-Zr-Y	1.9	0.09	79

a: The pore diameter (D_P) determined by BJH method
b: The pore volume (V_P) determined by BJH method
c: The specific surface area (S_{BET}) determined by the BET method

The physical properties of catalyst were evaluated from the N_2 adsorption isotherms acquired at -196 °C. The special surface area, the pore diameter and the pore volume on Ni-Zr catalysts listed in Table 6-2. Obviously, the Ni-Zr catalyst exhibited the highest specific surface area of about 113 m^2/g. Generally, higher specific surface area could contribute to the distribution of nickel species, which might increase the dispersion of nickel [213, 253]. Talkhoncheh et al. [253] found that Ni/Al_2O_3 nanocatalyst exhibited the highest conversions (93% and 96% for CH_4 and CO_2 at 850 °C) and yields (90% and 93% for H_2 and CO), as compared with nickel supported on clinoptilolite or CeO_2 support. Ni/Al_2O_3 nanocatalyst showed the best performance due to its high specific surface area, homogenous distributions and good dispersion of Ni. The author thought that the high specific surface area could not only improve the NiO dispersion, but also increase the availability of reactant molecules and further improve the activity of the catalyst. Besides, the Ni-Zr-Al catalyst illustrated the highest pore diameter (6.1 nm) and pore volume (0.25 cm^3/g). It implied that the promoter Al could modify the pore structure of ZrO_2. While the introduction of other promoters (Mn, Y or Mg) led a decrease of the special surface area, the pore diameter and the pore volume on Ni-Zr catalysts. Those opposite effects might lead to a decrease of catalytic performance of catalyst for DRM.

6.3.3 Basicity of a series of promoted Ni-Zr catalysts

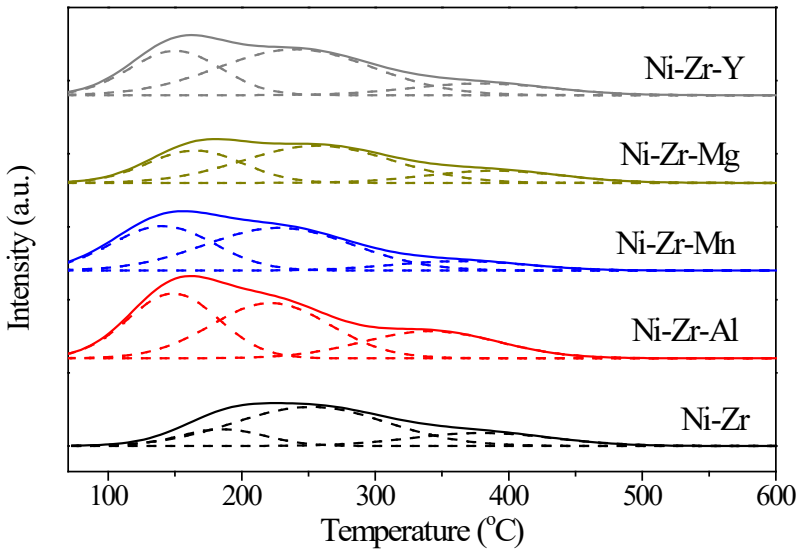

Figure 6-2 The CO_2-TPD profiles of Ni-Zr catalysts with different metal promoters

The basicity of Ni-Zr catalysts was measured by CO_2-TPD, as presented in Figure 6-2. All Ni-Zr catalysts have three typical CO_2 desorption peaks ranging from 100 to 600 °C. On one hand, the peaks on promoted Ni-Zr catalysts shifted to low temperature area compared to non-promoted Ni-Zr catalyst. It implied that the promoter could decrease the basicity of Ni-Zr catalyst. On the other hand, the amount of basic sites varies differently by addition of the second metal. According to the table 6-2, the basic sites increased from 73 μmol CO_2/g to 102, 92 and 100 μmol CO_2/g on Ni-Zr catalysts modified by Al, Mn and Y, respectively. However, the introduction of basic oxide metal Mg resulted in a decrease of basic sites on Ni-Zr-Mg catalyst. It decreased to 69 μmol CO_2/g. García et al. [226] found the amount of basic sites over ZrO_2–2.3wt.%MgO support (4.3 μmol CO_2/m^2) was higher than those on ZrO_2 support (1.0 μmol CO_2/m^2). Similar results over magnesia–zirconia oxides were reported by Aramendía et al [291]. It is known that the addition of basic promoters favors CO_2 adsorption and its dissociation, which contributes to gasify the carbonaceous deposits and to decrease the deactivation by coke formation [114, 116, 226]. Therefore, the decrease of basic sites on Ni-Zr-Mg catalyst might cause the carbon deposition.

We had explained in the chapter 4.4.3. The peak was dissociated into three peaks. Peak

1, 2 and 3 are the weak basic site, medium-strength basic sites and strong basic sites, which are mainly consisted of weak Brønsted basic sites such as surface OH groups, Lewis base sites such as unsaturated (cus) O^{2-} and Zr^{4+}–O^{2-} centers, and the CO_2 adsorption of the cus Zr^{4+} centers with strong Lewis acidity, respectively [72, 114]. The position and content of peaks are listed in Table 6-3. The position of peaks on the Ni-Zr catalyst is located at 180, 252 and 380 °C, respectively. Most of peaks on promoted catalysts shifts to low temperature. Especially, the existence of Al decreases the centers of peak 1, 2 and 3 by 36, 30 and 39 °C, respectively. The addition of Mn and Y mainly shifts the weak and medium-strength basic sites. Mg-promoted catalyst slightly changes the weak and strong basicity, and the variations are about -20 and -10 °C. Besides, the content of each peak is different on non-promoted and promoted catalysts. For Ni-Zr catalyst, it is about 15.5, 64.4 and 20.1 % for weak, medium-strength and strong basic sites, respectively. The content of weak basic sites on all the promoted catalyst increases to equal to or greater than 30 % compared to Ni-Zr catalyst. The introduction of Mn, Y and Mg lead to a decrease in the amount of CO_2 on strong basic sites compared to non-promoted catalysts. While it slightly increases on Ni-Zr-Al catalyst, which might give rise to coke. Because the weak and medium-strength basic sites could promote the adsorption and/or activation of CO_2, and further reduce the carbon deposition, as well as the deactivation of catalyst. [5, 89, 245].

Table 6-3 the CO_2-TPD data of Ni-Zr catalysts with different metal promoters

	CO_2 desorbed (%)						Total basicity μmol CO_2/g
	Peak 1 weak		Peak 2 medium-strength		Peak 3 strong		
Catalysts	Position	Content	Position	Content	Position	Content	
Ni-Zr	185	15.5	252	64.4	380	20.1	73
Ni-Zr-Al	149	31.6	222	40.6	341	22.5	102
Ni-Zr-Mn	141	30.0	228	51.9	389	10.6	92
Ni-Zr-Mg	165	37.5	256	53.9	370	16.1	69
Ni-Zr-Y	150	36.9	240	55.4	380	13.0	100

6.3.4 XRD analysis of a series of promoted Ni-Zr catalysts

The XRD patterns of calcined and reduced promoted Ni-Zr based catalysts are shown in Figure 6-3. The formation NiO-ZrO_2 solid solution on Ni-Zr catalyst results in a shift to higher Bragg angles in ZrO_2 peaks, like a peak at 2θ = 30.65 °, which shifts from 2θ = 30.14 °, as is explained in detail in Chapter 4.3.2. This movement is getting smaller on all of the promoted catalyst, especially Al-promoted catalyst. It just shifts by 0.1 °. It means that those promoters decrease the formation of NiO-ZrO_2 solid solution. While after reduction, this peak on all the catalysts is located at 30.40 °.

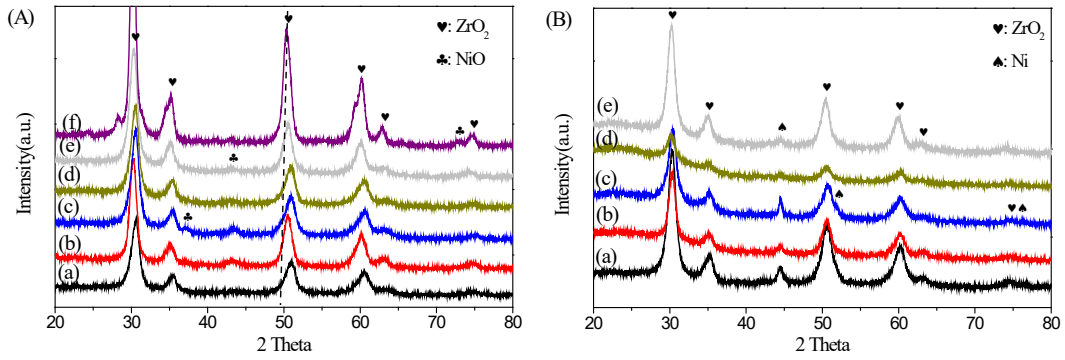

Figure 6-3 XRD profiles of (a) Ni-Zr, (b) Ni-Zr-Al, (c) Ni-Zr-Mn, (d) Ni-Zr-Mg and (e) Ni-Zr-Y catalysts, and (f) ZrO_2 (A), after reduction (B) at 700 °C for 1 hour.

The crystalline sizes of ZrO_2, NiO and Ni^0 species on promoted Ni-Zr based catalysts are calculated by the Scherrer Equation and the results are listed in Table 6-4. The size of ZrO_2 on most calcined catalysts is 7 nm and even on reduced catalysts. While the existence of Al increases the size of ZrO_2 to 8 nm for calcined catalyst and to 9 nm for reduced catalyst. It implies that the structure of ZrO_2 might be changed by the introduction of Al. This change might decrease the crystalline sizes of NiO, since Ni-Zr-Al catalyst has the smallest sizes of NiO (7 nm). Ni-Zr-Mg catalyst exhibits the biggest sizes of NiO (12 nm). Besides, NiO peaks disappear on all the reduced catalysts, indicating that the nickel species have been reduced on all the reduced catalysts. After reduction, Ni-Zr and Ni-Zr-Al have the same crystalline sizes of Ni^0, about 12 nm. For Ni-Zr and Ni-Zr-Al catalysts, the lower Ni particle sizes might contribute to its higher

catalytic performance. Similar results have also been reported by He et al [292]. While it increases to 29, 20 and 16 on Ni-Zr-Mn, Ni-Zr-Y and Ni-Zr-Mg catalysts, respectively. Those relatively large sizes of crystal nickel metal can lead to carbon deposition [50, 237, 238].

Table 6-4 Crystalline sizes of Ni-Zr, Ni-Zr-Al, Ni-Zr-Mn, Ni-Zr-Mg and Ni-Zr-Y catalysts, after reduction at 700 °C for 1 hour and after reaction at 700 °C for 8 hours

	ZrO_2			NiO	Ni^0	
Catalyst	Calcined	Reduction	Reaction	Calcined	Reduction	Reaction
Ni-Zr	7	7	7	10	12	24
Ni-Zr-Al	8	9	8	7	12	11
Ni-Zr-Mn	7	7	9	10	29	24
Ni-Zr-Mg	7	8	7	12	20	17
Ni-Zr-Y	7	7	7	10	16	10

6.3.5 XPS analysis of a series of promoted Ni-Zr catalysts

Table 6-5 presents the surface content of element on a series of promoted Ni-Zr catalysts after reduction. For the Ni-Zr catalyst, the content of Zr, Ni and O is about 22.5 %, 5.6 and 71.9 %, respectively. For promoted Ni-Zr catalysts, the content of Zr species decreases slightly. One observation can be note that the surface nickel content on Y and Mg promoted catalysts decreases to 3.4 % and 5.0 %, respectively, compared to the Ni-Zr catalyst. Yao et al. [120] reported that the relatively high content of surface Ni species might contribute to the activity of ZrO_x/Ni-MnO_x/SiO_2 catalyst reduced at 550 °C for DRM. Therefore, the decrease of surface content of nickel species might result in a lower catalytic performance for DRM. Especially, Y-modified catalysts exhibit the lowest surface content of nickel species, which is reduced by 1.2 %. The existence of Mn results in almost no change in the surface content of nickel species. It just decreases by 0.1 %. It's worth noting that the addition of Al increases slightly the surface content of nickel species, which might enhance the activity for DRM. The dosages of nickel and promoters are 10 % (table 6-1), while the surface content of nickel

and most promoter is about 5 %. It implies that parts of nickel and promoters exist inside the catalysts, which might form the solid solutions, such as NiO-ZrO_2, Y_2O_3-ZrO_2 [50]. The solid solutions are explained in detail in Chapter 4.3. Meanwhile, the surface content of Mg species is 13.5 %, which is above 10 %. This phenomenon indicates that the most of Mg species form on the surface, resulting in a decrease of surface content of nickel species.

Table 6-5 The content of element on the surface of non-promoted and promoted catalysts, determined by XPS.

	Zr %	Ni %	O %	Al %	Mn %	Y %	Mg %
Ni-Zr	22.5	5.6	71.9				
Ni-Zr-Al	19.2	5.8	68.9	6.1			
Ni-Zr-Mn	18.1	5.5	71.7		4.7		
Ni-Zr-Y	17.8	3.4	74.2			4.6	
Ni-Zr-Mg	18.7	5.0	62.8				13.5

6.4 The catalytic performance on a series of promoted Ni-Zr catalysts

6.4.1 The activity test on a series of promoted Ni-Zr catalysts in literatures

Table 6-6 summarized the catalytic performance of ZrO_2 supported nickel catalysts modified by various promoters for DRM reaction. Generally, promoters are classified into two types: textural (structural) and chemical (electronic) [293]. Textural promoters enhance the textural properties of the catalysts. Mn [273] and Cu [294] promoted the dispersion of the nano-sized CoO_x crystallites and NiO species, respectively. The conversion of CO_2 and CH_4 at 700 ºC increase from 36 % and 25 % to 74 and 70 %, respectively by the introduction of Mn. At the same time, the ratio of H_2/CO increases from 0.6 to 1 [273]. On the contrary, although the good Ni dispersion, a slight decrease of activity observed on Cu-promoted catalyst. The conversion of CH_4 decreases from 100 % to 90 % at 750 ºC DRM [294]. Chemical promoters provide new active sites or enhance the chemical property relating to the reactivity of the catalysts such as basicity or redox property [295]. The introduction of MgO could enhance the reducibility of Ni species and the interaction between Ni and support [226]. Besides, MgO [122, 226] and CaO [224] could increase basic property of catalysts, which improved the chemisorption of CO_2 and promoted the gasification of deposited coke on the catalysts, and further enhance the stability of the catalysts. Mg-promoted Ni-$Ce_{0.8}Zr_{0.2}O_2$ catalyst exhibits higher stability for 800 ºC DRM without deactivation even after reaction for 40 h, while the activity of non-promoted Ni-$Ce_{0.8}Zr_{0.2}O_2$ catalyst decreases over 40 h on stream with the rate of 0.43 %·h^{-1} [122]. In addition, the formation of oxygen vacancies promotes removal of the coke deposited on the nickel surface, and further enhance the stability of catalysts, reported by Asencios [146]. The author also observed that the CH_4 conversion on Y-promoted catalyst decreased with the rate of 1.3 %·h^{-1} at 750 ºC, while it decreased with the rate of 1.8 %·h^{-1} on non-promoted catalyst. The

calcium oxide phase easily carbonated by CO_2 acts as a continuous supplier of gaseous CO and active oxygen species which react with the surface carbon arising from the methane cracking. Thus, the non-promoted Ni/ZrO_2-La_2O_3 catalyst is deactivated within 6 h reaction, while the conversion of CH_4 on Ca-modified Ni/ZrO_2-La_2O_3 catalyst decreases with the rate of 5.2 %·h^{-1} over 14 h DRM reaction [296].

Table 6-6 the property of the different catalysts at various temperature

Catalysts	T (°C) Reduction/ Reaction	Reactant ($ml.g^{-1}.h^{-1}$)	Conversion % CH_4	Conversion % CO_2	Ratio H_2/CO	Time h	Lost [a] %·h^{-1}	Ref.
8%Ni/Zr	800/750	120000 CH_4:CO_2:He=3:2:5	~50	~79	0.93	28	~1-2	[118]
8%Ni/LaZr			~52	~78	0.91			
8%Ni/CeZr			~55	~67	0.97			
15%Ni-CeO_2	700/800	100800 CH_4:CO_2:N_2=1:1.04:1	>97		0.97	100	S	[297]
15%Ni-ZrO_2							S	
15%Ni-Ce-ZrO_2						95	0.042	
10%Ni/CeO_2			nd					
10%Ni/ZrO_2			nd			2		
10%Ni/Ce-ZrO_2			80				32.5	
Ni/a-Al_2O_3	327/550	12320 CH_4:CO_2=1:1	8.4	34.7		7	4.08	[140]
Ni/CeO_2			11.7	29.7			D	
Ni/La_2O_3			4.4	24.3			D	
Ni/ZrO_2			10.4	30.6			1.10	
Ni-CaO-ZrO_2	700/700	96000 CH_4:CO_2=1:1	~30	~52	~0.53	>35	S	[298]
Ni-CaO-ZrO_2-NaOH			~72	~85	~0.91			
Ni/CaO-ZrO_2			~60	~73	~0.80			
0.2Ni-0.2CaO-ZrO_2	700/700	12000 CH_4:CO_2:N_2=1:1:3	~87.5				S	[224]
0.2Ni-0.5CaO-ZrO_2			~86	80			~0.15	
0.2Ni-ZrO_2			~85.5	73			~0.29	
0.1Ni-0.2CaO-ZrO_2			~87	81			~0.14	
0.5Ni-0.2CaO-ZrO_2			~86	73			~30	
Ce-Zr-$Ni_{0.49}$	750/750	30000 CH_4:CO_2:N_2=1:1:8		~80		25	0.8	[299]
Ce-Zr-$Ni_{0.49}$-$Co_{0.29}$				~80		17	2.53	
Ce-Zr-$Ni_{0.49}$-$Fe_{0.23}$				~50		2	29.5	
Ce-Zr-$Ni_{0.49}$-$Rh_{0.03}$				~90		150	0.13	
$NiCeO_2ZrO_2MgAl_2O_4$	670/670	40000 CH_4:CO_2=1:1	~54			5	0.15	[300]
$Ni/Ce_{0.2}Zr_{0.1}Al_{0.7}O$	750/750		~100		4.8			[294]
$Ni/Fe_{0.05}Ce_{0.2}Zr_{0.1}Al_{0.65}O$			~88		3.5			
$Ni/Co_{0.05}Ce_{0.2}Zr_{0.1}Al_{0.65}O$			~90		3.8			
$Ni/Cu_{0.05}Ce_{0.2}Zr_{0.1}Al_{0.65}O$			~90		4.8			
10%Ni/ZrO_2	500/600	240000 CH_4:CO_2:He=1:1:2	34	33		5	0.08	[226]
10%Ni/ZrO_2-0.4Mg			27	34			S	
Ni-Mo/MgAl	800/800	60000 CH_4:CO_2=1:1	~94	~95.5	~0.95	24	S	[301]
Ni-Mo/5%CeZr-MgAl			~96	~96	~0.93		~1.48	
Ni-Mo/10%CeZr-MgAl			~97	~96	~0.95		~2.10	
Ni-Mo/15%CeZr-MgAl			~96	~94.5	~0.94		~1.43	
Ni-Mo/20%CeZr-MgAl			~94	~94.5	~0.95		~0.04	

5%Ni/8%Y_2O_3-ZrO_2	750/800	360000 CH_4:CO_2=1:1	~81	~82	0.7	6	~2.29	[147]
5%Ni/ ZrO_2			~11	~10				
10%Ni-MgO-$Ce_{0.8}Zr_{0.2}O_2$	800/800	480000 CH_4:CO_2:N_2=1:1:3	95	96	0.97	200	S	[302]
10%Ni-$Ce_{0.8}Zr_{0.2}O_2$			93	93	0.97	40	0.46	
Ni/$CeZrO_2$/Al_2O_3	750/800	24000 CH_4:CO_2 =1:1	~70	~75	0.85	24		[303]
Ni/Al					0.86			
Ni(10)CeO_2(5) /$MgAl_2O_4$	960/670	CH_4:CO_2 =1:1	80	87	0.89	8	D	[264]
Ni(10)CeO_2(4.8) ZrO_2(0.6)/$MgAl_2O_4$			68	76	0.73	25	S	
Co-Ce-Zr-O_x	700/700	36000 CH_4:CO_2 =1:1	25	36	0.60	20	S	[273]
Co-Ce-Zr-Mn-O_x			70	74	1			
Ni-$Ce_{0.8}Zr_{0.2}O_2$	800/800	480000 CH_4:CO_2:N_2=1:1:3	92	93	0.96	40	0.43	[122]
Ni-MgO-$Ce_{0.8}Zr_{0.2}O_2$			95	96	0.97		S	
Ni-CaO-$Ce_{0.8}Zr_{0.2}O_2$			98	98	0.98		0.33	
Ni-La_2O_3-$Ce_{0.8}Zr_{0.2}O_2$			94	96	0.97		0.43	
Ni-Co/0.1MgO-0.9ZrO_2	750/750	125000 CH_4:CO_2 =1:1	75	80	0.97	40	S	[304]
Ni/0.1MgO-0.9ZrO_2			75	80	0.88		0.17	
Co/0.1MgO-0.9ZrO_2			78	78	0.91		0.22	
NiO-Y_2O_3-ZrO_2	800/750	64200 CH_4:CO_2 =1.5:1	~63	~74	0.75	6	~1.3	[146]
NiO-ZrO_2			~35	~57	0.84		~1.8	
NiO-Y_2O_3			~67	~77	0.85		~8.97	
Ni/K-5MgO-2ZrO_2	750/750	CH_4:CO_2:N_2=1:1:8	85			14	S	[305]
Ni/K-2MgO-5ZrO_2			84				0.36	
Ni/K-MgO			85				S	
Ni/K-ZrO_2			10				S	
Ni-Co/Al_2O_3-MgO-ZrO_2	700/850	24000 CH_4:CO_2 =1:1	~99	~99	~1	24	S	[81]
10Ni-CaO-ZrO_2	650/750	48000 CH_4:CO_2 =1:1	~81	~85	~0.91	100	~0.07	
8Ni-MgO-ZrO_2	750/750	CH_4:CO_2:Ar=1:1:8	~90	~90		14	~0.79	[306]
8Ni-K-MgO-ZrO_2			~89	~93			S	
Ni-MgO-$Ce_{0.8}Zr_{0.2}O_2$	800/800	240000 CH_4:CO_2:N_2=1:1:3	96	97	0.97	200	S	[307]
Ni-MgO/$Ce_{0.8}Zr_{0.2}O_2$			~95			10	~1.58	
Ni-CaO/ZrO_2-La_2O_3	500/500	CH_4:CO_2:Ar=1:1:1	~21			14	~5.2	[296]
Ni/ZrO_2-La_2O_3			~18			6	D	

a : lost inactivity, calculated by methane

~: about, read by the figure

S: Stable

D: deactivation

nd: no date

6.4.2 The activity test on a series of promoted Ni-Zr catalysts

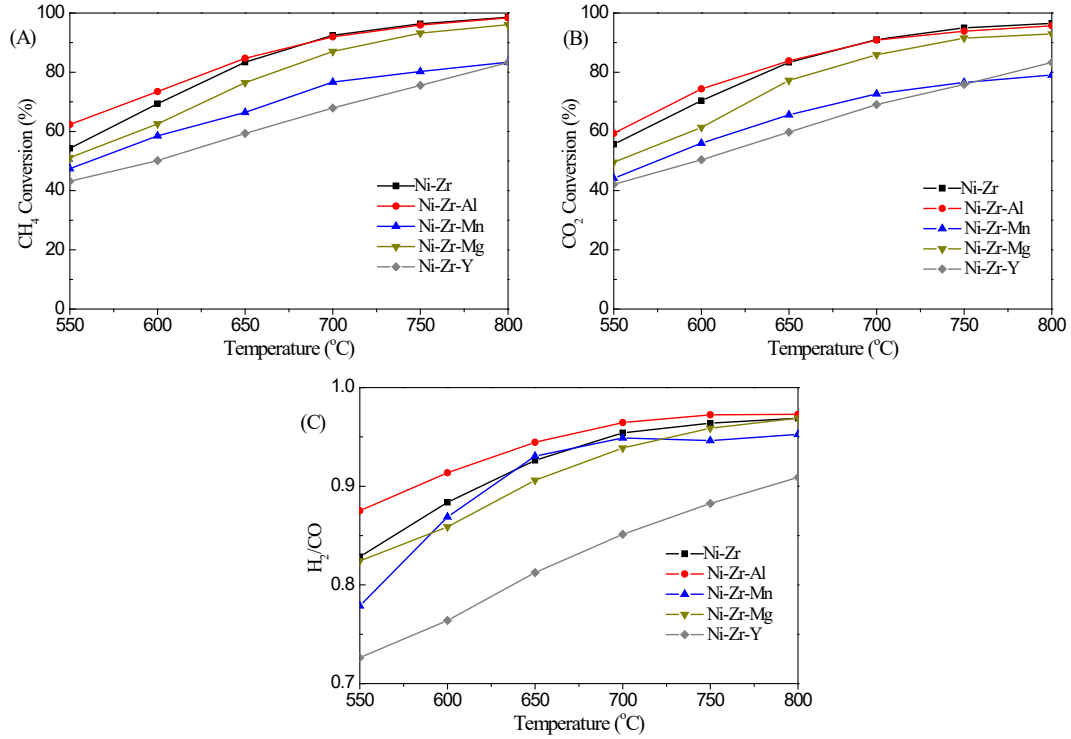

Figure 6-4 The average conversion of CH_4 (A) and CO_2 (B) and the rate of H_2/CO (C) of Ni-Zr-M catalyst (M=Al, Mg, Y, Mn).

The results of activity tests are presented in Figure 6-1, including both conversions of CH_4 and CO_2, and H_2/CO molar ratio for non-promoted/promoted Ni-Zr catalysts, as a function of reaction temperature. CH_4 and CO_2 conversions increase with reaction temperatures, together with H_2/CO molar ratio overall catalysts. When the reaction temperature reaches 700 °C, the conversion of CH_4 and CO_2 for non-promoted and Al-promoted catalysts do not show noticeable difference between them, suggesting that the activity at elevated temperature for these two catalysts displays a more significant dependence on reaction temperature than the catalyst composition. This can be understood considering the strong endothermic nature of the reaction. In the whole temperature process, Ni-Zr-Al catalyst exhibited the highest activity and selectivity for dry reforming of methane. The higher activity observed on Al promoted catalysts can be attributed to its high surface content of nickel species, Ni dispersion and basic sites. Liu et al. [88] and He et al. [292] also reported the introduction of Al results in a low Ni particle sizes, thereby enhance the activity for DRM. While the introduction of Mg,

Y and Mn resulted in a decrease in both CO_2 and CH_4 conversion. Jang [122] found Mg promoted the activity for DRM reaction over Ni-MgO-$Ce_{0.8}Zr_{0.2}O_2$. Because the presence of MgO could enhance in strong resistance against Ni sintering, due to the basic property of MgO and an intimate interaction between Ni and MgO. Herein, the low basic sites on Ni-Zr-Mg catalyst results in a decrease of activity for DRM. The lowest catalytic performance for DRM on Y-promoted catalysts might be ascribed to the lowest surface content of nickel species since the content of the surface Ni species play an important role in the catalytic activity [120]. Except for the surface Ni species and basic sites, the lower specific surface area and larger particle size of nickel metal over Mn, Y and Mg-promoted catalysts also lead to a decrease of activity.

The same trend in the selectivity can be observed on all the catalysts, as is presented in Figure 6-4 (C). All the catalysts showed increasing indicative of selectivity along with the increase of reaction temperature from 550 to 800 °C. The Ni-Zr-Al catalyst is the best catalyst, always delivering higher ratio of H_2/CO than the others in the whole reaction temperature studied. For instance, at a low reaction temperature of 550 °C, the Ni-Zr-Al catalyst delivered a H_2/CO ratio of 0.87, slightly higher than the others (0.83 for Ni-Zr, 0.82 for Ni-Zr-Mg, 0.78 for Ni-Zr-Mn and 0.73 for Ni-Zr-Y). At a high temperature of 800 °C, a very high H_2/CO ratio of 0.972 could be achieved over Ni-Zr-Al catalyst. Same H_2/CO ratio of 0.968 was obtained on both Ni-Zr and Ni-Zr-Mg catalysts. Ni-Zr-Y catalyst also exhibited the lowest of the H_2/CO ratio, about 0.90. Side reactions such as the reverse water-shift reaction (RWGS) and the disproportionation of CO reaction could results in the lower than unity H_2/CO ratio [62, 96, 146]. The disproportionation of CO reaction ($2CO \rightarrow CO_2 + C$, $\Delta H = -172.4\ kJ/mol$) is a highly exothermal reaction [48]. Thermodynamically, the reaction is favored at low temperature and high pressure. Besides, the RWGS reaction is thermodynamically favorable and rapid to reach equilibrium under the reaction temperature between 500 and 700 °C [83, 308]. Thus, both RWGS and disproportionation of CO could give rise to the lower H_2/CO ratio at 550 °C. While at 800 °C, the side reaction is mainly RWGS reaction. It implies that the Y, Mn and Mg promote Ni-Zr catalysts show higher activity

for the reverse water-shift reaction. In contrast, Al-promoted catalyst exhibits lower activity for the RWGS reaction.

6.4.3 Isotherm stability test on the Ni-Zr catalysts

Besides activity and selectivity, stability is also a very important practical consideration for a heterogeneous catalyst. Figure 6-5 presents the 8 h runs experiments for non-promoted and promoted catalysts at 700 ºC. For non-promoted Ni-Zr catalyst, the CH_4 conversion decreases within 60 min, as well as the ratio of H_2/CO. Meanwhile, the CO_2 conversion is higher than that of CH_4 and the H_2/CO ratio is lower than unity during the whole process, indicating the occurrence of side reactions, mainly of RWGS [96, 146]. For Ni-Zr-Al catalyst, higher stability is observed in comparison to Ni-Zr catalyst. Chai et al [260]. reported that the Ni-Al_2O_3/Ni-foam catalyst exhibited an on-stream time of 85 h till the reaction terminated at a CH_4 conversion of ~70%, almost 7 times longer than Ni-ZrO_2/Ni-foam catalyst, since the former had a more stable pore-structure during the reaction condition. It is worth noting that the activity of both CO_2 and CH_4 conversion, and ratio of H_2/CO on Ni-Zr-Mn catalyst increases over the first 300 minutes. And it exceeds the activity of Al-promoted catalyst after reaction for 300 min. Li et al. [281] found Mn could improve the dispersion of nickel and enhance the interaction between nickel and support during the dry reforming of methane. Thus, the catalytic performance of Mn-modified catalyst increases with time on stream. Besides, the CH_4 conversion during the reaction is higher than the CO_2 conversion, which suggests that the introduction of Al and Mn is conducive to the activation of CH_4, similar results were reported by Li et al. [301]. However, Y and Mg promoted catalysts exhibits lower stability for DRM. The CO_2 and CH_4 conversion are slowly decreasing, as well as the ratio of H_2/CO. Besides, the CO_2 conversion is higher than CH_4 conversion. Meanwhile, the ratio of H_2/CO shows a decreasing trend, suggesting that the reverse water-shift reaction is promoted [301].

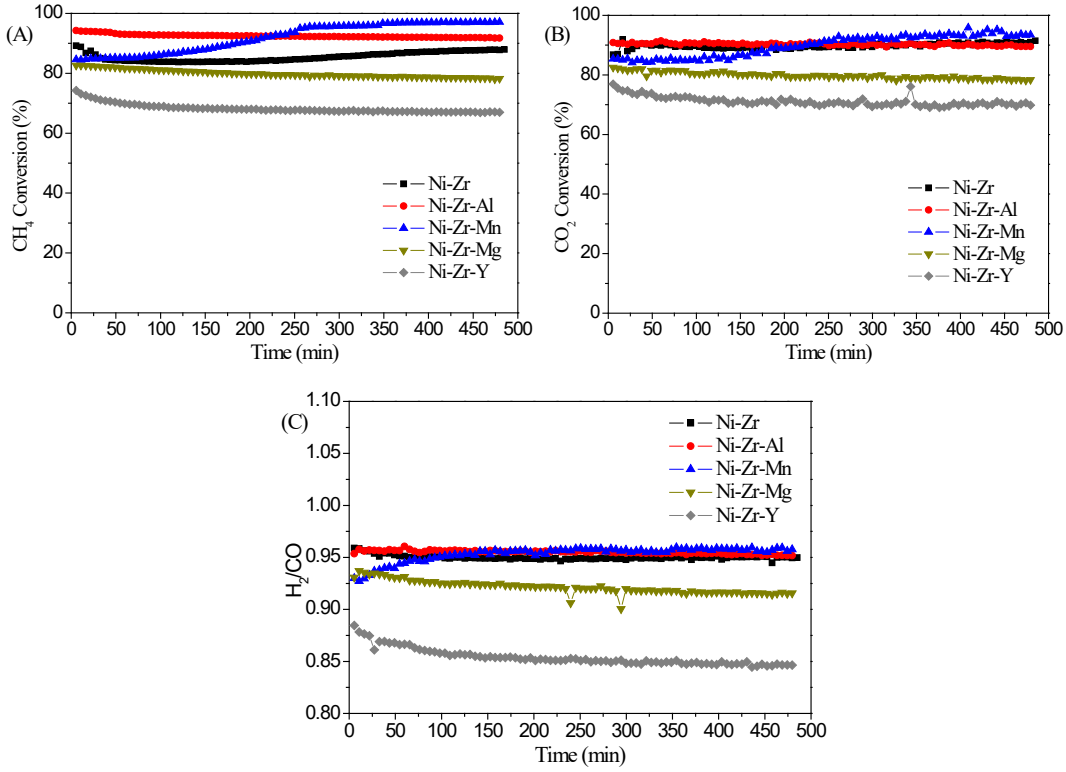

Figure 6-5 The conversion of CH_4 and CO_2, and the rate of H_2/CO of Ni-Zr-M (M=Al, Mg, Y, Mn) catalyst at 700 °C with the mixed flow of CH_4:CO_2:Ar=10:10:80, GSHV=48000 h^{-1}.

6.5 The physicochemical features of Ni-Zr catalysts after runs

6.5.1 XRD analysis of a series of used Ni-Zr catalysts

Figure 6-6 shows XRD patterns of the spent catalysts after 8 h DRM activity tests. The crystallite sizes of the metallic Ni^0 and ZrO_2 are summarized in Table 6-4. Very serious sintering occurred on non-promoted catalyst after DRM tests, and the crystallite Ni^0 sizes increased from 12 nm to 24 nm. While for promoted catalysts, the crystallite Ni^0 sizes on used catalysts are slightly smaller than those on the reduced catalysts, since might be the Ni redispersion upon continuous reduction and oxidation of nickel [50, 309]. Similar phenomenon was reported by Świrk [96]. It implies that the promoted catalysts could suppress the sintering of nickel metal during the DRM reaction. Interestingly, the crystallite Ni^0 sizes on Mn-modified catalyst decreased from 29 nm to 24 nm, at the same time, the activity increased. It means the Ni redispersion might promote the activity for DRM by existence of Mn, which is in agreement with the results reported by Li et al. [281]. While for Al-promoted catalyst, the slight decrease of the crystallite Ni^0 sizes did not affect the activity for DRM. The crystallite Ni^0 sizes on Y and Mg modified catalysts decrease from 16 and 20 nm to 10 and 17 nm, respectively. On the contrary, the activity is decreasing during the 8 h DRM. Those phenomena manifests that the effect of particle size is different for different catalysts.

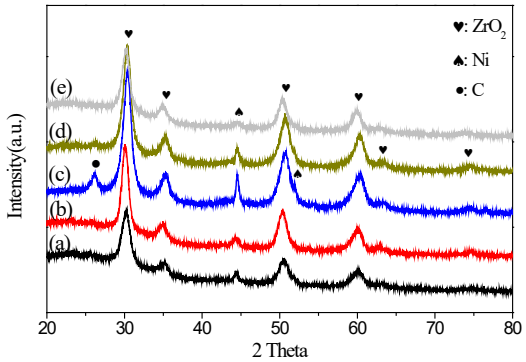

Figure 6-6 XRD profiles of (a) Ni-Zr, (b) Ni-Zr-Al, (c) Ni-Zr-Mn, (d) Ni-Zr-Mg and (e) Ni-Zr-Y catalysts after reaction at 700 °C for 8 hours.

6.5.2 The morphology of carbon deposition on used Ni-Zr catalyst

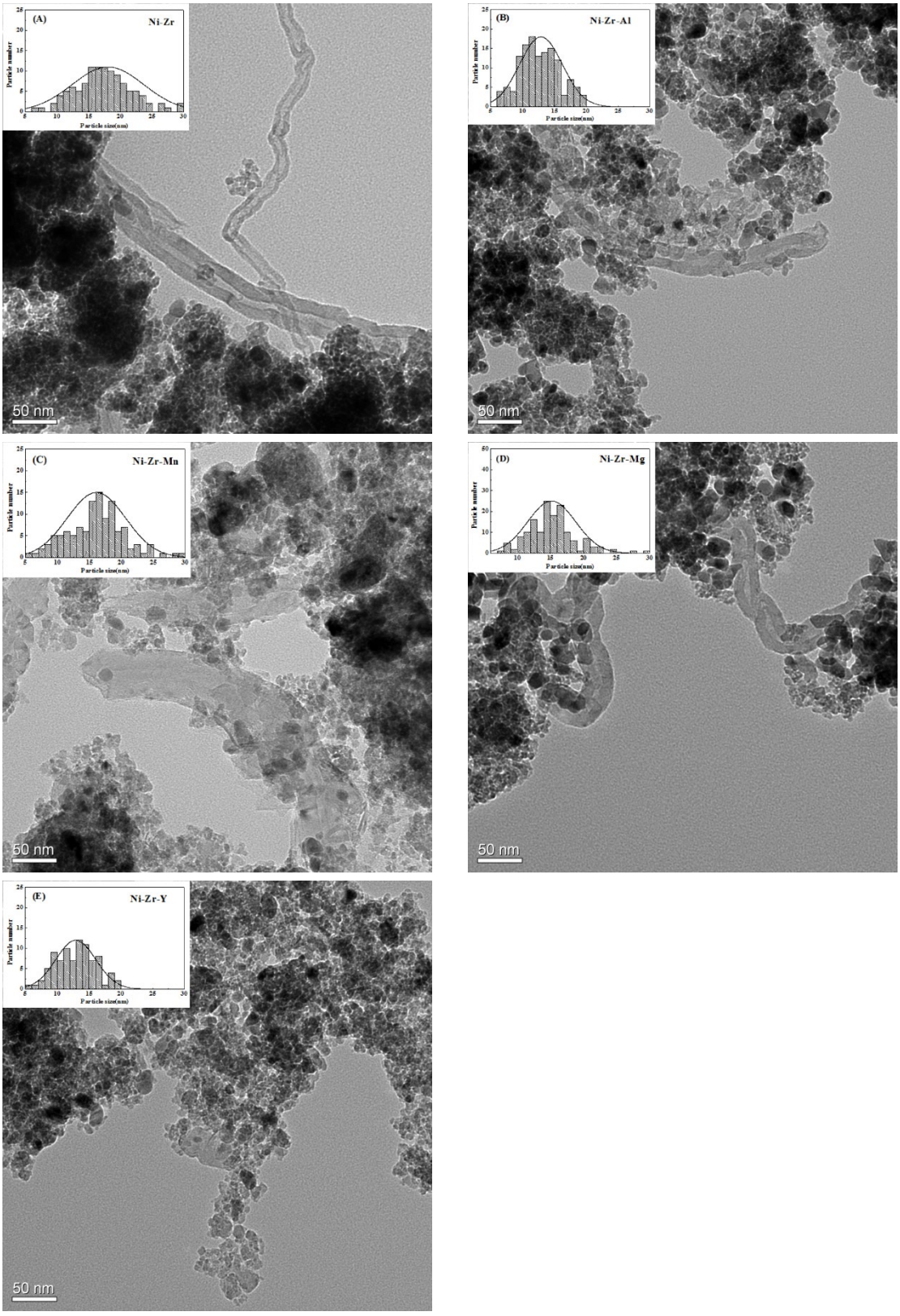

Figure 6-7 The TEM profiles of used catalysts (A) Ni-Zr, (B) NI-Zr-Al, (C) Ni-Zr-Mn, (D) Ni-Zr-Mg and (E) Ni-Zr-Y.

The Figure 6-7 is presented the morphology of used catalysts. It is very clearly observed that large particles form on Ni-Zr and Ni-Zr-Mn catalysts. The nickel particle size distribution on both Ni-Zr and Ni-Zr-Mn catalysts is a wide range from 15 to 20 nm (Table 6-7), which is corresponded to the XRD results. A significant metal sintering occurs on Ni-Zr catalyst during the reaction. While for the Ni-Zr-Mn catalyst, the particle size decrease to the same as Ni-Zr catalyst. Small particles with 15-17 nm can be seen on Mg-modified catalyst. Most notably, nickel particles presented on spent Ni-Zr-Al and Ni-Zr-Y catalysts distribute fairly uniformly, where Ni particle size mostly falls between 10 and 15 nm, with only few large particles almost smaller than 20 nm. On the other hand, carbon accumulation can be observed on spent catalysts. It is very easy to observe the carbon nanotubes formed on used Ni-Zr, Ni-Zr-Mn and Ni-Zr-Mg catalysts. While few carbon nanotubes are presented on spend Ni-Zr-Al catalyst. In addition, we note that no coke is formed on Ni-Zr-Y catalyst.

6.5.3 The content of carbon on used Ni-Zr catalysts

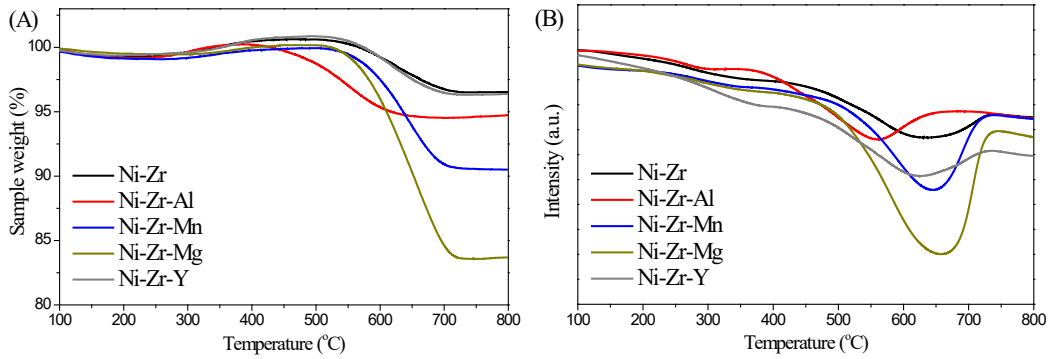

Figure 6-8 The TGA profiles of used catalysts (A) TG and (B) DSC.

The amount of carbon deposition was studied by TC-DCS experiments, as shown in Figure 6-8 and Table 6-7. It could be found that the introduction of Mg, Mn and Al promotes, the carbon deposition for Ni-Zr catalysts increases to 9.5 % and 5.3 %, respectively. While Y-promoted catalyst (3.6 %) exhibits a slightly lower amount of carbon deposition than those obtained by Ni-Zr catalyst (3.7 %). From the Figure 6-8

(B), all the DSC curve, all the peaks indicate this is the endothermic reaction, which is corresponded to the removal of coke. One can be observed a slight deactivation (Ni-Zr-Mg) mainly due to carbon deposition (16.3 %) that is the highest content on used catalyst. Generally, large nickel particle size maybe lead to carbon deposition [237, 238]. Besides, the low basic sites also affect the carbon deposition [88, 135]. For Ni-Zr-Mg catalyst, both large nickel and low basic sites result in the carbon deposition. It has been also found that the addition of these basic oxides reduces not only the formation of coke but also the rate of the reforming reaction [310], therefore, the Ni-Zr-Mg exhibits higher carbon deposition and lower activity for DRM. While for Al-promoted catalyst, the initial carbon removal temperatures (the initial decrease of sample weight) shifts to low temperature as compared to the non-promoted Ni-Zr catalyst. It means the carbon deposition on Al-promoted catalyst is easier to be removed. Thus, the coke about 5.3 % is not effect on activity of Al-modified catalyst for DRM. More amount of weak and medium-strong basic sites formed on catalyst by the addition of Y, therefore enhanced the ability for carbon removal. Since the weak and medium-strength basic sites could promote the adsorption and/or activation of CO_2, and further reduce the carbon deposition [5, 89, 245].

Table 6-7 The amount of carbon deposition on used catalysts.

Catalyst	Coke (%)	Particle size (nm) [a]	I_G/I_D [b]
Ni-Zr	3.7	15-20	1.7
Ni-Zr-Al	5.3	10-15	1.3
Ni-Zr-Mn	9.5	15-20	2.0
Ni-Zr-Mg	16.3	15-17	1.8
Ni-Zr-Y	3.6	10-15	-

a: The particle size of nickel species, determined by TEM

6.5.4 The type of carbon on used Ni-Zr catalysts

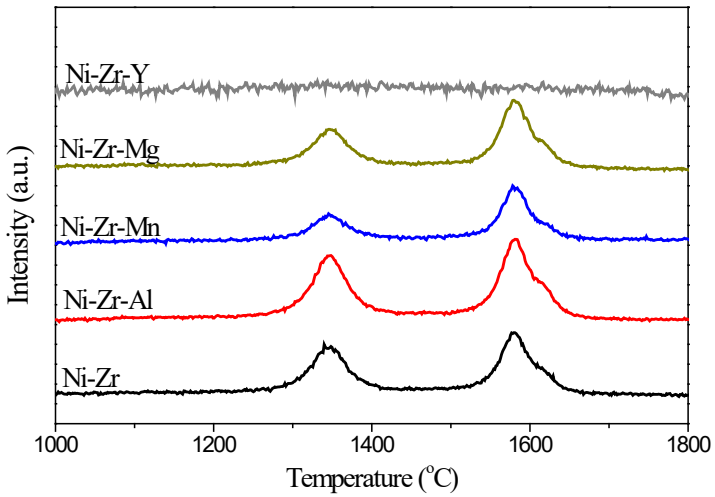

Figure 6-9 Raman profiles of used catalysts.

Raman patterns of different promoters Ni-Zr catalysts are presented in Figure 6-9. It is very clearly observed that no peak can be found on Y-promoted catalyst. It indicates the carbon deposition on Y-promoted catalyst is too low to be detected. While for others catalysts, two peaks could be observed. Generally, D band is belonged to the disorder of carbon materials, G band is ascribed to the graphite of carbon materials [247, 262]. The I_D and I_G are represented the intensity of D band and G band, respectively. The ratio of I_G/I_D is related to the crystalline degree of the carbon materials, and the results of I_G/I_D on all the catalysts are listed in Table 6-7. The crystalline degree of the carbon on non-promoted, and Al, Mn and Mg-promoted catalysts is 1.7, 1.3, 2.0 and 1.8 respectively. It is worthy pointing that the lowest of I_G/I_D on Al-modified catalyst means more much disorder of carbon. Considering the easy removal of carbon formed on Al-promoted catalyst, the disordered carbon is the one that can be removed very easily [62].

6.6 Summary

Al, Mn, Y and Mg-promoted Ni catalysts supported on ZrO_2 were synthesized by one-step synthesis method and tested in DRM at temperatures between 550 and 800 °C. Based on the DRM results, Al-modified catalysts promote the catalytic performance whereas Mn, Y and Mg-modified catalysts inhibited it. For the stability test, the addition of Mn resulted in the increase of the catalytic activity during the 300 min DRM. The existence of Al exhibited the highest stability for 8 h DRM.

In addition, according to the characterization results, such as BET, XRD, H_2-TPR, CO_2-TPR, XPS, TEM and Raman, a relationship between the catalytic performance and the texture properties, Ni^0 dispersion, and CO_2 basicity is evidenced. The addition of Al leads to an increase of the pore diameter, the CO_2 basicity and the surface nickel content and the Ni^0 dispersion during the reaction. Thus, an enhancement of the activity, stability and selectivity for DRM is observed. Meanwhile, the formation of carbon easy to be removed on Al-promoted catalyst is also observed and does not impact the activity for DRM. The presence of Mn leads to the redistribution of nickel particles during the reaction process, thus increase in the performance of catalyst for DRM. On the contrary, the addition of Mg and Y results in the large Ni^0 particle size, lower nickel content at the surface, and pore physical structure (specific surface area). Thus, lower performance on Mg and Y-modified catalysts are obtained. Besides, the lowest amount of basic sites and large particle size on Mg-promoted catalyst results in the highest amount of carbon deposition. The promotion by Y affects the adsorbed CO_2 on each type of basic sites, and the almost suppress the strong basic sites, which inhibits the carbon deposition during the reaction.

Chapter VII

Conclusions and perspectives of this work

7. Conclusions and perspectives of this work

7.1 Conclusions

In the first part of this work, a series of Ni-Zr catalysts with different Ni loadings were prepared by a novel one-step urea hydrolysis method, and compared to 10Ni/ZrO_2 catalyst prepared by ethanol impregnation method. The catalysts were tested in dry reforming of methane (DRM) at 750 °C with a mixed flow of CH_4:CO_2:Ar=10:10:80 and GHSV= 24,000 h-1. The materials were characterized by BET, XRD, XPS, H_2-TPR, CO_2-TPD, TEM, TGA and Raman. 10Ni-Zr and 15Ni-Zr catalysts prepared by the one-step method exhibited higher activity, long-run stability, and selectivity of H_2/CO compared to 10Ni/ZrO_2 catalysts. This could be ascribed to the smaller Ni crystallite size, increased specific surface area and enhanced weak and medium-strength basic sites over reduced 10Ni-Zr and 15Ni-Zr catalysts. The 10Ni-Zr and 15Ni-Zr catalysts showed a suppression of metallic nickel sintering, due to the formation of NiO–ZrO_2 solid solution, leading to the stronger interaction between Ni and ZrO_2 matrix. Moreover, stability enhancement for these catalysts was possibly linked with a higher amount of adsorbed oxygen species.

In the second part, modified the Ni-Zr catalysts were synthesized in order to improve catalytic activity and stability. Y, Mg, Al and Mn were respectively used as promoters on Ni-ZrO_2 catalysts. Yttrium-doped NiO–ZrO_m catalyst was found to be novel for carbon resistance in the CO_2 reforming of methane. The addition of Y to NiO–ZrO_m catalyst resulted in higher interaction between Ni and ZrO_2, higher distribution of weak and medium basic sites, and smaller Ni crystallite size, as compared to the Y-free NiO–ZrO_m catalyst after reaction. The DRM catalytic tests were conducted at 700 °C for 8 h, leading to a significant decrease of activity and selectivity for the yttrium-doped NiO–ZrO_m catalyst, due to the larger initial particle size of nickel species and lower surface nickel content. The carbon deposition after the DRM reaction on yttrium-doped

$NiO–ZrO_m$ catalyst (1.0 %) was lower than on yttrium-free $NiO–ZrO_m$ catalyst (3.7 %), which indicated that yttrium could promote the inhibition of carbon deposition during the DRM process.

$NiO\text{-}MgO\text{-}ZrO_2$ catalysts were also studied. The activity was carried out at 700 °C in a fixed-bed micro-reactor under $CH_4:CO_2:Ar=1:1:8$. It was shown that the introduction of Mg led to an unexpected decrease in the activity when compared to non-promoted catalyst. It was also shown that the surface area, pore-volume, pore diameter, and weak basicity decreased when the Mg was introduced into $NiO\text{-}ZrO_2$ catalyst. All these properties can cause a decrease in the activity, selectivity, and stability of $NiO\text{-}MgO\text{-}ZrO_2$ catalyst for DRM.

Introduction of aluminum was used to promote $NiO\text{-}ZrO_2$ catalysts. The Al-doped catalyst exhibited higher catalytic performance in comparison with Al-free catalyst. The enhancement of catalytic activity in dry reforming could be associated with the alterations in surface properties due to Al promotion. First, the introduction of Al changes the structure of ZrO_2, leading to an increase in its pore volume and pore diameter. Moreover, the promotion of ZrO_2 supported Ni catalysts with Al led to a better distribution of Ni species in the $NiO–10Al_2O_3–ZrO_2$ catalysts. Besides, it was found that in the presence of aluminum, higher content of surface Ni species were present on $NiO–ZrO_2$ catalyst. Finally, an enhanced ability for the sintering resistance and high suppression to loss of nickel during a long-term catalytic test was also found on Al promoted catalyst.

Finally, Mn was used as dopant for $NiZrO_2$ catalyst. This catalyst studied versus time of stream during the DRM reaction. The activity increased on $Ni–Mn–ZrO_x$ with 300 min on stream, while it decreased on $Ni–ZrO_x$ within 100 min. Because an increase of surface nickel content and a decrease of Ni particle size on $Ni–Mn–ZrO_x$ catalyst have been observed by applying in XRD and XPS after reaction for 100 min, 300 min and 480 min. While a decrease of activity and surface nickel content and an increase of Ni

particle size formed on Ni–ZrO_x catalyst. Simultaneously, the Zr species on Ni–ZrO_x reduced to Zr^{1+} after reaction for 480 min. Whereas, the Zr species did not change on Ni–Mn–ZrO_x catalyst. This stable ZrO_2 structure on Mn-promoted catalyst might promote the redistribution of nickel and the resistance to the loss of nickel species during the reaction, thereby promoted the activity for DRM.

7.2 Perspectives

In producing syngas, which offers environmental benefits, dry reforming of methane (DRM) could promote the installation of the future carbon tax. This reaction has been already extensively studied. Since nickel shows as excellent catalytic activity as noble ones (Pt, Ru, and Rh), Ni-based catalysts have been widely reported on the DRM reaction. While the catalytic performance of Ni-based catalyst is influenced by supports, promoters, catalyst preparation, reaction conditions and so on. Generally, these factors affect the dispersion, basicity, particle size, oxygen storage capacity, interaction between components, porosity and surface area, which are known for playing a significant role in the catalytic performance for dry reforming of methane. Based on this doctoral work, there are some problems that still need to be addressed in the process of industrialization. As a result, a few promising perspectives are listed as follows

- Enhancement of interaction between the active metal and support from the formation of a solid solution eg. NiO-ZrO_2, NiO-MgO. Some solid solution components help to incorporate the active metals into supports or promoters, resulting in the high dispersion and small size of active metals and further improving the catalytic performance of catalysts.

- Investigation of the detailed kinetic and mechanistic study. The study of the reaction mechanism plays an important guiding role in the development and optimization of the catalyst for dry reforming of methane.

- Further characterization techniques should be applied. For example, to trace the process of reaction through *in-situ* experiment. Such as *in-situ* XPS*, in-situ* XRD and *in-situ* TEM could be performed

- Pore structure offers the excellent resistance against sintering and carbon formation. In particular, the pore structure is much more important in the DRM reaction because of the high reaction temperature of DRM (> 750 °C) and larger carbon source compared to the conventional reforming reaction. Thus, a dedicated study on pore structure modification would be useful.

- Design a more stable ZrO_2 support. The structure of ZrO_2 plays an important role in the activity of catalyst. Thus, a more stable ZrO_2 results in higher stability for dry reforming of methane. This point would also be addressed in a future study.

Reference

[1] Q. Liu, L. Wu, R. Jackstell, M. Beller, Using carbon dioxide as a building block in organic synthesis, Nature communications, 6 (2015) 5933.

[2] Global Monitoring Division, Earth System Research Laboratory, National Oceanic and Atmospheric Administration. Trends in atmospheric carbon dioxide [online. Available on: <https://www.esrl.noaa.gov/gmd/ccgg/trends/index.html>.

[3] A. Abdulrasheed, A.A. Jalil, Y. Gambo, M. Ibrahim, H.U. Hambali, M.Y.S. Hamid, A review on catalyst development for dry reforming of methane to syngas: Recent advances, Renewable and Sustainable Energy Reviews, 108 (2019) 175-193.

[4] C. Wang, N. Sun, N. Zhao, W. Wei, Y. Sun, C. Sun, H. Liu, C.E. Snape, Coking and deactivation of a mesoporous Ni–CaO–ZrO_2 catalyst in dry reforming of methane: a study under different feeding compositions, Fuel, 143 (2015) 527-535.

[5] Y. Wang, L. Yao, S. Wang, D. Mao, C. Hu, Low-temperature catalytic CO_2 dry reforming of methane on Ni-based catalysts: a review, Fuel Processing Technology, 169 (2018) 199-206.

[6] J.F. Kennedy, J. Shimizu, Chemical fixation of carbon dioxide methods for recycling CO_2 into useful products: MM Halmann, CRC Press Inc., Boca Raton, Florida, 172 (1993) 1995.

[7] K. Sumida, D.L. Rogow, J.A. Mason, T.M. McDonald, E.D. Bloch, Z.R. Herm, T.-H. Bae, J.R. Long, Carbon dioxide capture in metal–organic frameworks, Chemical reviews, 112 (2012) 724-781.

[8] K.A. Mumford, Y. Wu, K.H. Smith, G.W. Stevens, Review of solvent based carbon-dioxide capture technologies, Frontiers of Chemical Science and Engineering, 9 (2015) 125-141.

[9] S.M. Benson, T. Surles, Carbon dioxide capture and storage: An overview with emphasis on capture and storage in deep geological formations, Proceedings of the IEEE, 94 (2006) 1795-1805.

[10] G.T. Rochelle, Amine scrubbing for CO_2 capture, Science, 325 (2009) 1652-1654.

[11] J. Cejka, A. Corma, S. Zones, Zeolites and catalysis: synthesis, reactions and applications, John Wiley & Sons2010.

[12] Z. Bao, L. Yu, Q. Ren, X. Lu, S. Deng, Adsorption of CO_2 and CH_4 on a magnesium-based metal organic framework, Journal of colloid and interface science, 353 (2011) 549-556.

[13] A.O.z.r. Yazaydın, R.Q. Snurr, T.-H. Park, K. Koh, J. Liu, M.D. LeVan, A.I. Benin, P. Jakubczak, M. Lanuza, D.B. Galloway, Screening of metal−organic frameworks for carbon dioxide capture from flue gas using a combined experimental and modeling approach, Journal of the American Chemical Society, 131 (2009) 18198-18199.

[14] D. Britt, H. Furukawa, B. Wang, T.G. Glover, O.M. Yaghi, Highly efficient separation of carbon dioxide by a metal-organic framework replete with open metal sites, Proceedings of the National Academy of Sciences, 106 (2009) 20637-20640.

[15] H. Furukawa, N. Ko, Y.B. Go, N. Aratani, S.B. Choi, E. Choi, A.Ö. Yazaydin, R.Q. Snurr, M. O'Keeffe, J. Kim, Ultrahigh porosity in metal-organic frameworks, Science, 329 (2010) 424-428.

[16] N. Ko, J. Kim, Enhanced carbon dioxide adsorption on post-synthetically modified metal-organic frameworks, Bull. Korean Chem. Soc, 32 (2011) 2705.

[17] T.M. McDonald, W.R. Lee, J.A. Mason, B.M. Wiers, C.S. Hong, J.R. Long, Capture of carbon dioxide from air and flue gas in the alkylamine-appended metal–organic framework mmen-Mg2 (dobpdc), Journal of the American Chemical Society, 134 (2012) 7056-7065.

[18] N. Huang, X. Chen, R. Krishna, D. Jiang, Two-dimensional covalent organic frameworks for carbon dioxide capture through channel-wall functionalization, Angewandte Chemie International Edition, 54 (2015) 2986-2990.

[19] M.M. Halmann, Chemical Fixation of Carbon Dioxide Methods for Recycling CO_2 into Useful Products, CRC press1993.

[20] S. Huang, B. Yan, S. Wang, X. Ma, Recent advances in dialkyl carbonates synthesis and applications, Chemical Society Reviews, 44 (2015) 3079-3116.

[21] B.M. Bhanage, M. Arai, Transformation and utilization of carbon dioxide, Springer 2014.

[22] I.A. Berg, Ecological aspects of the distribution of different autotrophic CO_2 fixation pathways, Appl. Environ. Microbiol., 77 (2011) 1925-1936.

[23] G. Fuchs, Alternative pathways of carbon dioxide fixation: insights into the early evolution of life, Annual review of microbiology, 65 (2011) 631-658.

[24] C. Martín, G. Fiorani, A.W. Kleij, Recent advances in the catalytic preparation of cyclic organic carbonates, Acs Catalysis, 5 (2015) 1353-1370.

[25] M. Aresta, A. Dibenedetto, L. Gianfrate, C. Pastore, Nb (V) compounds as epoxides carboxylation catalysts: the role of the solvent, Journal of Molecular Catalysis A: Chemical, 204 (2003) 245-252.

[26] H. Zhou, Y.-M. Wang, W.-Z. Zhang, J.-P. Qu, X.-B. Lu, N-Heterocyclic carbene functionalized MCM-41 as an efficient catalyst for chemical fixation of carbon dioxide, Green Chemistry, 13 (2011) 644-650.

[27] Y.-B. Wang, D.-S. Sun, H. Zhou, W.-Z. Zhang, X.-B. Lu, CO_2, COS and CS_2 adducts of N-heterocyclic olefins and their application as organocatalysts for carbon dioxide fixation, Green Chemistry, 17 (2015) 4009-4015.

[28] Y.M. Shen, W.L. Duan, M. Shi, Chemical Fixation of Carbon Dioxide Co-Catalyzed by a Combination of Schiff Bases or Phenols and Organic Bases, European Journal of Organic Chemistry, 2004 (2004) 3080-3089.

[29] S. Wang, X. Wang, Imidazolatsysteme zur CO_2-Abscheidung und photochemischen Reduktion, Angewandte Chemie, 128 (2016) 2352-2364.

[30] G. Fiorani, W. Guo, A.W. Kleij, Sustainable conversion of carbon dioxide: the advent of organocatalysis, Green Chemistry, 17 (2015) 1375-1389.

[31] S. Wang, X. Wang, Imidazolium ionic liquids, imidazolylidene heterocyclic carbenes, and zeolitic imidazolate frameworks for CO_2 capture and photochemical reduction, Angewandte Chemie International Edition, 55 (2016) 2308-2320.

[32] F.F. Chen, K. Huang, Y. Zhou, Z.Q. Tian, X. Zhu, D.J. Tao, D.e. Jiang, S. Dai, Multi-molar absorption of CO_2 by the activation of carboxylate groups in amino acid ionic liquids, Angewandte Chemie International Edition, 55 (2016) 7166-7170.

[33] V.B. Saptal, B.M. Bhanage, Bifunctional ionic liquids derived from biorenewable sources as sustainable catalysts for fixation of carbon dioxide, ChemSusChem, 10

(2017) 1145-1151.

[34] M. Aresta, A. Dibenedetto, A. Angelini, Catalysis for the valorization of exhaust carbon: from CO_2 to chemicals, materials, and fuels. Technological use of CO_2, Chemical reviews, 114 (2014) 1709-1742.

[35] W. Li, X. Jie, C. Wang, J.R. Dilworth, C. Xu, T. Xiao, P.P. Edwards, MnO_x-Promoted, Coking-Resistant Nickel-based Catalysts for Microwave-initiated CO_2 Utilization, Industrial & Engineering Chemistry Research, (2020).

[36] O. Bhusnure, S. Gholve, P. Giram, V. Borsure, P. Jadhav, V. Satpute, J. Sangshetti, Importance of supercritical fluid extraction techniques in pharmaceutical industry: A Review, IAJPR, 5 (2015) 3785-3801.

[37] E.A. Quadrelli, G. Centi, J.L. Duplan, S. Perathoner, Carbon dioxide recycling: emerging large-scale technologies with industrial potential, ChemSusChem, 4 (2011) 1194-1215.

[38] R.G. dos Santos, A.C. Alencar, Biomass-derived syngas production via gasification process and its catalytic conversion into fuels by Fischer Tropsch synthesis: A review, International Journal of Hydrogen Energy, (2019).

[39] A.N. Stranges, A history of the fischer-tropsch synthesis in Germany 1926-45, Studies in surface science and catalysis, (2007) 1-27.

[40] E. Van Steen, M. Claeys, K. Möller, D. Nabaho, Comparing a cobalt-based catalyst with iron-based catalysts for the Fischer-Tropsch XTL-process operating at high conversion, Applied Catalysis A: General, 549 (2018) 51-59.

[41] T. van Deelen, H. Yoshida, R. Oord, J. Zečević, B. Weckhuysen, K. de Jong, Cobalt nanocrystals on carbon nanotubes in the Fischer-Tropsch synthesis: Impact of support oxidation, Applied Catalysis A: General, 593 (2020) 117441.

[42] C. Panzone, R. Philippe, A. Chappaz, P. Fongarland, A. Bengaouer, Power-to-Liquid catalytic CO_2 valorization into fuels and chemicals: focus on the Fischer-Tropsch route, Journal of CO_2 Utilization, 38 (2020) 314-347.

[43] S. Mehariya, A. Iovine, P. Casella, D. Musmarra, A. Figoli, T. Marino, N. Sharma, A. Molino, Fischer–Tropsch synthesis of syngas to liquid hydrocarbons, Lignocellulosic Biomass to Liquid Biofuels (2020) 217-248.

[44] M.M. Yung, W.S. Jablonski, K.A. Magrini-Bair, Review of catalytic conditioning of biomass-derived syngas, Energy & Fuels, 23 (2009) 1874-1887.

[45] L. Devi, K.J. Ptasinski, F.J. Janssen, A review of the primary measures for tar elimination in biomass gasification processes, Biomass and bioenergy, 24 (2003) 125-140.

[46] K. Fang, D. Li, M. Lin, M. Xiang, W. Wei, Y. Sun, A short review of heterogeneous catalytic process for mixed alcohols synthesis via syngas, Catalysis Today, 147 (2009) 133-138.

[47] V. Mahdavi, M.H. Peyrovi, Synthesis of C1–C6 alcohols over copper/cobalt catalysts: investigation of the influence of preparative procedures on the activity and selectivity of Cu–Co_2O_3/ZnO, Al_2O_3 catalyst, Catalysis Communications, 7 (2006) 542-549.

[48] M.K. Nikoo, N. Amin, Thermodynamic analysis of carbon dioxide reforming of methane in view of solid carbon formation, Fuel Processing Technology, 92 (2011) 678-691.

[49] A. Gili, L. Schlicker, M.F. Bekheet, O. Görke, S. Penner, M. Grünbacher, T. Götsch, P. Littlewood, T.J. Marks, P.C. Stair, Surface carbon as a reactive intermediate in dry reforming of methane to syngas on a 5% Ni/MnO catalyst, ACS Catalysis, 8 (2018) 8739-8750.

[50] Y. Wang, L. Li, Y. Wang, P. Da Costa, C. Hu, Highly Carbon-Resistant Y Doped NiO–ZrO_m Catalysts for Dry Reforming of Methane, Catalysts, 9 (2019) 1055.

[51] Z. Li, Z. Wang, B. Jiang, S. Kawi, Sintering resistant Ni nanoparticles exclusively confined within SiO_2 nanotubes for CH_4 dry reforming, Catalysis Science & Technology, 8 (2018) 3363-3371.

[52] X. Tu, J.C. Whitehead, Plasma-catalytic dry reforming of methane in an atmospheric dielectric barrier discharge: Understanding the synergistic effect at low temperature, Applied Catalysis B Environmental, 125 (2012) 439-448.

[53] T. Yabe, K. Mitarai, K. Oshima, S. Ogo, Y. Sekine, Low-temperature dry reforming of methane to produce syngas in an electric field over La-doped Ni/ZrO_2 catalysts, Fuel Processing Technology, 158 (2017) 96-103.

[54] X. Zhu, P. Huo, Y.-p. Zhang, D.-g. Cheng, C.-j. Liu, Structure and reactivity of plasma treated Ni/Al_2O_3 catalyst for CO_2 reforming of methane, Applied Catalysis B: Environmental, 81 (2008) 132-140.

[55] W. Hua, L. Jin, X. He, J. Liu, H. Hu, Preparation of Ni/MgO catalyst for CO_2 reforming of methane by dielectric-barrier discharge plasma, Catalysis Communications, 11 (2010) 968-972.

[56] D. Li, X. Li, M. Bai, X. Tao, S. Shang, X. Dai, Y. Yin, CO_2 reforming of CH_4 by atmospheric pressure glow discharge plasma: a high conversion ability, International Journal of Hydrogen Energy, 34 (2009) 308-313.

[57] K. Shimura, S. Kato, T. Yoshida, H. Itoh, T. Hattori, H. Yoshida, Photocatalytic steam reforming of methane over sodium tantalate, The Journal of Physical Chemistry C, 114 (2010) 3493-3503.

[58] L. Yuliati, H. Itoh, H. Yoshida, Photocatalytic conversion of methane and carbon dioxide over gallium oxide, Chemical Physics Letters, 452 (2008) 178-182.

[59] D. Shi, Y. Feng, S. Zhong, Photocatalytic conversion of CH_4 and CO_2 to oxygenated compounds over Cu/CdS–TiO_2/SiO_2 catalyst, Catalysis Today, 98 (2004) 505-509.

[60] B. Fidalgo, A. Domínguez, J. Pis, J. Menéndez, Microwave-assisted dry reforming of methane, International Journal of Hydrogen Energy, 33 (2008) 4337-4344.

[61] R.J. Meredith, Engineers' handbook of industrial microwave heating, Iet1998.

[62] Y. Wang, L. Yao, Y. Wang, S. Wang, Q. Zhao, D. Mao, C. Hu, Low-temperature catalytic CO_2 dry reforming of methane on Ni-Si/ZrO_2 catalyst, ACS Catalysis, 8 (2018) 6495-6506.

[63] M. Németh, Z. Schay, D. Srankó, J. Károlyi, G. Sáfrán, I. Sajó, A. Horváth, Impregnated Ni/ZrO_2 and Pt/ZrO_2 catalysts in dry reforming of methane: Activity tests in excess methane and mechanistic studies with labeled $^{13}CO_2$, Applied Catalysis A General, 504 (2015) 608-620.

[64] P.G. Lustemberg, P.J. Ramirez, Z. Liu, R.A. Gutierrez, D.G. Grinter, J. Carrasco, S. Senanayake, J.A. Rodriguez, M.V. Ganduglia-pirovano, Room Temperature Activation of Methane and Dry Reforming with CO_2 on Ni-CeO_2(111) Surfaces: Effect

of Ce^{3+} Sites and Metal-Support Interactions on C-H bond Cleavage, Catalysis Letters, 2015 (2015) 1-1.

[65] L. Yao, J. Shi, H. Xu, W. Shen, C. Hu, Low-temperature CO_2 reforming of methane on Zr-promoted Ni/SiO_2 catalyst, Fuel Processing Technology, 144 (2016) 1-7.

[66] S. Jiang, Y. Lu, S. Wang, Y. Zhao, X. Ma, Insight into the reaction mechanism of CO_2 activation for CH_4 reforming over NiO-MgO: A combination of DRIFTS and DFT study, Applied Surface Science, 416 (2017).

[67] Z. Liang, T. Li, M. Kim, A. Asthagiri, J.F. Weaver, Low-temperature activation of methane on the IrO_2 (110) surface, Science, 356 (2017) 299-303.

[68] J. Guo, Z. Hou, J. Gao, X. Zheng, DRIFTS Study on Adsorption and Activation of CH_4 and CO_2 over Ni/SiO_2 Catalyst with Various Ni Particle Sizes, Chinese Journal of Catalysis, 28 (2007) 22-26.

[69] X. Huang, G. Xue, C. Wang, N. Zhao, N. Sun, W. Wei, Y. Sun, Highly stable mesoporous NiO–Y_2O_3–Al_2O_3 catalysts for CO_2 reforming of methane: effect of Ni embedding and Y_2O_3 promotion, Catalysis Science & Technology, 6 (2016) 449-459.

[70] K. Li, X. Chang, C. Pei, X. Li, S. Chen, X. Zhang, S. Assabumrungrat, Z.-J. Zhao, L. Zeng, J. Gong, Ordered mesoporous Ni/La_2O_3 catalysts with interfacial synergism towards CO_2 activation in dry reforming of methane, Applied Catalysis B: Environmental, 259 (2019) 118092.

[71] X. Li, Z.-J. Zhao, L. Zeng, J. Zhao, H. Tian, S. Chen, K. Li, S. Sang, J. Gong, On the role of Ce in CO_2 adsorption and activation over lanthanum species, Chemical science, 9 (2018) 3426-3437.

[72] X. Zhang, Q. Zhang, N. Tsubaki, Y. Tan, Y. Han, Carbon dioxide reforming of methane over Ni nanoparticles incorporated into mesoporous amorphous ZrO_2 matrix, Fuel, 147 (2015) 243-252.

[73] T. Viinikainen, H. Rönkkönen, H. Bradshaw, H. Stephenson, S. Airaksinen, M. Reinikainen, P. Simell, O. Krause, Acidic and basic surface sites of zirconia-based biomass gasification gas clean-up catalysts, Applied Catalysis A: General, 362 (2009) 169-177.

[74] B. Bachiller-Baeza, I. Rodriguez-Ramos, A. Guerrero-Ruiz, Interaction of carbon

dioxide with the surface of zirconia polymorphs, Langmuir, 14 (1998) 3556-3564.

[75] M. Usman, W.W. Daud, H.F. Abbas, Dry reforming of methane: Influence of process parameters—A review, Renewable and Sustainable Energy Reviews, 45 (2015) 710-744.

[76] I.V. Yentekakis, G. Goula, M. Hatzisymeon, I. Betsi-Argyropoulou, G. Botzolaki, K. Kousi, D.I. Kondarides, M.J. Taylor, C.M. Parlett, A. Osatiashtiani, Effect of support oxygen storage capacity on the catalytic performance of Rh nanoparticles for CO_2 reforming of methane, Applied Catalysis B: Environmental, 243 (2019) 490-501.

[77] Z. Wu, B. Yang, S. Miao, W. Liu, J. Xie, S. Lee, M.J. Pellin, D. Xiao, D. Su, D. Ma, Lattice Strained Ni-Co alloy as a High-Performance Catalyst for Catalytic Dry Reforming of Methane, ACS Catalysis, 9 (2019) 2693-2700.

[78] J. Horlyck, C. Lawrey, E.C. Lovell, R. Amal, J. Scott, Elucidating the impact of Ni and Co loading on the selectivity of bimetallic NiCo catalysts for dry reforming of methane, Chemical Engineering Journal, 352 (2018) 572-580.

[79] Z. Bian, S. Kawi, Highly carbon-resistant Ni–Co/SiO_2 catalysts derived from phyllosilicates for dry reforming of methane, Journal of CO_2 Utilization, 18 (2017) 345-352.

[80] S.A. Singh, G. Madras, Sonochemical synthesis of Pt, Ru doped TiO_2 for methane reforming, Applied Catalysis A: General, 518 (2016) 102-114.

[81] S.M. Sajjadi, M. Haghighi, F. Rahmani, Sol–gel synthesis of Ni–Co/Al_2O_3–MgO–ZrO_2 nanocatalyst used in hydrogen production via reforming of CH_4/CO_2 greenhouse gases, Journal of Natural Gas Science and Engineering, 22 (2015) 9-21.

[82] C. Dai, S. Zhang, A. Zhang, C. Song, C. Shi, X. Guo, Hollow zeolite encapsulated Ni–Pt bimetals for sintering and coking resistant dry reforming of methane, Journal of Materials Chemistry A, 3 (2015) 16461-16468.

[83] M.M. Souza, D.A. Aranda, M. Schmal, Reforming of methane with carbon dioxide over Pt/ZrO_2/Al_2O_3 catalysts, Journal of Catalysis, 204 (2001) 498-511.

[84] F. Wang, B. Han, L. Zhang, L. Xu, H. Yu, W. Shi, CO_2 reforming with methane over small-sized Ni@SiO_2 catalysts with unique features of sintering-free and low carbon, Applied Catalysis B: Environmental, 235 (2018) 26-35.

[85] J. Xu, Q. Xiao, J. Zhang, Y. Sun, Y. Zhu, NiO-MgO nanoparticles confined inside SiO_2 frameworks to achieve highly catalytic performance for CO_2 reforming of methane, Molecular Catalysis, 432 (2017) 31-36.

[86] M. Wang, Q. Zhang, T. Zhang, Y. Wang, J. Wang, K. Long, Z. Song, X. Liu, P. Ning, Facile one-pot synthesis of highly dispersed Ni nanoparticles embedded in HMS for dry reforming of methane, Chemical Engineering Journal, 313 (2017) 1370-1381.

[87] Y. Lou, M. Steib, Q. Zhang, K. Tiefenbacher, A. Horváth, A. Jentys, Y. Liu, J.A. Lercher, Design of stable Ni/ZrO_2 catalysts for dry reforming of methane, Journal of catalysis, 356 (2017) 147-156.

[88] H. Liu, H.B. Hadjltaief, M. Benzina, M.E. Gálvez, P. Da Costa, Natural clay based nickel catalysts for dry reforming of methane: On the effect of support promotion (La, Al, Mn), International Journal of Hydrogen Energy, 44 (2019) 246-255.

[89] R. Dębek, M. Motak, M.E. Galvez, T. Grzybek, P. Da Costa, Influence of Ce/Zr molar ratio on catalytic performance of hydrotalcite-derived catalysts at low temperature CO_2 methane reforming, International Journal of Hydrogen Energy, 42 (2017) 23556-23567.

[90] M. Steib, A. Jentys, J. Lercher, Structural response of Ni/ZrO_2 to feed modulations during CH4 reforming reactions, Journal of Physics: Conference Series, IOP Publishing, 2016, pp. 012049.

[91] N.A. Pechimuthu, K.K.P. And, S.C. Dhingra, Deactivation Studies over $Ni{-}K/CeO_2{-}Al_2O_3$ Catalyst for Dry Reforming of Methane, Industrial & Engineering Chemistry Research, 46 (2016) 1731-1736.

[92] P.G. Lustemberg, P.J. Ramírez, Z. Liu, R.A. Gutiérrez, D.G. Grinter, J. Carrasco, S.D. Senanayake, J.A. Rodriguez, M.V. Ganduglia-Pirovano, Room-Temperature Activation of Methane and Dry Re-forming with CO_2 on Ni-CeO_2(111) Surfaces: Effect of Ce^{3+} Sites and Metal–Support Interactions on C–H Bond Cleavage, ACS Catalysis, 6 (2016) 8184-8191.

[93] K. Świrk, M. Rønning, M. Motak, P. Beaunier, P. Da Costa, T. Grzybek, Ce-and Y-Modified Double-Layered Hydroxides as Catalysts for Dry Reforming of Methane: On the Effect of Yttrium Promotion, Catalysts, 9 (2019) 56.

[94] K. Świrk, M. Motak, T. Grzybek, M. Rønning, P. Da Costa, Effect of low loading of yttrium on Ni-based layered double hydroxides in CO_2 reforming of CH_4, Reaction kinetics, mechanisms and catalysis, 126 (2019) 611-628.

[95] L. Yao, M.E. Galvez, C. Hu, P. Da Costa, Synthesis Gas Production via Dry Reforming of Methane over Manganese Promoted Nickel/Cerium–Zirconium Oxide Catalyst, Industrial & Engineering Chemistry Research, 57 (2018) 16645-16656.

[96] K. Świrk, M.E. Galvez, M. Motak, T. Grzybek, M. Rønning, P. Da Costa, Dry reforming of methane over Zr-and Y-modified Ni/Mg/Al double-layered hydroxides, Catalysis Communications, 117 (2018) 26-32.

[97] Z. Taherian, M. Yousefpour, M. Tajally, B. Khoshandam, A comparative study of ZrO_2, Y_2O_3 and Sm_2O_3 promoted Ni/SBA-15 catalysts for evaluation of CO_2/methane reforming performance, International Journal of Hydrogen Energy, 42 (2017) 16408-16420.

[98] W.Y. Kim, Y.H. Lee, H. Park, Y.H. Choi, M.H. Lee, J.S. Lee, Coke tolerance of Ni/Al_2O_3 nanosheet catalyst for dry reforming of methane, Catalysis Science & Technology, 6 (2016) 2060-2064.

[99] J.W. Han, C. Kim, J.S. Park, H. Lee, Highly coke-resistant Ni nanoparticle catalysts with minimal sintering in dry reforming of methane, ChemSusChem, 7 (2014) 451-456.

[100] R.K. Singha, A. Yadav, A. Shukla, M. Kumar, R. Bal, Low temperature dry reforming of methane over Pd-CeO_2 nanocatalyst, Catalysis Communications, 92 (2017) 19-22.

[101] N. El Hassan, M. Kaydouh, H. Geagea, H. El Zein, K. Jabbour, S. Casale, H. El Zakhem, P. Massiani, Low temperature dry reforming of methane on rhodium and cobalt based catalysts: active phase stabilization by confinement in mesoporous SBA-15, Applied Catalysis A: General, 520 (2016) 114-121.

[102] M. Zhang, J. Zhang, Y. Wu, J. Pan, Q. Zhang, Y. Tan, Y. Han, Insight into the effects of the oxygen species over Ni/ZrO_2 catalyst surface on methane reforming with carbon dioxide, Applied Catalysis B: Environmental, 244 (2019) 427-437.

[103] S. Aghamohammadi, M. Haghighi, M. Maleki, N. Rahemi, Sequential

impregnation vs. sol-gel synthesized Ni/Al_2O_3-CeO_2 nanocatalyst for dry reforming of methane: Effect of synthesis method and support promotion, Molecular Catalysis, 431 (2017) 39-48.

[104] Q. Zhang, T. Zhang, Y. Shi, B. Zhao, M. Wang, Q. Liu, J. Wang, K. Long, Y. Duan, P. Ning, A sintering and carbon-resistant Ni-SBA-15 catalyst prepared by solid-state grinding method for dry reforming of methane, Journal of CO_2 Utilization, 17 (2017) 10-19.

[105] C. Wang, N. Sun, N. Zhao, W. Wei, Y. Zhao, Template-free preparation of bimetallic mesoporous Ni-Co-CaO-ZrO_2 catalysts and their synergetic effect in dry reforming of methane, Catalysis Today, 281 (2017) 268-275.

[106] X. Zhang, Q. Zhang, N. Tsubaki, Y. Tan, Y. Han, Influence of zirconia phase on the performance of Ni/ZrO_2 for carbon dioxide reforming of methane, Advances in CO_2 Capture, Sequestration, and Conversion, ACS Publications (2015) 135-153.

[107] M. Németh, Z. Schay, D. Srankó, J. Károlyi, G. Sáfrán, I. Sajó, A. Horváth, Impregnated Ni/ZrO_2 and Pt/ZrO_2 catalysts in dry reforming of methane: Activity tests in excess methane and mechanistic studies with labeled $^{13}CO_2$, Applied Catalysis A: General, 504 (2015) 608-620.

[108] V.M. Gonzalez-Delacruz, R. Pereñiguez, F. Ternero, J.P. Holgado, A. Caballero, Modifying the Size of Nickel Metallic Particles by H_2/CO Treatment in Ni/ZrO_2 Methane Dry Reforming Catalysts, ACS Catalysis, 1 (2011) 82-88.

[109] A. Solis-Garcia, J.F. Louvier-Hernandez, A. Almendarez-Camarillo, J.C. Fierro-Gonzalez, Participation of Surface Bicarbonate, Formate and Methoxy Species in the Carbon Dioxide Methanation Catalyzed by ZrO_2-Supported Ni, Applied Catalysis B Environmental, 218 (2017).

[110] J.F. Li, C. Xia, C.T. Au, B.S. Liu, Y_2O_3-promoted NiO/SBA-15 catalysts highly active for CO_2/CH_4 reforming, International Journal of Hydrogen Energy, 39 (2014) 10927-10940.

[111] S. Zhang, S. Muratsugu, N. Ishiguro, M. Tada, Ceria-Doped Ni/SBA-16 Catalysts for Dry Reforming of Methane, Acs Catalysis, 3 (2013) 1855–1864.

[112] B. Li, S. Zhang, Methane reforming with CO_2 using nickel catalysts supported on

yttria-doped SBA-15 mesoporous materials via sol–gel process, International Journal of Hydrogen Energy, 38 (2013) 14250-14260.

[113] A. Albarazi, P. Beaunier, P. Da Costa, Hydrogen and syngas production by methane dry reforming on SBA-15 supported nickel catalysts: On the effect of promotion by $Ce_{0.75}Zr_{0.25}O_2$ mixed oxide, International journal of hydrogen energy, 38 (2013) 127-139.

[114] H. Liu, D. Wierzbicki, R. Debek, M. Motak, T. Grzybek, P.D. Costa, M.E. Gálvez, La-promoted Ni-hydrotalcite-derived catalysts for dry reforming of methane at low temperatures, Fuel, 182 (2016) 8-16.

[115] R. Dębek, M. Motak, D. Duraczyska, F. Launay, M.E. Galvez, T. Grzybek, P. Da Costa, Methane dry reforming over hydrotalcite-derived Ni–Mg–Al mixed oxides: the influence of Ni content on catalytic activity, selectivity and stability, Catalysis Science & Technology, 6 (2016) 6705-6715.

[116] R. Dębek, M.E. Galvez, F. Launay, M. Motak, T. Grzybek, P. Da Costa, Low temperature dry methane reforming over Ce, Zr and CeZr promoted Ni–Mg–Al hydrotalcite-derived catalysts, International Journal of Hydrogen Energy, 41 (2016) 11616-11623.

[117] K. Świrk, M.E. Galvez, M. Motak, T. Grzybek, M. Rønning, P. Da Costa, Yttrium promoted Ni-based double-layered hydroxides for dry methane reforming, Journal of CO_2 Utilization, 27 (2018) 247-258.

[118] M. Goula, N. Charisiou, G. Siakavelas, L. Tzounis, I. Tsiaoussis, P. Panagiotopoulou, G. Goula, I. Yentekakis, Syngas production via the biogas dry reforming reaction over Ni supported on zirconia modified with CeO_2 or La_2O_3 catalysts, international journal of hydrogen energy, 42 (2017) 13724-13740.

[119] Ş. Özkara-Aydınoğlu, A.E. Aksoylu, Carbon dioxide reforming of methane over Co-X/ZrO_2 catalysts (X= La, Ce, Mn, Mg, K), Catalysis Communications, 11 (2010) 1165-1170.

[120] L. Yao, Y. Wang, J. Shi, H. Xu, W. Shen, C. Hu, The influence of reduction temperature on the performance of ZrO_x/Ni-MnO_x/SiO_2 catalyst for low-temperature CO_2 reforming of methane, Catalysis Today, (2016).

[121] Y. Lu, J. Zhu, X. Peng, D. Tong, C. Hu, Comparative study on the promotion effect of Mn and Zr on the stability of Ni/SiO_2 catalyst for CO_2 reforming of methane, International Journal of Hydrogen Energy, 38 (2013) 7268-7279.

[122] W.-J. Jang, D.-W. Jeong, J.-O. Shim, H.-M. Kim, W.-B. Han, J.W. Bae, H.-S. Roh, Metal oxide (MgO, CaO, and La_2O_3) promoted $Ni-Ce_{0.8}Zr_{0.2}O_2$ catalysts for H_2 and CO production from two major greenhouse gases, Renewable energy, 79 (2015) 91-95.

[123] K. Sutthiumporn, T. Maneerung, Y. Kathiraser, S. Kawi, CO_2 dry-reforming of methane over $La_{0.8}Sr_{0.2}Ni_{0.8}M_{0.2}O_3$ perovskite (M= Bi, Co, Cr, Cu, Fe): Roles of lattice oxygen on C–H activation and carbon suppression, International Journal of Hydrogen Energy, 37 (2012) 11195-11207.

[124] M. Akri, S. Zhao, X. Li, K. Zang, A.F. Lee, M.A. Isaacs, W. Xi, Y. Gangarajula, J. Luo, Y. Ren, Atomically dispersed nickel as coke-resistant active sites for methane dry reforming, Nature communications, 10 (2019) 1-10.

[125] C. Wang, N. Sun, W. Wei, Y. Zhao, Carbon intermediates during CO_2 reforming of methane over $Ni–CaO–ZrO_2$ catalysts: A temperature-programmed surface reaction study, International Journal of Hydrogen Energy, 41 (2016) 19014-19024.

[126] I.H. Son, S. Kwon, J.H. Park, S.J. Lee, High coke-resistance $MgAl_2O_4$ islands decorated catalyst with minimizing sintering in carbon dioxide reforming of methane, Nano Energy, 19 (2016) 58-67.

[127] Ş. Özkara-Aydınoğlu, E. Özensoy, A.E. Aksoylu, The effect of impregnation strategy on methane dry reforming activity of Ce promoted Pt/ZrO_2, international journal of hydrogen energy, 34 (2009) 9711-9722.

[128] H. Wang, E. Ruckenstein, Carbon dioxide reforming of methane to synthesis gas over supported rhodium catalysts: the effect of support, Applied Catalysis A: General, 204 (2000) 143-152.

[129] A. Moral, I. Reyero, C. Alfaro, F. Bimbela, L.M. Gandía, Syngas production by means of biogas catalytic partial oxidation and dry reforming using Rh-based catalysts, Catalysis Today, 299 (2018) 280-288.

[130] C. Fernández, N. Miranda, X. García, P. Eloy, P. Ruiz, A. Gordon, R. Jiménez, Insights into dynamic surface processes occurring in Rh supported on Zr-grafted γ-

Al_2O_3 during dry reforming of methane, Applied Catalysis B: Environmental, 156 (2014) 202-212.

[131] A. Movasati, S.M. Alavi, G. Mazloom, Dry reforming of methane over CeO_2-$ZnAl_2O_4$ supported Ni and Ni-Co nano-catalysts, Fuel, 236 (2019) 1254-1262.

[132] Y.J. Asencios, J.D. Bellido, E.M. Assaf, Synthesis of NiO–MgO–ZrO_2 catalysts and their performance in reforming of model biogas, Applied Catalysis A: General, 397 (2011) 138-144.

[133] F. Guo, J.-Q. Xu, W. Chu, CO_2 reforming of methane over Mn promoted Ni/Al2O3 catalyst treated by N2 glow discharge plasma, Catalysis Today, 256 (2015) 124-129.

[134] T. van Haasterecht, M. Swart, K.P. de Jong, J.H. Bitter, Effect of initial nickel particle size on stability of nickel catalysts for aqueous phase reforming, Journal of Energy Chemistry, 25 (2016) 289-296.

[135] R. Dębek, M.E. Galvez, F. Launay, M. Motak, T. Grzybek, P.D. Costa, Low temperature dry methane reforming over Ce, Zr and CeZr promoted Ni–Mg–Al hydrotalcite-derived catalysts, International Journal of Hydrogen Energy, 41 (2016) 11616-11623.

[136] R. Dębek, M. Radlik, M. Motak, M.E. Galvez, W. Turek, P.D. Costa, T. Grzybek, Ni-containing Ce-promoted hydrotalcite derived materials as catalysts for methane reforming with carbon dioxide at low temperature – On the effect of basicity, Catalysis Today, 257 (2015) 59-65.

[137] R. Dębek, M. Motak, M.E. Galvez, T. Grzybek, P.D. Costa, Influence of Ce/Zr molar ratio on catalytic performance of hydrotalcite-derived catalysts atlow temperature CO_2 methane reforming, International Journal of Hydrogen Energy, (2017).

[138] U. Oemar, Y. Kathiraser, L. Mo, X.K. Ho, S. Kawi, CO_2 reforming of methane over highly active La-promoted Ni supported on SBA-15 catalysts: Mechanism and kinetic modelling, Catalysis Science & Technology, 6 (2016) 1173-1186.

[139] J.S. Chang, S.E. Park, J.W. Yoo, J.N. Park, Catalytic Behavior of Supported KNiCa Catalyst and Mechanistic Consideration for Carbon Dioxide Reforming of Methane, Journal of Catalysis, 195 (2000) 1-11.

[140] M.M. Barroso-Quiroga, A.E. Castro-Luna, Catalytic activity and effect of modifiers on Ni-based catalysts for the dry reforming of methane, International Journal of Hydrogen Energy, 35 (2010) 6052-6056.

[141] J.W.S. And, G.F.F. ‡, M. Fowles, Steam/CO_2 Reforming of Methane. Carbon Formation and Gasification on Catalysts with Various Potassium Contents, Industrial & Engineering Chemistry Research, 41 (2002) 3548-3556.

[142] X. Zhao, Y. Cao, H. Li, J. Zhang, L. Shi, D. Zhang, Sc promoted and aerogel confined Ni catalysts for coking-resistant dry reforming of methane, RSC Adv., 7 (2017) 4735-4745.

[143] C.V. Grossi, E.D.O. Jardim, M.H.D. Araújo, R.M. Lago, M.J.D. Silva, Sulfonated polystyrene: A catalyst with acid and superabsorbent properties for the esterification of fatty acids, Fuel, 89 (2010) 257-259.

[144] A. Albarazi, P. Beaunier, P. D. Costa, Hydrogen and syngas production by methane dry reforming on SBA-15 supported nickel catalysts: On the effect of promotion by $Ce_{0.75}Zr_{0.25}O_2$ mixed oxide, International Journal of Hydrogen Energy, 38 (2013) 127–139.

[145] M.H. Youn, J.G. Seo, J.C. Jung, S. Park, I.K. Song, Hydrogen production by auto-thermal reforming of ethanol over nickel catalyst supported on mesoporous yttria-stabilized zirconia, International journal of hydrogen energy, 34 (2009) 5390-5397.

[146] Y.J. Asencios, C.B. Rodella, E.M. Assaf, Oxidative reforming of model biogas over NiO–Y_2O_3–ZrO_2 catalysts, Applied Catalysis B: Environmental, 132 (2013) 1-12.

[147] J.D. Bellido, E.M. Assaf, Effect of the Y_2O_3–ZrO_2 support composition on nickel catalyst evaluated in dry reforming of methane, Applied Catalysis A: General, 352 (2009) 179-187.

[148] M.C.J. Bradford, M.A. Vannice, Catalytic reforming of methane with carbon dioxide over nickel catalysts I. Catalyst characterization and activity, Applied Catalysis A General, 142 (1996) 73-96.

[149] P. Kumar, Y. Sun, R.O. Idem, Nickel-based ceria, zirconia, and ceria–zirconia catalytic systems for low-temperature carbon dioxide reforming of methane, Energy & fuels, 21 (2007) 3113-3123.

[150] A.A. Lemonidou, I.A. Vasalos, Carbon dioxide reforming of methane over 5 wt.% Ni/CaO-Al_2O_3 catalyst, Applied Catalysis A General, 228 (2002) 227-235.

[151] B. Bachiller-Baeza, C. Mateos-Pedrero, M.A. Soria, A. Guerrero-Ruiz, U. Rodemerck, I. Rodríguez-Ramos, Transient studies of low-temperature dry reforming of methane over Ni-CaO/ZrO_2-La_2O_3, Applied Catalysis B Environmental, 129 (2013) 450-459.

[152] M.E. Gálvez, A. Albarazi, P.D. Costa, Enhanced catalytic stability through non-conventional synthesis of Ni/SBA-15 for methane dry reforming at low temperatures, Applied Catalysis A General, 504 (2014) 143-150.

[153] M.N. Kaydouh, N.E. Hassan, A. Davidson, S. Casale, H.E. Zakhem, P. Massiani, Effect of the order of Ni and Ce addition in SBA-15 on the activity in dry reforming of methane, Comptes Rendus Chimie, 18 (2015) 293-301.

[154] S. Sokolov, E.V. Kondratenko, M.M. Pohl, A. Barkschat, U. Rodemerck, Stable low-temperature dry reforming of methane over mesoporous La_2O_3-ZrO_2 supported Ni catalyst, Applied Catalysis B Environmental, s 113–114 (2012) 19-30.

[155] R. Dbek, M.F.G. Ribeiro, A. Fernandes, M. Motak, Ni–Al hydrotalcite-like material as the catalyst precursors for the dry reforming of methane at low temperature, Comptes Rendus Chimie, 18 (2015) 1205-1210.

[156] R. Dębek, M. Motak, T. Grzybek, M. Galvez, P.D. Costa, A Short Review on the Catalytic Activity of Hydrotalcite-Derived Materials for Dry Reforming of Methane, (2017).

[157] S. Pengpanich, V. Meeyoo, T. Rirksomboon, K. Bunyakiat, Catalytic oxidation of methane over CeO_2-ZrO_2 mixed oxide solid solution catalysts prepared via urea hydrolysis, Applied Catalysis A General, 234 (2002) 221–233.

[158] A. Trovarelli, P. Fornasiero, Catalysis by Ceria and Related Materials, 2013.

[159] J.M. Wei, B.Q. Xu, J.L. Li, Z.X. Cheng, Q.M. Zhu, Highly active and stable Ni/ZrO_2 catalyst for syngas production by CO_2 reforming of methane, Applied Catalysis A General, 196 (2000) L167–L172.

[160] R. Dębek, M. Motak, M.E. Galvez, P.D. Costa, T. Grzybek, Catalytic activity of hydrotalcite-derived catalysts in the dry reforming of methane: on the effect of Ce

promotion and feed gas composition, Reaction Kinetics Mechanisms & Catalysis, (2017) 1-24.

[161] X. Li, Q. Hu, Y. Yang, Y. Wang, F. He, Studies on stability and coking resistance of Ni/$BaTiO_3$–Al_2O_3 catalysts for lower temperature dry reforming of methane (LTDRM), Applied Catalysis A General, s 413–414 (2012) 163-169.

[162] U. Oemar, K. Hidajat, S. Kawi, Pd-Ni catalyst over spherical nanostructured Y_2O_3 support for oxy-CO_2 reforming of methane: Role of surface oxygen mobility, International Journal of Hydrogen Energy, 40 (2015) 12227-12238.

[163] K. Sutthiumporn, T. Maneerung, Y. Kathiraser, S. Kawi, CO_2 dry-reforming of methane over $La_{0.8}Sr_{0.2}Ni_{0.8}M_{0.2}O_3$ perovskite (M=Bi, Co, Cr, Cu, Fe): Roles of lattice oxygen on C–H activation and carbon suppression, International Journal of Hydrogen Energy, 37 (2012) 11195-11207.

[164] T. Maneerung, K. Hidajat, S. Kawi, $LaNiO_3$ perovskite catalyst precursor for rapid decomposition of methane: Influence of temperature and presence of H_2 in feed stream, Catalysis Today, 171 (2011) 24-35.

[165] J.-M. Wei, B.-Q. Xu, J.-L. Li, Z.-X. Cheng, Q.-M. Zhu, Highly active and stable Ni/ZrO_2 catalyst for syngas production by CO_2 reforming of methane, Applied Catalysis A: General, 196 (2000) L167-L172.

[166] Q. Jing, X. Zheng, Combined catalytic partial oxidation and CO_2 reforming of methane over ZrO_2-modified Ni/SiO_2 catalysts using fluidized-bed reactor, Energy, 31 (2006) 2184-2192.

[167] J. Lercher, J. Bitter, W. Hally, W. Niessen, K. Seshan, Design of stable catalysts for methane-carbon dioxide reforming, Studies of Surface Science and Catalysis, 101 (1996) 463-472.

[168] F. Pompeo, N.N. Nichio, M.M. Souza, D.V. Cesar, O.A. Ferretti, M. Schmal, Study of Ni and Pt catalysts supported on α-Al_2O_3 and ZrO_2 applied in methane reforming with CO_2, Applied Catalysis A: General, 316 (2007) 175-183.

[169] K. Nagaoka, K. Seshan, K.-i. Aika, J.A. Lercher, Carbon deposition during carbon dioxide reforming of methane—comparison between Pt/Al_2O_3 and Pt/ZrO_2, Journal of Catalysis, 197 (2001) 34-42.

[170] I. Chorkendorff, J.W. Niemantsverdriet, Concepts of modern catalysis and kinetics, John Wiley & Sons2017.

[171] G. Leofanti, G. Tozzola, M. Padovan, G. Petrini, S. Bordiga, A. Zecchina, Catalyst characterization: applications, Catalysis Today, 34 (1997) 329-352.

[172] T. Ishii, T. Kyotani, Temperature Programmed Desorption, Materials Science and Engineering of Carbon, (2016) 287-305.

[173] G. Leofanti, G. Tozzola, M. Padovan, G. Petrini, S. Bordiga, A. Zecchina, Catalyst characterization: characterization techniques, Catalysis today, 34 (1997) 307-327.

[174] A. Monshi, M.R. Foroughi, M.R. Monshi, Modified Scherrer equation to estimate more accurately nano-crystallite size using XRD, World journal of nano science and engineering, 2 (2012) 154-160.

[175] S. Brunauer, P.H. Emmett, The use of low temperature van der Waals adsorption isotherms in determining the surface areas of various adsorbents, Journal of the American Chemical Society, 59 (1937) 2682-2689.

[176] B. Rasneur, J. Charpin, Isothermbgraphe: automatic appartus for surface area mesurement and pore size analysis of porous materials or fine powders from nitrogen adsorption isotherm, Fine Particles: Second International Conference, Electrothermics and Metallurgy Division, Electrochemical Society, 1974, pp. 58.

[177] K.S. Sing, Reporting physisorption data for gas/solid systems with special reference to the determination of surface area and porosity (Recommendations 1984), Pure and applied chemistry, 57 (1985) 603-619.

[178] J.M. Barton, The application of differential scanning calorimetry (DSC) to the study of epoxy resin curing reactions, Epoxy resins and composites I, Springer1985, pp. 111-154.

[179] J. Wei, C.D. Prater, The structure and analysis of complex reaction systems, Advances in Catalysis, (1962) 203-392.

[180] E. Rauch, M. Véron, J. Portillo, D. Bultreys, Y. Maniette, S. Nicolopoulos, Automatic crystal orientation and phase mapping in TEM by precession diffraction, Microscopy and Analysis-UK, 128 (2008) S5-S8.

[181] F.R. Brown, L.E. Makovsky, K.H. Rhee, Raman spectra of supported molybdena catalysts: I. Oxide catalysts, Journal of Catalysis, 50 (1977) 162-171.

[182] M. Iliev, M. Abrashev, A. Litvinchuk, V. Hadjiev, H. Guo, A. Gupta, Raman spectroscopy of ordered double perovskite La_2CoMnO_6 thin films, Physical review B, 75 (2007) 104118.

[183] G. Xiong, C. Li, H. Li, Q. Xin, Z. Feng, Direct spectroscopic evidence for vanadium species in V-MCM-41 molecular sieve characterized by UV resonance Raman spectroscopy, Chemical Communications, (2000) 677-678.

[184] D. Liu, Y. Wang, D. Shi, X. Jia, X. Wang, A. Borgna, R. Lau, Y. Yang, Methane reforming with carbon dioxide over a $Ni/ZiO_2–SiO_2$ catalyst: Influence of pretreatment gas atmospheres, International Journal of Hydrogen Energy, 37 (2012) 10135-10144.

[185] A.R. Mcfarlane, I.P. Silverwood, E.L. Norris, R.M. Ormerod, C.D. Frost, S.F. Parker, D. Lennon, The application of inelastic neutron scattering to investigate the steam reforming of methane over an alumina-supported nickel catalyst, Chemical Physics, 427 (2013) 54-60.

[186] T. Bai, X. Zhang, F. Wang, W.T. Qu, X.L. Liu, C. Duan, Coking behaviors and kinetics on HZSM-5/SAPO-34 catalysts for conversion of ethanol to propylene, Journal of Energy Chemistry, 25 (2016) 545-552.

[187] A.M. Venezia, X-ray photoelectron spectroscopy (XPS) for catalysts characterization, Catalysis Today, 77 (2003) 359-370.

[188] D. Briggs, J.T. Grant, Surface analysis by Auger and X-ray photoelectron spectroscopy, Surface Spectra 2012.

[189] H. Xin, K. Guo, D. Li, H. Yang, C. Hu, Production of high-grade diesel from palmitic acid over activated carbon-supported nickel phosphide catalysts, Applied Catalysis B: Environmental, 187 (2016) 375-385.

[190] L.C. Buelens, V.V. Galvita, H. Poelman, C. Detavernier, G.B. Marin, Super-dry reforming of methane intensifies CO_2 utilization via Le Chatelier's principle, Science, 354 (2016) 449-452.

[191] S. Bhattar, A. Krishnakumar, S. Kanitkar, A. Abedin, D. Shekhawat, D.J. Haynes, J.J. Spivey, 110th Anniversary: Dry Reforming of Methane over Ni-and Sr-Substituted

Lanthanum Zirconate Pyrochlore Catalysts: Effect of Ni Loading, Industrial & Engineering Chemistry Research, 58 (2019) 19386-19396.

[192] J.-S. Bae, S.Y. Hong, J.C. Park, G.B. Rhim, M.H. Youn, H. Jeong, S.W. Kang, J.-I. Yang, H. Jung, D.H. Chun, Eco-friendly prepared iron-ore-based catalysts for Fischer-Tropsch synthesis, Applied Catalysis B: Environmental, 244 (2019) 576-582.

[193] O.H. Ojeda-Niño, F. Gracia, C. Daza, Role of Pr on Ni–Mg–Al Mixed Oxides Synthesized by Microwave-Assisted Self-Combustion for Dry Reforming of Methane, Industrial & Engineering Chemistry Research, 58 (2019) 7909-7921.

[194] L.V. Mattos, E. Rodino, D.E. Resasco, F.B. Passos, F.B. Noronha, Partial oxidation and CO_2 reforming of methane on Pt/Al_2O_3, Pt/ZrO_2, and $Pt/Ce–ZrO_2$ catalysts, Fuel Processing Technology, 83 (2003) 147-161.

[195] J.G. Jakobsen, T.L. Jørgensen, I. Chorkendorff, J. Sehested, Steam and CO_2 reforming of methane over a Ru/ZrO_2 catalyst, Applied Catalysis A: General, 377 (2010) 158-166.

[196] N.-o. Matsui, K. Anzai, N. Akamatsu, K. Nakagawa, N.-o. Ikenaga, T. Suzuki, Reaction mechanisms of carbon dioxide reforming of methane with Ru-loaded lanthanum oxide catalyst, Applied Catalysis A: General, 179 (1999) 247-256.

[197] A.E. Abasaeed, A.S. Al-Fatesh, M.A. Naeem, A.A. Ibrahim, A.H. Fakeeha, Catalytic performance of CeO_2 and ZrO_2 supported Co catalysts for hydrogen production via dry reforming of methane, International Journal of Hydrogen Energy, 40 (2015) 6818-6826.

[198] V.M. Gonzalez-delaCruz, R. Pereñiguez, F. Ternero, J.P. Holgado, A. Caballero, In Situ XAS Study of Synergic Effects on $Ni–Co/ZrO_2$ Methane Reforming Catalysts, The Journal of Physical Chemistry C, 116 (2012) 2919-2926.

[199] Q.S. Jing, X.M. Zheng, Combined catalytic partial oxidation and CO_2 reforming of methane over ZrO_2-modified Ni/SiO_2 catalysts using fluidized-bed reactor, Energy, 31 (2006) 2184-2192.

[200] F. Pompeo, N.N. Nichio, M.M.V.M. Souza, D.V. Cesar, O.A. Ferretti, M. Schmal, Study of Ni and Pt catalysts supported on α-Al_2O_3 and ZrO_2 applied in methane reforming with CO_2, Applied Catalysis A: General, 316 (2007) 175-183.

[201] S.G. Liu, H. Wang, J.P. Li, N. Zhao, W. Wei, Y.H. Sun, A facile route to synthesize mesoporous zirconia with ultra high thermal stability, Materials Research Bulletin, 42 (2007) 171-176.

[202] S. Pengpanich, V. Meeyoo, T. Rirksomboon, K. Bunyakiat, Catalytic oxidation of methane over CeO_2-ZrO_2 mixed oxide solid solution catalysts prepared via urea hydrolysis, Applied Catalysis A: General, 234 (2002) 221-233.

[203] H.-S. Roh, K.-W. Jun, W.-S. Dong, J.-S. Chang, S.-E. Park, Y.-I. Joe, Highly active and stable Ni/Ce–ZrO_2 catalyst for H_2 production from methane, Journal of Molecular Catalysis A: Chemical, 181 (2002) 137-142.

[204] C.G. Anchieta, E.M. Assaf, J.M. Assaf, Effect of ionic liquid in Ni/ZrO_2 catalysts applied to syngas production by methane tri-reforming, International Journal of Hydrogen Energy, 44 (2019) 9316-9327.

[205] Z. Li, X. Hu, L. Zhang, S. Liu, G. Lu, Steam reforming of acetic acid over Ni/ZrO_2 catalysts: Effects of nickel loading and particle size on product distribution and coke formation, Applied catalysis A: general, 417 (2012) 281-289.

[206] S. Xu, X. Wang, Highly active and coking resistant Ni/CeO_2–ZrO_2 catalyst for partial oxidation of methane, Fuel, 84 (2005) 563-567.

[207] A. Iriondo, J. Cambra, M. Güemez, V. Barrio, J. Requies, M. Sánchez-Sánchez, R. Navarro, Effect of ZrO_2 addition on Ni/Al_2O_3 catalyst to produce H_2 from glycerol, international journal of hydrogen energy, 37 (2012) 7084-7093.

[208] J.G. Seo, M.H. Youn, S. Park, J.S. Chung, I.K. Song, Hydrogen production by steam reforming of liquefied natural gas (LNG) over Ni/Al_2O_3–ZrO_2 xerogel catalysts: effect of calcination temperature of Al_2O_3–ZrO_2 xerogel supports, international journal of hydrogen energy, 34 (2009) 3755-3763.

[209] G. Štefanić, M. Didović, S. Musić, The influence of thermal treatment on the phase development of ZrO_2–NiO precursors, Journal of Molecular Structure, 834 (2007) 435-444.

[210] S. Chen, P. Shen, D. Gan, Growth kinetics of sintered NiO/ZrO_2 (5 mol.% Y_2O_3) composites, Materials Science and Engineering: A, 158 (1992) 251-258.

[211] M.H. Youn, J.G. Seo, J.C. Jung, S. Park, D.R. Park, S.-B. Lee, I.K. Song,

Hydrogen production by auto-thermal reforming of ethanol over Ni catalyst supported on ZrO_2 prepared by a sol–gel method: Effect of H_2O/P123 mass ratio in the preparation of ZrO_2, Catalysis Today, 146 (2009) 57-62.

[212] J. Chen, Q. Wu, J. Zhang, J. Zhang, Effect of preparation methods on structure and performance of $Ni/Ce_{0.75}Zr_{0.25}O_2$ catalysts for CH_4–CO_2 reforming, Fuel, 87 (2008) 2901-2907.

[213] M. Rezaei, S.M. Alavi, S. Sahebdelfar, L. Xinmei, L. Qian, Z.-F. Yan, CO_2− CH_4 Reforming over Nickel Catalysts Supported on Mesoporous Nanocrystalline Zirconia with High Surface Area, Energy & fuels, 21 (2007) 581-589.

[214] D. Baudouin, U. Rodemerck, F. Krumeich, A. de Mallmann, K.C. Szeto, H. Ménard, L. Veyre, J.-P. Candy, P.B. Webb, C. Thieuleux, Particle size effect in the low temperature reforming of methane by carbon dioxide on silica-supported Ni nanoparticles, Journal of catalysis, 297 (2013) 27-34.

[215] M.A. Naeem, A.S. Al-Fatesh, W.U. Khan, A.E. Abasaeed, A.H. Fakeeha, Syngas production from dry reforming of methane over nano Ni polyol catalysts, International Journal of Chemical Engineering and Applications, 4 (2013) 315.

[216] K.Y. Koo, H.-S. Roh, U.H. Jung, D.J. Seo, Y.-S. Seo, W.L. Yoon, Combined H_2O and CO_2 reforming of CH_4 over nano-sized Ni/MgO-Al_2O_3 catalysts for synthesis gas production for gas to liquid (GTL): Effect of Mg/Al mixed ratio on coke formation, Catalysis Today, 146 (2009) 166-171.

[217] V. Choudhary, S. Mulla, B. Uphade, Oxidative coupling of methane over alkaline earth oxides deposited on commercial support precoated with rare earth oxides, Fuel, 78 (1999) 427-437.

[218] H. Takano, Y. Kirihata, K. Izumiya, N. Kumagai, H. Habazaki, K. Hashimoto, Highly active Ni/Y-doped ZrO_2 catalysts for CO_2 methanation, Applied Surface Science, 388 (2016) 653-663.

[219] W. Li, Z. Zhao, G. Wang, Modulating morphology and textural properties of ZrO_2 for supported Ni catalysts toward dry reforming of methane, AIChE Journal, 63 (2017) 2900-2915.

[220] J.D.A. Bellido, E.M. Assaf, Effect of the Y_2O_3–ZrO_2 support composition on

nickel catalyst evaluated in dry reforming of methane, Applied Catalysis A: General, 352 (2009) 179-187.

[221] B.-Q. Xu, J.-M. Wei, Y.-T. Yu, Y. Li, J.-L. Li, Q.-M. Zhu, Size Limit of Support Particles in an Oxide-Supported Metal Catalyst: Nanocomposite Ni/ZrO_2 for Utilization of Natural Gas, The Journal of Physical Chemistry B, 107 (2003) 5203-5207.

[222] Y.J.O. Asencios, C.B. Rodella, E.M. Assaf, Oxidative reforming of model biogas over NiO–Y_2O_3–ZrO_2 catalysts, Applied Catalysis B: Environmental, 132-133 (2013) 1-12.

[223] M.A. Goula, N.D. Charisiou, G. Siakavelas, L. Tzounis, I. Tsiaoussis, P. Panagiotopoulou, G. Goula, I.V. Yentekakis, Syngas production via the biogas dry reforming reaction over Ni supported on zirconia modified with CeO_2 or La_2O_3 catalysts, International Journal of Hydrogen Energy, 42 (2017) 13724-13740.

[224] S. Liu, L. Guan, J. Li, N. Zhao, W. Wei, Y. Sun, CO_2 reforming of CH_4 over stabilized mesoporous Ni–CaO–ZrO_2 composites, Fuel, 87 (2008) 2477-2481.

[225] S. Irusta, L.M. Cornaglia, E.A. Lombardo, Hydrogen Production Using Ni–Rh on ZrO_2 as Potential Low-Temperature Catalysts for Membrane Reactors, Journal of Catalysis, 210 (2002) 263-272.

[226] V. García, J.J. Fernández, W. Ruíz, F. Mondragón, A. Moreno, Effect of MgO addition on the basicity of Ni/ZrO_2 and on its catalytic activity in carbon dioxide reforming of methane, Catalysis Communications, 11 (2009) 240-246.

[227] D. Li, K. Nishida, Y. Zhan, T. Shishido, Y. Oumi, T. Sano, K. Takehira, Sustainable Ru-doped Ni catalyst derived from hydrotalcite in propane reforming, Applied Clay Science, 43 (2009) 49-56.

[228] J. Wei, E. Iglesia, Isotopic and kinetic assessment of the mechanism of reactions of CH_4 with CO_2 or H_2O to form synthesis gas and carbon on nickel catalysts, Journal of Catalysis, 224 (2004) 370-383.

[229] U. Oemar, K. Hidajat, S. Kawi, Pd–Ni catalyst over spherical nanostructured Y_2O_3 support for oxy-CO_2 reforming of methane: role of surface oxygen mobility, International Journal of Hydrogen Energy, 40 (2015) 12227-12238.

[230] M. Miyamoto, A. Hamajima, Y. Oumi, S. Uemiya, Effect of basicity of metal

doped ZrO_2 supports on hydrogen production reactions, International Journal of Hydrogen Energy, 43 (2018) 730-738.

[231] Z. Liang, T. Li, M. Kim, A. Asthagiri, J.F. Weaver, Low-temperature activation of methane on the IrO_2(110) surface, Science, 356 (2017) 299-303.

[232] F. Polo-Garzon, D. Pakhare, J.J. Spivey, D.A. Bruce, Dry reforming of methane on Rh-doped pyrochlore catalysts: A steady-state isotopic transient kinetic study, Acs Catalysis, 6 (2016) 3826-3833.

[233] M. García-Diéguez, I. Pieta, M. Herrera, M. Larrubia, L. Alemany, Nanostructured Pt-and Ni-based catalysts for CO_2-reforming of methane, Journal of Catalysis, 270 (2010) 136-145.

[234] J. Guo, H. Lou, H. Zhao, D. Chai, X. Zheng, Dry reforming of methane over nickel catalysts supported on magnesium aluminate spinels, Applied Catalysis A: General, 273 (2004) 75-82.

[235] K.O. Christensen, D. Chen, R. Lødeng, A. Holmen, Effect of supports and Ni crystal size on carbon formation and sintering during steam methane reforming, Applied Catalysis A: General, 314 (2006) 9-22.

[236] Y. Kathiraser, W. Thitsartarn, K. Sutthiumporn, S. Kawi, Inverse $NiAl_2O_4$ on $LaAlO_3$–Al_2O_3: unique catalytic structure for stable CO_2 reforming of methane, The Journal of Physical Chemistry C, 117 (2013) 8120-8130.

[237] K. Sutthiumporn, S. Kawi, Promotional effect of alkaline earth over Ni–La_2O_3 catalyst for CO_2 reforming of CH_4: role of surface oxygen species on H_2 production and carbon suppression, International Journal of Hydrogen Energy, 36 (2011) 14435-14446.

[238] K. Świrk, M.E. Gálvez, M. Motak, T. Grzybek, M. Rønning, P. Da Costa, Syngas production from dry methane reforming over yttrium-promoted nickel-KIT-6 catalysts, International Journal of Hydrogen Energy, 44 (2019) 274-286.

[239] B. Li, W. Su, X. Wang, X. Wang, Alumina supported Ni and Co catalysts modified by Y_2O_3 via different impregnation strategies: Comparative analysis on structural properties and catalytic performance in methane reforming with CO_2, International Journal of Hydrogen Energy, 41 (2016) 14732-14746.

[240] Y.J. Asencios, P.A. Nascente, E.M. Assaf, Partial oxidation of methane on NiO–MgO–ZrO_2 catalysts, Fuel, 97 (2012) 630-637.

[241] W.-P. Dow, Y.-P. Wang, T.-J. Huang, Yttria-stabilized zirconia supported copper oxide catalyst: I. Effect of oxygen vacancy of support on copper oxide reduction, Journal of Catalysis, 160 (1996) 155-170.

[242] T.A. Maia, E.M. Assaf, Catalytic features of Ni supported on CeO_2–ZrO_2 solid solution in the steam reforming of glycerol for syngas production, RSC Advances, 4 (2014) 31142-31154.

[243] C. Imparato, M. Fantauzzi, C. Passiu, I. Rea, C. Ricca, U. Aschauer, F. Sannino, G. D'Errico, L. De Stefano, A. Rossi, Unraveling the Charge State of Oxygen Vacancies in ZrO_{2-x} on the Basis of Synergistic Computational and Experimental Evidence, The Journal of Physical Chemistry C, 123 (2019) 11581-11590.

[244] G.M. Ingo, Origin of Darkening in 8 wt% Yttria—Zirconia Plasma-Sprayed Thermal Barrier Coatings, Journal of the American Ceramic Society, 74 (1991) 381-386.

[245] R. Dębek, M. Motak, M.E. Galvez, P. Da Costa, T. Grzybek, Catalytic activity of hydrotalcite-derived catalysts in the dry reforming of methane: on the effect of Ce promotion and feed gas composition, Reaction kinetics, mechanisms and catalysis, 121 (2017) 185-208.

[246] C. Wang, N. Sun, M. Kang, X. Wen, N. Zhao, F. Xiao, W. Wei, T. Zhao, Y. Sun, The bi-functional mechanism of CH_4 dry reforming over a Ni–CaO–ZrO_2 catalyst: further evidence via the identification of the active sites and kinetic studies, Catalysis Science & Technology, 3 (2013) 2435-2443.

[247] T. Bai, X. Zhang, F. Wang, W. Qu, X. Liu, C. Duan, Coking behaviors and kinetics on HZSM-5/SAPO-34 catalysts for conversion of ethanol to propylene, Journal of Energy Chemistry, 25 (2016) 545-552.

[248] D. Liu, Y. Wang, D. Shi, X. Jia, X. Wang, A. Borgna, R. Lau, Y. Yang, Methane reforming with carbon dioxide over a Ni/ZiO_2–SiO_2 catalyst: Influence of pretreatment gas atmospheres, international journal of hydrogen energy, 37 (2012) 10135-10144.

[249] K.Y. Koo, H.-S. Roh, Y.T. Seo, D.J. Seo, W.L. Yoon, S.B. Park, Coke study on

MgO-promoted Ni/Al_2O_3 catalyst in combined H_2O and CO_2 reforming of methane for gas to liquid (GTL) process, Applied Catalysis A: General, 340 (2008) 183-190.

[250] Y.-H. Wang, H.-M. Liu, B.-Q. Xu, Durable Ni/MgO catalysts for CO_2 reforming of methane: activity and metal–support interaction, Journal of Molecular Catalysis A: Chemical, 299 (2009) 44-52.

[251] X. Wang, Y. Hong, H. Shi, J. Szanyi, Kinetic modeling and transient DRIFTS–MS studies of CO_2 methanation over Ru/Al_2O_3 catalysts, Journal of catalysis, 343 (2016) 185-195.

[252] J. Titus, T. Roussiere, G. Wasserschaff, S. Schunk, A. Milanov, E. Schwab, G. Wagner, O. Oeckler, R. Gläser, Dry reforming of methane with carbon dioxide over NiO–MgO–ZrO_2, Catalysis Today, 270 (2016) 68-75.

[253] S.K. Talkhoncheh, M. Haghighi, Syngas production via dry reforming of methane over Ni-based nanocatalyst over various supports of clinoptilolite, ceria and alumina, Journal of Natural Gas Science and Engineering, 23 (2015) 16-25.

[254] X.E. Verykios, Catalytic dry reforming of natural gas for the production of chemicals and hydrogen, International Journal of Hydrogen Energy, 28 (2003) 1045-1063.

[255] S. Liu, H. Wang, J. Li, N. Zhao, W. Wei, Y. Sun, A facile route to synthesize mesoporous zirconia with ultra high thermal stability, Materials research bulletin, 42 (2007) 171-176.

[256] Z. Miao, Z. Li, C. Suo, J. Zhao, W. Si, J. Zhou, S. Zhuo, One-pot synthesis of Al_2O_3 modified mesoporous ZrO_2 with excellent thermal stability and controllable crystalline phase, Advanced Powder Technology, 29 (2018) 3569-3576.

[257] S. Therdthianwong, A. Therdthianwong, C. Siangchin, S. Yongprapat, Synthesis gas production from dry reforming of methane over Ni/Al_2O_3 stabilized by ZrO_2, International Journal of Hydrogen Energy, 33 (2008) 991-999.

[258] S. Therdthianwong, C. Siangchin, A. Therdthianwong, Improvement of coke resistance of Ni/Al_2O_3 catalyst in CH_4/CO_2 reforming by ZrO_2 addition, Fuel Processing Technology, 89 (2008) 160-168.

[259] H. Li, J. Wang, Study on CO_2 reforming of methane to syngas over Al_2O_3–ZrO_2

supported Ni catalysts prepared via a direct sol–gel process, Chemical Engineering Science, 59 (2004) 4861-4867.

[260] R. Chai, Y. Li, Q. Zhang, G. Zhao, Y. Liu, Y. Lu, Monolithic Ni–MO_x/Ni-foam (M= Al, Zr or Y) catalysts with enhanced heat/mass transfer for energy-efficient catalytic oxy-methane reforming, Catalysis Communications, 70 (2015) 1-5.

[261] N.A. Pechimuthu, K.K. Pant, S.C. Dhingra, Deactivation studies over Ni−K/CeO_2−Al_2O_3 catalyst for dry reforming of methane, Industrial & engineering chemistry research, 46 (2007) 1731-1736.

[262] A.R. McFarlane, I.P. Silverwood, E.L. Norris, R.M. Ormerod, C.D. Frost, S.F. Parker, D. Lennon, The application of inelastic neutron scattering to investigate the steam reforming of methane over an alumina-supported nickel catalyst, Chemical Physics, 427 (2013) 54-60.

[263] K. Singh, J. Rouquerol, G. Bergeret, P. Gallezot, M. Vaarkamp, D. Koningsberger, A. Datye, J. Niemantsverdriet, T. Butz, G. Engelhardt, Characterization of Solid Catalysts: Sections 3.1. 1–3.1. 3, Handbook of heterogeneous catalysis, (1997) 427-582.

[264] S. Corthals, J. Van Nederkassel, J. Geboers, H. De Winne, J. Van Noyen, B. Moens, B. Sels, P. Jacobs, Influence of composition of $MgAl_2O_4$ supported $NiCeO_2ZrO_2$ catalysts on coke formation and catalyst stability for dry reforming of methane, Catalysis today, 138 (2008) 28-32.

[265] C. Li, Y. Fu, G. Bian, T. Hu, Y. Xie, J. Zhan, CO_2 reforming of CH4 over Ni/CeO_2-ZrO_2-Al_2O_3 prepared by hydrothermal synthesis Method, Journal of Natural Gas Chemistry, 12 (2003) 167-177.

[266] W. Ma, F.W. Herbert, S.D. Senanayake, B. Yildiz, Non-equilibrium oxidation states of zirconium during early stages of metal oxidation, Applied Physics Letters, 106 (2015) 101603.

[267] G. Liu, J.A. Rodriguez, J. Hrbek, J. Dvorak, C.H. Peden, Electronic and chemical properties of $Ce_{0.8}Zr_{0.2}O_2$ (111) surfaces: photoemission, XANES, density-functional, and NO_2 adsorption studies, The Journal of Physical Chemistry B, 105 (2001) 7762-7770.

[268] E. Saw, U. Oemar, X. Tan, Y. Du, A. Borgna, K. Hidajat, S. Kawi, Bimetallic Ni–

Cu catalyst supported on CeO_2 for high-temperature water–gas shift reaction: Methane suppression via enhanced CO adsorption, Journal of catalysis, 314 (2014) 32-46.

[269] I. Alirezaei, A. Hafizi, M. Rahimpour, Syngas production in chemical looping reforming process over ZrO_2 promoted Mn-based catalyst, Journal of CO_2 Utilization, 23 (2018) 105-116.

[270] N. Laosiripojana, D. Chadwick, S. Assabumrungrat, Effect of high surface area CeO_2 and Ce-ZrO_2 supports over Ni catalyst on CH_4 reforming with H_2O in the presence of O2, H2, and CO2, Chemical Engineering Journal, 138 (2008) 264-273.

[271] B.-Q. Xu, J.-M. Wei, Y.-T. Yu, Y. Li, J.-L. Li, Q.-M. Zhu, Size limit of support particles in an oxide-supported metal catalyst: Nanocomposite Ni/ZrO_2 for utilization of natural gas, The Journal of Physical Chemistry B, 107 (2003) 5203-5207.

[272] H. Forutan, E. Karimi, A. Hafizi, M. Rahimpour, P. Keshavarz, Expert representation chemical looping reforming: A comparative study of Fe, Mn, Co and Cu as oxygen carriers supported on Al_2O_3, Journal of Industrial and Engineering Chemistry, 21 (2015) 900-911.

[273] N. Wang, W. Chu, T. Zhang, X.-S. Zhao, Manganese promoting effects on the Co–Ce–Zr–O_x nano catalysts for methane dry reforming with carbon dioxide to hydrogen and carbon monoxide, Chemical Engineering Journal, 170 (2011) 457-463.

[274] S.-H. Seok, S.H. Choi, E.D. Park, S.H. Han, J.S. Lee, Mn-promoted Ni/Al2O3 catalysts for stable carbon dioxide reforming of methane, Journal of Catalysis, 209 (2002) 6-15.

[275] A.E.C. Luna, M.E. Iriarte, Carbon dioxide reforming of methane over a metal modified Ni-Al_2O_3 catalyst, Applied Catalysis A: General, 343 (2008) 10-15.

[276] C. Shi, P. Zhang, Effect of a second metal (Y, K, Ca, Mn or Cu) addition on the carbon dioxide reforming of methane over nanostructured palladium catalysts, Applied Catalysis B: Environmental, 115 (2012) 190-200.

[277] Y. Wang, Q. Zhao, Y. Wang, C. Hu, P. Da Costa, One-step synthesis of highly active and stable Ni-ZrO_x for dry reforming of methane, Industrial & Engineering Chemistry Research, (2020).

[278] C. Cannilla, G. Bonura, E. Rombi, F. Arena, F. Frusteri, Highly effective $MnCeO_x$

catalysts for biodiesel production by transesterification of vegetable oils with methanol, Applied Catalysis A: General, 382 (2010) 158-166.

[279] C. Cannilla, G. Bonura, F. Arena, F. Frusteri, Catalytic Behaviour of $MnZrO_x$ System for Heterogenous Biodiesel Production, The Open Renewable Energy Journal, 5 (2012).

[280] S.-H. Seok, S.H. Han, J.S. Lee, The role of MnO in Ni/MnO-Al_2O_3 catalysts for carbon dioxide reforming of methane, Applied Catalysis A: General, 215 (2001) 31-38.

[281] X. Li, J.S. Chang, M. Tian, S.E. Park, CO_2 reforming of methane over modified Ni/ZrO_2 catalysts, Applied organometallic chemistry, 15 (2001) 109-112.

[282] J.-H. Kim, D.J. Suh, T.-J. Park, K.-L. Kim, Effect of metal particle size on coking during CO_2 reforming of CH_4 over Ni–alumina aerogel catalysts, Applied Catalysis A: General, 197 (2000) 191-200.

[283] Z. Liu, S.D. Senanayake, J.A. Rodriguez, Elucidating the interaction between Ni and CeO_x in ethanol steam reforming catalysts: A perspective of recent studies over model and powder systems, Applied Catalysis B Environmental, 197 (2016) 184-197.

[284] Y. Wang, M. Chen, Z. Yang, T. Liang, S. Liu, Z. Zhou, X. Li, Bimetallic Ni-M (M= Co, Cu and Zn) supported on attapulgite as catalysts for hydrogen production from glycerol steam reforming, Applied Catalysis A: General, 550 (2018) 214-227.

[285] H. Li, C. Rameshan, A.V. Bukhtiyarov, I.P. Prosvirin, V.I. Bukhtiyarov, G. Rupprechter, CO_2 activation on ultrathin ZrO_2 film by H_2O co-adsorption: In situ NAP-XPS and IRAS studies, Surface Science, 679 (2019) 139-146.

[286] Z. Song, X. Bao, U. Wild, M. Muhler, G. Ertl, Oxidation of amorphous Ni–Zr alloys studied by XPS, UPS, ISS and XRD, Applied surface science, 134 (1998) 31-38.

[287] C. Gionco, M.C. Paganini, E. Giamello, R. Burgess, C. Di Valentin, G. Pacchioni, Paramagnetic defects in polycrystalline zirconia: an EPR and DFT study, Chemistry of Materials, 25 (2013) 2243-2253.

[288] G. Lu, S.L. Bernasek, J. Schwartz, Oxidation of a polycrystalline titanium surface by oxygen and water, Surface Science, 458 (2000) 80-90.

[289] Y.J. Asencios, E.M. Assaf, Combination of dry reforming and partial oxidation of methane on NiO–MgO–ZrO_2 catalyst: effect of nickel content, Fuel processing

technology, 106 (2013) 247-252.

[290] F. Pompeo, N.N. Nichio, O.A. Ferretti, D. Resasco, Study of Ni catalysts on different supports to obtain synthesis gas, International Journal of Hydrogen Energy, 30 (2005) 1399-1405.

[291] M.A. Aramendıa, V. Borau, C. Jiménez, A. Marinas, J.M. Marinas, J.R. Ruiz, F.J. Urbano, Magnesium-containing mixed oxides as basic catalysts: base characterization by carbon dioxide TPD–MS and test reactions, Journal of Molecular Catalysis A: Chemical, 218 (2004) 81-90.

[292] S. He, H. Wu, W. Yu, L. Mo, H. Lou, X. Zheng, Combination of CO_2 reforming and partial oxidation of methane to produce syngas over Ni/SiO_2 and Ni–Al_2O_3/SiO_2 catalysts with different precursors, international journal of hydrogen energy, 34 (2009) 839-843.

[293] M.S. Fan, A.Z. Abdullah, S. Bhatia, Catalytic technology for carbon dioxide reforming of methane to synthesis gas, ChemCatChem, 1 (2009) 192-208.

[294] X. Dong, X. Cai, Y. Song, W. Lin, Effect of Transition Metals (Cu, Co and Fe) on the Autothermal Reforming of Methane over Ni/$Ce_{0.2}Zr_{0.1}Al_{0.7}O_{\delta}$ Catalyst, Journal of natural gas chemistry, 16 (2007) 31-36.

[295] W.-J. Jang, J.-O. Shim, H.-M. Kim, S.-Y. Yoo, H.-S. Roh, A review on dry reforming of methane in aspect of catalytic properties, Catalysis Today, 324 (2019) 15-26.

[296] B. Bachiller-Baeza, C. Mateos-Pedrero, M. Soria, A. Guerrero-Ruiz, U. Rodemerck, I. Rodríguez-Ramos, Transient studies of low-temperature dry reforming of methane over Ni-CaO/ZrO_2-La_2O_3, Applied Catalysis B: Environmental, 129 (2013) 450-459.

[297] H.-S. Roh, H. Potdar, K.-W. Jun, Carbon dioxide reforming of methane over co-precipitated Ni–CeO_2, Ni–ZrO_2 and Ni–Ce–ZrO_2 catalysts, Catalysis Today, 93 (2004) 39-44.

[298] N. Sun, X. Wen, F. Wang, W. Peng, N. Zhao, F. Xiao, W. Wei, Y. Sun, J. Kang, Catalytic performance and characterization of Ni–CaO–ZrO_2 catalysts for dry reforming of methane, Applied Surface Science, 257 (2011) 9169-9176.

[299] B. Koubaissy, A. Pietraszek, A. Roger, A. Kiennemann, CO_2 reforming of methane over Ce-Zr-Ni-Me mixed catalysts, Catalysis Today, 157 (2010) 436-439.

[300] S. Corthals, J. Van Nederkassel, H. De Winne, J. Geboers, P. Jacobs, B. Sels, Design of active and stable $NiCeO_2ZrO_2MgAl_2O_4$ dry reforming catalysts, Applied Catalysis B: Environmental, 105 (2011) 263-275.

[301] C. Li, P.-J. Tan, X.-D. Li, Y.-L. Du, Z.-H. Gao, W. Huang, Effect of the addition of Ce and Zr on the structure and performances of Ni–Mo/CeZr–MgAl (O) catalysts for CH_4–CO_2 reforming, Fuel Processing Technology, 140 (2015) 39-45.

[302] W.-J. Jang, D.-W. Jeong, J.-O. Shim, H.-S. Roh, I.H. Son, S.J. Lee, H_2 and CO production over a stable Ni–MgO–$Ce_{0.8}Zr_{0.2}O_2$ catalyst from CO_2 reforming of CH_4, International journal of hydrogen energy, 38 (2013) 4508-4512.

[303] E. Faria, R. Neto, R. Colman, F. Noronha, Hydrogen production through CO_2 reforming of methane over $Ni/CeZrO_2/Al_2O_3$ catalysts, Catalysis Today, 228 (2014) 138-144.

[304] M.-S. Fan, A.Z. Abdullah, S. Bhatia, Utilization of greenhouse gases through carbon dioxide reforming of methane over Ni–Co/MgO–ZrO_2: preparation, characterization and activity studies, Applied Catalysis B: Environmental, 100 (2010) 365-377.

[305] B.M. Nagaraja, D.A. Bulushev, S. Beloshapkin, S. Chansai, J.R. Ross, Potassium-doped Ni–MgO–ZrO_2 catalysts for dry reforming of methane to synthesis gas, Topics in Catalysis, 56 (2013) 1686-1694.

[306] B.M. Nagaraja, D.A. Bulushev, S. Beloshapkin, J.R. Ross, The effect of potassium on the activity and stability of Ni–MgO–ZrO_2 catalysts for the dry reforming of methane to give synthesis gas, Catalysis today, 178 (2011) 132-136.

[307] D.-W. Jeong, W.-J. Jang, J.-O. Shim, H.-S. Roh, I.H. Son, S.J. Lee, The effect of preparation method on the catalytic performance over superior MgO-promoted Ni–$Ce_{0.8}Zr_{0.2}O_2$ catalyst for CO_2 reforming of CH_4, international journal of hydrogen energy, 38 (2013) 13649-13654.

[308] J. Rostrupnielsen, J.B. Hansen, CO_2-reforming of methane over transition metals, Journal of Catalysis, 144 (1993) 38-49.

[309] T. Nakayama, M. Arai, Y. Nishiyama, Dispersion of nickel particles supported on alumina and silica in oxygen and hydrogen, Journal of Catalysis, 87 (1984) 108-115.
[310] T. Osaki, T. Mori, Role of potassium in carbon-free CO_2 reforming of methane on K-promoted Ni/Al_2O_3 catalysts, Journal of Catalysis, 204 (2001) 89-97.

Table des illustrations

Table des tableaux

Annexes

Annex. 1 Abbreviation and symbols

Table annex 1-1 List abbreviation and explanations

Abbreviation	Explanations
DRM	Dry Reforming of Methane
RWGS	Reverse Water-Gas Shift
CCS	Capture of Carbon dioxide and Storage
ILs	Ionic liquids
MOF	Metal-Organic Frameworks
2D COFs	two-dimensional covalent organic frameworks
$Zn_4O(BDC)_3$	ZnO_4 units doped by C, O and H atoms
F-T synthesis	Fischer-Tropsch synthesis
GTL	Gas-to-Liquids Reaction
CNT	Carbon Nanotube
MAS	Mixed Alcohol Synthesis
FWHM	Line Broadening at Half the Maximum Intensity
GHSV	Gas Hourly Space Velocity
BET	N_2 adsorption-desorption
XRD	X-ray diffraction
H_2-TPR	Temperature-Programmed Reduction by H_2
CO_2-TPD	Temperature-Programmed Desorption of CO_2
TGA	Thermogravimetry Analysis
TGA-DSC	Thermogravimetry Analysis coupled
TG-MS	Thermogravimetry Analysis coupled by Mass Spectrometry
TEM	Transmission Electron Microscopy
XPS	X-ray Photoelectron Spectroscopy
ppm	parts per million
WMO	World Meteorological Organization
GWP	Global Warming Potential

Table annex 1-2 List symbols and explanations

Symbols	Explanations
Ni/ZrO_2	10 wt.%Ni/ZrO_2 catalyst prepared by traditional impregnation
5Ni-Zr	5 wt.%$NiO-ZrO_2$ catalysts prepared by one-step synthesis
10Ni-Zr	10 wt.%$NiO-ZrO_2$ catalysts prepared by one-step synthesis
15Ni-Zr	15 wt.% $NiO-ZrO_2$ catalysts prepared by one-step synthesis
$NiO-MgO-ZrO_2$	Mg-promoted 10 wt.%$NiO-ZrO_2$ catalyst
$NiO-ZrO_m-YO_n$	Y-promoted 10 wt.%$NiO-ZrO_2$ catalyst
$10NiO-10Al_2O_3-ZrO_2$	10 wt. %Al-promoted 10 wt.%$NiO-ZrO_2$ catalyst
$10NiO-20Al_2O_3-ZrO_2$	20 wt. %Al-promoted 10 wt.%$NiO-ZrO_2$ catalyst
$10NiO-45Al_2O_3-ZrO_2$	45 wt. %Al-promoted 10 wt.%$NiO-ZrO_2$ catalyst
$10NiO-Al_2O_3$	10 wt.%$NiO-Al_2O_3$ catalyst
$Ni-Mn-ZrO_x$	Mn-promoted 10 wt.%$NiO-ZrO_2$ catalyst
P123	Pluronic P123 amphiphilic block copolymer
$t-ZrO_2$	Tetragonal-ZrO_2
$m-ZrO_2$	Monoclinic-ZrO_2
B-a	Bragg angles
S	stable
D	deactivation
-	No data
d-s	d-spacing
D_{Ni}	The dispersion of nikcle species
I_G/I_D	The crystalline degree of carbon materials
D_p	Pore diameter
S_{BET}	Specific surface area
V_p	Pore volume
ΔH^0	Standard enthalpy of formation
GT	1 GT = $1*10^9$ tons
X_{CO_2}	The conversion of CO_2
X_{CH_4}	The conversion of CH_4